

TECHNISCHE UNIVERSITÄT MÜNCHEN  
TUM School of Engineering and Design

# Efficient and robust interpolation-based model order reduction of vibro-acoustic problems

Quirin Johannes Aumann

Vollständiger Abdruck der von der TUM School of Engineering and Design der Technischen Universität München zur Erlangung des akademischen Grades eines

Doktors der Ingenieurwissenschaften

genehmigten Dissertation.

Vorsitzender: Prof. Dr.-Ing. habil. Fabian Duddeck

Prüfer der Dissertation:

1. Prof. Dr.-Ing. habil. Gerhard Müller
2. Prof. dr. ir. Wim Desmet

Die Dissertation wurde am 24.01.2022 bei der Technischen Universität München eingereicht und durch die TUM School of Engineering and Design am 21.07.2022 angenommen.



# Abstract

The correct assessment of vibration and the resulting radiation of sound is required in many engineering tasks, for example in the design of vehicles, buildings, or machinery. The encountered physical phenomena, commonly known as vibro-acoustics, can be described by mathematical models. Their discretization as numerical models often leads to very large systems which are difficult and costly to evaluate. To reduce this computational cost, surrogate models representing certain aspects of the system's behavior are often employed in engineering practice. However, such models are not universally applicable and require close investigations of the considered original problem. As an alternative, the computational complexity of numerical models can be reduced using techniques from linear algebra. Many of these methods project the original system onto a lower dimensional subspace chosen to contain the desired solution. This is referred to as projection-based model order reduction.

Several state-of-the-art projection-based reduction methods can directly be applied to reduce the computational complexity of vibro-acoustic systems modeling dissipation effects by classical viscous damping. However, many damping materials encountered in vibro-acoustic systems need to be modeled using more complex mathematical models as their damping effect is typically nonlinearly frequency dependent. Examples are viscoelastic or poroelastic materials, which are often employed to improve the acoustic performance of lightweight structures, especially in the design of vehicles and machines. A method to obtain accurate reduced models of such systems is presented. It automatically approximates the nonlinear frequency dependency by a polynomial, thus enabling its efficient reduction. The method is not relying on analytic derivatives and can be employed for different kinds of frequency dependent material parameters without modification.

The prerequisites for the efficient application of model order reduction methods in the design workflow of vibro-acoustic structures are a sufficient accuracy of the obtained surrogate model and the robustness of the reduction procedure. The accuracy of the reduced models is depending on properties for which reasonable values are typically only available from the solution of the original system or not known before the reduction process, such as size of the reduced model or placement of expansion points. Adaptive algorithms can determine these unknown parameters while still requiring less computational resources than the solution of the full order system. The main goal is to obtain procedures which require as few

input parameters as possible, preferably only a frequency range in which the reduced model should be valid. Such adaptive algorithms often use error estimators to obtain appropriate locations for expansion points and to derive a reasonable stopping criterion. This approach is typically employed in greedy methods establishing new expansion points at the location where the approximation error is estimated to be maximal. An alternative method is to consider the locations of the reduced model's eigenvalues. It can be argued that the size of a reduced model might be too small if all its eigenvalues lie in the frequency range where the surrogate should be valid and that its size has therefore to be increased further. Examples for both approaches are presented and applied to different types of vibro-acoustic systems.

The design process of vibro-acoustic structures often includes an optimization regarding certain model parameters. The large size of the original numerical models prohibits the repeated evaluation for many different sets of parameters and also the reduction of each individual parameter realization is not efficient. Reduced models retaining the dependence on certain parameters are therefore required to use them efficiently in an optimization framework. Two approaches relying on the extraction of the features significant for the parametric model from a database are presented and applied to vibro-acoustic systems. One finds the reduced model considering transfer function evaluations of the original system at certain parameter realizations. This method is non-intrusive in terms of that no access to the original system matrices is required. The other approach uses regression methods to obtain near-optimal locations for expansion points for previously not considered parameter realizations. Here, the original system's matrices need to be accessed to compute the reduction basis.

This thesis presents techniques to obtain accurate reduced order models of not necessarily classically damped vibro-acoustic systems and compares them regarding their efficiency. If applicable, the methods are employed on different types of vibro-acoustic systems. A focus is put on the robustness of adaptive methods requiring as few input parameters as possible. This is a prerequisite to make model order reduction available also to users without expert knowledge regarding the underlying mathematical methods and to use it efficiently in the design process of various vibro-acoustic structures.

# Kurzfassung

Die Bewertung von Schwingungen und der daraus resultierenden Schallabstrahlung ist essenziell für viele technische Aufgabenstellungen, zum Beispiel bei der Konstruktion von Fahrzeugen, Gebäuden oder Maschinen. Die dabei auftretenden physikalischen Phänomene werden als Vibroakustik bezeichnet und können durch mathematische Modelle beschrieben werden. Ihre numerische Diskretisierung führt meist zu sehr großen Gleichungssystemen, deren Auswertung speicher- und zeitintensiv ist. Um den Rechenaufwand zu verringern, werden in der Praxis häufig Ersatzmodelle verwendet, die bestimmte Aspekte des Systemverhaltens darstellen. Solche Modelle sind jedoch nicht universell anwendbar und erfordern eine genaue Untersuchung des ursprünglichen Problems. Alternativ kann die Komplexität numerischer Modelle durch Methoden der linearen Algebra reduziert werden. Viele dieser Methoden projizieren das ursprüngliche System auf einen niedrigdimensionalen Unterraum, der die gewünschte Lösung enthält. Dies wird als projektionsbasierte Modellordnungsreduktion bezeichnet.

Einige solcher Reduktionsmethoden können direkt auf viskos gedämpfte vibroakustische Systeme angewendet werden. Viele in vibroakustischen Systemen verwendete Dämpfungsmaterialien werden jedoch durch komplexere mathematische Modelle beschrieben, da ihre Dämpfungswirkung typischerweise nichtlinear frequenzabhängig ist. Beispiele sind viskoelastische oder poroelastische Materialien, die häufig eingesetzt werden, um die akustischen Eigenschaften von Leichtbaustrukturen, insbesondere bei der Konstruktion von Fahrzeugen und Maschinen, zu verbessern. Es wird eine Methode vorgestellt, um genaue reduzierte Modelle solcher Systeme zu erhalten. Sie approximiert automatisch die nichtlineare Frequenzabhängigkeit durch ein Polynom und ermöglicht so eine effiziente Reduktion. Die Methode ist nicht auf analytische Ableitungen angewiesen und kann ohne Modifikation für verschiedene Arten von frequenzabhängigen Materialparametern eingesetzt werden.

Voraussetzung für den effizienten Einsatz von Modellordnungsreduktionsverfahren im Entwurf vibroakustischer Strukturen ist eine ausreichende Genauigkeit des erhaltenen Ersatzmodells und eine hohe Robustheit des Reduktionsverfahrens. Die Genauigkeit der reduzierten Modelle hängt von Eigenschaften ab, die typischerweise nur aus der Lösung des ursprünglichen Systems abgeleitet werden können oder anderweitig vor dem Reduktionsprozess nicht bekannt sind. Hierzu zählen zum Beispiel die Größe des reduzierten Modells oder die Platzierung

der Stützstellen. Adaptive Algorithmen können diese Unbekannten bestimmen und benötigen dabei weniger Rechenressourcen als eine volle Lösung des ursprünglichen Systems. Für die Anwendung solcher Algorithmen muss vorzugsweise nur der Frequenzbereich, in dem das reduzierte Modell gültig sein soll, definiert werden. Adaptive Algorithmen verwenden häufig Fehlerschätzer, um geeignete Orte für Stützstellen zu erhalten und ein geeignetes Abbruchkriterium abzuleiten. Dieser Ansatz wird typischerweise in Verbindung mit Greedy-Algorithmen angewandt, die neue Stützstellen an der Position des höchsten geschätzten Approximationsfehlers platzieren. Eine alternative Methode besteht darin, die Position und Anzahl der Eigenwerte des reduzierten Modells zu berücksichtigen. Liegen alle Eigenwerte in dem Frequenzbereich, in dem ein reduziertes Modell gültig sein soll, kann mit großer Wahrscheinlichkeit davon ausgegangen werden, dass dessen Dimension zu klein gewählt wurde und sie daher erhöht werden muss. In der Arbeit werden Beispiele für beide Ansätze vorgestellt und auf verschiedene Arten von vibroakustischen Systemen angewandt.

Der Entwurfsprozess von vibroakustischen Strukturen beinhaltet oft eine Optimierung hinsichtlich bestimmter Modellparameter. Eine wiederholte Auswertung hochdimensionaler numerischer Modelle vibroakustischer Systeme für verschiedene Parametersätze ist aufgrund limitierter Rechenzeit oftmals nicht möglich und auch die Reduzierung jeder zu berücksichtigenden Parameterrealisierung ist nicht immer effizient. Daher sind reduzierte Modelle, die die Abhängigkeit von bestimmten Parametern im reduzierten Raum beibehalten, für eine Verwendung in Optimierungsalgorithmen erforderlich. Es werden zwei Ansätze vorgestellt, die auf der Extraktion der für das parametrische Modell signifikanten Merkmale aus einer Datenbank beruhen und auf vibroakustische Systeme angewendet werden. Ein Ansatz berechnet das reduzierte Modell unter Berücksichtigung von Messungen der Übertragungsfunktion des ursprünglichen Systems bei bestimmten Parameterkombinationen. Diese Methode ist nicht intrusiv, da kein Zugriff auf die ursprünglichen Systemmatrizen erforderlich ist. Der andere Ansatz verwendet Regressionsmethoden, um nahezu optimale Positionen für Stützstellen zuvor nicht berücksichtigter Parameterrealisierungen zu erhalten. Hier muss auf die Matrizen des ursprünglichen Systems zugegriffen werden, um die Reduktionsbasis zu berechnen.

In dieser Arbeit werden Verfahren zur Berechnung von Modellen reduzierter Ordnung für nicht zwingend klassisch gedämpfte vibroakustische Systeme vorgestellt und hinsichtlich ihrer Effizienz verglichen. Falls anwendbar, werden die Methoden auf verschiedene Arten von vibroakustischen Systemen angewandt. Ein Schwerpunkt liegt dabei auf der Robustheit adaptiver Methoden, die möglichst wenige Eingabeparameter benötigen. Dies ist eine Voraussetzung, um die Modellordnungsreduktion auch Anwendern ohne Expertenwissen über die zugrundeliegenden mathematischen Methoden zugänglich zu machen und sie effizient im Entwurfsprozess verschiedener vibroakustischer Strukturen einsetzen zu können.

# Acknowledgments

First of all, I would like to thank Prof. Gerhard Müller for his constant support during the projects leading to this thesis and the opportunity to work at the Chair of Structural Mechanics. I am grateful that I had the chance to experience many aspects of academic life while working with the group, especially for the possibility to attend international conferences. In these settings I met interesting and inspiring people and I always returned with new ideas.

I would also like to thank Prof. Wim Desmet for being part of the examination committee. Prof. Desmet gave me the opportunity to stay at his research group at KU Leuven in 2019, for which I am very grateful. I had the chance to meet inspiring scientists working on interesting problems and the work conducted during this stay spawned successive collaborations. Specifically I would like to thank Prof. Elke Deckers and Dr. Stijn Jonckheere for their supervision during the stay and their continued support.

I would also like to thank my mentor Prof. Roland Wüchner for providing me guidance through the project and I gratefully remember our inspiring conversations.

My colleagues at the Chair of Structural Mechanics made it a great work environment. I thank all of them for providing a great atmosphere, for their support on all kinds of work-related issues, and the occasional card-related breaks from work. Especially the conversations with my colleagues Franziska Weber and Matthias Miksch, with whom I shared an office during most of my time at TUM, and Felix Schneider are the basis for many parts of this work.

This work would also not have been possible without the constant support from my family for which I cannot thank them enough. However, my biggest gratitude goes to Dodo, who initially spawned my interest in academic research. She is the person suffering most from this project, as I did not always spend my time wisely and occasionally invested too much of it in this thesis. I cannot express how grateful I am for your patience, you are my recipe for happiness in anyplace.



# Contents

<b>Abstract</b>	<b>III</b>
<b>Kurzfassung</b>	<b>V</b>
<b>Acknowledgments</b>	<b>VII</b>
<b>List of Figures</b>	<b>XII</b>
<b>List of Tables</b>	<b>XV</b>
<b>List of Symbols</b>	<b>XVI</b>
<b>List of Acronyms</b>	<b>XX</b>
<b>1 Introduction</b>	<b>1</b>
1.1 Vibro-acoustic systems . . . . .	1
1.1.1 Examples for vibro-acoustic systems in practice . . . . .	2
1.1.2 Numerical evaluation of vibro-acoustic systems . . . . .	5
1.2 Model order reduction . . . . .	6
1.2.1 Examples for model order reduction in practice . . . . .	7
1.3 Research objectives and achievements . . . . .	8
1.4 Outline of the thesis . . . . .	10
<b>2 Dynamical systems</b>	<b>11</b>
2.1 Mathematical system descriptions . . . . .	12
2.1.1 First-order systems . . . . .	12
2.1.2 Second-order systems . . . . .	14
2.1.3 Transfer functions and poles . . . . .	15
2.2 Vibro-acoustic systems . . . . .	17
2.2.1 Acoustic waves . . . . .	19
2.2.2 Structural vibration . . . . .	21
2.2.3 Poroelastic materials . . . . .	25
2.2.4 Vibro-acoustic coupling conditions . . . . .	30
2.3 Modeling vibro-acoustic systems . . . . .	33
2.3.1 The finite element method for vibro-acoustic systems . . . . .	35
2.3.2 The perfectly matched layer method . . . . .	44
2.4 Analysis of vibro-acoustic systems . . . . .	49
2.4.1 Eigenvalue analysis . . . . .	50
2.4.2 Modal superposition . . . . .	51
2.4.3 Logarithmic scale . . . . .	53

2.5	Numerical examples of vibro-acoustic problems . . . . .	53
2.5.1	Academic example . . . . .	55
2.5.2	Structural vibration . . . . .	55
2.5.3	Sound transmission . . . . .	57
2.5.4	Acoustic scattering . . . . .	58
2.5.5	Coupled poroacoustic system . . . . .	59
<b>3</b>	<b>Model order reduction</b>	<b>61</b>
3.1	Reduction by projection . . . . .	62
3.2	Error assessment . . . . .	63
3.3	Modal reduction . . . . .	66
3.3.1	Modal truncation . . . . .	66
3.3.2	Component mode synthesis . . . . .	67
3.4	Proper orthogonal decomposition . . . . .	69
3.5	Balanced truncation . . . . .	70
3.6	Interpolatory methods . . . . .	74
3.6.1	Second-order Krylov subspaces . . . . .	78
3.6.2	Expansion point selection . . . . .	81
3.6.3	Data-driven interpolatory model reduction . . . . .	85
3.7	Parametric model order reduction . . . . .	87
<b>4</b>	<b>Model order reduction for vibro-acoustic systems</b>	<b>91</b>
4.1	Applicability of model order reduction methods . . . . .	91
4.1.1	Structural vibration . . . . .	95
4.1.2	Sound transmission . . . . .	100
4.1.3	Acoustic scattering . . . . .	101
4.1.4	Coupled poroacoustic system . . . . .	103
4.1.5	Conclusive remarks . . . . .	104
4.2	Reduction of systems with nonlinear frequency dependent terms . . . . .	106
4.2.1	Automatic approximation of frequency dependent nonlinearities . . . . .	109
4.2.2	Model order reduction with higher order Krylov subspaces . . . . .	112
4.2.3	Numerical experiments . . . . .	113
4.2.4	Conclusive remarks . . . . .	120
4.3	Frequency-limited approximation of vibro-acoustic systems . . . . .	121
4.3.1	Optimization using intermediate models . . . . .	124
4.3.2	Choice of initial expansion points . . . . .	127
4.3.3	Conclusive remarks . . . . .	129
4.4	Automatic model order reduction for vibro-acoustic systems . . . . .	131
4.4.1	Estimation of the approximation error . . . . .	132
4.4.2	A greedy algorithm for automatic model order reduction . . . . .	135
4.4.3	Frequency windowing for automatic model order reduction . . . . .	139
4.4.4	Automatic approximation in a frequency range using SO-IRKA . . . . .	143
4.4.5	Conclusive remarks . . . . .	150

---

<b>5</b>	<b>Parametric model order reduction for vibro-acoustic systems</b>	<b>151</b>
5.1	Parametric model order reduction using the Loewner framework . . . . .	152
5.1.1	The parametric model order reduction algorithm . . . . .	156
5.1.2	Numerical examples . . . . .	156
5.1.3	Concluding remarks . . . . .	160
5.2	Prediction of near optimal interpolation points for parametric model order reduction . . . . .	160
5.2.1	Regression methods . . . . .	161
5.2.2	Parametric model order reduction algorithm . . . . .	163
5.2.3	Numerical experiments . . . . .	167
5.2.4	Conclusive remarks . . . . .	173
<b>6</b>	<b>Conclusions and Outlook</b>	<b>175</b>
6.1	Assessment of research objectives . . . . .	175
6.2	Suggestions for future work . . . . .	178
<b>A</b>	<b>Appendix</b>	<b>181</b>
A.1	Equivalent first-order systems for second-order systems . . . . .	181
A.2	A decomposed FE formulation for poroelastic materials . . . . .	181
	<b>Bibliography</b>	<b>183</b>

# List of Figures

1.1	Example of a locally resonant material. . . . .	3
1.2	Example for a unit cell with a porous material. . . . .	4
1.3	Example for acoustic radiation and scattering. . . . .	5
2.1	Sketch of a vibro-acoustic system. . . . .	18
2.2	Comparison between the stress strain relation of an elastic and a viscoelastic material. . . . .	24
2.3	Sketch of a vibro-acoustic system including normal vectors. . . . .	30
2.4	Fluid structure fluid coupling of a plate like structure $\Omega_e$ separating two individual acoustic cavities $\Omega_{a_1}$ and $\Omega_{a_2}$ . . . . .	31
2.5	Determination of Rayleigh damping parameters $\alpha$ and $\beta$ . . . . .	39
2.6	The concept of PML as an absorbing boundary condition. . . . .	46
2.7	The effect of complex coordinate stretching on a one dimensional wave. . . . .	47
2.8	Sketch of the locally conformal PML. . . . .	47
2.9	Sketch and transfer function of the cantilever beam model. . . . .	55
2.10	Sketch of the plate model. The TVAs are depicted in blue. . . . .	56
2.11	Transfer functions of both plate models with different damping mechanisms. . . . .	57
2.12	Sketch and transmission loss of the sound transmission problem. . . . .	57
2.13	Transfer function of the sound transmission problem. . . . .	58
2.14	Sketch and transfer function of the “radiattinger” model. . . . .	59
2.15	Sketch and transfer function of the poroacoustic model. . . . .	60
3.1	Illustration of the MORscore concept. . . . .	65
3.2	Transfer function and relative error of a reduced model of the cantilever beam obtained from the dominant pole algorithm. . . . .	68
3.3	Transfer function and relative error of a reduced model of the cantilever beam obtained from a POD. . . . .	71
3.4	Transfer function and relative error of a reduced model of the cantilever beam obtained from BT. . . . .	75
3.5	Transfer functions and relative errors of reduced models of the cantilever beam obtained from moment matching. . . . .	81
3.6	Transfer functions and relative errors of reduced models of the cantilever beam obtained from IRKA. . . . .	84
3.7	Transfer functions and relative errors of reduced models of the cantilever beam obtained from the Loewner framework. . . . .	87
4.1	MORscore $\mu(250; 10^{-6})$ of all employed reduction and projection methods for the plate with hysteretic damping. . . . .	96

4.2	Relative $\mathcal{L}_\infty$ -error for reduced models of the plate model with hysteretic damping computed by several reduction methods and <i>osimaginput</i> projection. . . . .	96
4.3	MORscore $\mu(250; 10^{-16})$ of all employed reduction and projection methods for the proportionally damped plate. . . . .	97
4.4	Relative $\mathcal{L}_\infty$ -error for reduced models of the plate model with proportional damping computed by several reduction methods. . . . .	98
4.5	Comparison of original and reduced transfer functions as well as relative errors for reduced models of the proportionally damped plate. . . . .	98
4.6	Transfer functions and relative errors for the proportionally damped plate reduced with <i>SO-BT</i> . . . . .	99
4.7	MORscore $\mu(250; 10^{-16})$ of all employed reduction and projection methods for the proportionally damped plate with a single output. . . . .	100
4.8	MORscore $\mu(100; 10^{-16})$ of all employed reduction and projection methods for the sound transmission problem. . . . .	100
4.9	Comparison of the relative $\mathcal{L}_\infty$ -error for reduced models of the sound transmission problem . . . . .	101
4.10	MORscore $\mu(200; 10^{-16})$ of all employed reduction and projection methods for the scattering problem. . . . .	102
4.11	Relative $\mathcal{L}_\infty$ -error for reduced models of the acoustic scattering problem computed by several reduction methods. . . . .	103
4.12	Reduced transfer functions with relative errors for the scattering problem. . . . .	104
4.13	MORscore $\mu(1e - 16; 200)$ of all employed reduction and projection methods for the poroacoustic system. . . . .	105
4.14	Relative $\mathcal{L}_\infty$ -error for reduced models of the poroacoustic system. . . . .	105
4.15	Real and imaginary parts of effective bulk modulus and viscous drag. . . . .	114
4.16	Approximation error of the original and modified poroacoustic models. . . . .	115
4.17	Approximation errors for different $k$ compared to the Neumann expansion error. . . . .	116
4.18	The maximum relative error of reduced models of different sizes and Krylov subspace orders. . . . .	117
4.19	The maximum relative error of reduced models of different sizes and Krylov subspace orders over the required computation time. . . . .	118
4.20	Approximation error of a reduced model approximating the poroacoustic system. . . . .	118
4.21	A sketch of the sandwich beam with viscoelastic core. The steel face sheets are depicted gray, the viscoelastic core orange. . . . .	119
4.22	The maximum relative error of reduced models of the sandwich beam. . . . .	120
4.23	Transfer functions and approximation errors of the sandwich beam model. . . . .	121
4.24	Transfer functions of the sound transmission model and the model reduced with SO-IRKA as well as relative error. . . . .	124
4.25	Transfer functions of the sound transmission model and the model reduced with SO-IRKA valid in a specified frequency range as well as relative error. . . . .	125
4.26	Transfer functions of the sound transmission model and the model reduced with confined SO-IRKA valid in a specified frequency range as well as relative error. . . . .	127
4.27	Transfer functions of the sound transmission model and the model reduced with SO-IRKA using the mode count. . . . .	130

4.28	Beam model reduced with algorithm 4.3. . . . .	137
4.29	Relative errors of the reduced models of the double plate acoustic cavity model. . . . .	139
4.30	Relative errors of the reduced models for the sound transmission model computed with algorithm 4.3 and different error estimators. . . . .	140
4.31	Comparison of required computation time and resulting reduced order to the obtained maximum relative errors for the starting configuration with $n_s = 4$ . . . . .	144
4.32	Comparison of required computation time and resulting reduced order to the obtained maximum relative errors for the starting configuration with $n_s = 5$ . . . . .	144
4.33	Comparison of required computation time and resulting reduced order to the obtained maximum relative errors for the starting configuration with $n_s = 6$ . . . . .	144
4.34	Transfer functions and relative errors of two reduced models of the cantilevered beam obtained from algorithm 4.5. . . . .	147
4.35	Transfer functions and relative errors of reduced models of the sound transmission problem valid in $\zeta_c = 2\pi [1, 500]$ obtained from the adaptive algorithms. . . . .	148
4.36	Transfer functions and relative errors of reduced models of the sound transmission problem valid in $\zeta_c = 2\pi [700, 1000]$ obtained from the adaptive algorithms. . . . .	149
5.1	The frequency response functions of a parametric beam evaluated at different cross section heights $a$ . . . . .	153
5.2	Beam model reduced with the parametric Loewner framework. . . . .	158
5.3	Plate with ABH and applied constrained layer damping (orange). . . . .	159
5.4	Frequency response function of the parametric reduced plate model. . . . .	159
5.5	The absolute value of the first expansion point of a cantilevered beam. . . . .	165
5.6	The required orders for IRKA to compute a reduced model of a cantilevered beam valid up to 10 kHz. . . . .	166
5.7	Transfer functions of two beam models at different parameter samples. . . . .	169
5.8	NRMSE for the reduced models obtained with expansion points from $k$ NN, MPR, and SVR models with parameters from test data from $\mathcal{P}_1$ . . . . .	169
5.9	NRMSE for the reduced models obtained with expansion points from $k$ NN and MPR models with parameters from test data from $\mathcal{P}_2$ . . . . .	170
5.10	Transfer functions and relative errors for one dataset directly reduced with SO-IRKA and with near optimal expansion points. . . . .	171
5.11	Sketch of the 2d acoustic cavity. . . . .	172
5.12	Transfer functions of two cavity models at different parameters. . . . .	172
5.13	NRMSE for the cavity reduced models obtained with expansion points from $k$ NN, MPR, and SVR models with parameters from the test dataset. . . . .	173

## List of Tables

2.1	Material parameters for poroelastic materials described by the Biot theory.	29
2.2	Material properties considered for air and interstitial fluid. . . . .	60
2.3	Material properties for the two employed poroelastic materials. . . . .	60
3.1	Second-order balanced truncation formulas. . . . .	74
4.1	Comparison of reduced models for the vibrating beam computed with algorithm 4.3 and different error estimators. . . . .	136
4.2	Comparison of reduced models for the sound transmission problem computed with algorithm 4.3 and different error estimators. . . . .	138
4.3	Comparison of reduced models of the sound transmission problem valid in a specific frequency range computed with algorithm 4.3. . . . .	140
4.4	Results of the adaptive algorithm applied to the poroacoustic model . . . . .	143
4.5	Comparison of the different reduced models valid in $\varsigma_c = 2\pi [1, 500]$ . . . . .	148
4.6	Comparison of the different reduced models valid in $\varsigma_c = 2\pi [700, 1000]$ . . . . .	150
5.1	Parameter ranges, number of samples, and sample distribution for the two beam datasets. . . . .	168

# List of Symbols

Vectors are given in bold lowercase Latin letters; matrices in bold uppercase Latin letters; tensors in bold lowercase Greek letters. Real numbers are denoted by  $\mathbb{R}$ , complex numbers by  $\mathbb{C}$ .

$\mathbf{i}$	Imaginary unit $\mathbf{i} = \sqrt{-1}$
$\text{Re}(\square)$	Real part of a complex number
$\text{Im}(\square)$	Imaginary part of a complex number
$\bar{\square}$	Complex conjugate
$\square^T$	Transpose
$\square^H$	Hermitian transpose
$\cdot$	Scalar product
$\otimes$	Tensor product
$\circ$	Hadamard product
$\nabla \cdot$	Divergence
$\nabla \times$	Curl
$\Delta$	Laplacian operator
$ \square $	Absolute value
$\ \square\ $	Norm
$\text{diag}(m_1 \ \cdots \ m_n)$	Diagonal matrix
$\text{rank}(\mathbf{M})$	Rank of matrix $\mathbf{M}$
$\text{span}(\mathbf{V})$	Span of vectors in $\mathbf{V}$
$\text{trace}(\mathbf{M})$	Trace of matrix $\mathbf{M}$
$\check{\square}$	Quantity in time domain
$\dot{\square}$	First derivative with respect to time
$\ddot{\square}$	Second derivative with respect to time

## Greek letters

$\alpha$	$s^{-1}$	Rayleigh damping mass parameter	
$\alpha_{\infty}$		Tortuosity	
$\beta$	s	Rayleigh damping stiffness parameter	
$\Gamma$		Problem boundary	
$\gamma$		Heat capacity	
$\delta_{ij}$		Kronecker delta	
$\epsilon$		Approximation error	
$\epsilon$		Strain vector	
$\epsilon$		Volumetric strain	
$\eta$		Loss factor	$\eta = 2\xi$
$\Lambda$	m	Viscous characteristic length	
$\Lambda'$	m	Thermal characteristic length	
$\lambda$		Eigenvalue	
$\lambda$	m	Also wave length	
$\lambda$	Pa	Also Lamé's first parameter	
$\mu$	$N\ s\ m^{-2}$	Viscosity	
$\mu(r_{\max}; \epsilon_{\text{ref}})$		MORscore regarding $r_{\max}$ and $\epsilon_{\text{ref}}$	
$\nu$		Poisson ratio	
$\xi$		Fraction of critical damping	$\xi = \frac{\eta}{2}$
$\rho$	$kg\ m^{-3}$	Density	
$\Sigma$		Dynamical system	
$\sigma$		Stress vector	
$\sigma(\mathbf{M})$		Singular values of matrix $\mathbf{M}$	
$\sigma$	$N\ s\ m^{-2}$	Flow resistivity	
$\varsigma_c$		Convergence interval	
$\phi$		Porosity	
$\psi$		Stretching function for a PML	
$\Omega$		Problem domain	
$\omega$	$rad\ s^{-1}$	Angular frequency	

## Latin letters

<b>A</b>		State matrix of a descriptor system	
<i>A</i>	$\text{m Pa}^{-1} \text{s}^{-1}$	Admittance	
<b>B</b>		Input matrix of a descriptor system	
<b>B</b>		Also matrix of shape function derivatives	
<b>b</b>		Body forces	
<b>C</b>		Damping matrix of a second-order system	
<b>C</b>		Also output matrix of a descriptor system	
<i>c</i>	$\text{m s}^{-1}$	Wave speed	
<b>D</b>		Feedthrough matrix of a descriptor system	
<b>D</b>		Also constitutive matrix	
<b>E</b>		Descriptor matrix of a descriptor system	
<i>E</i>	Pa	Young's modulus	
<i>e</i>		Euler's number	$e = \sum_{k=0}^{\infty} \frac{1}{k!}$
<b>F</b>		Input matrix of a second-order system	
<i>f</i>	Hz	Frequency	
<b>f</b>		Right tangential interpolation directions	
<b>G</b>		Output matrix of a second-order system	
<i>G</i>	Pa	Shear modulus, Lamé's second parameter	
$\mathcal{G}_r$		Krylov space of size $r$	
<b>g</b>		Left tangential interpolation directions	
<b>H</b> ( <i>s</i> )		Transfer function	
<b>I</b>		Identity matrix	
<b>K</b>		Stiffness matrix of a second-order system	
<i>K</i>	Pa	Bulk modulus	
$\widetilde{K}_f$		Effective bulk modulus of a Biot material	
<i>k</i>	$\text{rad m}^{-1}$	Wavenumber	$k = \frac{2\pi}{\lambda}$
<b>L</b>		Strain-displacement relation matrix	
$\mathbb{L}$		Loewner matrix	
<b>M</b>		Mass matrix of a second-order system	
<i>m</i>		Number of system inputs	
<b>N</b>		Matrix of shape functions	
<b>n</b>		Normal vector	
<i>n</i>		System order	
<b>P</b>		Controllability Gramian	
$P_0$	Pa	Standard pressure	

---

<b>p</b>		Vector of parameters	
$p$		Number of system outputs	
$p$	Pa	Also pressure	
$Pr$		Prandtl number	
<b>Q</b>		Observability Gramian	
<b>r</b>		Location in space	$\mathbf{r} = [x \ y \ z]^T$
$r$		Reduced order	
$s$	$\text{rad s}^{-1}$	Complex frequency	
$\mathcal{S}_r$		Second-order Krylov space of size $r$	
$\mathcal{S}_r^{(k)}$		$k$ -order Krylov space of size $r$	
$t$	s	Time	
<b>u</b>		System input	
<b>u</b>	m	Also displacement	
<b>V</b>		Right projection matrix	
<b>v</b>		Right eigenvector	
<b>v</b>	$\text{m s}^{-1}$	Velocity	
$V$	$\text{m}^3$	Volume	
<b>W</b>		Left projection matrix	
<b>w</b>		Left eigenvector	
<b>w</b>		Vector of test functions	
<b>x</b>		State vector	
<b>y</b>		System output	

# List of Acronyms

AAA	Adaptive Antoulas-Anderson
ABC	Absorbing boundary condition
BEM	Boundary element method
BT	Balanced truncation
CIRKA	Confined iterative rational Krylov algorithm
CMS	Component mode synthesis
DtN	Dirichlet-to-Neumann
FETI	Finite element tearing and interconnecting
FEM	Finite element method
IE	Infinite element
IRKA	Iterative rational Krylov algorithm
JCAM	Johnson-Champoux-Allard model
$k$ NN	$k$ -nearest neighbor
MIMO	Multi-input/Multi-output system
MOR	Model order reduction
MPR	Multivariate polynomial regression
NRMSE	Normalized root mean square error
PML	Perfectly matched layer
PMOR	Parametric model order reduction
POD	Proper orthogonal decomposition
SBEM	Stochastic boundary element method
SEA	Statistical energy analysis
SISO	Single-input/Single-output system
SOAR	Second-order Arnoldi procedure
SO-IRKA	Second-order IRKA
SVD	Singular value decomposition
SVR	Support vector regression
TF-IRKA	Transfer function IRKA
TOAR	Two-level orthogonal Arnoldi procedure

---

WCAWE	Well-conditioned asymptotic waveform evaluation
WFEM	Wave finite element method

## Model order reduction strategies

<i>equi</i>	Equidistant sampling with interpolation order 1
<i>avg</i>	Oversampling with averaging
$\mathcal{L}_\infty$	Oversampling with greedy subspace selection
<i>minrel</i>	Determination of dominant subspaces from oversampling
<i>SO-BT</i>	Second-order balanced truncation
<i>POD</i>	Proper orthogonal decomposition
<i>sp</i>	Structure preserving presampling for second-order systems
<i>soa</i>	Structure preserving presampling with higher interpolation orders
<i>tsimag</i>	Complex-valued double-sided projection
<i>tsreal</i>	Real-valued double-sided projection
<i>osimaginput</i>	Complex-valued single-sided projection regarding input
<i>osrealinput</i>	Real-valued single-sided projection regarding input
<i>osimagoutput</i>	Complex-valued single-sided projection regarding output
<i>osrealoutput</i>	Real-valued single-sided projection regarding output
<i>v</i>	Velocity balancing
<i>fv</i>	Free-velocity balancing
<i>pv</i>	Position-velocity balancing
<i>vp</i>	Velocity-position balancing
<i>p</i>	Position balancing
<i>so</i>	Second-order balancing



# 1 Introduction

We are constantly surrounded by sound and noise coming from a variety of sources. Two main mechanisms generating sound are turbulent airflow—coming from wind, air conditioning, or passing vehicles, among others—and radiation of vibrating structures—for example machines, building ceilings and floors, or the membrane in loudspeakers. Often, these sounds are generated on purpose, for example in musical instruments or the human voice, but in many cases, the produced sound is an undesired byproduct of other mechanisms, often structural vibration. These sounds are considered as noise and a constant exposure to noise is known to be a large factor in the development of a variety of diseases [192, 244]. It is therefore be a major goal to prevent unnecessary noise, especially in densely populated areas and places where people are required to stay for a longer time, for example their workplaces.

## 1.1 Vibro-acoustic systems

Vibro-acoustic systems help to understand the processes involved in the creation of noise caused by the mechanical vibration of elastic structures. Under certain circumstances, the vibration energy is radiated into the acoustic fluid surrounding the elastic structure and can then be perceived as sound (or noise). The reverse effect is that pressure oscillations in the acoustic fluid excite a structure, causing structural vibrations. Both is known as the vibro-acoustic effect. The radiation effect is, for example, the basis of the functional principle of loudspeakers, where electric impulses excite a membrane, the vibration of which is causing the air in its vicinity to oscillate and thus generates sound. The reverse effect is the basis of many microphones, where the oscillating air is exciting a membrane inside the microphone, which can then be translated to, for example, electric impulses. Apart from these applications, where these mechanisms are utilized, machines and vehicles emit noise caused by vibration of parts of their structure, which is mostly undesirable. Assessing the vibration properties regarding possible radiation of noise and an accurate modeling of the vibro-acoustic mechanisms is therefore an important task during the design of structures which are aimed to be optimal regarding their vibration and acoustic behavior. The focus of the following work will be put on techniques allowing an efficient assessment and evaluation

of vibro-acoustic systems.

Numerical models are a common choice to analyze vibro-acoustic systems, as they are more flexible than physical models and can be modified more easily. An essential mechanism, which often needs to be assessed and the structures need to be optimized for, is the dissipation of energy inside vibro-acoustic systems. To reduce structural vibration, damping measures dissipating the spurious vibration energy are employed. Mathematical models are available to describe their dynamic behavior and allow the assessment of their effect on the original system. A considerable amount of research has been conducted in the past to establish models being able to describe the physical effects governing vibro-acoustic systems [96]. In the following, exemplary application cases for vibro-acoustic systems are outlined.

### 1.1.1 Examples for vibro-acoustic systems in practice

**Locally resonant materials** A main prerequisite for materials and structures used in the design of vehicles is their high stiffness while weighing as little as possible. The high stiffness is crucial for structural integrity, while the low weight is favorable in terms of energy consumption of the vehicle. However, this high ratio of stiffness to mass leads to unfavorable vibration and acoustic properties and the structures are prone to emit noise in an audible frequency spectrum. Adding mass to a system is a classic method to increase the impedance in certain frequency bands which leads to more favorable vibration behavior. However, this contradicts the design goal of having a lightweight structure. Another measure is to add absorbing materials dissipating the acoustic energy. Depending on the nature of the excitation, a large amount of such materials needs to be added in order to have the desired effect. These space requirements can often be met if slender structures are required. An alternative idea, which is further promoted by the emerging possibilities of additive manufacturing (i.e. “3d printing”), is to introduce locally resonant substructures which are able to dissipate vibration energy in a desired frequency range. Such structures are often referred to as “meta-materials” [84, 185].

An established idea is to attach oscillating mass-spring-systems, so called “tuned mass dampers” or “tuned vibration absorbers”, to the host structure. These substructures are tuned to a specific frequency and dissipate vibration energy if the host structure is vibrating at frequencies near of this tuning frequency. The concept of tuned mass dampers has applications in civil engineering [242], for example to modify the vibration response of the London Millennium Bridge [170]. The emergence of additive manufacturing made it possible to manufacture such tuned vibration absorbers in much smaller scales such that they can be attached to, for example, honeycomb structures being used in aircraft fuselages [84, 144, 185]. Such periodically distributed microstructures are able to change the vibration

properties of the host structure in a favorable way. An example is sketched in fig. 1.1.

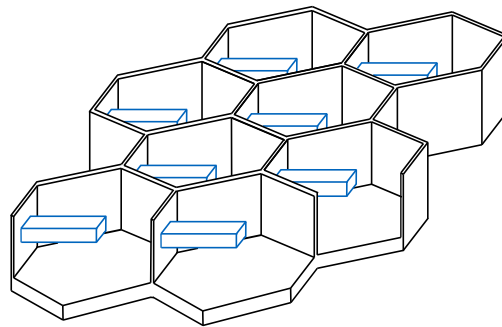


**Figure 1.1:** Example of a locally resonant material. A honeycomb panel acts as the host structure, the local resonance is introduced by cantilevered beams (depicted in blue) added to each cell of the honeycomb [144].

An alternative approach to designing locally resonant materials is to include local thickness variations in the host structure. By gradually reducing the thickness of a plate, the wave speed decreases while the vibration amplitude increases. This may sound undesirable, but as these effects are highly localized, this surplus energy can be dissipated by using either an absorbing material or some other dissipative measure. The thickness variation is required to be smooth such that the waves are not reflected at its boundary and is often following a circular pattern to further minimize reflection. The resulting substructure is often termed “acoustic black hole” [86, 159, 207].

**Poroelastic materials for sound absorption** Porous materials are a typical choice to dissipate acoustic energy in cavities such as vehicle interiors or rooms. Such materials consist of an elastic solid skeleton, which is surrounded by a fluid filling the material’s pores. The energy dissipation inside porous materials is governed by structural damping of the elastic frame, thermal losses, and viscous losses due to the sub-wavelength dimensions of the pores [222]. These complex coupling effects can be described by a variety of models, the Biot-Allard theory being a prominent example [5, 58, 59]. Porous foams are often applied in combination with slit gypsum plates to increase sound absorption or to be able to control undesired sound reflections in rooms.

If applied as sound absorbing materials without attached plates, the main restriction is that at least a material thickness of one fourth of the wavelength of the waves to be attenuated is required to observe the dissipation effect [5]. This makes these materials ineffective for cases where a low frequent excitation has to be damped. Recently, there have been efforts to design porous materials being able to dissipate energy also for low frequent excitation by adding resonant inclusions as substructures. Several approaches have been proposed, for example using Helmholtz resonators [1] or mass-spring-systems [188]. Another

approach is to combine a porous material for the absorption of high frequent excitation with a tuned vibration absorber to attenuate low frequent excitation. This concept is exemplarily illustrated in fig. 1.2, where a unit cell consisting of two metal sheets surrounding a porous material and an air gap is sketched. A periodic assembly of these unit cells forms a plate-like structure which can, for example, be used attenuate noise in passenger cabins of vehicles [182].

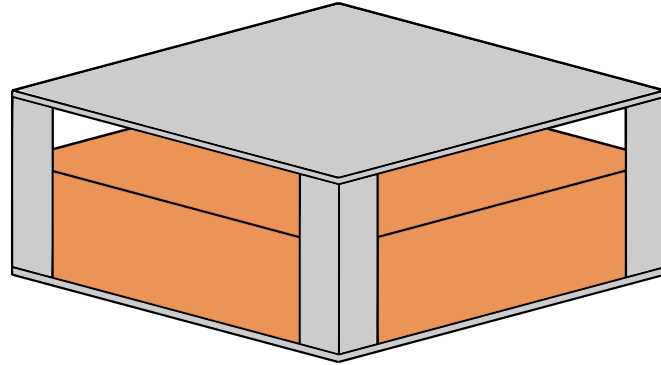


**Figure 1.2:** An example for a unit cell of a periodic structure equipped with a porous material. Multiple unit cells combined form the resulting periodic structure. The cross section of the unit cell consists out of two sheets of metal (depicted in gray), a porous material (depicted in orange), and an air gap. The setup is inspired by [182].

**Radiation and scattering** The sound radiation caused by machinery needs to be assessed during the design phase. This can, for example, be conducted experimentally in anechoic chambers, but numerical models are often employed as they can be altered and evaluated more flexible. As it would be inefficient to model, for example, the complete anechoic chamber with the specimen inside, arbitrary boundaries are introduced, where the modeled domain is truncated. This arbitrary boundary must ensure that it does not prevent any energy from leaving the system. Additionally, no energy that left the system through this boundary may reenter the system. Various numerical methods have been established in order to fulfill this condition and thus allow free radiation of sound. Examples are the boundary element method [66, 178], infinite elements [16], or adapted boundary conditions for the finite element method, for example the Dirichlet-to-Neumann operator [119, 152] or the perfectly matched layer [131, 196]. Figure 1.3 shows an application example of a perfectly matched layer. A free radiation of the energy is ensured by the boundary condition such that the wave pattern inside the physical domain is not altered by the artificial truncation boundary.

Acoustic scattering is considered as the effect of surfaces disturbing a sound field, possibly leading to echoes or backscattering. Figure 1.3 is also an example for a pressure field resulting from scattering following an example from Bermúdez et al. [56]. Exact knowledge about this vibration pattern can, for example, be used to obtain information about the location of

objects inside the wave field. The numerical investigation of such phenomena is typically complex, as large dimensions need to be considered and a free radiation must be modeled at the system boundaries. Such localization techniques are especially interesting for underwater acoustics [275]. The radiation of noise emitted by a vehicle has, for example, been assessed by Zinner and Duddeck [278].

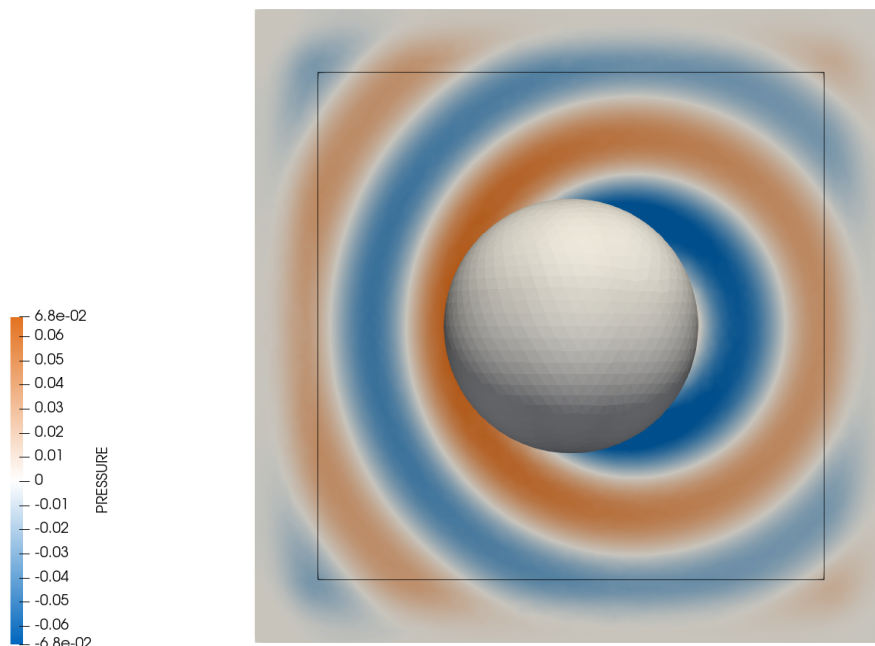


**Figure 1.3:** Example for acoustic radiation and scattering. The model is inspired by Bermúdez et al. [56] and the radiating boundary condition is ensured by a perfectly matched layer.

### 1.1.2 Numerical evaluation of vibro-acoustic systems

Vibro-acoustic systems, such as the aforementioned examples, are typically assessed and analyzed using numerical models. Although the available computing power is still constantly growing, even numerical models for standard vibro-acoustic problems quickly grow too large to use them efficiently in many cases of engineering practice. The main reason for the large size of such numerical models is the fine spatial discretization required to resolve wave phenomena when using an element based method to discretize the governing differential equations. A rule of thumb is to use around six to ten discretization nodes per wavelength [142, 176]. A discretization of an acoustic cavity in shape cube with edge lengths of 1 m filled with air already leads to a numerical system of order  $n \approx 27\,000$  if frequencies up to 1000 Hz should be considered. Often larger problems and higher frequencies need to be considered, quickly leading to numerical systems with orders of  $n \sim 1 \cdot 10^6$  and larger. The numerical complexity is further increased as the coupling between the different phases present

in vibro-acoustic systems need to be considered. Instead of only solving a pressure field for an acoustical problem, displacement fields of vibrating structures or the interaction of solid and fluid phases in porous materials needs to be considered. While mathematical models to describe these interactions exist, they often require a large number of degrees of freedom to validly depict the physical behavior. Vibro-acoustic models are typically evaluated using frequency sweeps, as their response to a possibly wide range of frequencies is of interest. Using a direct evaluation method requires the solution of one linear system of equations with the size of the model per frequency step, thus also increasing the computational cost of the model.

During their design phase, parts of vibro-acoustic systems need to be optimized regarding an often large set of parameters. These can include material properties of employed damping materials or the geometry of resonant substructures. Even if one numerical model of the regarded problem can be evaluated with reasonable effort, optimization algorithms typically require many evaluations of the system under varying parameters, again leading to very long computation times. A related challenge is the need to consider uncertainties regarding material or geometry in vibro-acoustic systems. In order to assess the influence of such uncertainties, the considered system needs to be evaluated many times under varying parameters, which may be prohibitive for large numerical models. Another challenge is the nonlinear dependency on the excitation frequency of many damping mechanisms occurring in vibro-acoustic systems. Classic evaluation strategies for a frequency sweep analysis of vibro-acoustic systems, such as modal superposition, are not applicable here. So in order to avoid the costly direct evaluation of such systems, new strategies allowing an efficient solution need to be employed.

## 1.2 Model order reduction

One possible remedy to reduce the numerical complexity of vibro-acoustic systems are model order reduction (MOR) methods. They aim at reproducing the input/output relation of a large scale system using a reduced system of much lower order. The response of the low order system can be obtained with a low computational effort. Modal methods are classic complexity reduction methods, where the system modes obtained from an eigendecomposition are used to compute a set of decoupled linear equations constituting the frequency response of the original system. Such methods are nowadays a standard part of finite element software aiming at solving dynamical systems. However, classic modal methods cannot be applied to all kinds of vibro-acoustic systems and are typically only applicable for special cases of damping. Additionally, the computational effort necessary to obtain an eigendecomposition

of a very large system may be prohibitive. Alternative reduction methods have emerged from the field of electrical engineering, being applicable to a problems modeling a wide range of physical phenomena. Some of these methods are also applicable to vibro-acoustic problems [11]. An important task is the reduction of parametric systems while retaining the dependency on certain parameters in the reduced model. This is especially interesting for optimization tasks, as the computational burden of evaluating many varying full order systems can be significantly reduced [47].

Model order reduction methods are typically divided in two separate phases: The offline phase, in which the original full order model is utilized to obtain a low order representation of the system, and the online phase, during which the reduced order model is evaluated and the full scale model is not required anymore. Moreover, two different objectives for model order reduction can be identified:

1. Obtain a reduced model which is as cheap as possible to evaluate in the online phase. Such reduced models should be of very small size to allow an efficient direct evaluation. This is required for models which need to be evaluated in real-time, for example as they are implemented in embedded control devices. In this case, the cost during the offline phase may be very high and the result of the full order model is considered to be available in some cases.
2. Obtain a reduced model under as low as possible computational effort in the offline phase. The cost of the offline phase is crucial in this use-case and is kept low at the cost of potential larger reduced models. However, their size is still small compared to the full-order model and their evaluation is much less computationally expensive. This strategy is typically applied if the design phase of structures needs to be accelerated and the full order model is never completely evaluated.

The second case is applicable to many settings where vibro-acoustic systems are encountered, for example in the design of vehicles or structures. Here, employed measures to reduce noise and vibration, for example inside the passenger compartment, need to be evaluated efficiently for many combinations of parameters. A computationally cheap model is necessary in order to keep the computational costs low, even if many system evaluations are required.

### 1.2.1 Examples for model order reduction in practice

Various model order reduction methods have been established over the last years and successfully applied to obtain efficient models of systems depicting different physical phenomena. Originally, many reduction methods were employed to obtain efficient models of microelectromechanical systems (MEMS) [164, 232]. Consequently, the methods have been adapted

to be applicable to a wide range of engineering problems. Some examples showing the benefit of reduced models are presented in the following. Lieu, Farhat, and Lesoinne [167] reduced the model of a complete jet plane to a model several magnitudes smaller, which estimates the aeroelastic damping ratio coefficients given the Mach number. Peherstorfer and Willcox [205] proposed a method to update existing reduced models by considering data collected from sensors. This can, for example, be used to monitor the integrity of vibrating structures. Model order reduction methods are also frequently used during the design process of mechanical structures. For example, Fehr, Holzwarth, and Eberhard [104] used substructuring techniques to decrease the required amount of computation time for the analysis of vehicle crash models. Several other examples from the field of mechanical engineering are reported in [169]. Results of model order reduction methods applied to acoustic and vibro-acoustic systems are, for example, reported in [92, 153, 254].

Efficient model order reduction methods are an enabling technology for so called “digital twins”. They can be defined as digital representations of complex systems, such as power plants, bridges, or machinery, which help design, monitor, and optimize such structures [216]. Without robust and efficient representations of important processes inside these systems, such digital twins are not possible. Digital twins have been identified as an important factor in the transition towards “Industry 4.0” and have been established for many products, processes, and structures [204]. Vehicles are a natural application for digital twins, so there is the need of robust and accurate reduced order modeling methods being specifically applicable to vibro-acoustic problems [132].

### 1.3 Research objectives and achievements

This thesis compiles the efforts underdone to achieve the following research objectives regarding reduced order models of vibro-acoustic systems:

**Accurate and reliable representation of complex vibro-acoustic systems in reduced space, especially for systems with frequency dependent material properties**

Due to the large size of numerical models of vibro-acoustic systems, methods to reduce the computational complexity are required. Such methods should yield models depicting the input/output relation of the original system accurately while being applicable to a wide range of vibro-acoustic systems without the need of specialized adjustments for different system types. This includes systems with frequency dependent material properties, for example complex damping treatments, as well as systems with radiating boundary conditions, for example perfectly matched layers.

Several projection-based model order reduction methods are assessed regarding their applicability to different cases of vibro-acoustic systems, also including radiating boundary conditions. This overview compares the efficiency of the employed methods regarding their ability to compute as small as possible reduced models. A new strategy to reduce systems with frequency dependent damping behavior based on a higher order Krylov subspace is proposed, which does not require adding additional states to the system.

### **Robust and reliable automatic model order reduction methods for the application to vibro-acoustic systems**

If the response of the full order system is not available, automatic methods are required to compute accurate reduced models. These methods should be robust, i.e. always result in a reduced model depicting the full system's response under a specified tolerance, while still be less computationally expensive than solving the full order model. To achieve this goal, the approximation error of the reduced models needs to be estimated and adaptive algorithms are required to find appropriate reduced models.

The performance of different error estimation techniques are evaluated regarding vibro-acoustic systems. They are used in an algorithm which determines the required size of a reduced model automatically by using a greedy method in combination with a frequency windowing technique. Additionally, the iterative rational Krylov algorithm (IRKA) in its second order form is extended such that it automatically finds reduced models valid in a predefined frequency range without predefining the size of the reduced model.

### **Model order reduction strategies for parametrized vibro-acoustic systems**

Efficient models depending on a set of parameters are required during the design phase of many vibro-acoustic structures. Techniques to obtain these models under reasonable computational costs are therefore required and strategies need to be applicable to vibro-acoustic problems. It shall be evaluated if considering the physics of the underlying problems yields benefits regarding starting parameters of certain algorithms or the computation of parametrized reduced order models.

Two different approaches to obtain efficient and parametric reduced models of vibro-acoustic systems are proposed and evaluated. First, a data-driven method based on the Loewner framework is applied to a vibro-acoustic system with spatially varying damping effects. A large amount of data is required for applying this method, which can be computationally expensive to obtain. Regression models to obtain near optimal frequency shifts for a model order reduction based on moment-matching are considered in the second approach.

## 1.4 Outline of the thesis

The following thesis aims at answering these open questions and proposes methods and algorithms to solve the associated problems. It is structured as follows: The mathematical description of general dynamical systems is discussed and applied to vibro-acoustic systems in chapter 2. The underlying physical relations for acoustic and structural waves as well as the behavior of poroelastic materials are presented along with corresponding boundary and coupling conditions. Formulations for a discretization of vibro-acoustic problems using the finite element method are presented in the following, accompanied by fundamental solving strategies for such systems. The chapter concludes with benchmark examples for different kinds of vibro-acoustic problems which will be used throughout the thesis as illustrative examples.

General methods for model order reduction using projection are presented in chapter 3. Starting with modal methods, which are classically applied to vibro-acoustic structures, methods based on system decompositions are presented as well as moment matching methods. Techniques to assess the error introduced by reducing a large scale system are also discussed. Following, methods preserving the dependency on parameters in the reduced space are presented and discussed.

Model order reduction methods specifically applicable to vibro-acoustic systems are discussed in chapter 4. First, the classic methods presented in chapter 3 are assessed regarding their applicability to various types of vibro-acoustic systems in section 4.1. Section 4.2 introduces a new method to apply moment matching to systems with material parameters described by frequency dependent functions. Following are some considerations about  $\mathcal{H}_2$ -optimal model order reduction applied to vibro-acoustic systems in section 4.3 and strategies and algorithms for the automatic and adaptive computation of reduced order models for systems, which full order solution is not available, in section 4.4.

Two strategies for the parametric model order reduction of vibro-acoustic systems are presented in chapter 5: one is based on the parametric Loewner framework, the other combines moment matching with data-driven regression methods.

Chapter 6 concludes the thesis with a summary and assessment of the research objectives. An outlook regarding the considered topics and further research ideas are presented.

## 2 Dynamical systems

Many mechanisms and phenomena occurring in nature can be described by a models relating actions and reactions in a way resembling the real world. Such processes may be described by systems, which are defined as being enclosed by a boundary, taking a number of inputs, and providing a number of outputs. Their input/output relation is typically described by a combination of mathematical laws specifically formulated for the given problem. This leads to mathematical expressions, often consisting of differential equations, governing the model and resembling changes of affected variables caused by the considered physical phenomena. Thus, the investigation of suitable mathematical models allows predicting the behavior of such processes and the description of natural phenomena by mathematical models is therefore essential in science and engineering. As the same physical phenomenon can be described by different mathematical models, the term *system* is used to describe the behavior of the corresponding mathematical model, rather than the physical phenomenon [13]. Depending on the nature of the considered problem and the effects to be modeled, the corresponding systems have different properties: A system may be linear or nonlinear, time-varying or time-invariant, deterministic or stochastic or a combination thereof. Although real world systems are most accurately described by nonlinear relations, linearization is often desirable and many effects to be modeled can be considered linear in a certain range of interest. We put a focus on systems describing the change of a variable over time, often termed dynamical systems.

In the following chapter, the fundamentals for the modeling of dynamical systems in general and specialized formulations for vibro-acoustic systems will be introduced. Mathematical descriptions of systems governed by first or second-order differential equations are given in section 2.1. Following, differential equations for physical phenomena occurring in vibro-acoustic systems are shown: acoustic wave propagation in section 2.2.1, elastic waves in section 2.2.2, vibration and dissipation behavior of poroelastic materials in section 2.2.3, and conditions for the coupling of the different phases in section 2.2.4. Formulations for vibro-acoustic systems discretized by the finite element method are given in section 2.3.1 and boundary conditions enabling free radiation are discussed in section 2.3.2. Methods to evaluate the dynamic response of vibro-acoustic systems are shortly reviewed in section 2.4 and benchmark examples for different vibro-acoustic problems are presented in section 2.5.

## 2.1 Mathematical system descriptions

### 2.1.1 First-order systems

A linear, time-invariant dynamical system is described by a combination of constant matrices mapping system inputs  $\check{\mathbf{u}}(t) \in \mathbb{R}^m$  over the system state  $\check{\mathbf{x}}(t) \in \mathbb{R}^n$  to system outputs  $\check{\mathbf{y}}(t) \in \mathbb{R}^p$

$$\Sigma: \begin{cases} \mathbf{E}\dot{\check{\mathbf{x}}}(t) = \mathbf{A}\check{\mathbf{x}}(t) + \mathbf{B}\check{\mathbf{u}}(t) \\ \check{\mathbf{y}}(t) = \mathbf{C}\check{\mathbf{x}}(t) + \mathbf{D}\check{\mathbf{u}}(t), \end{cases} \quad (2.1)$$

where  $\mathbf{E}, \mathbf{A} \in \mathbb{R}^{n \times n}$ ,  $\mathbf{B} \in \mathbb{R}^{n \times m}$ ,  $\mathbf{C} \in \mathbb{R}^{p \times n}$ , and  $\mathbf{D} \in \mathbb{R}^{p \times m}$ .  $n$  is the number of states in the system,  $m$  the number of inputs, and  $p$  the number of outputs. Equation (2.1) is termed a descriptor state space model. Systems with exactly one input and one output  $m = p = 1$  are called SISO (single input, single output) systems, other input and output configurations are considered as MIMO (multiple input, multiple output). The dot operator marks a derivative with respect to time:  $\dot{\check{\mathbf{x}}}(t) = \frac{d}{dt}\check{\mathbf{x}}(t)$ . The individual matrices stem from a discretization of the mathematical problem, while this realization is not necessarily unique. Thus, different sets of matrices ( $\mathbf{E}, \mathbf{A}, \mathbf{B}, \mathbf{C}, \mathbf{D}$ ) can result in the same input/output relation. Matrix  $\mathbf{A}$  is called state or system matrix,  $\mathbf{E}$  is called descriptor or mass matrix,  $\mathbf{B}$  and  $\mathbf{C}$  resemble the input and output matrix respectively, and  $\mathbf{D}$  is the feedthrough matrix of the system. If  $n$  is large,  $\mathbf{A}$  and  $\mathbf{E}$  are typically sparsely populated, which will be assumed for the following considerations. Given an exponentially bounded input  $\check{\mathbf{u}}(t)$ , i.e.  $\check{\mathbf{u}}(t)$  approaches a certain value for  $t \rightarrow \infty$ , the descriptor system (2.1) can be transformed to the Laplace domain

$$\mathbf{y}(s) = \mathbf{H}(s) \mathbf{u}(s), \quad (2.2)$$

where  $\mathbf{y}(s)$  is the system output in the Laplace domain, i.e. the transform of  $\check{\mathbf{y}}(t)$ , in terms of the Laplace transform  $\mathbf{u}(s)$  of the system input  $\check{\mathbf{u}}(t)$ .  $\mathbf{H}(s)$  defines the system's transfer function

$$\mathbf{H}(s) = \mathbf{C}(s\mathbf{E} - \mathbf{A})^{-1}\mathbf{B} + \mathbf{D}, \quad (2.3)$$

which is a matrix valued rational function of dimensions  $\mathbb{C}^{p \times m}$  and  $s \in \mathbb{C}$  is the complex driving frequency. In the following, we consider systems with an equal amount of inputs and outputs, i.e.  $m = p$ . Many dynamical systems are passive, meaning they do not generate energy. So if the system is given a bounded input, the output will also be bounded. A linear system is passive if, and only if, its transfer function  $\mathbf{H}(s)$  is positive real [111]. A matrix-

valued function  $\mathbf{H} \in \mathbb{C}^{m \times m}$  is positive real, if  $\mathbf{H}$  has no poles in the right half plane of  $\mathbb{C}$ , i.e. no pole has a positive real part, if  $\mathbf{H}(\bar{s}) = \overline{\mathbf{H}(s)}$  for all  $s \in \mathbb{C}$ , and if  $\text{Re}(\mathbf{x}^H \mathbf{H}(s) \mathbf{x}) \geq 0$  for all  $s$  with a positive real part and for arbitrary  $\mathbf{x} \in \mathbb{C}^m$ . Such matrix functions are also necessarily stable [111]. Additionally, the system is considered asymptotically stable, if the matrix pencil  $s\mathbf{E} - \mathbf{A}$  in eq. (2.3) is regular, i.e. is invertible for some finite  $s \in \mathbb{C}$ . If this is the case, the pencil's eigenvalues correspond to the poles of the transfer function [12]. Consequently, the eigenvalues of a stable system lie only in the left open half-plane of  $\mathbb{C}$ .

Observability and controllability are concepts describing if the internal states of a system can be determined from the system outputs or controlled by system inputs. A linear system is considered controllable, if

$$\text{rank} \begin{bmatrix} \lambda \mathbf{E} - \mathbf{A} & \mathbf{B} \end{bmatrix} = n, \forall \lambda \in \mathbb{C} \quad \text{and} \quad \text{rank} \begin{bmatrix} \mathbf{E} & \mathbf{B} \end{bmatrix} = n. \quad (2.4)$$

If a system is controllable, every possible state can be reached by providing suitable values for the system input. Observability is the analogous principle regarding the system output. A system is considered observable, if

$$\text{rank} \begin{bmatrix} \lambda \mathbf{E} - \mathbf{A} \\ \mathbf{C} \end{bmatrix} = n, \forall \lambda \in \mathbb{C} \quad \text{and} \quad \text{rank} \begin{bmatrix} \mathbf{E} \\ \mathbf{C} \end{bmatrix} = n. \quad (2.5)$$

This means that the internal state of the system can be fully predicted by knowing only its output [77]. Related concepts are the controllability and observability Gramians which allow considerations regarding the minimal energy required to reach a certain state, respectively the maximum observation energy obtained from a certain state. In frequency domain, the controllability and observability Gramians  $\mathbf{P}$  and  $\mathbf{Q}$  of a stable system are defined by

$$\mathbf{P} = \frac{1}{2\pi} \int_{-\infty}^{\infty} \boldsymbol{\chi}(s) \mathbf{B} \mathbf{B}^T \boldsymbol{\chi}(s)^T ds, \quad (2.6)$$

$$\mathbf{Q} = \frac{1}{2\pi} \int_{-\infty}^{\infty} \boldsymbol{\chi}(s)^T \mathbf{C}^T \mathbf{C} \boldsymbol{\chi}(s) ds, \quad (2.7)$$

with  $\boldsymbol{\chi}(s) = (s\mathbf{E} - \mathbf{A})^{-1}$ . The expression  $\boldsymbol{\chi}(s) \mathbf{B}$  in eq. (2.6) maps the system input to the Laplace transform of the state;  $\mathbf{C} \boldsymbol{\chi}(s)$  in eq. (2.7) maps the state's Laplace transform to the system output. The Gramians are computed by solving the Lyapunov equations

$$\mathbf{E} \mathbf{P} \mathbf{A}^T + \mathbf{A} \mathbf{P} \mathbf{E}^T = -\mathbf{B} \mathbf{B}^T, \quad (2.8)$$

$$\mathbf{E} \mathbf{Q} \mathbf{A}^T + \mathbf{A} \mathbf{Q} \mathbf{E}^T = -\mathbf{C} \mathbf{C}^T. \quad (2.9)$$

With help of the Gramians, the minimal energy required to reach a state  $\mathbf{x}_1$  from a zero

initial condition is computed from

$$E_c = \mathbf{x}_1^H \mathbf{P}^{-1} \mathbf{x}_1. \quad (2.10)$$

Similarly, the maximum energy obtained by observing a state  $\mathbf{x}_1$  is given by

$$E_o = \mathbf{x}_1^H \mathbf{Q} \mathbf{x}_1. \quad (2.11)$$

These considerations result in measures regarding the degree of controllability and the degree of observability of the states of a system. If a state is difficult to reach, i.e. the system requires much energy to reach a certain state, its corresponding eigenvector in  $\mathbf{P}$  is associated with a small eigenvalue. Similarly, if a small amount of energy is obtained by observing a state, its corresponding eigenvector in  $\mathbf{Q}$  is associated with a small eigenvalue [11].

## 2.1.2 Second-order systems

Depending on the nature of the considered problem, the structure of eq. (2.1) may differ. Examples of other system types include bilinear, delay, or higher order systems. As structural vibration is described by a second order differential equation, it is beneficial to also use a second order system to model its behavior. Such systems are given by

$$\Sigma: \begin{cases} \mathbf{M}\ddot{\mathbf{x}}(t) + \mathbf{C}\dot{\mathbf{x}}(t) + \mathbf{K}\mathbf{x}(t) = \mathbf{F}\ddot{\mathbf{u}}(t), \\ \mathbf{y}(t) = \mathbf{G}\mathbf{x}(t), \end{cases} \quad (2.12)$$

where  $\mathbf{M}$ ,  $\mathbf{C}$ ,  $\mathbf{K} \in \mathbb{R}^{n \times n}$  resemble the mass, damping, and stiffness matrix of the system and  $\mathbf{F} \in \mathbb{R}^{n \times m}$  and  $\mathbf{G} \in \mathbb{R}^{p \times n}$  are the input and output mapping. The first expression related to the system input is also referred to as equation of motion. How the involved matrices can be obtained depends on the modeled problem and the discretization method and will be outlined in section 2.3 for vibro-acoustic systems. After a transformation to the Laplace domain, the system's transfer function is given by

$$\mathbf{H}(s) = \mathbf{G} (s^2 \mathbf{M} + s \mathbf{C} + \mathbf{K})^{-1} \mathbf{F}. \quad (2.13)$$

As for the first-order systems, a second-order system is called asymptotically stable, if the eigenvalues  $\lambda$  of the matrix pencil  $\lambda^2 \mathbf{M} + \lambda \mathbf{C} + \mathbf{K}$  all lie in the left half plane of  $\mathbb{C}$ , i.e. have a negative or zero real part. Observability and controllability can be stated similarly to first-order systems: A second-order system (2.12) is controllable, if

$$\text{rank} \begin{bmatrix} \lambda^2 \mathbf{M} + \lambda \mathbf{C} + \mathbf{K} & \mathbf{F} \end{bmatrix} = n, \forall \lambda \in \mathbb{C}, \quad (2.14)$$

and analogously observable, if

$$\text{rank} \left[ \lambda^2 \mathbf{M}^\top + \lambda \mathbf{C}^\top + \mathbf{K}^\top \quad \mathbf{G}^\top \right] = n, \forall \lambda \in \mathbb{C}. \quad (2.15)$$

In order to apply also the concepts of controllability and observability Gramians, the second-order system eq. (2.12) is reformulated to a corresponding first order system

$$\Sigma: \left\{ \begin{array}{l} \underbrace{\begin{bmatrix} \mathbf{J} & 0 \\ 0 & \mathbf{M} \end{bmatrix}}_{\mathbf{E}^{(1)}} \underbrace{\begin{bmatrix} \dot{\check{\mathbf{x}}}(t) \\ \check{\mathbf{x}}(t) \end{bmatrix}}_{\check{\mathbf{x}}^{(1)}(t)} = \underbrace{\begin{bmatrix} 0 & \mathbf{J} \\ -\mathbf{K} & -\mathbf{C} \end{bmatrix}}_{\mathbf{A}^{(1)}} \underbrace{\begin{bmatrix} \check{\mathbf{x}}(t) \\ \dot{\check{\mathbf{x}}}(t) \end{bmatrix}}_{\check{\mathbf{x}}^{(1)}(t)} + \underbrace{\begin{bmatrix} 0 \\ \mathbf{F} \end{bmatrix}}_{\mathbf{B}^{(1)}} \check{\mathbf{u}}(t), \\ \check{\mathbf{y}}(t) = \underbrace{\begin{bmatrix} \mathbf{G} & 0 \end{bmatrix}}_{\mathbf{C}^{(1)}} \underbrace{\begin{bmatrix} \check{\mathbf{x}}(t) \\ \dot{\check{\mathbf{x}}}(t) \end{bmatrix}}_{\check{\mathbf{x}}^{(1)}(t)}. \end{array} \right. \quad (2.16)$$

The quantities under the braces marked with superscript (1) are the matrices and vectors in the corresponding first-order system and have the dimensions  $\mathbf{E}^{(1)}, \mathbf{A}^{(1)} \in \mathbb{R}^{2n \times 2n}$ ,  $\mathbf{B}^{(1)} \in \mathbb{R}^{2n \times m}$ ,  $\mathbf{C}^{(1)} \in \mathbb{R}^{p \times 2n}$ . Matrix  $\mathbf{J} \in \mathbb{R}^{n \times n}$  is an arbitrary invertible matrix, for example identity. This equivalent representation can, for example, be used to obtain the Gramians eqs. (2.6) and (2.7) given by [217]. Alternative formulations, which can be used with a singular mass matrix or preserve the symmetry of the original second-order system, are given in appendix A.1. Alternatively to eqs. (2.14) and (2.15), the controllability and observability of a second-order system can also be expressed in terms of the corresponding first-order system (2.16). A second-order system is controllable, respectively observable, if its first-order representation is controllable, respectively observable [217]. Converting a second-order system to a first-order system doubles the size of the involved matrices and vectors and changes the structure of the system and transfer function, so the original meaning of the system matrices is not valid anymore. In the following, we will mainly refer to second-order systems, as all models considered in the scope of this work are described by such systems.

### 2.1.3 Transfer functions and poles

Contrary to the internal description of systems relying on a state-space representation, external descriptions like transfer functions may be simpler to apply and to assess. The transfer function is the direct representation of the map between system input and output and is an important tool for assessing the system behavior. Its matrix representations eqs. (2.3) and (2.13) can be reformulated and sometimes be interpreted physically. Some of these forms are presented in the following.

The modal properties of a system are depending on its eigenvalues and can be illustrated using the pole-residue form of the transfer function of a SISO system. Here, the transfer function is expressed by relating each pole of the system  $\lambda_i$  to its corresponding residual  $r_i$  using a partial fraction expansion:

$$H(s) = \sum_{i=1}^n \frac{r_i}{s - \lambda_i}. \quad (2.17)$$

From this representation it is obvious, that it is not sufficient to only know the eigenvalues of a system to fully describe its transfer function, as the dominance, i.e. the influence on the transfer function, of single poles is depending on the corresponding residual. This also suggests, that  $H(s)$  can be approximated using less than  $n$  pairs of poles and residuals. If the expansion term in eq. (2.17) corresponding to a certain pair  $(r_i, \lambda_i)$  evaluates to small values for all excitation frequencies  $s$ , this pair can be excluded from the sum without considerably changing the transfer function. Note, that if the system has poles with  $\text{Re}(\lambda_i) = 0$ , the value of the transfer function grows towards infinity for  $s \rightarrow \lambda_i$ . Classic analysis methods for structural systems rely on such a modal representation of the dynamical system. The eigenvalues  $\lambda_i$  are physically interpreted as resonance frequencies of the system in this context.

Another way to express a system's transfer function is by a Taylor series about a frequency  $s_0 = 0$ . The expansion is given by

$$\mathbf{H}(s) = \sum_{i=0}^{\infty} \mathbf{m}_i s^i, \quad (2.18)$$

where  $\mathbf{m}_i$  is the  $i$ th moment of the system. The moments are the transfer function value and its derivatives at  $s = 0$  and are given by

$$\mathbf{m}_i = \mathbf{C} \left( \mathbf{A}^{-1} \mathbf{E} \right)^i \mathbf{A}^{-1} \mathbf{B}, \quad i = 0, 1, \dots \quad (2.19)$$

for a first-order system, where  $\mathbf{A}$  is invertible. The moments are matrices  $\mathbf{m}_i \in \mathbb{C}^{p \times m}$ . An equivalent second-order representation of the  $i$ th moment about zero is given by

$$\mathbf{m}_i = \begin{bmatrix} \mathbf{G} & 0 \end{bmatrix} \begin{bmatrix} -\mathbf{K}^{-1} \mathbf{C} & -\mathbf{K}^{-1} \mathbf{M} \\ \mathbf{I} & 0 \end{bmatrix}^i \begin{bmatrix} -\mathbf{K}^{-1} \mathbf{F} \\ 0 \end{bmatrix}, \quad (2.20)$$

where  $\mathbf{K}$  needs to be invertible [228].  $\mathbf{I}$  is an identity matrix of appropriate size and the moments are  $\mathbf{m}_i \in \mathbb{C}^{p \times m}$  in the MIMO case and complex scalar in the SISO case. Similarly, the transfer function can be given in terms of the impulse response at  $t = 0$  and its derivatives,

the so called Markov parameters. The corresponding expansion is given by

$$\mathbf{H}(s) = \sum_{i=0}^{\infty} \mathbf{m}_{-i} s^{-i}, \quad (2.21)$$

where  $\mathbf{m}_{-i}$  is the  $i$ th Markov parameter of the system. They are defined by

$$\mathbf{m}_{-i} = \mathbf{C} \left( \mathbf{E}^{-1} \mathbf{A} \right)^i \mathbf{E}^{-1} \mathbf{B}, \quad i = 0, 1, \dots \quad (2.22)$$

for a first-order system, given that  $\mathbf{E}$  is invertible. The  $i$ th Markov parameter of a second-order system can be expressed by

$$\mathbf{m}_{-i} = \begin{bmatrix} \mathbf{G} & 0 \end{bmatrix} \begin{bmatrix} 0 & \mathbf{I} \\ -\mathbf{M}^{-1} \mathbf{K} & -\mathbf{M}^{-1} \mathbf{C} \end{bmatrix}^i \begin{bmatrix} 0 \\ \mathbf{M}^{-1} \mathbf{F} \end{bmatrix}, \quad (2.23)$$

assuming that  $\mathbf{M}$  is invertible [228]. The dimensions of the Markov parameters are the same as those of the moments. The Hankel matrix is directly related to the Markov parameters of a system and is an important tool in the analysis of dynamical systems. It is given by

$$\mathcal{H} = \begin{bmatrix} \mathbf{m}_{-1} & \mathbf{m}_{-2} & \mathbf{m}_{-3} & \cdots \\ \mathbf{m}_{-2} & \mathbf{m}_{-3} & \mathbf{m}_{-4} & \cdots \\ \vdots & \vdots & \vdots & \ddots \end{bmatrix}, \quad (2.24)$$

which has infinitely many of rows and columns. The Hankel matrix relates the internal (state-space) representation of a system given to its external representation given by its Markov parameters. Finding a system  $\Sigma$  given  $\mathcal{H}$  is known as the realization problem, which can be solved if and only if  $\text{rank } \mathcal{H} = n < \infty$  [11]. The singular values of the Hankel matrix are related to the singular values of the product  $\mathbf{PQ}$  of the controllability and observability Gramians by

$$\sigma_i(\mathcal{H}) = \sqrt{\lambda_i(\mathbf{PQ})}. \quad (2.25)$$

This means, that large singular values  $\sigma_i$  of the Hankel matrix are associated to high energy states, which have a high influence on the system behavior.

## 2.2 Vibro-acoustic systems

Vibro-acoustic systems are characterized by the interaction of structural vibrations and the waves in a surrounding fluid. Examples are, among others, the vibration of a membrane

in a loudspeaker radiating sound into the adjacent cavity or free field, or the vibration of a submarine hull emitting traceable low frequent waves into the surrounding water. The coupling between the structural and fluid parts of the system is two-fold: the vibrating structure excites the adjacent fluid, thus emitting waves into the fluid; waves impinging upon the structure in turn cause a vibration of the structure. The interaction effects between both regimes are heavily influenced by the frequency and the wave patterns in which the corresponding parts of the system are vibrating. Energy can enter the system from external loading of the structure by, for example, pressure forces. The fluid may contain energy sources such as monopole radiators or be excited by volume flow.

Energy dissipation inside such systems is caused by different effects: The damping of structural vibration is influenced by the structure's material and geometry and the frequency in which the structure is vibrating. It may be governed by viscous, hysteretic, or friction effects; friction effects also cause energy dissipation in the fluid phase. As vibration energy is an unwanted byproduct in many applications and may cause noise radiated from the system or also lead to fatigue related damage, damping mechanisms are introduced into vibro-acoustic systems to dissipate surplus vibration. These dampers can be distinct devices, for example dashpot dampers introducing viscous damping into the structural part of the system, or porous materials dissipating energy from both fluid and solid parts of the system due to their specific microstructure. The different parts of a vibro-acoustic system and their interconnections are sketched in [Figure 2.1](#).

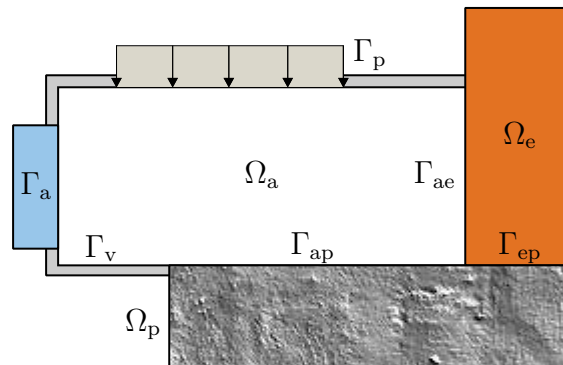


**Figure 2.1:** A vibro-acoustic system with acoustic fluid and elastic solid domains  $\Omega_a$  and  $\Omega_e$ , a poroelastic domain  $\Omega_p$ , different boundary conditions  $\Gamma_p$ ,  $\Gamma_a$ ,  $\Gamma_v$ , and coupling conditions between the phases  $\Gamma_{ae}$ ,  $\Gamma_{ap}$ ,  $\Gamma_{ep}$ .

For analysis of the resulting interconnected systems, a time harmonic or steady state vibration is often considered, where all parts of the system are oscillating and transient effects of a beginning vibration are not present anymore. Using this assumption and given a complex angular driving frequency  $s \in \mathbb{C}$ , the variables for time  $t$  and space  $\mathbf{r}$  can be

separated as

$$\check{p}(\mathbf{r}, t) = p(\mathbf{r}) e^{st}, \quad (2.26)$$

with scalar fields  $\check{p}$  and  $p$ , typically representing the fluid pressure in this context. In a Cartesian coordinate system the location vector is given by  $\mathbf{r} = [x \ y \ z]^T$ . The same concept for separating time and space holds for vector fields, which describe the displacement of solids in a vibro-acoustic setting. Instead of the complex frequency  $s$ , the real valued angular frequency  $\omega = \text{Im}(s)$  along with a damping factor  $\xi$  is often considered in literature concerning structural dynamics. Both formulations are mainly equivalent but differ for example in the location of the eigenvalues of resulting systems relative to the coordinate axes in complex space. We will follow the notation with a complex frequency  $s$ , as it is typically used in the model order reduction context. This separation is the basis for the following derivations of governing equations for all parts of the vibro-acoustic system. Discretization and numerical approximation of the solution of the governing equations allows the solution of arbitrarily shaped systems. In the following section, the relations describing all parts of vibro-acoustic systems and their coupling are presented along with numerical methods to solve the response of such systems.

### 2.2.1 Acoustic waves

Acoustic waves are oscillations of pressure and velocity inside a compressible, ideal fluid. Oscillations with frequencies from 16 Hz to about 16 kHz are perceived as sound by the human ear [189]. The wave speed  $c_a = \sqrt{\frac{K}{\rho}}$ , which is depending on the fluid's bulk modulus  $K$  and its density  $\rho$ , characterizes the propagation in the specific acoustic fluid. Wave propagation inside the acoustic medium is governed by the wave equation

$$\frac{\partial^2 \check{p}(\mathbf{r}, t)}{\partial t^2} - c_a^2 \nabla \cdot (\nabla \check{p}(\mathbf{r}, t)) = 0, \quad (2.27)$$

obtained from the linearized equation of motion and the requirement of mass conservation.  $\check{p}(\mathbf{r}, t)$  is a function of the pressure distribution in the sound field. A complete derivation is given in [142]. Assuming a steady state, the dependencies of the pressure variable regarding space and time can be separated as in (2.26) and transformed to the frequency domain by a Laplace transformation. Given small oscillations and an inviscid and adiabatic fluid, the transformed acoustic wave equation yields the Helmholtz equation

$$k^2 p(\mathbf{r}) + \Delta p(\mathbf{r}) = 0, \quad (2.28)$$

with the Laplacian operator  $\Delta = \nabla \cdot \nabla$ , pressure  $p$  and wave number  $k = \frac{\text{Im}(s)}{c_a}$ . Because of the lack of shear forces inside the acoustic fluid, only compression waves, where the particles travel in the same direction as the wave propagates, are transmitted through the medium. If acoustic sources in the domain need to be considered, a right hand side is added to (2.28) resulting in the inhomogeneous Helmholtz equation

$$k^2 p(\mathbf{r}) + \Delta p(\mathbf{r}) = -q(\mathbf{r}). \quad (2.29)$$

The source term  $q$  is given as  $q(\mathbf{r}) = \rho s q_0 \delta(\mathbf{r}, \mathbf{r}_q)$  for a monopole source with amplitude  $q_0$ , the Dirac delta function  $\delta$  and the location of the source  $\mathbf{r}_q$ .

To be able to solve the Helmholtz equation for the unknown pressure field  $p$ , the conditions at the boundary of the acoustic medium must be known. Three main types of boundary conditions can be employed for a bounded acoustic wave propagation problem:

- Prescribing the pressure at the model boundaries corresponds to a Dirichlet boundary condition defined by

$$p(\mathbf{r}) - p_\Gamma = 0 \quad \forall \mathbf{r} \in \Gamma_p, \quad (2.30)$$

with the value of the prescribed pressure  $p_\Gamma$  at the boundary  $\Gamma_p$ . Setting  $p_\Gamma = 0$  corresponds to a fully reflecting boundary.

- A normal velocity  $v_n$  or displacement  $u_n$  is imposed by a Neumann boundary condition given by

$$\frac{1}{\rho s} \frac{\partial p(\mathbf{r})}{\partial n} + v_{n,\Gamma} = 0 \quad \forall \mathbf{r} \in \Gamma_v, \quad (2.31)$$

$$\frac{1}{\rho s^2} \frac{\partial p(\mathbf{r})}{\partial n} + u_{n,\Gamma} = 0 \quad \forall \mathbf{r} \in \Gamma_u, \quad (2.32)$$

where  $\frac{\partial p}{\partial n} = \nabla p \cdot \mathbf{n}$  is the normal derivative of  $p$  with respect to the normal vector  $\mathbf{n}$  of the respective boundary pointing outwards of the domain. Imposing  $v_n = 0$  is equivalent to a fully reflecting boundary.

- A Robin boundary condition imposes a normal admittance  $A_{n,\Gamma}$  at the boundary, prescribing the ratio of pressure and normal velocity at the boundary. It is given by

$$\frac{1}{\rho s} \frac{\partial p(\mathbf{r})}{\partial n} + p A_{n,\Gamma} = 0 \quad \forall \mathbf{r} \in \Gamma_A. \quad (2.33)$$

By setting  $A_{n,\Gamma}$  appropriately, the absorption effect of dissipative materials or an adjacent acoustic fluid can be modeled.

If an unbounded domain is considered, the Sommerfeld radiation condition is employed at the boundaries at infinity  $\Gamma_\infty$ . It ensures that no energy radiating towards infinity reenters the system and is given by

$$\lim_{\|\mathbf{r}\| \rightarrow \infty} \|\mathbf{r}\|^{(d-1)/2} \left( \frac{\partial p}{\partial \|\mathbf{r}\|} - ikp \right) = 0 \quad \forall \mathbf{r} \in \Gamma_\infty, \quad (2.34)$$

with the dimension of the modeled problem  $d$  [240]. Losses in the acoustic fluid can be considered by a complex wave velocity introducing an acoustic loss factor  $\eta_\delta$ :

$$\tilde{c}_\delta = c(1 - i\eta_\delta). \quad (2.35)$$

As  $c = \sqrt{\frac{K}{\rho}}$  either  $K$  or  $\rho$  or both can be considered complex to achieve the damping effect. A complex bulk modulus is related to thermal losses, a complex density to viscous losses [147]. However, thermal and viscous losses can often be neglected for cavities larger than most of the considered wavelengths and problems with moderate wave speed.

### 2.2.2 Structural vibration

We now consider a homogeneous elastic solid in a Cartesian coordinate system. Different types of waves can propagate through this medium, each with an individual vibration pattern and wave velocity. For an isotropic material with density  $\rho$ , the propagation is described by the elastic wave equation

$$-\rho \frac{\partial^2 \check{\mathbf{u}}(\mathbf{r}, t)}{\partial t^2} + (\lambda + 2G) \nabla \nabla \cdot \check{\mathbf{u}}(\mathbf{r}, t) - G \nabla \times (\nabla \times \check{\mathbf{u}}(\mathbf{r}, t)) = -\check{\mathbf{b}}(\mathbf{r}, t), \quad (2.36)$$

which also considers the shear forces inside the elastic medium, other than the standard wave equation for the acoustic fluid (2.27). The vector  $\check{\mathbf{u}} = [\check{u}_x \quad \check{u}_y \quad \check{u}_z]^\top$  contains the displacements along the Cartesian coordinate axes and  $\check{\mathbf{b}}$  contains the sources and body forces. The dependency on space and time is omitted in the following for better readability. The Lamé parameters  $\lambda$  and  $G$  represent the material and can be computed from the material's Young's modulus  $E$  and its Poisson ratio  $\nu$  by

$$\lambda = \frac{E\nu}{(1+\nu)(1-2\nu)}, \quad (2.37)$$

$$G = \frac{E}{2(1+\nu)}. \quad (2.38)$$

Assuming a steady state, (2.36) can be written in frequency domain as

$$-s^2 \rho \mathbf{u} + (\lambda + 2G) \nabla (\nabla \cdot \mathbf{u}) - G \nabla \times (\nabla \times \mathbf{u}) = -\mathbf{b}. \quad (2.39)$$

Given  $(\nabla \times \mathbf{u}) = \nabla (\nabla \cdot \mathbf{u}) - \Delta \mathbf{u}$  [150], eq. (2.39) can be rewritten in the form of the Navier-Cauchy equation

$$-s^2 \rho \mathbf{u} + (\lambda + G) \nabla (\nabla \cdot \mathbf{u}) + G \Delta \mathbf{u} = -\mathbf{b}. \quad (2.40)$$

To obtain a relation between the wave equation and the resulting strains and stresses, the displacements  $\mathbf{u}$  are related to the strain vector  $\boldsymbol{\epsilon} = [\epsilon_x \ \epsilon_y \ \epsilon_z \ \epsilon_{yz} \ \epsilon_{xz} \ \epsilon_{xy}]^T$  by

$$\boldsymbol{\epsilon} = \mathbf{L} \mathbf{u} = \begin{bmatrix} \frac{\partial}{\partial x} & 0 & 0 & 0 & \frac{\partial}{\partial z} & \frac{\partial}{\partial y} \\ 0 & \frac{\partial}{\partial y} & 0 & \frac{\partial}{\partial z} & 0 & \frac{\partial}{\partial x} \\ 0 & 0 & \frac{\partial}{\partial z} & \frac{\partial}{\partial y} & \frac{\partial}{\partial x} & 0 \end{bmatrix}^T \mathbf{u}. \quad (2.41)$$

The constitutive law linking stress and strain is given by

$$\boldsymbol{\sigma} = \mathbf{D} \boldsymbol{\epsilon}, \quad (2.42)$$

with the stress vector  $\boldsymbol{\sigma} = [\sigma_x \ \sigma_y \ \sigma_z \ \sigma_{yz} \ \sigma_{xz} \ \sigma_{xy}]^T$  and the constitutive matrix  $\mathbf{D}$  [150]. For an isotropic material, it is given by

$$\mathbf{D} = \begin{bmatrix} \lambda + 2G & \lambda & \lambda & 0 & 0 & 0 \\ \lambda & \lambda + 2G & \lambda & 0 & 0 & 0 \\ \lambda & \lambda & \lambda + 2G & 0 & 0 & 0 \\ 0 & 0 & 0 & G & 0 & 0 \\ 0 & 0 & 0 & 0 & G & 0 \\ 0 & 0 & 0 & 0 & 0 & G \end{bmatrix}. \quad (2.43)$$

Introducing eqs. (2.41) and (2.43) into eq. (2.40), we obtain the wave equation for an isotropic material in Cartesian coordinates:

$$-s^2 \rho \mathbf{u} + \mathbf{L}^T \mathbf{D} \mathbf{L} \mathbf{u} = \mathbf{b}. \quad (2.44)$$

Unlike in fluids, where only compression waves exist, different types of waves are propagating through elastic structures. By applying the gradient operator on eq. (2.39), we obtain the equation for compression waves, also labeled pressure waves or P-waves in the context

of elastic waves. Their wave speed is given by

$$c_P = \sqrt{\frac{\lambda + 2G}{\rho}}. \quad (2.45)$$

Applying the curl operator on eq. (2.39), the wave speed for shear waves, or S-waves, is obtained. It is given by

$$c_S = \sqrt{\frac{G}{\rho}}. \quad (2.46)$$

Shear waves are characterized by particles moving perpendicular to the wave's direction of propagation. Particularly important for sound radiation of structures are bending waves, as they are the main wave type occurring in plate like structures. Here, the particles move parallel and perpendicular to the propagation direction of the wave and are thus a combination of S- and P-waves. For a plate with thickness  $h$ , the bending wave speed is given by

$$c_B = \left( \text{Im}(s)^2 \frac{Eh^2}{12\rho(1-\nu^2)} \right)^{\frac{1}{4}}. \quad (2.47)$$

Other wave types are found in bounded or inhomogeneous media, but are not considered here. A thorough overview is provided by Cremer and Heckl [87].

Structures which extensions are much larger in one or two dimensions than in the remaining one, like beams or shells, are typically described by special theories. For slender beams, the Euler-Bernoulli theory is usually applied; the Timoshenko beam theory also takes shear deformation of the cross section into account and thus also holds for thicker beams. The Kirchhoff theory is valid for thin plates where no transverse shear strain is considered, the Reissner-Mindlin theory holds for thicker shells. The shell theory holds for thin structures being loaded parallel to its midplane. Formulations for all theories are available in [276].

The typical boundary conditions for structural systems are kinematic and mechanical boundary conditions. The displacement is prescribed with a kinematic boundary condition and is chosen to model supports, for example. This boundary condition of Dirichlet type is given by

$$\mathbf{u}(\mathbf{r}) - \mathbf{u}_\Gamma = 0 \quad \forall \mathbf{r} \in \Gamma_u, \quad (2.48)$$

where  $\mathbf{u}_\Gamma$  is the prescribed value of the displacement at the corresponding boundary  $\Gamma_u$ . Similarly, mechanical or Neumann boundary conditions are realized by prescribing the stress

resultant  $\boldsymbol{\sigma}_n$  with a value  $\sigma_{n,\Gamma}$  on the corresponding boundary  $\Gamma_\sigma$ :

$$\boldsymbol{\sigma}_n(\mathbf{r}) - \sigma_{n,\Gamma} = 0 \quad \forall \mathbf{r} \in \Gamma_\sigma. \quad (2.49)$$

Additional to purely elastic materials considered above, viscoelastic materials are often encountered in a vibro-acoustic setting. They are characterized by a time dependent stress strain relation. While linear elastic materials show a rate independent linear stress strain relation, this relation is load history dependent for viscoelastic materials. Loading and unloading a viscoelastic material dissipates energy; the amount of dissipated energy is characterized by a hysteresis loop in the material's stress strain relation, illustrated in fig. 2.2. Because of this behavior, viscoelastic materials are a typical choice to dissipate unwanted vibration energy in vibro-acoustic systems.

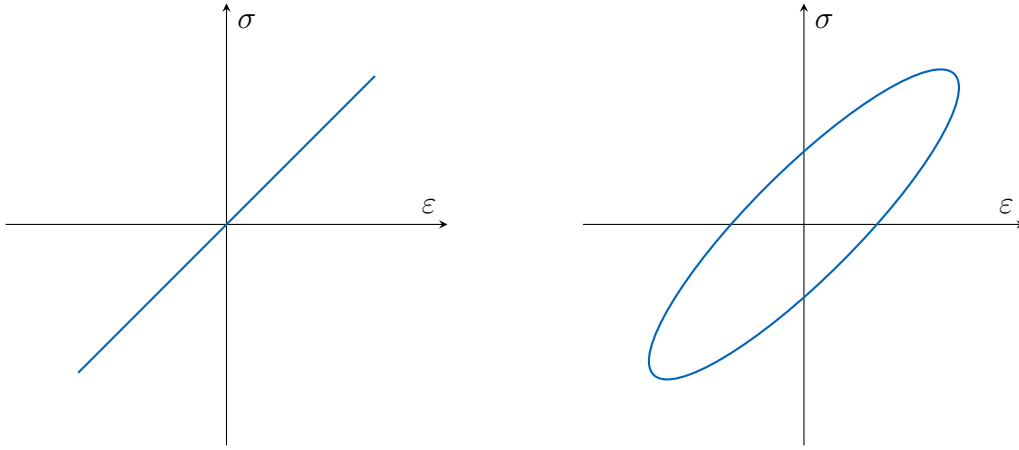


**Figure 2.2:** Comparison between the stress strain relation of an elastic (left) and a viscoelastic material (right). The area enclosed by the hysteresis loop of the viscoelastic material resembles the amount of dissipated energy in one loading cycle.

Their frequency dependent damping behavior is governed by the same constitutive law as used for standard elasticity (2.39) and can be modeled by, for example, a complex valued shear modulus  $\tilde{G}$ . In this context, the real part of  $\tilde{G}$  is termed storage modulus and the imaginary part is termed loss modulus, resembling the energy stored respectively dissipated during a loading cycle [67]. Various models to determine  $\tilde{G}$  depict the viscoelastic behavior by rheological models using springs with stiffnesses  $G_i$  and viscous dampers with damping coefficients  $\eta_j$ . In these equivalent models, a spring depicts the behavior of the elastic portion of the material, while the dashpot models the viscous part of the material response. Some of these models are:

- Kelvin-Voigt model:

$$\tilde{G} = G + \mathbf{i} \operatorname{Im}(s) \eta \quad (2.50)$$

- Maxwell model:

$$\tilde{G} = \frac{G \mathbf{i} \operatorname{Im}(s) \eta}{G + \mathbf{i} \operatorname{Im}(s) \eta} \quad (2.51)$$

- Generalized Maxwell model:

$$\tilde{G} = G_0 + \sum_{i=1}^n \frac{G_i \mathbf{i} \operatorname{Im}(s) \eta_i}{G_i + \mathbf{i} \operatorname{Im}(s) \eta_i} \quad (2.52)$$

A generalized Maxwell model with  $n = 1$  is also known as Zener model. In order to model a more complex time dependent relaxation inside the viscoelastic model, a model based on the concept of fractional derivatives can be employed. Such empirical models can be tuned to describe the behavior of viscoelastic materials using only a few parameters, which can be obtained from measurements [27]. Its complex valued shear modulus is given by

$$\tilde{G} = \frac{G_0 + G_\infty (\mathbf{i} \operatorname{Im}(s) \tau)^\alpha}{1 + (\mathbf{i} \operatorname{Im}(s) \tau)^\alpha}, \quad (2.53)$$

with static shear modulus  $G_0$ , asymptotic shear modulus  $G_\infty$ , relaxation time  $\tau$ , and the fractional parameter  $\alpha$ . An overview over other damping models proposed in literature is given in [2].

### 2.2.3 Poroelastic materials

Porous materials have a complex micro structure consisting of an elastic solid matrix which is surrounded and permeated by a fluid. Such materials are often used to dissipate unwanted vibration energy and typically labeled as foams of any kind [194, 260]. The friction between the two phases causes energy dissipation inside the material. Therefore, porous materials can be used to improve the acoustic properties of a cavity by reducing the overall energy or by damping unwanted echoes. The Biot theory [58, 59] is often used to model porous materials with an elastic skeleton. It describes the material's complex micro structure by an equivalent homogeneous material, characterized by its porosity. This is the fraction of fluid volume and the total volume of the material and denoted by  $\phi = V_{\text{fluid}}/V_{\text{porous}}$ . Additionally, four elastic coefficients  $\tilde{A}$ ,  $G$ ,  $\tilde{Q}$  and  $\tilde{R}$  need to be determined as described in [60] in order to describe the material.  $G$  is the shear modulus of the solid phase, the other coefficients

are obtained from the effective bulk modulus of the fluid phase  $\widetilde{K}_f$ . This is possible, if the solid phase is comprised of a material with a bulk modulus much higher than both the bulk modulus of the porous material in a vacuum and the effective bulk modulus of the fluid phase. Various models to describe this quantity have been proposed, all requiring different input parameters obtained by measurements [145]. In the following, we consider the semiphenomenological Johnson-Champoux-Allard model (JCAM) for porous materials with a non-uniform skeleton [5]. It requires five material parameters to be fully described. The Johnson-Champoux-Allard-Lafarge model [160] also considers thermal effects in the low frequency region and requires an additional parameter to be determined. Another extension is the Johnson-Champoux-Allard-Pride-Lafarge model [212] which additionally considers possible constrictions in the matrix of the porous material. Eight material parameters need to be determined for this representation. If the effects of an elastic frame of the Biot theory are not considered, all these models can also be used to describe the porous material as an equivalent fluid. In the following, the viscous effects of the porous material are described by the JCAM and the solid frame is considered to be elastic. For all models described above, the effective bulk modulus  $\widetilde{K}_f$  is a complex valued function of the excitation frequency  $s$ . For JCAM it is given by

$$\widetilde{K}_f(s) = \frac{\gamma P_0}{\gamma - (\gamma - 1) \left( 1 + \frac{8\mu}{i \operatorname{Im}(s) P r \Lambda^2 \rho_f} \sqrt{1 + \frac{i \operatorname{Im}(s) P r \Lambda^2 \rho_f}{16\mu}} \right)^{-1}}. \quad (2.54)$$

An overview over the material parameters required for the JCAM is presented in table 2.1. The remaining elastic coefficients are then given by

$$\widetilde{A}(s) = \lambda + \frac{\widetilde{Q}(s)^2}{\widetilde{R}(s)}, \quad (2.55)$$

$$\widetilde{Q}(s) = (1 - \phi) \widetilde{K}_f(s), \quad (2.56)$$

$$\widetilde{R}(s) = \phi \widetilde{K}_f(s). \quad (2.57)$$

Here,  $\lambda$  is the first Lamé coefficient. The constitutive relations for stresses in solid and fluid phase of the porous material as given by Biot are

$$\boldsymbol{\sigma}_s = \left( \widetilde{A}(\nabla \cdot \mathbf{u}_s) + \widetilde{Q}(\nabla \cdot \mathbf{u}_f) \right) \circ \mathbf{I} + 2G\boldsymbol{\epsilon}_s, \quad (2.58)$$

$$\boldsymbol{\sigma}_f = \left( \widetilde{Q}(\nabla \cdot \mathbf{u}_s) + \widetilde{R}(\nabla \cdot \mathbf{u}_f) \right) \circ \mathbf{I}. \quad (2.59)$$

$\boldsymbol{\sigma}_s$  is the Cauchy stress tensor for the solid phase and  $\boldsymbol{\sigma}_f$  contains the hydrostatic stress from the fluid pressure inside the material.  $\mathbf{u}_s$  and  $\mathbf{u}_f$  describe the macroscopic displacement

of solid and fluid phase and  $\boldsymbol{\epsilon}_s$  is the strain tensor of the solid phase given small displacements. Biot's governing equations for the solid and fluid phase of a porous material with homogeneous material properties under harmonic motion are then given by

$$\begin{cases} \nabla \cdot \boldsymbol{\sigma}_s(\mathbf{u}_s, \mathbf{u}_f) &= s^2 (\tilde{\rho}_s(s) \mathbf{u}_s + \tilde{\rho}_{sf}(s) \mathbf{u}_f), \\ \nabla \cdot \boldsymbol{\sigma}_f(\mathbf{u}_s, \mathbf{u}_f) &= s^2 (\tilde{\rho}_f(s) \mathbf{u}_f + \tilde{\rho}_{sf}(s) \mathbf{u}_s). \end{cases} \quad (2.60)$$

The effective densities  $\tilde{\rho}_s$ ,  $\tilde{\rho}_f$ ,  $\tilde{\rho}_{sf}$  are linked to the inertial effects between both phases by considering the tortuosity  $\alpha_\infty$  of the porous material. Viscous interaction effects are incorporated by the frequency dependent viscous drag  $\tilde{b}(s)$ . The effective densities are given by

$$\tilde{\rho}_s(s) = (1 - \phi) \rho_s + \phi \rho_f (\alpha_\infty - 1) + \frac{\tilde{b}(s)}{\mathbf{i} \operatorname{Im}(s)}, \quad (2.61a)$$

$$\tilde{\rho}_f(s) = \phi \rho_f \alpha_\infty + \frac{\tilde{b}(s)}{\mathbf{i} \operatorname{Im}(s)}, \quad (2.61b)$$

$$\tilde{\rho}_{sf}(s) = \phi \rho_f (1 - \alpha_\infty) - \frac{\tilde{b}(s)}{\mathbf{i} \operatorname{Im}(s)}, \quad (2.61c)$$

with the density of the solid phase  $\rho_s$  and the fluid phase  $\rho_f$ . The frequency dependent viscous drag is given by

$$\tilde{b}(s) = \sigma \phi^2 \sqrt{1 + \frac{4\mathbf{i} \operatorname{Im}(s) \alpha_\infty^2 \mu \rho_f}{\sigma^2 \Lambda^2 \phi^2}}. \quad (2.62)$$

This classic, or  $(\mathbf{u}_s, \mathbf{u}_f)$ , formulation requires the solution of two vector fields to obtain the displacement of both phases. In order to reduce computational complexity, the displacement of the fluid phase is expressed by the pressure inside the pores in the mixed, or  $(\mathbf{u}_s, p)$ , formulation [18]. Instead of solving two vector fields, one for the displacement of both phases, only a scalar field has to be solved for the fluid phase, which reduces the overall number of required degrees of freedom. This formulation has been extended in [17] to ease the coupling to other media. It couples naturally to an adjacent solid phase, while the standard coupling conditions for coupling a solid to an acoustic fluid phase can be employed for coupling the porous with the acoustic domain. The mixed formulation reads

$$\begin{cases} \nabla \cdot \hat{\boldsymbol{\sigma}}_s(\mathbf{u}_s) - s^2 \tilde{\rho}(s) \mathbf{u}_s + \tilde{\gamma}(s) \nabla p = 0 \\ \nabla^2 p - s^2 \frac{\tilde{\rho}_f(s)}{R(s)} p + s^2 \frac{\tilde{\rho}_f(s)}{\phi^2} \tilde{\gamma}(s) \nabla \cdot \mathbf{u}_s = 0, \end{cases} \quad (2.63)$$

where  $\hat{\boldsymbol{\sigma}}_s(\mathbf{u}_s)$  is the frequency invariant stress tensor of the elastic frame inside a vacuum. It is given by

$$\hat{\boldsymbol{\sigma}}_s(\mathbf{u}_s) = \left( K_b - \frac{2}{3}G \right) \nabla \cdot \mathbf{u}_s \circ \mathbf{I} + 2G\boldsymbol{\epsilon}_s, \quad (2.64)$$

with the bulk modulus of the porous material in vacuo  $K_b$ , its shear modulus  $G$ , and the strain tensor  $\boldsymbol{\epsilon}_s$ . No inertia effects are considered for this stress tensor. The total stress tensor of the poroelastic material  $\boldsymbol{\sigma}_t$  is related to  $\hat{\boldsymbol{\sigma}}_s$  by

$$\boldsymbol{\sigma}_t(\mathbf{u}_s, \mathbf{u}_f) = \hat{\boldsymbol{\sigma}}_s(\mathbf{u}_s) - \phi \left( 1 + \tilde{Q}/\tilde{R} \right) p \circ \mathbf{I}. \quad (2.65)$$

The remaining parameters required to describe the poro-elastic material (2.63) are the effective density  $\tilde{\rho}$ , given by

$$\tilde{\rho}(s) = \tilde{\rho}_s - \frac{\tilde{\rho}_{sf}^2}{\tilde{\rho}_f}, \quad (2.66)$$

and the parameter  $\tilde{\gamma}$ , relating the effective densities and the frequency dependent elastic coefficients to the porosity, defined as

$$\tilde{\gamma}(s) = \phi \left( \frac{\tilde{\rho}_{sf}(s)}{\tilde{\rho}_f(s)} - \frac{\tilde{Q}(s)}{\tilde{R}(s)} \right). \quad (2.67)$$

The hysteretic damping of the solid phase is defined by the loss factor  $\eta_s$  and is modeled by adding an imaginary part to the Lamé parameters of the material

$$\tilde{\lambda} = (1 + i\eta_s) \lambda, \quad (2.68a)$$

$$\tilde{G} = (1 + i\eta_s) G, \quad (2.68b)$$

making the elastic frame's stress tensor a complex valued quantity. In practice, all parameters required to describe the porous material can be estimated from sample measurements in an impedance tube [146]. Different configurations of the impedance tube considering two to four microphones and various thicknesses of the sample allow the measurement of  $\tilde{K}_f$  and  $\tilde{\rho}$  [193, 198]. The remaining parameters can be obtained by considering the porosity  $\phi$  and the flow resistivity  $\sigma$  [146].

Due to the coupling of solid and fluid phase inside the porous material, three types of waves can propagate through the medium: two compression waves and one shear wave. For porous materials saturated with air, one compression wave, termed airborne wave, propagates mostly through the air, while the other, termed frame-borne wave, propagates in both media.

**Table 2.1:** Material parameters for poroelastic materials described by the Biot theory.

Parameter	Unit	Description
$\phi$	-	Porosity
$\sigma$	$\text{N s m}^{-2}$	Flow resistivity
$\alpha_\infty$	-	Tortuosity
$\Lambda$	m	Viscous characteristic length
$\Lambda'$	m	Thermal characteristic length
$\rho_s$	$\text{kg m}^{-3}$	Density of the elastic frame
$\lambda$	Pa	First Lamé parameter of the elastic frame
$G$	Pa	Shear modulus (second Lamé parameter) of the elastic frame
$\eta_s$	-	Structural damping parameter of the elastic frame
$\rho_f$	$\text{kg m}^{-3}$	Density of the surrounding fluid
$\mu$	$\text{N s m}^{-2}$	Viscosity of the surrounding fluid
$P_0$	Pa	Standard pressure of the surrounding fluid
$\gamma$	-	Heat capacity of the surrounding fluid
$Pr$	-	Prandtl number of the surrounding fluid

The shear wave is only propagating in the elastic frame of the porous material. The wave speed of the two compression waves are given by

$$c_{\text{p},1,2} = \left( \frac{2(\tilde{P}\tilde{R} - \tilde{Q}^2)}{\tilde{P}\tilde{\rho}_f + \tilde{R}\tilde{\rho}_s - 2\tilde{Q}\tilde{\rho}_{\text{sf}} \mp \sqrt{\chi}} \right)^{\frac{1}{2}} \quad (2.69)$$

with  $\tilde{P} = \tilde{A} + 2G$  and  $\chi = (\tilde{P}\tilde{\rho}_f + \tilde{R}\tilde{\rho}_s - 2\tilde{Q}\tilde{\rho}_{\text{sf}})^2 - 4(\tilde{P}\tilde{R} - \tilde{Q}^2)(\tilde{\rho}_s\tilde{\rho}_f - \tilde{\rho}_{\text{sf}}^2)$ . The shear wave speed is given by

$$c_{\text{p},\text{S}} = \left( \frac{G\tilde{\rho}_f}{\tilde{\rho}_s\tilde{\rho}_f - \tilde{\rho}_{\text{sf}}^2} \right)^{\frac{1}{2}}. \quad (2.70)$$

The behavior of the different longitudinal waves is governed by the ratio of the velocities of the respective wave type inside the fluid and solid phase of the porous material [5, 149]. For frequency regions where the ratio is close to one, i.e. no relative motion between the phases is present, the slower compression wave propagates mainly in the fluid phase, while the faster compression wave and the shear wave propagate through the solid phase. In this region, viscous forces inside the material are governing. For higher frequencies, the fast compression wave propagates in the fluid, while the shear wave and the slower compression wave propagate mainly in the solid phase.

## 2.2.4 Vibro-acoustic coupling conditions

The correct representation of the coupling between the different phases present in vibro-acoustics is decisive for a correct description of the frequency response of such systems. In the following, conditions ensuring the continuity between the acoustic fluid, elastic solids, and poroelastic materials are outlined. Figure 2.3 gives an overview over all considered coupling surfaces as well as the definition of the corresponding normal vectors. All normal vectors are defined as pointing outwards of the respective domain.

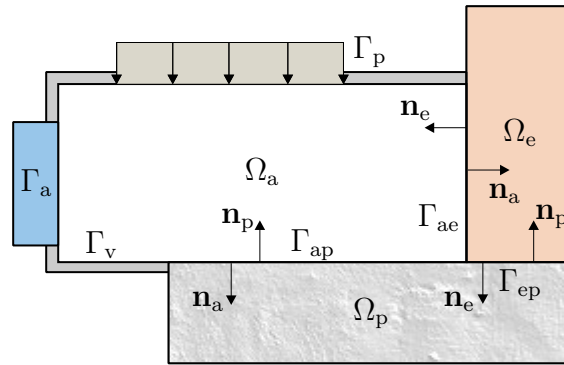


**Figure 2.3:** A vibro-acoustic system with acoustic fluid  $\Omega_a$ , structural elastic domain  $\Omega_e$ , a poroelastic domain  $\Omega_p$ , different boundary conditions  $\Gamma_p$ ,  $\Gamma_a$ ,  $\Gamma_v$ . The interfaces between the phases  $\Gamma_{ae}$ ,  $\Gamma_{ap}$ ,  $\Gamma_{ep}$  are displayed with their corresponding normal vectors  $\mathbf{n}$ .  $\mathbf{n}_a$  points outwards of the acoustic domain,  $\mathbf{n}_e$  outwards of the elastic domain, and  $\mathbf{n}_p$  outwards of the porous domain.

### Acoustic-structural coupling

The coupling between an elastic structure and an adjacent acoustic fluid is realized by relating the pressure field  $p$  in the acoustic domain to the velocity of the structure  $\mathbf{v}$  at the interaction surface between the two domains. In the following, an index  $\cdot_a$  denotes quantities related to the acoustic fluid, the elastic structure is denoted by an index  $\cdot_e$ . For better readability, the space dependency  $\mathbf{r}$  is omitted. The coupling acts in both ways, so variations in acoustic pressure excite the structure, while structural vibration causes pressure fluctuations. The velocity continuity at the interface  $\Gamma_{ae}$  between acoustic fluid and structure is given by

$$\nabla p_a \cdot \mathbf{n}_a + s\rho_a \mathbf{v} \cdot \mathbf{n}_e = 0, \quad (2.71)$$

where the normal vector  $\mathbf{n}_a$  points outside of the fluid domain and  $\mathbf{n}_e$  directs outside of the structural domain, i.e. inside of the acoustic fluid. Here, the fluid's density is denoted by  $\rho_a$ . The above relation is equivalent to the velocity boundary condition given by (2.31), here the velocity at the boundary is defined by the structural vibration. In the opposite direction,

the acoustic pressure acts as a pressure load on the structure. This coupling is given by

$$p_a \mathbf{n}_a - \mathbf{n}_e \cdot \boldsymbol{\sigma}_e = 0. \quad (2.72)$$

A special case needs to be considered, if a thin plate-like structure separates the acoustic fluid into two individual cavities as sketched in fig. 2.4. In this case, the vibrating plate radiates antiphase in both directions. The resulting pressure force acting on the plate is here given by the difference of the pressures  $p_{a_1}$  and  $p_{a_2}$  in both cavities and the vibration of the plate excites the acoustic fluids on both sides of the plate. Given the normal direction definitions as in fig. 2.4, the velocity continuity for both fluids can be written as

$$\nabla p_{a_1} \cdot \mathbf{n}_{a_1} - s\rho_{a_1} \mathbf{v} \cdot \mathbf{n}_e = 0, \quad (2.73)$$

$$\nabla p_{a_2} \cdot \mathbf{n}_{a_2} + s\rho_{a_2} \mathbf{v} \cdot \mathbf{n}_e = 0. \quad (2.74)$$

The excitation of structural vibration, governed by the difference of the pressures  $p_1$  and  $p_2$  is then given by

$$(p_{a_1} - p_{a_2}) \mathbf{n}_a - \mathbf{n}_e \cdot \boldsymbol{\sigma}_e = 0. \quad (2.75)$$

Given this definition of the normal directions, a pressure  $p > 0$  in the acoustic fluid acts as compression force on the structure. Obviously, the plate is not excited if the pressure is equal on both sides of the plate [110].

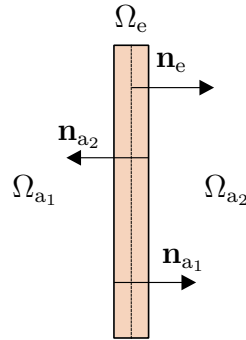


**Figure 2.4:** Fluid structure fluid coupling of a plate like structure  $\Omega_e$  separating two individual acoustic cavities  $\Omega_{a_1}$  and  $\Omega_{a_2}$ .

### Poroelastic-acoustic coupling

We now consider the coupling between an acoustic fluid and a poroelastic material, which pores are open towards the acoustic fluid and thus a mass flux is possible. Coefficients associated with the acoustic fluid are denoted by the index  $\cdot_a$ , coefficients describing the

poroelastic phase by the index  $\cdot_p$ . The continuity at the interface  $\Gamma_{ap}$  between both phases is given by

$$\begin{cases} \mathbf{n}_p \cdot \boldsymbol{\sigma}_t - p_a \cdot \mathbf{n}_a = 0, \\ \frac{1}{\rho_a s^2} \nabla p_a \cdot \mathbf{n}_a - (1 - \phi) \mathbf{u}_s \cdot \mathbf{n}_p - \phi \mathbf{u}_f \cdot \mathbf{n}_p = 0, \\ p_p - p_a = 0. \end{cases} \quad (2.76)$$

The first equation relates the total stress tensor of the poroelastic material to the pressure inside the acoustic cavity and ensures continuity of normal stresses. Continuity between acoustic pressure and total poroelastic displacement, in terms of  $\mathbf{u}_s$  and  $\mathbf{u}_f$ , is ensured by the second equation and the third equation ensures the continuity of fluid pressure at the interface [5].

### Poroelastic-structural coupling

In order to couple a porous material to an elastic structure, described by its displacement field  $\mathbf{u}_e$ , the following conditions need to be fulfilled at the coupling interface  $\Gamma_{ep}$ :

$$\begin{cases} \mathbf{n}_p \cdot \boldsymbol{\sigma}_t + \mathbf{n}_e \cdot \boldsymbol{\sigma}_e = 0, \\ \mathbf{u}_f \cdot \mathbf{n}_p - \mathbf{u}_s \cdot \mathbf{n}_p = 0, \\ \mathbf{u}_s - \mathbf{u}_e = 0. \end{cases} \quad (2.77)$$

Relating the normal parts of the total stress tensor of the poroelastic material and the stress tensor of the elastic structure in the first equation ensures the continuity of normal stresses at the interface. The positive sign results from the definition of the normal vectors, pointing in opposite directions. The fact, that no relative mass flux between the two phases of the poroelastic material is possible at the boundary, is expressed by the second equation. Continuity of the displacements of the elastic structure and the solid phase of the porous material are ensured by the third equation [5].

### Poroelastic-poroelastic coupling

Two separate poroelastic phases, denoted by subscripts  $\cdot_1$  and  $\cdot_2$ , are coupled by relating their displacement vectors and pore pressures. The following conditions need to be fulfilled

at the interface between the two materials  $\Gamma_{pp}$  to ensure continuity:

$$\begin{cases} \mathbf{n}_{p_1} \cdot \boldsymbol{\sigma}_{t_1} + \mathbf{n}_{p_2} \cdot \boldsymbol{\sigma}_{t_2} = 0, \\ \phi_1 (\mathbf{u}_{f_1} - \mathbf{u}_{s_1}) \cdot \mathbf{n}_{p_1} + \phi_2 (\mathbf{u}_{f_2} - \mathbf{u}_{s_2}) \cdot \mathbf{n}_{p_2} = 0, \\ \mathbf{u}_{s_1} - \mathbf{u}_{s_2} = 0, \\ p_{p_1} - p_{p_2} = 0. \end{cases} \quad (2.78)$$

Similar to the poroelastic-structural coupling, the first two equations ensure continuity of total normal stresses and continuity of relative mass flux at the interface between both materials. The continuity between displacements of the solid phases is enforced by the third equation and the fourth equation expresses the pressure continuity of the fluid phases at the boundary [5].

## 2.3 Modeling vibro-acoustic systems

A variety of modeling techniques is used to predict the solution of vibro-acoustic systems following the descriptions derived above. The choice of a specific method is depending on the properties of the model, such as the considered boundary conditions, if the model is bounded or unbounded towards infinity, and the frequency range in which the model is evaluated. Given simple boundary conditions and regular geometries, analytical solutions can be derived for many vibro-acoustic phenomena. They are typically valid for a wide frequency range and solutions are available for both bounded and unbounded domains. If more complex boundary situations as well as arbitrary geometries need to be considered, analytical methods may not be valid anymore and the continuous domain needs to be approximated by numerical methods. The choice of the specific method is governed by the considered frequency range. The number of modes in a specific frequency band of interest is a often considered as a measure if a problem is considered a low or high frequency problem [172]. The finite element method (FEM) and boundary element method (BEM) are deterministic approaches and are typically applied to problems with a low to medium number of modes being present in the frequency range of interest. Contrary, the statistical energy analysis (SEA) is considered for systems with a large number of modes. The main concepts of the methods are outlined in the following.

FEM and BEM or a combination of both can be used for problems with a moderate amount of modes. Using FEM the domain and its boundary and using BEM only the model boundaries are discretized as elements of finite size in which the solution is approximated by shape functions. The spatial discretization must be able to capture all important wave

phenomena, so the element size shrinks with increasing frequency, leading to very large and computationally demanding models if high frequency vibration is considered at large geometries. Contrary to FEM, where the solution is directly approximated in the complete domain, BEM obtains the field solution in a post-processing step from the solution at the model boundaries using Green's functions. This allows the direct modeling of the Sommerfeld radiation condition allowing, for example, a free radiation at the boundaries. Modeling free radiation with the FEM requires specialized elements, which will be covered in section 2.3.2. Although solely discretizing the boundary with the BEM leads to less degrees of freedom compared to discretizing the same problem with finite elements, the resulting frequency dependent linear system of equations is densely populated. This prohibits the application of solving algorithms relying on the sparsity of the system to be solved and thus diminishes the benefits of a smaller size of the equation system [227]. A coupling of domains discretized by FEM and BEM is possible. This allows, for example, the modeling of a fluid structure interaction problem using finite elements and the free radiation into infinity by boundary elements [114].

An extension to the standard finite element method which can be applied to periodic structures is the wave finite element method (WFEM). Here, the wave propagation in such structures is computed by relating the wave solutions at the boundaries of a unit cell, the smallest recurring element in the periodic setup of the structure. This approach is based on the Floquet theorem for one-dimensional periodicity and the Bloch theorem for higher order periodicity, both stating that the wave solution in the periodic structure is also periodic. The unit cell is discretized with finite elements and the periodic structure is considered infinite [175]. Applying the WFEM allows to identify frequency ranges in which waves cannot travel through the periodic structure, making it an important tool for the development of wave attenuating materials and structures [85, 184, 188].

The accuracy of deterministic approaches like FEM, BEM, and derived methods, is limited if systems with very large numbers of modes need to be considered. With the increasing mode order, the dynamic response's sensitivity to small changes in model geometry, boundary conditions, or damping behavior also increases. As these model parameters are at least to some extent subject to uncertainty, a purely deterministic method becomes unreliable. Additionally, the dynamic influence of the system is dominantly governed by more than one mode if many modes appear in direct vicinity, making considerations depending on single modes unreliable. In such cases the overall energy in the system and its subsystems provides a better measure for the system behavior. The SEA considers the probabilistic nature of the frequency response of such systems with the help of averaging techniques. Its main concept is to treat parts of the main system as interconnected subsystems and depict their vibrational flow by an energy equilibrium [98]. Here, the subsystems are considered

as groups of similar modes. The energy responses of the subsystems are averaged over a frequency range containing enough modes to justify this statistical average. Therefore, a certain modal density, i.e. number of modes in a specified frequency band, is required for SEA to be applicable [172]. The SEA calculates the energy flow through and storage in a system by discretizing it as interconnected subsystems. The subsystems store energy, which is generated by external, often random, sources, transmit it to other subsystems, and dissipate or radiate energy, which is then not part of the system anymore. All energies are averaged, which accounts for the uncorrelated state of the overlapping wave patterns at high frequencies. A generalization of the SEA which allows the coupling of deterministic and statistical subsystems has been established by Shorter and Langley [236]. The energy flow analysis introduced by Mace and Shorter [173] follows a similar concept than the SEA but allows different wave types to be present in a subsystem and has less requirements on the coupling of multiple subsystems [265, 266].

The frequency region in which the SEA is not yet applicable but the models required for FEM or BEM tend to be very large is considered as mid-frequency region [174]. Combinations of deterministic and statistical methods, such as the stochastic boundary element method (SBEM), can be used to model problems which are required to be accurate in this frequency range. Coupling SEA subsystems with finite element systems is also possible [83]. Another approach are Trefftz methods, a deterministic approach where exact solutions of the governing differential equations are used as shape functions to approximate the solution in the domain of interest, allowing accurate solutions also for high frequencies using a reasonable amount of degrees of freedom. The method, however, yields densely populated matrices which are often ill-conditioned [258]. Using higher order shape functions in the FEM can also decrease the number of required degrees of freedom to achieve sufficient accuracy in the mid-frequency region [54].

In the following, we will focus on the FEM, as it is a widely used method to model low to mid-frequency vibro-acoustic problems. Additionally, the resulting sparsely populated system matrices are a prerequisite for many complexity reduction methods described in chapters 3 and 4.

### 2.3.1 The finite element method for vibro-acoustic systems

Let  $\mathcal{A}(\mathbf{x}) = 0$  be a set of differential equations satisfied by an unknown function vector  $\mathbf{x}$  in the domain  $\Omega$  and  $\mathcal{B}(\mathbf{x}) = 0$  the set of corresponding boundary conditions on  $\Gamma$ . The vector  $\mathbf{x}$  contains the field variables being described by the differential equations, for example pressure or displacements. The finite element method seeks an approximation to this vector function by employing shape functions  $\mathbf{N}$  defined by spatial coordinates. For this, the domain  $\Omega$  is

divided into a finite number of nodes  $n$  which form a number of elements with predefined shape. The approximate solution of the field variables is then given by the series

$$\mathbf{x} \approx \hat{\mathbf{x}} = \sum_{i=1}^n N_i \mathbf{x}_i = \mathbf{N} \bar{\mathbf{x}}. \quad (2.79)$$

The matrix  $\mathbf{N}$  contains  $n$  locally defined shape functions, which evaluate to 1 at node  $i$  and zero at every other node.  $\bar{\mathbf{x}}$  is the corresponding set of parameters ensuring a proper approximation. To obtain a standardized way of evaluating the shape functions also for distorted elements, the element geometry is typically mapped onto an equivalent element where the spatial coordinate is defined in the range  $[-1,1]$ . This is known as the isoparametric concept and the necessary mapping operator is given by the element's Jacobian matrix. This concept is explained in detail in Zienkiewicz, Taylor, and Zhu [277].

The solution for  $\bar{\mathbf{x}}$  in (2.79) is obtained from an integral form approximating  $\mathcal{A}$  and  $\mathcal{B}$  in the domain. As the shape functions do not satisfy the differential equations nor their boundary conditions, a weighting has to be applied to find a solution for  $\mathbf{x}_i$  with a minimal error. This is known as the method of weighted residuals. The required integral form is given by

$$\int_{\Omega} \mathbf{w}_A^T \mathcal{A}(\mathbf{x}) \, d\Omega + \int_{\Gamma} \mathbf{w}_B^T \mathcal{B}(\mathbf{x}) \, d\Gamma = 0, \quad (2.80)$$

with vectors of arbitrary weighting functions  $\mathbf{w}_A$ ,  $\mathbf{w}_B$  of appropriate length. As the integral expression needs to be evaluated numerically, the derivatives of the employed functions  $\mathbf{x}$  must be continuous. Performing an integration by parts lowers the required order of continuity for  $\mathbf{x}$  while increasing it for  $\mathbf{w}$ , resulting in the so called weak integral form. As the functions in  $\mathbf{w}$  are often polynomials, the requirements on continuity can be easily met. To find the weighting functions  $\mathbf{w}$  satisfying eq. (2.80), they are, similarly to eq. (2.79), approximated by a sum of shape functions  $N_i$  and nodal weights  $\mathbf{w}_i$  as

$$\mathbf{w} \approx \hat{\mathbf{w}} = \sum_{i=1}^n N_i \mathbf{w}_i. \quad (2.81)$$

If the same shape functions are chosen for both approximations eqs. (2.79) and (2.81), the method is referred to as Galerkin method. Inserting both approximations into the integral form eq. (2.80) yields

$$\mathbf{w}_i^T \left( \int_{\Omega} \mathbf{N}_A^T \mathcal{A}(\mathbf{N} \bar{\mathbf{x}}) \, d\Omega + \int_{\Gamma} \mathbf{N}_B^T \mathcal{B}(\mathbf{N} \bar{\mathbf{x}}) \, d\Gamma \right) = 0. \quad (2.82)$$

As the expression needs to be valid for arbitrary weights  $\mathbf{w}_i$ , the function vector can be

omitted. Again, performing and integration by parts yields an expression with a lower requirement on continuity for the functions  $\bar{\mathbf{x}}$ . Performing the necessary discretization steps and applying all boundary conditions results in a linear system of equations of the form

$$\mathbf{A}\bar{\mathbf{x}} = \mathbf{b}. \quad (2.83)$$

$\mathbf{A}$  is called dynamic stiffness matrix in a vibro-acoustic context,  $\mathbf{b}$  contains the external loads, and  $\bar{\mathbf{x}}$  is the approximation of the unknown field parameters  $\mathbf{x}$  under the assumption of (2.79). Depending on the modeled problem, post-processing steps to obtain derived quantities, for example stresses, may be required. The approximations performed by the shape functions can be reused for this procedure. Details on the implementation of the finite element method in a computer program can be found, for example, in the books of Zienkiewicz, Taylor, and Zhu [277], Bathe [33], and Hughes [139]. In the following, weak formulations for the differential equations describing different parts of a vibro-acoustic system introduced in section 2.2 are presented.

### Finite element formulation for structural waves

A weak form of the elastic wave equation (2.40) is given by

$$\int_{\Omega} \hat{\mathbf{w}}_{\epsilon} \otimes \boldsymbol{\sigma} \, d\Omega + s^2 \rho_e \int_{\Omega} \hat{\mathbf{w}}_{\mathbf{u}} \mathbf{u} \, d\Omega - \int_{\Omega} \hat{\mathbf{w}}_{\mathbf{u}} \mathbf{b} \, d\Omega - \int_{\Gamma_{\sigma}} \hat{\mathbf{w}}_{\mathbf{u}} \boldsymbol{\sigma}_{\mathbf{n},\Gamma} \, d\Gamma_{\sigma} = 0, \quad (2.84)$$

with prescribed normal stresses  $\boldsymbol{\sigma}_{\mathbf{n},\Gamma}$  at the corresponding boundary  $\Gamma_{\sigma}$ . Following the Galerkin principle, we use the same shape functions to approximate the test functions  $\mathbf{w}$  and the unknowns  $\boldsymbol{\sigma}$  and  $\mathbf{u}$ . Assembly into matrix form yields a second order dynamical system given by

$$\Sigma: \begin{cases} (s^2 \mathbf{M}_e + s \mathbf{C}_e + \mathbf{K}_e) \mathbf{x}(s) = \mathbf{f}_e u(s), \\ y(s) = \mathbf{g} \mathbf{x}(s). \end{cases} \quad (2.85)$$

Here,  $\mathbf{K}_e$  represents the stiffness distribution in the elastic medium,  $\mathbf{C}_e$  is the viscous damping matrix,  $\mathbf{M}_e$  defines the system's mass distribution, and the external forces are collected in  $\mathbf{f}_e$ . Stiffness, mass, and loading are given by

$$\mathbf{K}_e = \int_{\Omega} \mathbf{B}^T \mathbf{D} \mathbf{B} \, d\Omega, \quad (2.86)$$

$$\mathbf{M}_e = \rho_e \int_{\Omega} \mathbf{N}^T \mathbf{N} \, d\Omega, \quad (2.87)$$

$$\mathbf{f}_e = \int_{\Omega} \mathbf{N}^T \mathbf{b} \, d\Omega + \int_{\Gamma_{\sigma}} \mathbf{N}^T \boldsymbol{\sigma}_{\mathbf{n},\Gamma} \, d\Gamma_{\sigma}, \quad (2.88)$$

with matrix  $\mathbf{B}$  containing the derivatives of the shape functions with respect to  $\mathbf{L}$  as defined by eq. (2.41) at each node. The system's transfer function is

$$H(s) = \mathbf{g} \left( s^2 \mathbf{M}_e + s \mathbf{C}_e + \mathbf{K}_e \right)^{-1} \mathbf{f}_e. \quad (2.89)$$

The damping matrix can have different forms, which are depending on the employed damping model. If viscous damping is realized by a complex and frequency dependent shear modulus,  $\mathbf{C}_e$  is given by the imaginary part of  $\mathbf{K}_e$ . Another concept to compute a system's viscous damping is using a stiffness and/or mass proportional damping, where  $\mathbf{C}_e$  is a linear combination of  $\mathbf{K}_e$  and  $\mathbf{M}_e$ . Proportional damping matrices are particularly interesting in the context of modal analysis, as they can be diagonalized in the same way as mass and stiffness matrices. A widely used form of proportional damping is Rayleigh damping, where the damping matrix is given by

$$\mathbf{C}_e = \alpha \mathbf{M}_e + \beta \mathbf{K}_e, \quad (2.90)$$

with two parameters  $\alpha, \beta$ . The damping in the low frequency region is governed by inertia effects and regulated with parameter  $\alpha$ , while the influence of stiffness controlled damping in the higher frequency region is governed by  $\beta$ . The parameters can be determined by specifying two loss factors  $\eta_1$  and  $\eta_2$  at two arbitrary frequencies  $f_1$  and  $f_2$ . However, a single loss factor  $\eta = \eta_1 = \eta_2$  is often chosen, resulting in a similar damping behavior for frequencies  $f_1 \leq f \leq f_2$ . The resulting damping is lower than  $\eta$  in this frequency region and higher for all other frequencies. The Rayleigh parameters are then given by

$$\alpha = 2\pi \frac{\eta f_1 f_2}{f_1 + f_2} \quad (2.91)$$

$$\beta = \frac{\eta}{2\pi (f_1 + f_2)}. \quad (2.92)$$

Figure 2.5 illustrates the influence of both parameters on the resulting loss factor. The loss factors can, for example, be obtained from measurements or are found in literature.

As the effect of Rayleigh damping is always affecting the complete frequency range in which the system is evaluated, it may be difficult to tune  $\alpha$ , and  $\beta$  according to a more complex damping behavior over a larger frequency region. Caughey [73] proposed a generalization of the classical Rayleigh damping allowing  $n$  damping parameters  $d$ , where  $n$  must be lower than the number of degrees of freedom in the system. The according damping matrix is

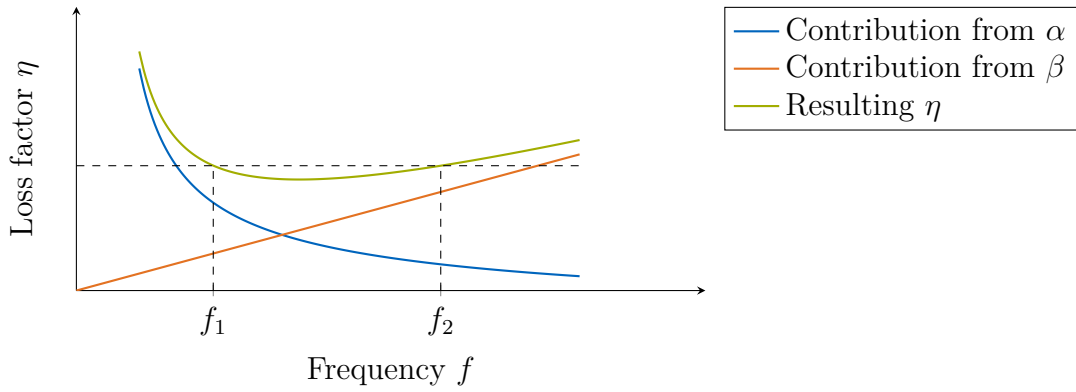


**Figure 2.5:** Determination of Rayleigh damping parameters  $\alpha$  and  $\beta$  by specifying the loss factors at two distinct frequencies. Influence of  $\alpha$  and  $\beta$  on the resulting system damping ratio  $\eta$ .

computed by

$$\mathbf{C}_e = \mathbf{M}_e^{\frac{1}{2}} \left( \sum_{i=0}^{n-1} d_i \left( \mathbf{M}_e^{-\frac{1}{2}} \mathbf{K}_e \mathbf{M}_e^{-\frac{1}{2}} \right)^{\frac{i}{p}} \right) \mathbf{M}_e^{\frac{1}{2}}, \quad (2.93)$$

with an integer  $p$  that may be negative, if  $\mathbf{K}_e$  is invertible. The case  $p = 1$ ,  $n = 2$  is equivalent to Rayleigh damping and the damping matrix obtained from eq. (2.93) is also diagonalizable. The unknown parameters  $d$  can be computed from a linear system of equations as described, for example, in [151, Section 3.5.6]. However, this system is prone to be ill-conditioned for a large number of  $n$  and the resulting parameters might lead to negative damping for some frequencies or highly oscillating damping behavior between the expansion frequencies. Additionally, the matrix powers in eq. (2.93) require a substantial computational effort to compute  $\mathbf{C}_e$ , especially for higher  $n$ .

### Finite element formulation for acoustic waves

The weak form of the Helmholtz equation (2.28) and its boundary conditions is obtained from its integral formulation by integrating by parts. This results in

$$\frac{s^2}{c_a^2} \int_{\Omega} \hat{\mathbf{w}}_p p \, d\Omega + \int_{\Omega} \nabla \hat{\mathbf{w}}_p \nabla p \, d\Omega + s \rho_a \int_{\Gamma_v} \hat{\mathbf{w}}_p \mathbf{v}_{n,\Gamma} \, d\Gamma_v + s \rho_a \int_{\Gamma_A} \hat{\mathbf{w}}_p (p A_{n,\Gamma}) \, d\Gamma_A = 0, \quad (2.94)$$

with prescribed values  $\mathbf{v}_{n,\Gamma}$  for particle velocity in normal direction and normal admittance  $A_{n,\Gamma}$ . Using the Galerkin method, the same shape functions are used to approximate the pressure  $p$  and the corresponding test functions  $\hat{\mathbf{w}}_p$ . After discretization and assembly, a

second order system of shape

$$\Sigma: \begin{cases} \left( \frac{s^2}{c_a^2} \mathbf{M}_a + s \mathbf{C}_a + \mathbf{K}_a \right) \mathbf{x}(s) = \mathbf{f}_a(s) u(s), \\ y(s) = \mathbf{g} \mathbf{x}(s), \end{cases} \quad (2.95)$$

is obtained. The matrices and vector are related to (2.94) by

$$\mathbf{K}_a = \int_{\Omega} \nabla \mathbf{N}^T \nabla \mathbf{N} \, d\Omega \quad (2.96)$$

$$\mathbf{C}_a = \rho_a \int_{\Gamma_A} \mathbf{N}^T A_{n,\Gamma} \mathbf{N} \, d\Gamma_A \quad (2.97)$$

$$\mathbf{M}_a = \frac{1}{c_a^2} \int_{\Omega} \mathbf{N}^T \mathbf{N} \, d\Omega \quad (2.98)$$

$$\mathbf{f}_a(s) = -s \rho_a \int_{\Gamma_v} \mathbf{N}^T v_{n,\Gamma} \, d\Gamma_v \quad (2.99)$$

The acoustic mass matrix  $\mathbf{M}_a$  represents the compressibility of the medium, the acoustic stiffness matrix  $\mathbf{K}_a$  its mobility. If an admittance boundary condition is considered, the acoustic damping matrix  $\mathbf{C}_a$  is not proportional to  $\mathbf{M}_a$  or  $\mathbf{K}_a$ . All three material matrices are typically symmetric. The input mapping  $\mathbf{f}_a(s)$  is frequency dependent due to the definition of the Neumann boundary condition for the acoustic fluid (2.31). Specifying a normal displacement boundary according to (2.32) is performed analogously, the frequency dependency is quadratic regarding  $s$  in this case. The system's transfer function is given by

$$H(s) = \mathbf{g} \left( \frac{s^2}{c_a^2} \mathbf{M}_a + s \mathbf{C}_a + \mathbf{K}_a \right)^{-1} \mathbf{f}_a(s). \quad (2.100)$$

The system described above is only valid for bounded domains, i.e. interior problems. The treatment of unbounded domains and their finite element discretization is presented in section 2.3.2.

### Finite element formulation of poroelastic materials

A weak integral form of the mixed displacement-pressure formulation for poroelastic materials (2.63) is given in [17] as

$$\left\{ \begin{array}{l} \int_{\Omega} \hat{\mathbf{w}}_{\epsilon_s} \otimes \hat{\boldsymbol{\sigma}}_s \, d\Omega + s^2 \tilde{\rho} \int_{\Omega} \hat{\mathbf{w}}_{\mathbf{u}_s} \cdot \mathbf{u}_s \, d\Omega - \left( \tilde{\gamma} + \phi \left( 1 + \frac{\tilde{Q}}{\tilde{R}} \right) \right) \int_{\Omega} \hat{\mathbf{w}}_{\mathbf{u}_s} \cdot \nabla p \, d\Omega \\ \quad - \phi \left( 1 + \frac{\tilde{Q}}{\tilde{R}} \right) \int_{\Omega} \nabla \hat{\mathbf{w}}_{\mathbf{u}_s} \cdot p \, d\Omega - \int_{\Gamma} \hat{\mathbf{w}}_{\mathbf{u}_s} \cdot \boldsymbol{\sigma}_{t,n,\Gamma} \, d\Gamma = 0, \\ - \frac{\phi^2}{s^2 \tilde{\rho}_f} \int_{\Omega} \nabla \hat{\mathbf{w}}_p \cdot \nabla p \, d\Omega - \frac{\phi^2}{\tilde{R}} \int_{\Omega} \hat{\mathbf{w}}_p p \, d\Omega - \left( \tilde{\gamma} + \phi \left( 1 + \frac{\tilde{Q}}{\tilde{R}} \right) \right) \int_{\Omega} \nabla \hat{\mathbf{w}}_p \cdot \mathbf{u}_s \, d\Omega \\ \quad - \phi \left( 1 + \frac{\tilde{Q}}{\tilde{R}} \right) \int_{\Omega} \hat{\mathbf{w}}_p \nabla \cdot \mathbf{u}_s \, d\Omega - \phi \int_{\Gamma} \hat{\mathbf{w}}_p (\mathbf{u}_{f,n} - \mathbf{u}_{s,n}) \, d\Gamma = 0, \end{array} \right. \quad (2.101)$$

regarding the corresponding test functions  $\hat{\mathbf{w}}$ . The index  $n$  marks the normal component of a quantity regarding the corresponding surface  $\Gamma$ , where the normal vector is defined pointing outwards of the porous domain. The frequency dependency of the parameters marked with a tilde are not stated explicitly for better readability. Note, that for porous materials where the bulk modulus of the skeleton structure inside a vacuum is much lower than the bulk modulus of an elastic solid consisting of the material of which the skeleton is comprised of, it holds  $\phi \left( 1 + \tilde{Q}/\tilde{R} \right) \cong 1$ . The relations regarding the coupling of solid and fluid phase in (2.101) can therefore be simplified. A complete derivation is given, for example, in [5, Chapter 13]. A discretization of the equations above leads to the following linear system of equations

$$\begin{bmatrix} \mathbf{K}_{p,s} + s^2 \tilde{\mathbf{M}}_{p,s} & -\tilde{\mathbf{Z}}_{p,sf} \\ s^2 \tilde{\mathbf{Z}}_{p,sf}^T & \tilde{\mathbf{K}}_{p,f} + s^2 \tilde{\mathbf{M}}_{p,f} \end{bmatrix} \begin{bmatrix} \mathbf{u}_s \\ \mathbf{p} \end{bmatrix} = \begin{bmatrix} \mathbf{f}_{p,s} \\ s^2 \mathbf{f}_{p,f} \end{bmatrix} \quad (2.102)$$

with the individual matrices representing the stiffness and mass distribution of the solid phase, the coupling between both phases, and the compressibility of the interstitial fluid. They are given by

$$\mathbf{K}_{p,s} = \int_{\Omega} \mathbf{B}_s^T \mathbf{D} \mathbf{B}_s \, d\Omega, \quad (2.103)$$

$$\tilde{\mathbf{M}}_{p,s} = \tilde{\rho} \int_{\Omega} \mathbf{N}_s^T \mathbf{N}_s \, d\Omega, \quad (2.104)$$

$$\tilde{\mathbf{K}}_{p,f} = \frac{\phi^2}{\tilde{\rho}_f} \int_{\Omega} \nabla \mathbf{N}_f^T \nabla \mathbf{N}_f \, d\Omega, \quad (2.105)$$

$$\widetilde{\mathbf{M}}_{p,f} = \frac{\phi^2}{\widetilde{R}} \int_{\Omega} \mathbf{N}_f^T \mathbf{N}_f \, d\Omega, \quad (2.106)$$

$$\widetilde{\mathbf{Z}}_{p,sf} = \left( \widetilde{\gamma} + \phi \left( 1 + \frac{\widetilde{Q}}{\widetilde{R}} \right) \right) \int_{\Omega} \mathbf{N}_s^T \nabla \mathbf{N}_f \, d\Omega + \phi \left( 1 + \frac{\widetilde{Q}}{\widetilde{R}} \right) \int_{\Omega} \nabla \mathbf{N}_s^T \mathbf{N}_f \, d\Omega, \quad (2.107)$$

$$\mathbf{f}_{p,s} = \int_{\Gamma} \mathbf{N}_s^T \boldsymbol{\sigma}_{t,n,\Gamma} \, d\Gamma, \quad (2.108)$$

$$\mathbf{f}_{p,f} = \phi \int_{\Gamma} \mathbf{N}_f^T (\mathbf{u}_{f,n} - \mathbf{u}_{s,n}) \, d\Gamma. \quad (2.109)$$

The subscripts  $\cdot_s$  and  $\cdot_f$  denote the shape functions respectively their derivatives corresponding to the structural or fluid degrees of freedom. In the above relations,  $\mathbf{K}_{p,s}$  and  $\mathbf{M}_{p,s}$  represent the equivalent stiffness and mass distribution of the elastic skeleton,  $\mathbf{K}_{p,f}$  and  $\mathbf{M}_{p,f}$  the equivalent mobility and compressibility of the interstitial fluid,  $\mathbf{Z}_{p,sf}$  the coupling between the phases,  $\mathbf{f}_{p,s}$  the loading of the skeleton, and  $\mathbf{f}_{p,f}$  the kinematic coupling between solid and fluid phase. Note, that all above matrices except eq. (2.103) are complex valued and frequency dependent. In order to efficiently use the discretized system for frequency sweep analyses, it is beneficial to make the individual matrices in (2.102) independent from the excitation frequency  $s$ , such that

$$\begin{bmatrix} \mathbf{K}_{p,s} + s^2 \widetilde{\mathbf{M}}_{p,s} & -\widetilde{\mathbf{Z}}_{p,sf} \\ s^2 \widetilde{\mathbf{Z}}_{p,sf}^T & \widetilde{\mathbf{K}}_{p,f} + s^2 \widetilde{\mathbf{M}}_{p,f} \end{bmatrix} = \sum_{i=1}^n \phi_i(s) \mathbf{A}_i. \quad (2.110)$$

This allows to perform the computationally expensive assembly process once prior to the analysis. Afterwards, the linear system of equations in eq. (2.102) can be computed by a linear combination of  $n$  constant matrices  $\mathbf{A}$  and  $n$  scalar functions  $\phi_i(s)$  for each frequency step. A possible decomposition is given in the appendix in eq. (A.3).

### Finite element formulation for vibro-acoustic coupling conditions

In the following, the weak forms of the vibro-acoustic coupling conditions outlined in section 2.2.4 and the corresponding finite element discretization are summarized. The weak form of the acoustic-structural coupling governed by eqs. (2.71) and (2.72) is given by

$$\int_{\Gamma} \widehat{\mathbf{w}}_{\mathbf{u}_e} p_a + \widehat{\mathbf{w}}_{p_a} \mathbf{u}_e \, d\Gamma = 0. \quad (2.111)$$

A discretization leads to two coupling matrices

$$\mathbf{Z}_{ae} = - \int_{\Gamma} \mathbf{N}_e^T \mathbf{n}_e \mathbf{N}_a \, d\Gamma, \quad (2.112)$$

$$\mathbf{Z}_{ea} = s^2 \rho_a \int_{\Gamma} \mathbf{N}_a^T \mathbf{n}_a \mathbf{N}_e \, d\Gamma, \quad (2.113)$$

where the index  $\cdot_a$  marks shape functions corresponding to the acoustic domain and normal vectors pointing outwards of this domain. Index  $e$  marks the respective quantities for the domain of the elastic structure. The fully discretized system is then given by

$$\begin{bmatrix} s^2\mathbf{M}_e + s\mathbf{C}_e + \mathbf{K}_e & \mathbf{Z}_{ae} \\ \mathbf{Z}_{ea} & s^2\mathbf{M}_a + s\mathbf{C}_a + \mathbf{K}_a \end{bmatrix} \begin{bmatrix} \mathbf{u} \\ \mathbf{p} \end{bmatrix} = \begin{bmatrix} \mathbf{f}_e \\ \mathbf{f}_a(s) \end{bmatrix}. \quad (2.114)$$

Using the modified weak integral formulation for poroelastic materials described by skeleton displacement and interstitial fluid pressure as proposed by Atalla, Hamdi, and Paneton [17] ease the coupling to other media. Rewriting the boundary integrals regarding an interface of a poroelastic material and an acoustic fluid using eqs. (2.94) and (2.101) leads to the coupling term

$$s^2\rho_a \int_{\Gamma} \hat{\mathbf{w}}_{p_a} \mathbf{u}_{n_a,\Gamma} d\Gamma + \int_{\Gamma} \hat{\mathbf{w}}_{\mathbf{u}_s} \cdot \boldsymbol{\sigma}_{t,n_p,\Gamma} d\Gamma + \phi \int_{\Gamma} \hat{\mathbf{w}}_p (\mathbf{u}_{f,n_p} - \mathbf{u}_{s,n_p}) d\Gamma = 0, \quad (2.115)$$

where index  $\cdot_p$  denotes a quantity referring to the porous material and the corresponding normal vector is pointing outwards of the poroelastic domain. Introducing the boundary conditions for poroelastic-acoustic coupling eq. (2.76) leads to

$$\int_{\Gamma} \hat{\mathbf{w}}_{\mathbf{u}_s} p_a + \hat{\mathbf{w}}_p \mathbf{u}_s d\Gamma = 0. \quad (2.116)$$

This means, that the poroelastic material couples to an acoustic fluid in the same way an elastic structure couples to an acoustic fluid (c.f. eqs. (2.71), (2.72) and (2.111)). The last boundary condition from eq. (2.76),  $p_p - p_a = 0$ , can automatically be enforced during the assembly process.

The boundary integrals at the interface of an elastic structure and a poroelastic medium can be rewritten as

$$\int_{\Gamma} \hat{\mathbf{w}}_{\mathbf{u}} \boldsymbol{\sigma}_{n_e,\Gamma} d\Gamma + \int_{\Gamma} \hat{\mathbf{w}}_{\mathbf{u}_s} \cdot \boldsymbol{\sigma}_{t,n_p,\Gamma} d\Gamma + \phi \int_{\Gamma} \hat{\mathbf{w}}_p (\mathbf{u}_{f,n_p} - \mathbf{u}_{s,n_p}) d\Gamma = 0, \quad (2.117)$$

with the same definition of the normal vectors as above. All terms vanish after substituting the boundary conditions at the interface given in (2.77) in the boundary integral, meaning that the coupling between the two phases is enforced naturally. Only the kinematic boundary condition  $\mathbf{u}_s - \mathbf{u}_e = 0$  needs to be enforced, which is again ensured by the assembly process.

Combining the weak formulation of the boundary integrals of the interface between two porous media, denoted by subscripts  $\cdot_1$  and  $\cdot_2$ , the following relation is obtained:

$$\int_{\Gamma} \hat{\mathbf{w}}_{\mathbf{u}_{s_1}} \cdot \boldsymbol{\sigma}_{t_1, n_{p_1}, \Gamma} d\Gamma + \phi \int_{\Gamma} \hat{\mathbf{w}}_{p_1} (\mathbf{u}_{f_1, n_{p_1}} - \mathbf{u}_{s_1, n_{p_1}}) d\Gamma + \int_{\Gamma} \hat{\mathbf{w}}_{\mathbf{u}_{s_2}} \cdot \boldsymbol{\sigma}_{t_2, n_{p_2}, \Gamma} d\Gamma + \phi \int_{\Gamma} \hat{\mathbf{w}}_{p_2} (\mathbf{u}_{f_2, n_{p_2}} - \mathbf{u}_{s_2, n_{p_2}}) d\Gamma = 0. \quad (2.118)$$

The normal vectors of both materials have opposite directions, each pointing outwards of the respective domain. By inserting the boundary conditions (2.78), all terms in the equation above again cancel out. So the only conditions required to be enforced at the interface are the kinematic boundary conditions  $\mathbf{u}_{s_1} - \mathbf{u}_{s_2} = 0$  and  $p_{p_1} - p_{p_2} = 0$ , which are ensured during the assembly process.

### 2.3.2 The perfectly matched layer method

In order to perform numerical analysis of wave phenomena using the finite element method, the discretized domain needs to be truncated at artificial model boundaries to obtain a reasonably sized problem. As physical waves would travel through these boundaries without reflection or diffraction, special boundary conditions need to be employed to ensure the Sommerfeld radiation condition (2.34). This means, that no energy is reflected at or can re-enter the system from outside the boundary. If this condition is fulfilled, all energy radiates from the system towards infinity and no energy can radiate from infinity into the bounded problem [240]. This radiation pattern can be modeled using absorbing boundary conditions (ABC), for example impedance boundary conditions or Dirichlet-to-Neumann conditions, infinite elements, or perfectly matched layers (PML).

Impedance boundary conditions are numerically inexpensive as they only require the application of a Robin boundary condition as of eq. (2.33). However, they only absorb the waves impinging the boundary at normal incidence and may therefore yield unsatisfactory results for arbitrarily shaped boundaries. A remedy is to increase the distance between the problem of interest and the artificial boundary in order to ensure a direction normal to the boundaries for the majority of waves, which in turn increases computational complexity [94, 110].

Dirichlet-to-Neumann (DtN) conditions impose the analytic solution of the Dirichlet problem of the exterior domain on the arbitrary model boundary as a Neumann boundary condition [119, 152]. As the method requires an analytic solution of the problem in the infinite domain, problems with multiple sources or scatterers require additional treatment [125]. The non-locality of the DtN operator leads to densely populated system matrices, which is undesirable for many equation solving algorithms [267].

Infinite elements provide a local non-reflecting boundary condition by adding a layer of

special elements at the radiating boundary [15]. These elements map the solution of decaying waves traveling outwards of the physical domain of interest towards infinity to a finite set of nodes on which a numerical integration can be performed [253]. Compared to standard finite elements, IE require special shape functions which allow a reasonable discretization of the waves traveling to infinity. After the evaluation of the frequency response in the system, the solution in the far field can directly be obtained from the infinite elements. Various formulations for infinite elements exist, differing, for example, in the symmetry of the resulting system matrices or their inherent frequency dependency [14, 16, 116, 117].

The perfectly matched layer method is also based on adding layers of absorbing material around the domain of interest of the discretized problem. It is called perfectly matched because waves can enter this region without reflections, the concept is sketched in fig. 2.6. Here, the region of interest is termed physical domain; the wave motion inside the perfectly matched layer is non-physical and only ensures the Sommerfeld radiation condition. The layer material is chosen in a way that all waves are damped inside the perfectly matches layer and no energy is reflected at the boundaries of the outermost layer. Thus no energy can re-enter the domain of interest. After it was originally introduced for electromagnetic problems [52], the method has been used for various kinds of wave phenomena [53, 56, 148, 195]. Originally defined along coordinate axes, allowing the application for example for rectangular, circular, or elliptical regions, the locally conformal PML can be used for an arbitrary convex shape enclosing the domain of interest [196]. This allows to place the model boundaries closer to the region of interest, resulting in smaller numerical models. A strategy to automatically compute the grid in the PML region has been proposed recently [53]. Perfectly matched layers are easy to implement in a finite element framework as already existing finite element definitions can be reused. Therefore it is a common choice to model free radiation in engineering practice. The perfectly matched layer method can also be employed for different types of structural waves, a review over recent methods is given in [209]. In the following, however, only PML for compression waves in an acoustic fluid are considered. The locally conformal PML is reviewed and an implementation with finite elements is given in the next section.

The main concept behind perfectly matched layers is the complex coordinate stretching. To illustrate this, we consider oscillating waves given by  $e^{ik\mathbf{r}}$ , which satisfy the Helmholtz equation (2.28). The physical coordinate  $\mathbf{r}$  is transformed (or stretched) to a complex coordinate  $\tilde{\mathbf{r}}$ , thus introducing a decay in the wave propagation

$$e^{ik\tilde{\mathbf{r}}} = e^{ik(\text{Re}(\tilde{\mathbf{r}})+i\text{Im}(\tilde{\mathbf{r}}))} = e^{ik\text{Re}(\tilde{\mathbf{r}})}e^{-k\text{Im}(\tilde{\mathbf{r}})}. \quad (2.119)$$

The imaginary part of the stretched coordinate  $\tilde{\mathbf{r}}$  governs the decay of waves inside the PML.

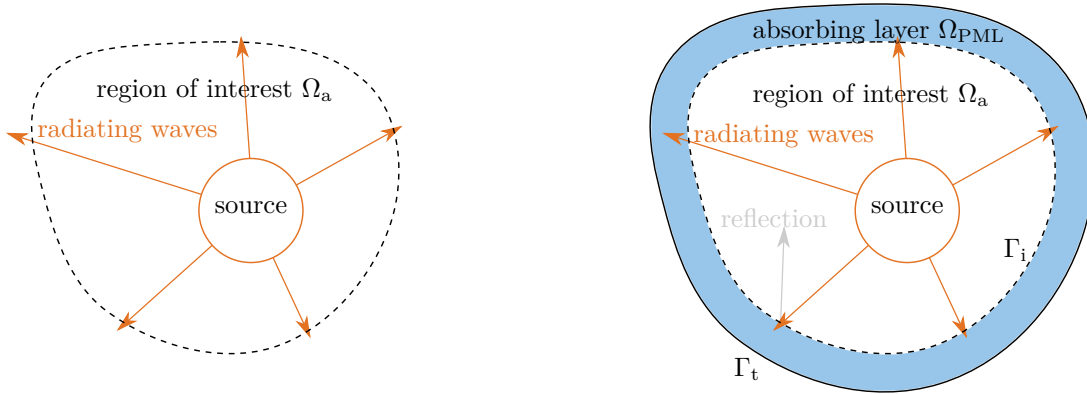


**Figure 2.6:** The concept of PML as an absorbing boundary condition. The free radiation problem with region of interest  $\Omega_a$  (left) is truncated by an artificial non-reflecting boundary  $\Gamma_t$  and a PML in  $\Omega_{\text{PML}}$  is added to prohibit reflections at the truncation boundary (right). The interface is denoted by  $\Gamma_i$ .

It is defined as a function  $\psi(\mathbf{r})$  of the physical coordinates of the discretized problem; the stretched coordinate is therefore given by  $\tilde{\mathbf{r}}(\mathbf{r}) = \mathbf{r} + i\psi(\mathbf{r})$ . Choosing a function which vanishes inside the physical domain and grows smoothly from the interface  $\Gamma_i$  to the exterior model boundary  $\Gamma_t$ , where the numerical model is truncated, ensures a smooth transition at the boundary, i.e. waves can enter the PML without reflections. Because the stretching function vanishes for all  $\mathbf{r}$  outside the PML region, the stretching function can be applied everywhere in the model without affecting the solution in the physical domain  $\Omega_a$ . Figure 2.7 illustrates the concept of complex coordinate stretching for a one-dimensional wave traveling along  $0 < x < 10$ . The physical coordinate  $x$  is stretched by the function

$$\psi(x) = \begin{cases} 0, & 0 \leq x < 5, \\ 0.04(x-5)^2, & 5 \leq x < 10. \end{cases} \quad (2.120)$$

It is obvious that the wave solution is not changed in the region  $0 \leq x < 5$ , while the wave is attenuated in the PML region  $5 \leq x < 10$ .

Similarly, the complex coordinate stretch for a locally conformal PML is given by

$$\tilde{\mathbf{r}}(\mathbf{r}) = \mathbf{r} - \frac{1}{s}\psi(\mathbf{r})\mathbf{n}(\mathbf{r}), \quad (2.121)$$

where the minus results from a different definition of the stretching function. The absorption vector  $\mathbf{n}(\mathbf{r})$  defines the direction in which the wave is attenuated and is obtained from

$$\mathbf{n}(\mathbf{r}) = \frac{\mathbf{r} - \mathbf{r}_i}{\|\mathbf{r} - \mathbf{r}_i\|}, \quad (2.122)$$

where  $\mathbf{r}_i \in \Gamma_i$  is the nearest node on the PML interface regarding  $\mathbf{r}$ . Figure 2.8 sketches the

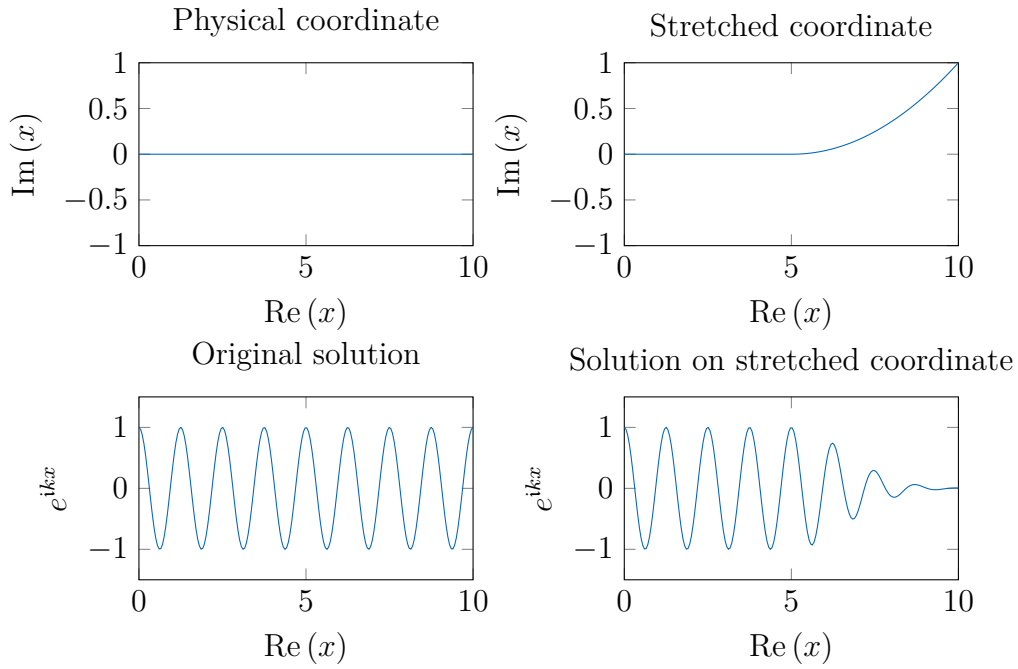


**Figure 2.7:** The effect of complex coordinate stretching on a one dimensional wave.

conformal PML with direction  $\mathbf{n}(\mathbf{r})$  and distance  $\zeta = \|\mathbf{r} - \mathbf{r}_i\|$ .

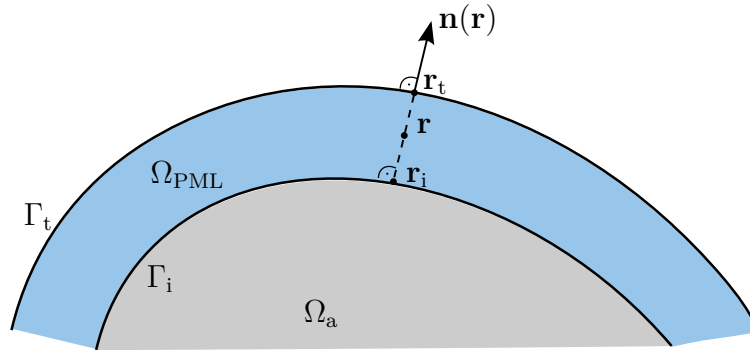


**Figure 2.8:** Sketch of the locally conformal PML and the definitions of the absorption vector for the point  $\mathbf{r}$  inside  $\Omega_{\text{PML}}$ .

As the physical domain is required to be convex, a unique  $\mathbf{r}_i$  can be found for all  $\mathbf{r} \in \Omega_{\text{PML}}$ . The factor  $\frac{1}{s}$  in eq. (2.121) is typically introduced to make the attenuation rate inside the PML independent of the frequency. However, Nannen and Wess [191] argue, that retaining the frequency dependency in the PML formulation leads to models which are less sensitive to the parameters of the attenuation function. The exact location of  $\mathbf{r}_i$  in a discretized geometry can be difficult to obtain. Using a node based approach, the direction of  $\mathbf{n}(\mathbf{r})$  might not be assessed correctly given unstructured or coarse grids, while discontinuities at discretized curvatures cause problems for an element based approach. Bériot and Tournour [55] therefore

suggest to compute  $\mathbf{n}(\mathbf{r})$  from the boundary value problem

$$\nabla^2 \varphi(\mathbf{r}) = 0, \quad \forall \mathbf{r} \in \Omega_{\text{PML}}, \quad (2.123)$$

where  $\varphi(\mathbf{r})$  is a potential field. Given the boundary conditions

$$\varphi(\mathbf{r}) = -1, \quad \forall \mathbf{r} \in \Gamma_i, \quad \varphi(\mathbf{r}) = 1, \quad \forall \mathbf{r} \in \Gamma_t, \quad (2.124)$$

the potential flux from the PML interface to the truncation surface is modeled. Normalizing the corresponding vector field, which is obtained from the potential field by

$$\mathbf{v}(\mathbf{r}) = \nabla \varphi(\mathbf{r}), \quad (2.125)$$

yields an approximation for the absorption vector  $\mathbf{n}(\mathbf{r})$ .

The stretching function  $\psi(\mathbf{r})$  governs the attenuation effect inside the PML and thus has a great influence on the effectiveness of the method. A typical polynomial stretching function is given by

$$\psi(\mathbf{r}) = \frac{\alpha c_a \|\mathbf{r} - \mathbf{r}_i\|^m}{m \|\mathbf{r}_t - \mathbf{r}_i\|^{m-1}}, \quad (2.126)$$

where  $\mathbf{r}_t$  is the location on the truncation boundary obtained by extending a straight line from  $\mathbf{r}_i$  to  $\mathbf{r}$ , i.e. the local PML width and  $c_a$  is the wave speed in the considered acoustic fluid.  $\alpha$  and  $m$  are tuning parameters controlling the wave attenuation inside the PML area. They have to be chosen in a way that all waves can enter  $\Omega_{\text{PML}}$  without reflections at the interface  $\Gamma_i$ , the waves decay monotonously inside the PML region, and the remaining amplitude is negligible at  $\Gamma_t$ . An extensive study on the choice of the parameters is given in [196]. Various other stretching functions have been proposed and argued to perform better in specific cases [56]. As the overall formulation of the PML is not affected by the choice of the stretching function, we do not explicitly consider other function types. The complex coordinate transformation is applied to the homogeneous Helmholtz equation (2.28)—source terms are omitted here, but can be included—which now reads

$$k^2 \tilde{p}(\tilde{\mathbf{r}}) + \tilde{\nabla}^2 \tilde{p}(\tilde{\mathbf{r}}) = 0. \quad (2.127)$$

$\tilde{p}$  is the analytic continuation of the pressure field inside the PML and the nabla operator in

complex space  $\tilde{\nabla}$  is given by

$$\tilde{\nabla} = \tilde{\mathbf{J}}^{-\top} \cdot \nabla = \begin{bmatrix} \frac{\partial \tilde{x}}{\partial x} & \frac{\partial \tilde{x}}{\partial y} & \frac{\partial \tilde{x}}{\partial z} \\ \frac{\partial \tilde{y}}{\partial x} & \frac{\partial \tilde{y}}{\partial y} & \frac{\partial \tilde{y}}{\partial z} \\ \frac{\partial \tilde{z}}{\partial x} & \frac{\partial \tilde{z}}{\partial y} & \frac{\partial \tilde{z}}{\partial z} \end{bmatrix}^{-\top} \cdot \nabla \quad (2.128)$$

Substitution into eq. (2.127) yields

$$\left( \tilde{\mathbf{J}}^{-\top} \cdot \nabla \right) \cdot \left( \tilde{\mathbf{J}}^{-\top} \cdot \nabla p(\mathbf{r}) \right) + k^2 p(\mathbf{r}) = 0, \quad (2.129)$$

where the Helmholtz equation in complex space is expressed in terms of real coordinates. The weak form of the Helmholtz equation for the complete domain is given by

$$\frac{s^2}{c_a^2} \int_{\Omega_a} \hat{\mathbf{w}}_p p \, d\Omega_a + \int_{\Omega_a} \nabla \hat{\mathbf{w}}_p \nabla p \, d\Omega_a + \frac{s^2}{c_a^2} \int_{\Omega_{\text{PML}}} \hat{\mathbf{w}}_{\tilde{p}} \tilde{p} \, d\Omega_{\text{PML}} + \int_{\Omega_{\text{PML}}} \tilde{\nabla} \hat{\mathbf{w}}_{\tilde{p}} \tilde{\nabla} \tilde{p} \, d\Omega_{\text{PML}} = 0, \quad (2.130)$$

where  $p$  is the pressure field inside the physical domain at  $\mathbf{r}$  and  $\tilde{p}$  the pressure field inside the PML given by the complex coordinate  $\tilde{\mathbf{r}}$ . In order to ensure continuity at the transition from physical domain to PML, it is sufficient to ensure  $\psi(\tilde{\mathbf{r}}) = 0 \, \forall \tilde{\mathbf{r}} \in \Gamma_i$ . The main advantage of this formulation is, that a standard implementation of the finite element method can be used. All computations are simply conducted considering the complex coordinate  $\tilde{\mathbf{r}}$  rather than  $\mathbf{r}$ , all other tools, like shape functions and their derivatives, can be reused.

Due to the introduction of the driving frequency in the coordinate transformation in eq. (2.121), the weak integral formulation of the PML contains a non-separable dependency on space and frequency. Using this in a frequency sweep analysis means that the PML needs to be recomputed for each frequency step, making the method computationally demanding. Vermeil de Conchard, Mao, and Rumpler [259] approximated this frequency dependency by reusing the same PML for not only one frequency but for a range and proposed strategies to find a reasonable tuning frequency.

## 2.4 Analysis of vibro-acoustic systems

The analysis of vibro-acoustic systems is typically performed in frequency domain given a harmonic excitation. This allows to assess a system's properties regarding its vibrational behavior, if the steady state response has a more significant influence on the solution than transient effects. This representation can also help to identify resonance effects, which cannot

always be observed in a transient analysis. An overview over the most important analysis tools for vibro-acoustic systems is given in the following.

### 2.4.1 Eigenvalue analysis

The eigenvalues of a vibro-acoustic system are often taken into account to describe fundamental properties of the vibrational behavior as they can be physically interpreted as resonance frequencies, also termed eigenfrequencies. Together with the damping of the structure, the eigenfrequencies have a large influence on the system's transfer function. They are obtained from the solution of a generalized eigenvalue problem, if a first-order system or an undamped or proportionally damped second-order system is considered, or from a polynomial eigenvalue problem, if a arbitrarily damped second-order system is considered. The eigenvectors obtained from the eigenvalue analysis are interpreted as the modes of a system, which are the vibration patterns at the corresponding eigenfrequencies. The generalized eigenvalue problem is given by

$$\mathbf{A}\mathbf{v} = \lambda\mathbf{B}\mathbf{v}, \quad (2.131)$$

with eigenvalue  $\lambda$ , (right) eigenvector  $\mathbf{v}$  and the problem dependent matrices  $\mathbf{A}$  and  $\mathbf{B}$  of dimensions  $n \times n$ . Equation (2.131) has  $n$  solutions for pairs of eigenvalues and eigenvectors. The analysis of a general second-order system given by eq. (2.12) requires the linearization of the originally polynomial eigenvalue problem to obtain a problem with the form of eq. (2.131). This can be achieved, for example, by substitution and yields the first companion form

$$\mathbf{A} = \begin{bmatrix} 0 & \mathbf{I} \\ -\mathbf{K} & -\mathbf{C} \end{bmatrix}, \quad \mathbf{B} = \begin{bmatrix} \mathbf{I} & 0 \\ 0 & \mathbf{M} \end{bmatrix}. \quad (2.132)$$

The first companion form is not the only possible linearization for second-order systems [237, 245], see also appendix A.1. The solution of this problem yields  $2n$  eigenvalues and  $2n$  eigenvectors. Given Hermitian positive semidefinite matrices  $\mathbf{K}$ ,  $\mathbf{C}$  and a Hermitian positive definite  $\mathbf{M}$ , all eigenvalues have a negative real part, i.e. the considered system is stable, and the eigenvalues are either real or in complex conjugate pairs. If  $\mathbf{M}$  is regular, all eigenvalues are finite; eigenvectors corresponding to zero eigenvalues describe a system's rigid body motion. Additionally to the right eigenvectors in eq. (2.131), the corresponding left eigenvectors are computed by

$$\mathbf{w}^H \mathbf{A} = \lambda \mathbf{w}^H \mathbf{B}, \quad (2.133)$$

where  $\mathbf{w}$  is the left eigenvector. Using both eigenvectors and the eigenvalues, it is possible to obtain a formulation for the transfer function of a SISO system, similar to the pole-residue form (2.17)

$$H(s) = \sum_{i=1}^{2n} \frac{(\mathbf{g}\mathbf{v}_i) (\mathbf{w}_i^H \mathbf{f})}{s - \lambda_i}. \quad (2.134)$$

Here, the residual is given as a relation of the system input  $\mathbf{f}$  and output  $\mathbf{g}$  as well as the right and left eigenvectors. However, the explicit computation of the above form is not always efficient, as it is often ill-conditioned [245].

## 2.4.2 Modal superposition

Instead of directly expressing a system's transfer function by its poles and eigenvectors as in eq. (2.134), the modal superposition method uses the eigenvalues and eigenvectors of a system to transform it into modal space. This yields, under certain conditions,  $n$  decoupled equations describing each mode's behavior. If the damping matrix  $\mathbf{C}$  is proportional to  $\mathbf{K}$  and  $\mathbf{M}$ , this system of decoupled equations is obtained by using the modes of the undamped system. In this context, the modes are the eigenvectors of the system subjected to free vibration and are given by the generalized eigenvalue problem

$$(\lambda \mathbf{M} + \mathbf{K}) \mathbf{v} = 0, \quad (2.135)$$

which is obtained from the homogeneous equation of motion eq. (2.12) using an exponential approach  $\check{\mathbf{x}}(t) = \mathbf{v}e^{\lambda t}$  and setting  $\mathbf{C} = 0$ . If all matrices are (semi-)positive definite and real, there exist eigenvectors such that

$$\mathbf{X}^T \mathbf{M} \mathbf{X} = \mathbf{I}, \quad (2.136)$$

$$\mathbf{X}^T \mathbf{K} \mathbf{X} = \mathbf{\Lambda} = \text{diag}(\lambda_1, \dots, \lambda_n), \quad (2.137)$$

where  $\mathbf{X} = [\mathbf{v}_1 \ \mathbf{v}_2 \ \dots \ \mathbf{v}_n]$  is a matrix containing all eigenvectors and  $\mathbf{\Lambda}$  is the spectral matrix. The eigenvalues are related to the undamped real eigenfrequencies of the system by  $\omega = \sqrt{\lambda}$ . If  $\mathbf{C}$  is proportional to either  $\mathbf{K}$  or  $\mathbf{M}$  or both, it can be diagonalized using the undamped eigenvectors:

$$\mathbf{v}_j^T \mathbf{C} \mathbf{v}_i = 0, \quad j \neq i, i, j = 1, \dots, n, \quad (2.138)$$

This orthogonality condition can be assured by applying a proportional damping method from section 2.3. The transformation of the equation of motion to modal coordinates is performed by  $\check{\mathbf{x}}(t) = \mathbf{X}\check{\mathbf{q}}$ . Premultiplying the resulting expression by  $\mathbf{X}^T$  and considering only one input gives the modal equation

$$\ddot{\check{\mathbf{q}}}(t) + \mathbf{\Xi}\dot{\check{\mathbf{q}}}(t) + \mathbf{\Lambda}\check{\mathbf{q}}(t) = \mathbf{X}^T \mathbf{f}\check{u}(t), \quad (2.139)$$

with the generalized damping matrix

$$\mathbf{\Xi} = \mathbf{X}^T \mathbf{C} \mathbf{X} = \text{diag}(2\omega_1\xi_1, \dots, 2\omega_n\xi_n), \quad (2.140)$$

a diagonal matrix containing the modal damping ratios for each mode. No coupling between the  $n$  equations in eq. (2.139) is present. For the case of Rayleigh damping, the modal damping ratios are given by  $\xi_i = \frac{\alpha}{2\omega_i} + \frac{\beta\omega_i}{2}$ . After solving for  $\check{\mathbf{q}}$ , the solution in physical coordinates is obtained by  $\check{\mathbf{x}}(t) = \mathbf{X}\check{\mathbf{q}}$ . As the individual solutions for each mode are superposed to form the solution of the complete system, the method is referred to as modal superposition method. The solution in Laplace domain can also be expressed as

$$\mathbf{x}(s) = \sum_{i=1}^n \frac{\mathbf{v}_i \mathbf{v}_i^T \mathbf{f}}{(\omega_i^2 + s^2) + 2s\xi_i\omega_i}, \quad (2.141)$$

which can be transformed to a pole-residue form (2.17) of the transfer function by premultiplication with an output vector  $\mathbf{g}$ .

If proportional damping cannot correctly model the system behavior, the damped modes need to be considered for the modal superposition method. They can be obtained by solving the generalized eigenvalue problem of a system resulting from reformulating the equation of motion into an equivalent first-order system of order  $2n$ , such as eq. (2.16) or eq. (2.132). Using again an exponential approach  $\check{\mathbf{x}}^{(1)}(t) = \mathbf{v}e^{\lambda t}$ , a generalized eigenvalue problem of form eq. (2.131) with the matrix pair  $(\mathbf{A}, \mathbf{B})$  given by eq. (2.132) is obtained. The solution yields  $2n$  eigenvalues  $\lambda$  in complex conjugate pairs. All eigenvalues of a stable system have a zero or negative real part, otherwise the solution of the exponential approach would grow to infinity. Additionally, the right and left eigenvectors  $\mathbf{v}_i, \mathbf{w}_i \in \mathbb{C}^{2n}$  are required for the method. Similarly to the undamped case, the transformation  $\check{\mathbf{x}}^{(1)}(t) = \mathbf{X}\check{\mathbf{q}}$  to modal coordinates yields  $2n$  decoupled equations

$$\beta_i \dot{\check{q}}_i(t) + \alpha_i \check{q}_i(t) = \mathbf{w}_i^H \begin{bmatrix} 0 \\ \mathbf{f} \end{bmatrix} \check{u}(t), \quad (2.142)$$

where  $\alpha_i, \beta_i$  are the diagonal elements of the matrices

$$\begin{aligned}\mathbf{Y}^H \mathbf{A} \mathbf{X} &= \text{diag}(\alpha_1, \dots, \alpha_{2n}), \\ \mathbf{Y}^H \mathbf{B} \mathbf{X} &= \text{diag}(\beta_1, \dots, \beta_{2n}).\end{aligned}$$

$\mathbf{X}$  and  $\mathbf{Y}$  are the matrices of right respectively left eigenvectors. The solution for  $\check{\mathbf{x}}(t)$  is obtained from  $\check{\mathbf{x}}(t) = [\mathbf{I} \ 0] \mathbf{X} \check{\mathbf{q}}(t)$ . These transformations yield a system of order  $2n$ , thus increasing the computational effort required for solving such problems. Therefore, proportional damping models have been traditionally considered in many cases. Efficient solution strategies for cases where proportional damping is not applicable will be addressed in the following chapters.

### 2.4.3 Logarithmic scale

Transfer functions, such as frequency response functions, are often given logarithmically in the decibel scale. It is defined as the logarithm of the square amplitude of the parameter of interest referenced to a certain reference level; its unit is decibel dB. In acoustics, the sound pressure level is often given. It is defined by

$$L_p = 10 \log \left( \frac{p}{p_0} \right)^2 = 20 \log \frac{p}{p_0} \text{dB}, \quad (2.143)$$

where  $p_0 = 2 \cdot 10^{-5}$  Pa. A change of 1 dB is barely perceived as a change in loudness, and this expression accounts for the fact that sound pressure is perceived logarithmically instead of linearly by the human ear [189]. Other level descriptions are frequently used, for example the sound power level  $L_P$ , where the measured power is referenced to  $P_0 = 1 \cdot 10^{-12}$  W, so 1 W corresponds to a intensity of 120 dB.

## 2.5 Numerical examples of vibro-acoustic problems

After defining the governing equations and coupling conditions of the different domains being present in a vibro-acoustic setting and presenting a discretization with finite elements, numerical model problems for different kinds of vibro-acoustic systems are introduced. The type of modeled problem has an influence on the shape of the transfer function which needs to be evaluated, leading to different requirements for solving and reduction algorithms. Therefore, we divide the problems into groups defined by the shape of their transfer function. We will only consider systems with a single input and a single output (SISO), which can be grouped as follows:

- *Case A*: A structural or interior vibro-acoustic system with proportional damping and no acoustic source following

$$H(s) = \mathbf{g} \left( s^2 \mathbf{M} + s (d_1 \mathbf{M} + d_2 \mathbf{K}) + \mathbf{K} \right)^{-1} \mathbf{f},$$

where the damping factors  $d_1$  and  $d_2$  can represent any form of proportional damping, e.g. Rayleigh damping given by eq. (2.90) or Caughey damping as of eq. (2.93). Systems with hysteretic damping also belong to this category, here  $d_1 = 0$  and  $d_2 \in \mathbb{C}$ . The resulting system matrices may be complex valued if hysteretic damping is considered and non-symmetric for an interior vibro-acoustic problem.

- *Case B*: An interior acoustic or vibro-acoustic system with acoustic source following

$$H(s) = \mathbf{g} \left( s^2 \mathbf{M} + s \mathbf{C} + \mathbf{K} \right)^{-1} \mathbf{f}(s),$$

where the damping matrix  $\mathbf{C}$  is not necessarily proportional to the mass or stiffness of the system. An exterior radiation problem can be modeled with this system type, if, for example, a PML is tuned to a single frequency. The frequency dependency introduced by the acoustic source in  $\mathbf{f}(s)$  is either linear or quadratic regarding the excitation frequency  $s$ , depending on the imposed boundary condition.

- *Case C*: An interior vibro-acoustic system with acoustic source and frequency dependent material properties following

$$H(s) = \mathbf{g} \left( s^2 \mathbf{M} + s \mathbf{C} + \mathbf{K} + \sum_{i=1}^k \phi_i(s) \mathbf{C}_i \right)^{-1} \mathbf{f}(s),$$

where this frequency dependency can be described by an affine combination of  $k$  constant matrices  $\mathbf{C}_i$  and typically non-linear and complex valued functions  $\phi_i(s)$ . Exterior problems can be modeled, if the method ensuring the Sommerfeld radiation condition can be represented by either a constant matrix or a linear combination of matrices and corresponding frequency dependent functions.

A system with non-proportional damping without acoustic sources is not considered individually but as a special case of *Case B* without the frequency dependent input mapping. In the above transfer functions,  $\mathbf{g} \in \mathbb{R}^{1 \times n}$  is an  $n$ -dimensional row vector. To illustrate the different vibro-acoustic problem types, numerical examples for typical vibro-acoustic problems are presented in the following. The models are assessed regarding their requirements for solving algorithms as well as the applicability of model order reduction methods in the following chapters. Kratos Multiphysics [88, 179] was used to model the systems.

### 2.5.1 Academic example

The first considered system models the vibration of a cantilevered beam, excited by a single load at the free end. It can be considered an academic example, as the dynamic response can be obtained from analytic relations. Nevertheless, it can be used to illustrate the effectiveness of model order reduction techniques as the model is easy to handle and its dynamic behavior is well-known. Additionally, all poles of the transfer function are well separated, which also eases the interpretation of results and has therefore often been used as a validation example [11, 164, 200]. The beam's geometry is described by its length  $l$  and its quadratic cross section with width and height  $a$ . A sketch is given in fig. 2.9a. Young's modulus  $E$ , density  $\rho$ , and Poisson ratio  $\nu$  describe the beam's material. In this case, Rayleigh damping is applied, so the system can be considered as *Case A*. The transfer function measuring the displacement in  $z$ -direction—the same direction the load is applied—at the free end is given in fig. 2.9b. Here, the beam is discretized using 100 finite elements governed by the Euler-Bernoulli beam theory, leading to an order of  $n = 600$  after applying the boundary conditions. The considered geometric and material parameters are  $l = 0.8$  m with a quadratic cross section with edge length  $a = 0.01$  m,  $E = 210$  GPa,  $\rho = 7850$  kg m<sup>-3</sup>,  $\nu = 0.3$ , and Rayleigh damping parameters  $\alpha = 1.64 \cdot 10^{-1}$  s<sup>-1</sup>,  $\beta = 9.1 \cdot 10^{-6}$  s.

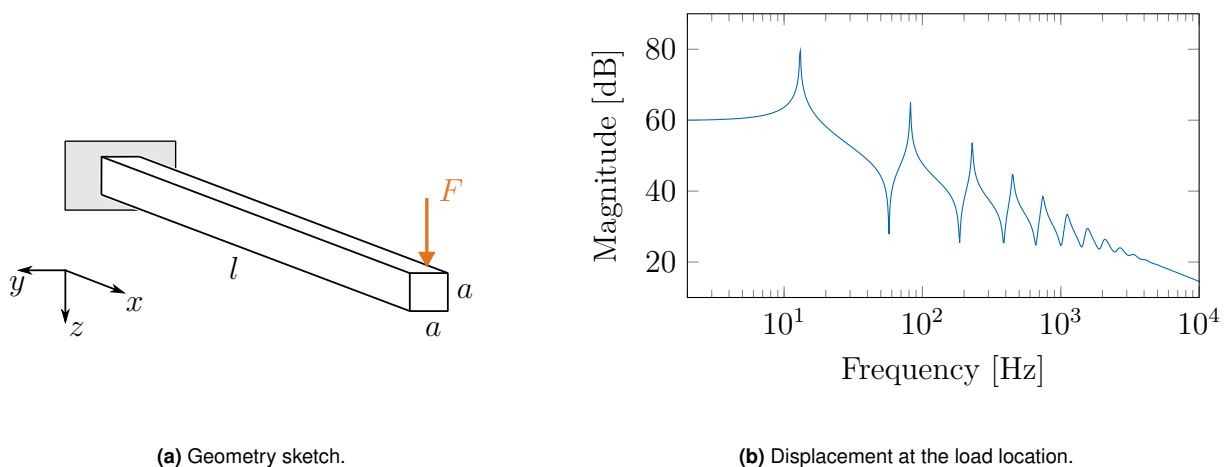


**Figure 2.9:** Sketch and transfer function of the cantilever beam model.

### 2.5.2 Structural vibration

The vibration response of strutted plates excited by a single force and considering different damping methods is modeled in the following example. The plates are simply supported at all surrounding edges and have dimensions of  $0.8 \times 0.8$  m, a thickness of  $t = 1$  mm and are made out of aluminum ( $E = 69$  GPa,  $\rho = 2650$  kg m<sup>-3</sup>,  $\nu = 0.22$ ). They are equipped with

arrays of tuned vibration absorbers (TVA) tuned to  $f = 48$  Hz to reduce the overall vibration response in this frequency region. All TVAs are placed on the struts of the plates and are modeled as spring-damper systems with a total mass of 10% of the plate structure. A point load at  $(x, y, z) = (0.7, -0.05, 0.0)$  m near a corner of the plate with amplitude 0.1 N excites the system. The system is sketched in fig. 2.10. A similar system has been experimentally examined in [84].

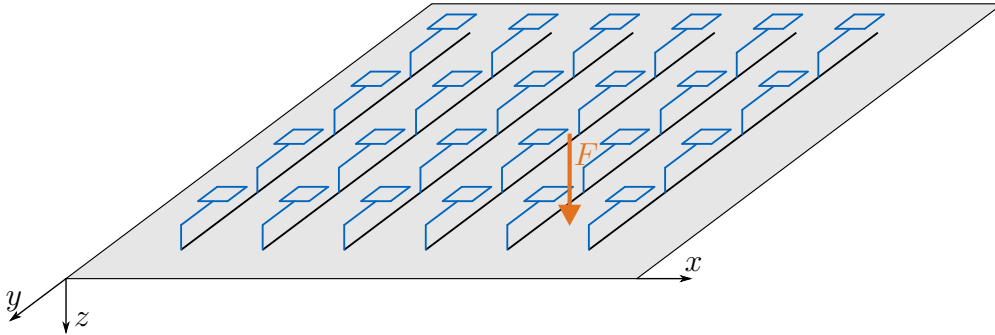


**Figure 2.10:** Sketch of the plate model. The TVAs are depicted in blue.

Two damping methods are considered. Proportional (Rayleigh) damping with  $\alpha = 0.01 \text{ s}^{-1}$ ,  $\beta = 1 \cdot 10^{-4} \text{ s}$  is applied to one model, hysteretic damping with  $\eta = 0.001$  is employed in the other experiment. The dissipation effect of the TVAs is limited to the frequency region directly adjacent to their tuning frequency which is clearly visible in the frequency response plot fig. 2.11 showing the root mean square of the displacement on the plate surface. Both transfer functions differ especially in the higher frequency region due to the different damping mechanisms employed. While the poles of the proportionally damped system are only visible in the lower frequency region, the hysteretically damped system's transfer function shows many peaks over the complete frequency range of interest. The discretized system has an order of  $n = 201\,900$  and is evaluated in a frequency range of  $[1, \dots, 250]$  Hz. As only structural loads excite the system, *Case A* transfer functions are used to describe the output of both systems. All system matrices are symmetric, respectively complex symmetric for the case of hysteretic damping, as no interaction effects between structure and fluid are present. In order to evaluate the root mean square of the displacement at all points on the plate surface, the displacement result must be recovered from reduced space. This is done using an output matrix  $\mathbf{G}$  with dimensions  $p \times n$ , where  $p$  is the number of nodes on the plate surface mapping the result of each node to an individual output.

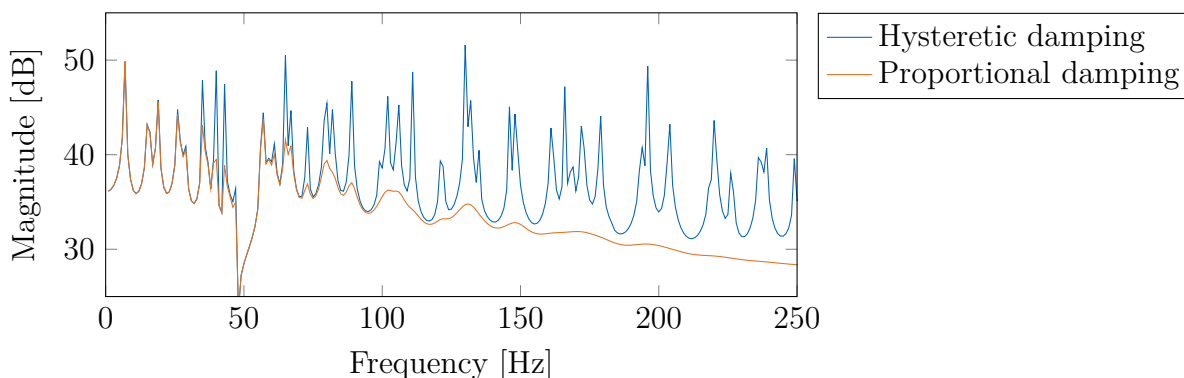
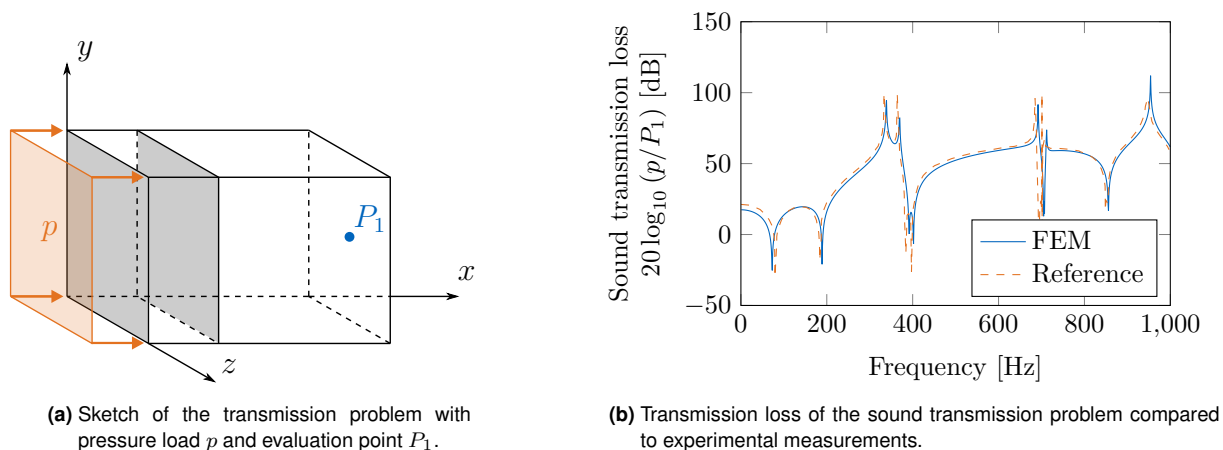


**Figure 2.11:** Transfer functions of both plate models with different damping mechanisms.

### 2.5.3 Sound transmission

Radiation of vibrating plates and excitation of a structure by the oscillating acoustic fluid are modeled in the following example. The system consists out of a cuboid acoustic cavity where one wall is considered a system of two parallel elastic brass plates with an air gap of 2 cm between them; all other walls are considered rigid. The plates measure  $0.2 \times 0.2$  m and have a thickness of  $t = 0.9144$  mm; the material parameters  $E = 104$  GPa,  $\rho_e = 8500$  kg m $^{-3}$ ,  $\nu = 0.37$  are considered for brass. The receiving cavity is 0.2 m wide and  $c_a = 343$  m s $^{-1}$ ,  $\rho_a = 1.21$  kg m $^{-3}$  are considered for the acoustic fluid. A uniform pressure load is applied to the outer plate located at  $x = 0$ . The configuration is based on an experiment conducted in [127] and is sketched in fig. 2.12a along with a plot of the transmission loss between the input pressure and the middle point of the wall opposite to the elastic plates in fig. 2.12b.



**(a)** Sketch of the transmission problem with pressure load  $p$  and evaluation point  $P_1$ .

**(b)** Transmission loss of the sound transmission problem compared to experimental measurements.

**Figure 2.12:** Sketch and transmission loss of the sound transmission problem. The reference transmission loss is taken from the experimental measurements conducted by Guy [127].

Energy dissipation inside the structural part of the system is modeled using proportional damping with  $\beta = 1 \cdot 10^{-7}$  s. The discretized system has  $n = 95\,480$  degrees of freedom. The

model follows the behavior of the experimental setup in a frequency range  $[1, \dots, 1000]$  Hz. No acoustic sources are present, so the excitation vector is frequency independent. Considering the two way coupling between structure and fluid leads to non-symmetric system matrices. Thus, a transfer function of *Case A* with real valued matrices describes the system. Rather than evaluating the transmission loss, the transfer function is computed from the sound pressure level at the midpoint of the rigid wall opposite of the vibrating double plate configuration. It is given in fig. 2.13.

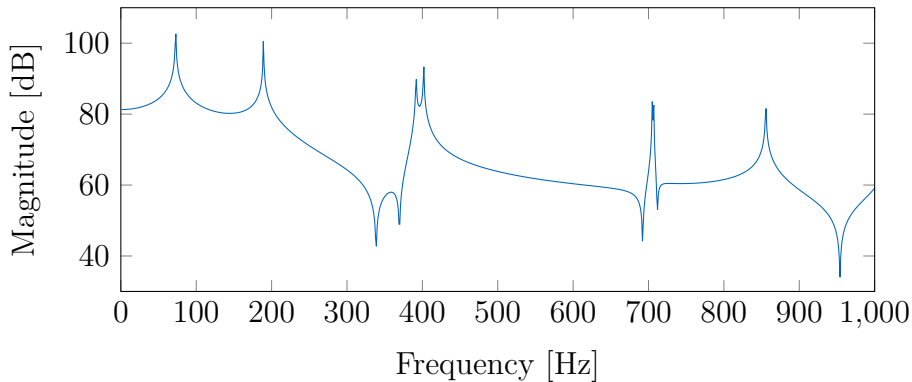


**Figure 2.13:** Transfer function of the sound transmission problem.

## 2.5.4 Acoustic scattering

We now consider a more complex geometry based on a rigid block with various openings, cavities, and sharp corners radiating into a surrounding acoustic fluid. Hornikx, Kaltenbacher, and Marburg [138] called this experiment “radiatterer” as both radiation and scattering effects are taken into account. The basic shape is a box with dimensions  $2.5 \times 2.0 \times 1.7$  m which is enclosed by an acoustic fluid of size  $3.5 \times 3.0 \times 2.7$  m; the geometry is described in detail in [138] and is sketched in fig. 2.14a. For the acoustic fluid,  $\rho_a = 1.21 \text{ kg m}^{-3}$  and  $c_a = 343.5 \text{ m s}^{-1}$  are assumed. A normal velocity of  $v_n = 0.001 \text{ m s}^{-1}$  acts on the complete surface of the geometry exciting the surrounding acoustic fluid. The free radiation from the geometry is realized with a PML of thickness  $d = 0.3$  m. It is tuned to  $f = 500$  Hz, eliminating the frequency dependency of the PML matrices [259]. The system’s transfer function is classified as *Case B*, as the acoustic source term introduces a frequency dependency to the system input. The PML leads to complex valued system matrices. As no interaction between the acoustic fluid and the structure is considered, the system matrices are complex symmetric. The numerical model has an order of  $n = 250\,000$  and is evaluated in the frequency range  $[1, \dots, 600]$  Hz. The transfer function measures the sound pressure level at an evaluation point inside the large cutout with coordinates  $P_5 : (x, y, z) = (0.6, 0.5, 0.8)$  m.

Its location is given in fig. 2.14a, the transfer function is plotted in fig. 2.14b. A reference solution for the same system is available in [177], where the same problem has been analyzed with a boundary element method.

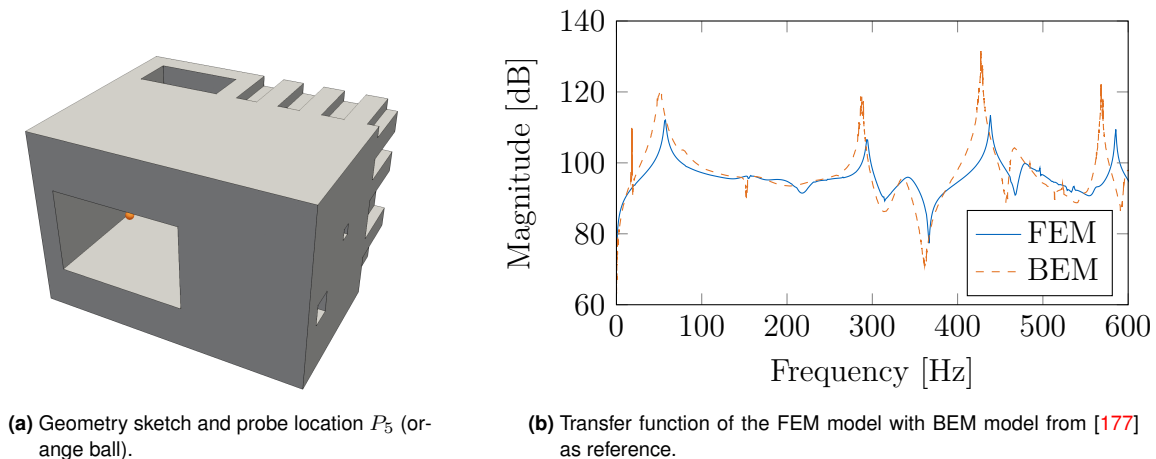


**Figure 2.14:** Sketch and transfer function of the “radiatrer” model.

### 2.5.5 Coupled poroacoustic system

A system with two porous materials coupled to a surrounding acoustic fluid is considered in the following. The system models an acoustic cavity with non-parallel walls having maximum extents of  $1.122 \text{ m} \times 0.82 \text{ m} \times 0.982 \text{ m}$ . Air with the properties given in table 2.2 is considered for the acoustic fluid. Two layers of different poroelastic materials cover one side of the cavity, their material parameters are given in table 2.3. All walls surrounding the acoustic fluid are considered rigid and a sliding boundary condition is employed between porous materials and the walls. The system is excited by an acoustic point source inside the cavity at  $(1.03, 0.12, 0.30)$  and the sound pressure level  $L_p$  is evaluated at  $(0.35, 0.80, 0.10)$ . A sketch of the system and its transfer function are given in fig. 2.15. More detailed information about the geometry and material parameters for the poroelastic material are available in [149]. A  $(\mathbf{u}, p)$  finite element formulation using mixed degrees of freedom in the porous material is used to discretize the problem, so each node in the porous domain has four degrees of freedom (c.f. section 2.2.3). Off-diagonal coupling terms ensure the continuity between the poroelastic and acoustic phase and between the two poroelastic materials, so the resulting system matrices are complex valued and non-symmetric. The system is discretized by a finite element model<sup>1</sup> with 61 460 degrees of freedom and the transfer function is evaluated in the frequency range  $[1, \dots, 800]$  Hz. The discretized system incorporates ten frequency dependent functions:

<sup>1</sup>The model is courtesy of Stijn Jonckheere. The permission to use is greatly appreciated.

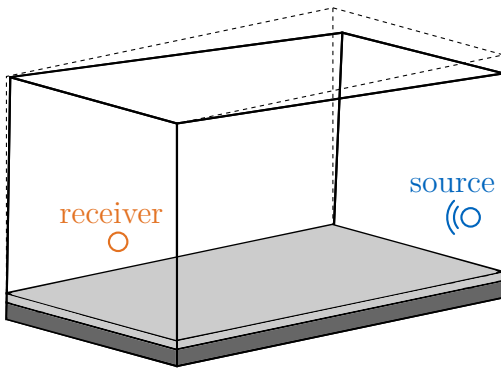
four for each poroelastic material, one for the acoustic cavity and one for the coupling of poroelastic material and acoustic fluid. Its transfer function is thus classified as *Case C*.

**Table 2.2:** Material properties considered for air and interstitial fluid.

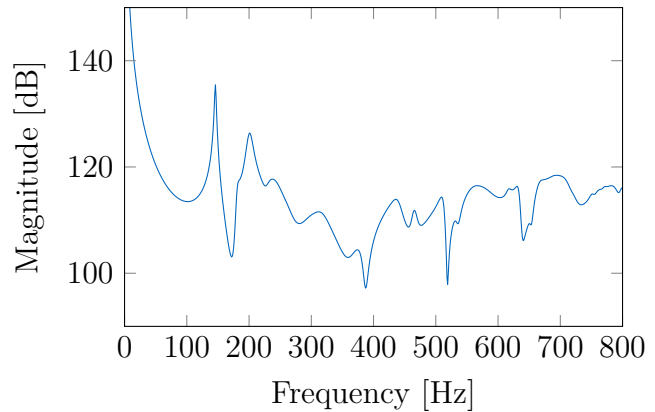
Parameter	Value	Parameter	Value
Density	$\rho_f = 1.205 \text{ kg m}^{-3}$	Heat capacity	$\gamma = 1.4$
Viscosity	$\mu = 1.8208 \cdot 10^{-5} \text{ N s m}^{-2}$	Prandtl number	$Pr = 0.712$
Standard pressure	$P_0 = 1.0128 \cdot 10^5 \text{ Pa}$		

**Table 2.3:** Material properties for the two employed poroelastic materials.

Parameter	Material 1 [260]	Material 2 [91]
Porosity	$\phi = 0.93$	$\phi = 0.99$
Flow resistivity	$\sigma = 8 \cdot 10^4 \text{ kg m}^{-3} \text{ s}^{-1}$	$\sigma = 2 \cdot 10^4 \text{ kg m}^{-3} \text{ s}^{-1}$
Tortuosity	$\alpha_\infty = 2.5$	$\alpha_\infty = 1$
Viscous characteristic length	$\Lambda = 1 \cdot 10^{-5} \text{ m}$	$\Lambda = 1.5 \cdot 10^{-3} \text{ m}$
Thermal characteristic length	$\Lambda' = 1 \cdot 10^{-4} \text{ m}$	$\Lambda' = 2.2 \cdot 10^{-3} \text{ m}$
Density of the elastic frame	$\rho_s = 30 \text{ kg m}^{-3}$	$\rho_s = 60 \text{ kg m}^{-3}$
Young's modulus of the elastic frame	$E = 4.3 \cdot 10^5 + i \cdot 1 \cdot 10^5 \text{ Pa}$	$E = 2 \cdot 10^4 \text{ Pa}$
Shear modulus of the elastic frame	$G = 1.6 \cdot 10^5 + i \cdot 3 \cdot 10^4 \text{ Pa}$	—
Structural loss factor	—	$\eta_s = 0.5$



(a) Sketch of the poroacoustic system. The dotted lines represent the maximum extents of the cavity, the solid lines show the walls of the box.



(b) Transfer function of the poroacoustic system.

**Figure 2.15:** Sketch and transfer function of the poroacoustic model.

### 3 Model order reduction

After introducing mathematical models describing vibro-acoustic systems and basic methods to evaluate them, the following chapter is concerned with more specialized solution techniques for dynamical systems. Discretizing a vibro-acoustic system with a finite element method typically results in very large linear equation systems, often with  $n > 1 \cdot 10^5$  degrees of freedom. Such high orders are necessary, because a fine spatial discretization is required to resolve all important wave phenomena in the system. Additionally, these large systems need to be solved at each frequency step for a frequency sweep analysis, leading to quickly growing computation times. This ultimately prohibits the efficient evaluation of such models.

To allow an efficient computation of large systems, various techniques to reduce their complexity have been used. A straightforward approach is to use surrogate models depicting a—at least regarding some features—similar behavior as the original system. This can, for example, be a model of a skyscraper where the floors are modeled as point masses, which are interconnected by beam elements. Compared to a discretized model of the complete building, this greatly reduces the required number of degrees of freedom, while the main modal characteristics may be accurately represented by the surrogate. However, this typically requires extensive knowledge of the original system and is not a suitable approach for all types of models [151].

Static condensation or Guyan reduction [128] is often used for static structural systems. Here, the degrees of freedom not subjected to loading can be condensed out of the system using matrix manipulations. This method can significantly reduce the number of equations required to be solved for a system and is often used in the definition of finite element formulations. However, it is only exact for a frequency  $s = 0$  and iterative methods are required to produce accurate results for dynamical systems [112, 215].

Another technique is to break down a numerical model into smaller parts, which can be computed individually, and the solution is obtained combining the results of all subsystems. This is especially relevant, if the original model does not fit into the memory of the simulation machine. Prominent examples for these methods are FETI (finite element tearing and interconnecting) methods, specifically developed for use with finite element models [99, 154]. Special conditions for the arbitrary boundaries between the subsystems need to be computed in a preprocessing step, making the individual models independent of each other. The

framework is especially suitable for parallel computing in a distributed memory environment.

Transforming or projecting of a problem from the original space onto a lower dimensional space, where the model is easier to evaluate, is also a widely used technique. Many different projection methods have been established in the past, allowing efficient computation of dynamical systems depicting all kinds of physical problems. Also the modal analysis of dynamical systems summarized in section 2.4.2 can be grouped into this category. Here, the transformation from physical to modal coordinates leads to uncoupled equations and the solution of a large linear system of equations is not required anymore. Projection based methods are typically divided in two phases: during the offline phase, expensive numerical operations are performed and the full order model may be used to generate data required to construct the reduced model; in the following online phase this model is evaluated at very low computational cost to obtain an approximate solution of the original model. The effectiveness of these methods can be measured by the achievable size reduction and the accuracy of the approximation.

We will focus on projection based methods in the following and important methods applicable to dynamical systems will be presented after the general projection framework is introduced in section 3.1 and measures for the approximation error are presented in section 3.2. Sections 3.3 to 3.6 summarize modal methods, proper orthogonal decomposition, balanced truncation, and moment matching methods, which are often employed for the reduction of dynamical systems. Techniques to retain the dependence on a specified set of parameters in reduced space are presented in section 3.7.

### 3.1 Reduction by projection

Consider a linear second-order system of the form (2.12) with transfer function (2.13). The direct computation of the transfer function requires the solution of a linear system of equations of order  $n$ , so a reduction of the order of this equation system is desirable. At the same time the original system's input output relation must be retained, at least in a certain frequency range, and the original structure of the system as well as properties such as positiveness or stability should be preserved. The main idea of projection based model order reduction is to find two subspaces  $\mathcal{V} \subset \mathbb{C}^r$  and  $\mathcal{W} \subset \mathbb{C}^r$  which contain the solution of the system instead of computing its solution in the high dimensional solution space  $\mathbb{C}^n$ . The order  $r$  of  $\mathcal{V}$  and  $\mathcal{W}$  should favorably be much lower than  $n$ . This projection is defined as:

$$\begin{aligned} &\text{Find } \mathbf{x}_r(s) \in \mathcal{V} \text{ such that } \mathbf{W}^H \left( (s^2 \mathbf{M} + s \mathbf{C} + \mathbf{K}) \mathbf{V} \mathbf{x}_r(s) - \mathbf{F} \mathbf{u}(s) \right) = 0, \\ &\text{then } \mathbf{y}_r(s) := \mathbf{G} \mathbf{V} \mathbf{x}_r(s). \end{aligned} \tag{3.1}$$

The resulting reduced order system for a second-order system has the shape

$$\Sigma_r: \begin{cases} (s^2\mathbf{M}_r + s\mathbf{C}_r + \mathbf{K}_r) \mathbf{x}_r(s) = \mathbf{F}_r \mathbf{u}(s), \\ \mathbf{y}_r(s) = \mathbf{G}_r \mathbf{x}_r(s), \end{cases} \quad (3.2)$$

where subscript  $r$  denotes the reduced order  $r \ll n$ . The projection is performed using two projection matrices  $\mathbf{V}, \mathbf{W} \in \mathbb{C}^{n \times r}$  spanning the two reduction spaces  $\mathcal{V} = \text{span}(\mathbf{V})$  and  $\mathcal{W} = \text{span}(\mathbf{W})$ . The reduced matrices in eq. (3.2) are computed by

$$\begin{aligned} \mathbf{M}_r &= \mathbf{W}^H \mathbf{M} \mathbf{V}, & \mathbf{C}_r &= \mathbf{W}^H \mathbf{C} \mathbf{V}, & \mathbf{K}_r &= \mathbf{W}^H \mathbf{K} \mathbf{V}, \\ \mathbf{F}_r &= \mathbf{W}^H \mathbf{F}, & \mathbf{G}_r &= \mathbf{G} \mathbf{V}. \end{aligned} \quad (3.3)$$

The reduced system's transfer function is consequently given by

$$\mathbf{H}_r(s) = \mathbf{G}_r (s^2\mathbf{M}_r + s\mathbf{C}_r + \mathbf{K}_r)^{-1} \mathbf{F}_r. \quad (3.4)$$

The original states can be obtained from the reduced system's states by  $\mathbf{x} \approx \mathbf{V} \mathbf{x}_r$ . The formulation of the projection for first-order systems is analogous. A projection with a left and right projection basis as in eq. (3.3) is referred to as Petrov-Galerkin projection. If the original system is symmetric, a one-sided projection with  $\mathbf{W} = \mathbf{V}$  preserves the symmetry in reduced space [268]. This is referred to as Galerkin projection. A real valued reduction basis is required if the reduced order is required to have real valued system matrices. It is obtained by setting  $\mathbf{V} = [\text{Re}(\mathbf{V}) \quad \text{Im}(\mathbf{V})]$ , respectively  $\mathbf{W} = [\text{Re}(\mathbf{W}) \quad \text{Im}(\mathbf{W})]$ , doubling the dimension of the reduced model. In any case, the bases must be chosen in a way, that the response of the reduced system approximates the original system's response sufficiently. This can be done, for example, by using the methods which are presented in the following.

## 3.2 Error assessment

Replacing a full order model of a dynamical system with a more compact surrogate introduces an approximation error, which is typically measured by the difference of the two systems' outputs. It is given by

$$\boldsymbol{\varepsilon}(s) = \mathbf{y}(s) - \mathbf{y}_r(s) = (\mathbf{H}(s) - \mathbf{H}_r(s)) \mathbf{u}(s), \quad (3.5)$$

expressed either directly by the system outputs or the transfer functions. The corresponding error system is described by its transfer function  $\mathbf{H}_\varepsilon(s) = \mathbf{H}(s) - \mathbf{H}_r(s)$ , which allows considerations about the approximation quality at each evaluated frequency. If the error

system's response approaches zero over the complete considered frequency range, the reduced model accurately approximates the original system. Equation (3.5) can be normalized by the original system's response and often the absolute values of the reduced and original systems' responses are considered. The absolute relative error of a reduced system with response  $\mathbf{y}_r$  is thus given by

$$\varepsilon_r(s) = \frac{|\mathbf{y}(s) - \mathbf{y}_r(s)|}{|\mathbf{y}(s)|}. \quad (3.6)$$

For a SISO system, this relation returns a scalar for each frequency  $s$ , while the error is given per output for a MIMO system.

The  $\mathcal{H}_2$  and  $\mathcal{H}_\infty$  norms of a resulting error system are typically considered if a single value for the approximation quality of the model in the complete considered frequency range is required. Hardy spaces  $\mathcal{H}$  are used here, which can be referred to as frequency domain spaces [11]. For a complex-valued function  $\mathbf{H}(s)$ , which is analytic in  $\mathbb{C}_+$ , i.e. the right half-plane of  $\mathbb{C}$ , they are given by

$$\|\mathbf{H}\|_{\mathcal{H}_\infty} = \max_{\omega \in \mathbb{R}} \|\mathbf{H}(i\omega)\|_2, \quad (3.7)$$

$$\|\mathbf{H}\|_{\mathcal{H}_2} = \left( \frac{1}{2\pi} \int_{-\infty}^{\infty} \|\mathbf{H}(i\omega)\|_F^2 \right)^{1/2} d\omega, \quad (3.8)$$

where  $\omega$  is the real frequency and  $\|\mathbf{H}\|_F^2 = \text{trace}(\bar{\mathbf{H}}\mathbf{H}^T)$ . Given a stable system, the  $\mathcal{H}_\infty$  norm of the error system eq. (3.5) is consequently defined as

$$\varepsilon_{\mathcal{H}_\infty} = \|\mathbf{H} - \mathbf{H}_r\|_{\mathcal{H}_\infty} = \max_{\omega} \|\mathbf{H}(i\omega) - \mathbf{H}_r(i\omega)\|_2. \quad (3.9)$$

A small  $\mathcal{H}_\infty$  norm ensures that, given a bounded input, the output error is small over all inputs in a root-mean-square sense, i.e.  $\sqrt{\int_0^\infty \|\mathbf{y}(t) - \mathbf{y}_r(t)\|_2^2 dt}$  is small [12]. Similarly, if the output error should be as small as possible for every point in time  $t > 0$ , i.e.  $\max_{t>0} \|\mathbf{y}(t) - \mathbf{y}_r(t)\|_\infty$  is small, the  $\mathcal{H}_2$  norm is used. It is defined as

$$\varepsilon_{\mathcal{H}_2} = \|\mathbf{H} - \mathbf{H}_r\|_{\mathcal{H}_2} = \left( \frac{1}{2\pi} \int_{-\infty}^{\infty} \|\mathbf{H}(i\omega) - \mathbf{H}_r(i\omega)\|_F^2 d\omega \right)^{1/2} \quad (3.10)$$

for the error system eq. (3.5). Additionally, any other suitable norm can be employed here, depending on the modeled problem. However, the computation of these norms requires the solution of the full order model or access to its Gramians; the exact norms are therefore difficult to obtain. Various techniques to estimate the actual approximation error (3.5) without relying on the full order system are available and will be further discussed in section 4.4.1.

The MORscore as introduced by Himpe [137] describes the error of reduced models related to their order as a scalar value, thus allowing a clear comparison of many different model reduction methods. It is defined as follows: Given is a relative error graph  $(e, \varepsilon(r))$  relating reduced order  $r$  to approximation error  $\varepsilon(r)$  given by a suitable norm as, for example,  $\mathcal{H}_2$  or  $\mathcal{H}_\infty$ . Both quantities are mapped to the range  $[0, 1]$  by

$$\begin{aligned} \varphi_r: \mathbb{N} &\mapsto [0, 1], & r &\mapsto \frac{r}{r_{\max}}, \\ \varphi_{\varepsilon(r)}: (0, 1] &\mapsto [0, 1], & \varepsilon(r) &\mapsto \frac{\log_{10}(\varepsilon(r))}{[\log_{10}(\varepsilon_{\text{ref}})]}. \end{aligned} \quad (3.11)$$

Here  $r_{\max}$  is the maximum reduced order considered in the experiment and  $\varepsilon_{\text{ref}}$  the reference accuracy, often chosen as machine precision  $\varepsilon_{\text{ref}} \approx 1 \cdot 10^{-16}$ . The MORscore is defined as the area below the normalized error graph

$$\mu(r_{\max}; \varepsilon_{\text{ref}}) := \text{area}(\varphi_r, \varphi_{\varepsilon(r)}). \quad (3.12)$$

Normalizing the relative error by  $\varepsilon_{\text{ref}}$  yields an  $\varepsilon(r)$  over  $r$  graph potentially reaching 1, if the approximation error is equal to the reference precision. Therefore, a high MORscore states that the desired accuracy is reached faster, as the area below the graph (3.11) is higher in this case. This concept is visualized in fig. 3.1. Note, that the definition of the MORscore does not include considerations about runtime or memory consumption of the used reduction algorithms.

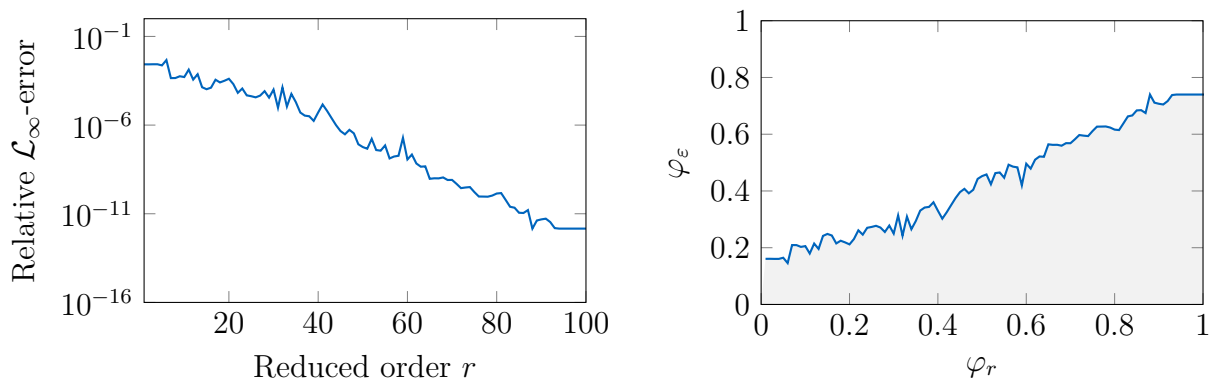


**Figure 3.1:** Illustration of the MORscore concept. Relative error over reduced order on the left, transformation according to eq. (3.11) on the right. The MORscore  $\mu(100; 10^{-16})$  is defined as the gray area beneath the right curve.

### 3.3 Modal reduction

The following methods compute the bases for a projection framework using the modal solution of the original system. They are closely linked to the modal and harmonic analyses presented in section 2.4.2 and therefore rely on an eigendecomposition of the original system. They typically benefit from modal damping, i.e.  $\mathbf{C}$  being proportional to  $\mathbf{K}$  and  $\mathbf{M}$ .

#### 3.3.1 Modal truncation

Modal truncation is classically applied to structural or acoustic systems and is often the standard choice for undamped or proportionally damped systems [90, 215]. Similarly to the modal superposition method, the mode shapes are obtained from an eigenvalue analysis of the original system. After selecting all modes with considerable influence on the transfer function in a frequency range of interest, they are concatenated and form a reduction basis  $\mathbf{V}$ . Contrary to the modal superposition, only a subset of modes is chosen, resulting in  $r$  instead of  $n$  decoupled equations. Typically the  $r$  eigenvalues having the smallest absolute value are chosen, so that the original system's frequency response is approximated starting at  $s = 0$ . The system inputs and outputs are not considered, as the free vibration modes form the projection matrix for a one-sided projection with  $\mathbf{W} = \mathbf{V}$ . It is given by

$$\mathbf{V} = [\mathbf{v}_1 \quad \mathbf{v}_2 \quad \cdots \quad \mathbf{v}_r], \quad (3.13)$$

where  $\mathbf{v}_i$ ,  $i = 1, \dots, r$  are the selected eigenvectors of the undamped system. The accuracy of a reduction basis obtained by truncating the eigenvector matrix to a certain size may be increased by including information about the significance of a certain mode given the input and output situation of the system. Given, for example, a plate with uniform pressure loading, antisymmetric mode shapes are not excited by this load configuration although their corresponding eigenfrequency lies inside the frequency region of interest.

The effect of certain modes on the transfer function can be estimated using a dominant pole algorithm [49, 219, 226], which also considers input and output of the system. The algorithm measures each mode's effect on the transfer function and instead of choosing the  $r$  modes with eigenvalues near the imaginary axis, the  $r$  modes with the highest dominance are considered for the reduced model. To obtain a relation about dominance of certain poles, the transfer function of the original system is rewritten as

$$H(s) = \mathbf{g}\mathbf{X} (s^2\mathbf{I} + s\mathbf{\Xi} + \mathbf{\Lambda})^{-1} \mathbf{X}^T \mathbf{f} = \sum_{i=1}^n \frac{\mathbf{g}\mathbf{v}_i \mathbf{v}_i^T \mathbf{f}}{(s - \omega_{d+,i})(s - \omega_{d-,i})}, \quad (3.14)$$

with modal mass, damping, and stiffness matrices as given by eqs. (2.136), (2.137) and (2.140)

and  $\mathbf{X}$  the matrix of eigenvectors  $\mathbf{v}$ . The damped eigenfrequencies  $\omega_{d\pm,i}$  appear as complex conjugate pairs and are given by

$$\omega_{d\pm,i} = -\omega_i \xi_i \pm \omega_i \sqrt{\xi_i - 1}. \quad (3.15)$$

A pole  $i$  with a corresponding pair of eigenfrequencies  $(\omega_{d+,i}, \omega_{d-,i})$  is considered dominant, if

$$\frac{\|\mathbf{g}\mathbf{v}_i\mathbf{v}_i^T\mathbf{f}\|_2}{\operatorname{Re}(\omega_{d+,i}) \operatorname{Re}(\omega_{d-,i})} > \frac{\|\mathbf{g}\mathbf{v}_j\mathbf{v}_j^T\mathbf{f}\|_2}{\operatorname{Re}(\omega_{d+,j}) \operatorname{Re}(\omega_{d-,j})} \quad \forall j \neq i. \quad (3.16)$$

The resulting algorithm returns the  $r$  most dominant poles of the original system. Their eigenvectors then form the reduction basis in terms of eq. (3.13). An advantage of the method is that it results in a system of decoupled equations, making its evaluation very efficient. However, an eigenvalue decomposition of the original system is required, which computation may involve a substantial computational effort.

The following numerical example shows the effectiveness of the dominant pole algorithm. We consider the beam example from section 2.5.1 with proportional damping. Therefore, the dominant pole algorithm can be applied without modifications. The implementation from [42] is used in the following. The original model is reduced to  $r = 10$  by finding the ten pairs of eigenvalues associated to the most dominant poles of the system's transfer function. The transfer function of the resulting reduced model as well as its relative approximation error are given in fig. 3.2. While the approximation quality at the location of the selected dominant modes is good, the relative error is substantially higher between these expansion points, especially in the region of the anti-resonances of the transfer function. The approximation quality over the considered frequency range is, however, acceptable given the relatively small size of the reduced model.

### 3.3.2 Component mode synthesis

The component mode synthesis (CMS) is a substructuring method where the substructures are represented in generalized coordinates instead of physical coordinates. Similar to condensation methods, only important degrees of freedom, for example load locations or the interface between subsystems, are described by physical coordinates, while the remaining model can be expressed by generalized coordinates [31, 215]. Expressing the inner parts of the substructure, which are not connected to other parts of the model, by a subset of the substructure's modes reduces the size of the assembly of all substructures compared to the original model. Different types of modes need to be considered in the reduction basis

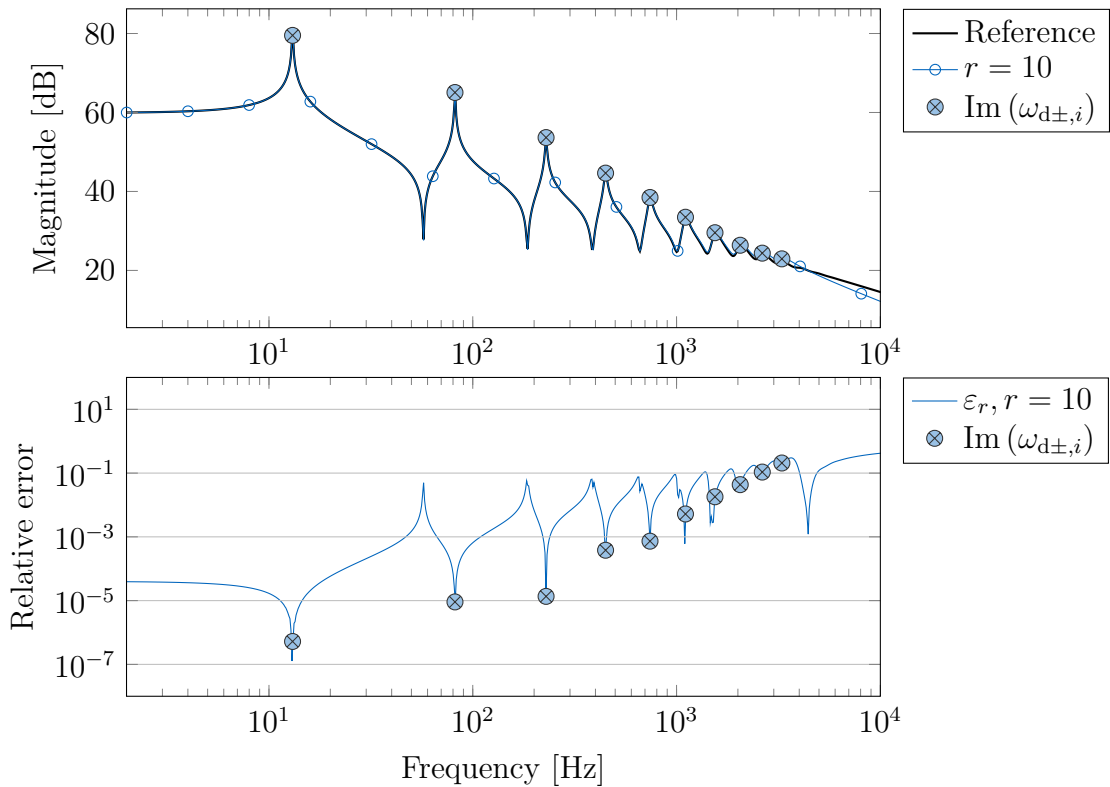


**Figure 3.2:** Transfer functions of the original and a reduced model of order  $r = 10$  obtained from the dominant pole algorithm applied to the cantilever beam as well as the relative error. The imaginary parts of the eigenvalues associated with the dominant modes are marked with circles.

for each substructure to obtain a valid representation. The choice of normal modes, which are obtained from the substructure alone where all interface nodes are fixed, follows similar guidelines as the choice of modes in the modal superposition method. Additionally, the coupling to other substructures must be considered by constraint modes, which are obtained by applying boundary conditions or constraints to the interfaces. A variety of methods on how to choose these modes has been established and been used for various structural and vibro-acoustic systems [144].

The (generalized) Bloch mode synthesis is an adapted version of CMS specifically applicable to periodic structures. Here, only a single unit cell needs to be discretized and its inner degrees of freedom can be expressed by a truncated set of boundary modes [157, 158]. This technique was successfully applied to vibro-acoustic systems in, for example, [251].

### 3.4 Proper orthogonal decomposition

The proper orthogonal decomposition (POD) is a model order reduction method based on a decomposition of snapshots in order to find the most important aspects of a system's dynamics. The snapshots are measured from the original system given meaningful initial conditions or inputs and POD tries to obtain a representation of the full system in terms of the observed system output. It results in a projection matrix in terms of eq. (3.3), which reduces the size of the original system. POD can be classified as data-driven and is applicable to a wide range of problems, not limited to physical systems. Also nonlinear systems can be processed, making POD an often applied method in this context. The snapshot data can come from different sources, such as experimental measurements or numerical models.

In order to reduce a linear dynamical system in Laplace domain, the snapshot matrix  $\mathbf{Y} \in \mathbb{C}^{n \times k}$  is obtained by concatenation of  $k$  snapshots of the system output  $\mathbf{y}(s)$  at distinct frequencies  $s_i, i = 1, \dots, k$  by

$$\mathbf{Y} = [\mathbf{y}(s_1) \quad \mathbf{y}(s_2) \quad \cdots \quad \mathbf{y}(s_k)]. \quad (3.17)$$

The POD finds a set of  $l < k$  orthonormal basis vectors in the subspace spanned by the snapshots, which optimally express the original snapshots in an average sense [11, 123]. This is an optimization problem and can be solved, for example, by principal component analysis (PCA), Karhunen-Loève decomposition, or singular value decomposition (SVD) [163]. The SVD of the snapshot matrix  $\mathbf{Y}$  is given by

$$\mathbf{Y} = \mathbf{U}\mathbf{\Sigma}\mathbf{S}^H, \quad (3.18)$$

where  $\mathbf{U} \in \mathbb{C}^{n \times n}$  and  $\mathbf{S} \in \mathbb{C}^{k \times k}$  are matrices containing the left and right singular values, respectively, and  $\mathbf{\Sigma} \in \mathbb{R}^{n \times k}$  is a diagonal matrix containing the  $l$  non-negative singular values  $\sigma_i, i = 1, \dots, l$  of  $\mathbf{X}$  in descending order, such that  $\sigma_1 \geq \cdots \geq \sigma_l > 0$ . Given a rapid decay of singular values, the matrix  $\mathbf{U}$  can be truncated to  $\mathbf{U}_r$  containing only the  $r$  most significant singular vectors. This truncated matrix can serve as a basis for Galerkin projection, such that  $\mathbf{V} = \mathbf{W} = \mathbf{U}_r \in \mathbb{C}^{n \times r}$ . The method is independent of the structure of the original problem and applying a Galerkin projection preserves this structure in reduced space. Another advantage is that the approximation error of a system reduced by such projection is directly linked to the value of the not considered singular values by

$$\varepsilon_{r,\text{POD}}^2 = \sum_{i=r+1}^l \sigma_i^2. \quad (3.19)$$

In practice,  $r$  can be determined by truncating all vectors with corresponding singular values  $\sigma_i < 10^{-8} \cdot \sigma_1$  or any threshold suitable for the specific model [78].

Being a data-driven method, the performance of the POD heavily depends on the choice of snapshots in the training phase. If an important aspect of the system dynamics is not present in the training data, the resulting model cannot show this behavior. The cost of obtaining the snapshot data can be significant and may be higher than evaluating the model once, so the solution of the system is typically known a-priori. Therefore and due to the knowledge of the approximation error (in sense of the provided snapshot data), POD is often used in a context where very small models of complex and nonlinear problems are required, for example in embedded control devices. A related method, the proper generalized decomposition (PGD), finds a similar representation of the system output by separating the dimensions of the system, for example space and time [79]. The dynamic mode decomposition (DMD) also finds a representation of an underlying dataset obtained from a dynamical system. While POD extracts dominant parts of the dataset based on its energy content, the DMD finds modes and eigenvalues describing the behavior of the observed system in terms of its oscillation or vibration [213, 230, 247].

Figure 3.3 shows the transfer function and the relative error of a reduced model based on the cantilever beam from section 2.5.1. Measurements at  $n_s = 50$  logarithmically distributed locations in the considered frequency range are used to form the snapshot matrix  $\mathbf{Y}$ . After performing the SVD, all vectors with corresponding singular values  $\sigma_i < 10^{-8} \cdot \sigma_1$  are truncated, leading to a reduced model of order  $r = 20$ . The reduced model has a very low approximation error over the complete considered frequency range. As the reduced order is obtained automatically as a byproduct of the SVD and the method does not require any input parameters except the desired error tolerance, the method is easily applicable to many systems. However, the generation of the snapshot matrix involves a substantial amount of computational effort, which might be unfeasible for very large systems.

### 3.5 Balanced truncation

Balanced truncation identifies states with little contribution to the energy transfer from system input to output by balancing the observability and controllability Gramians of the system introduced in section 2.1.1. Balancing in this context means that the original system is transformed to a representation where both Gramians are equivalent and can be seen as a simultaneous diagonalization of the two Gramian matrices  $\mathbf{P}$  and  $\mathbf{Q}$  [11]. Doing so helps identifying states which require much energy to reach and at the same time yield little energy if observed. Truncating such states from the system has little effect on the

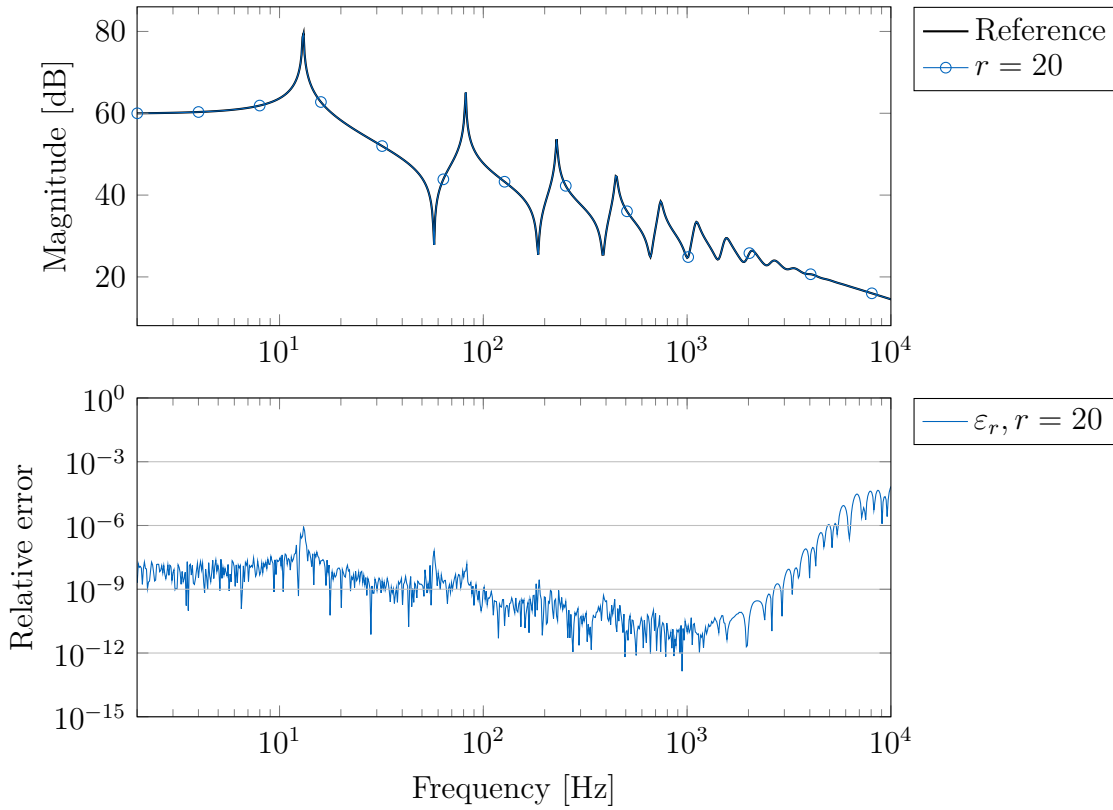


**Figure 3.3:** Transfer functions of the original and a reduced model of order  $r = 20$  obtained from a POD applied to the cantilever beam as well as the relative error. The reduction basis is obtained by truncating all vectors with corresponding singular values  $\sigma_i < 10^{-8} \cdot \sigma_1$ .

overall input/output relation, leading to a more compact system description. Truncating states from a balanced representation of a system retains the stability of the original system. Balanced truncation also provides an a-priori computable error bound for the reduction. The controllability and observability Gramians  $\mathbf{P}$  and  $\mathbf{Q}$  introduced in section 2.1.1 and given by

$$\mathbf{P} = \frac{1}{2\pi} \int_{-\infty}^{\infty} \boldsymbol{\chi}(s) \mathbf{B} \mathbf{B}^T \boldsymbol{\chi}(s)^T ds, \quad (2.6)$$

$$\mathbf{Q} = \frac{1}{2\pi} \int_{-\infty}^{\infty} \boldsymbol{\chi}(s)^T \mathbf{C}^T \mathbf{C} \boldsymbol{\chi}(s) ds, \quad (2.7)$$

with  $\boldsymbol{\chi}(s) = (s\mathbf{E} - \mathbf{A})^{-1}$  are the basis of the method. Recall, that the Gramians allow considerations about the energy required to reach a certain state and the energy obtained by observing a state. The goal is to represent the system to be reduced in terms of a balanced basis, i.e.  $\mathbf{P} = \mathbf{Q} = \text{diag}(\sigma_1 \ \dots \ \sigma_n)$ , with  $\sigma_i$  being the Hankel singular values of the system. They can be obtained from an eigenvalue decomposition of the sum of the controllability and observability Gramians using eq. (2.25). In this representation, the concepts of controllability and observability are equivalent, meaning that states can be identified which

are at the same time difficult to reach and difficult to observe. Truncating these states from the original system will yield a smaller model of order  $r$  which approximation error under the  $\mathcal{H}_\infty$  norm is bounded by the sum of not considered singular values

$$\varepsilon_{r,\text{BT},\mathcal{H}_\infty} \leq 2 \sum_{i=r+1}^n \sigma_i. \quad (3.20)$$

Given the Gramians of a first-order system  $\Sigma$ , its  $\mathcal{H}_2$  norm can be obtained from

$$\|\Sigma\|_{\mathcal{H}_2} = \sqrt{\text{trace}(\mathbf{B}^H \mathbf{Q} \mathbf{B})} = \sqrt{\text{trace}(\mathbf{C}^H \mathbf{P} \mathbf{C})}, \quad (3.21)$$

which could also be used to obtain a measure on the accuracy of a reduced model if applied to the corresponding error system [11].

In the following, the procedure to obtain truncation transformation matrices projecting a first-order system onto a reduced space is outlined. The Cholesky decompositions of both Gramians

$$\mathbf{P} = \mathbf{R} \mathbf{R}^T, \quad \mathbf{Q} = \mathbf{L} \mathbf{L}^T$$

are used to simultaneously balance the original system. The singular value decomposition

$$\begin{bmatrix} \mathbf{U}_1 & \mathbf{U}_2 \end{bmatrix} \begin{bmatrix} \Sigma_1 & 0 \\ 0 & \Sigma_2 \end{bmatrix} \begin{bmatrix} \mathbf{S}_1 & \mathbf{S}_2 \end{bmatrix}^T = \mathbf{L}^T \mathbf{E} \mathbf{R} \quad (3.22)$$

yields a diagonal matrix  $\Sigma_1 \in \mathbb{R}^{r \times r}$  containing the  $r$  most dominant Hankel singular values and their corresponding singular vectors  $\mathbf{U}_1, \mathbf{S}_1$ . The projection matrices  $\mathbf{V}, \mathbf{W}$  can now be obtained from

$$\mathbf{V} = \mathbf{R} \mathbf{S}_1 \Sigma_1^{-\frac{1}{2}}, \quad (3.23)$$

$$\mathbf{W} = \mathbf{L} \mathbf{U}_1 \Sigma_1^{-\frac{1}{2}}. \quad (3.24)$$

In order to apply balanced truncation to second-order systems, the two required Gramians are computed from the equivalent first-order system as shown in eqs. (2.8) and (2.9). These Gramians are partitioned as

$$\mathbf{P} = \begin{bmatrix} \mathbf{R}_p \\ \mathbf{R}_v \end{bmatrix} \begin{bmatrix} \mathbf{R}_p \\ \mathbf{R}_v \end{bmatrix}^T, \quad \mathbf{Q} = \begin{bmatrix} \mathbf{L}_p \\ \mathbf{L}_v \end{bmatrix} \begin{bmatrix} \mathbf{L}_p \\ \mathbf{L}_v \end{bmatrix}^T,$$

where subscripts  $\cdot_p$  and  $\cdot_v$  stand for position and velocity Gramians respectively. The

Cholesky decompositions are partitioned in the same way, resulting in  $\mathbf{R}_p$ ,  $\mathbf{R}_v$ ,  $\mathbf{L}_p$ ,  $\mathbf{L}_v$ . This description is based on the method of transforming the second-order system to a first-order system by expressing the first-order state as a combination of second-order states and the corresponding derivatives. The balancing (3.22) is now performed for both sets of Gramians according to

$$\begin{aligned} \begin{bmatrix} \mathbf{U}_{p,1} & \mathbf{U}_{p,2} \end{bmatrix} \begin{bmatrix} \boldsymbol{\Sigma}_{p,1} & 0 \\ 0 & \boldsymbol{\Sigma}_{p,2} \end{bmatrix} \begin{bmatrix} \mathbf{S}_{p,1} & \mathbf{S}_{p,2} \end{bmatrix}^\top &= \mathbf{L}_p^\top \mathbf{J} \mathbf{R}_p, \\ \begin{bmatrix} \mathbf{U}_{v,1} & \mathbf{U}_{v,2} \end{bmatrix} \begin{bmatrix} \boldsymbol{\Sigma}_{v,1} & 0 \\ 0 & \boldsymbol{\Sigma}_{v,2} \end{bmatrix} \begin{bmatrix} \mathbf{S}_{v,1} & \mathbf{S}_{v,2} \end{bmatrix}^\top &= \mathbf{L}_v^\top \mathbf{M} \mathbf{R}_v, \end{aligned} \quad (3.25)$$

where  $\mathbf{J}$  is the arbitrary invertible matrix chosen in the reformulation of the second-order system as first-order system. The four corresponding projection matrices  $\mathbf{V}_p$ ,  $\mathbf{V}_v$ ,  $\mathbf{W}_p$ ,  $\mathbf{W}_v$  are obtained by

$$\mathbf{V}_p = \mathbf{R}_p \mathbf{S}_{p,1} \boldsymbol{\Sigma}_{p,1}^{-\frac{1}{2}}, \quad (3.26)$$

$$\mathbf{V}_v = \mathbf{R}_v \mathbf{S}_{v,1} \boldsymbol{\Sigma}_{v,1}^{-\frac{1}{2}},$$

$$\mathbf{W}_p = \mathbf{L}_p \mathbf{U}_{p,1} \boldsymbol{\Sigma}_{p,1}^{-\frac{1}{2}}, \quad (3.27)$$

$$\mathbf{W}_v = \mathbf{L}_v \mathbf{U}_{v,1} \boldsymbol{\Sigma}_{v,1}^{-\frac{1}{2}}.$$

The corresponding reduced matrices are given by

$$\begin{aligned} \mathbf{M}_r &= \mathbf{T} \left( \mathbf{W}_v^\top \mathbf{M} \mathbf{V}_v \right) \mathbf{T}^{-1}, \quad \mathbf{C}_r = \mathbf{T} \left( \mathbf{W}_v^\top \mathbf{C} \mathbf{V}_v \right) \mathbf{T}^{-1}, \quad \mathbf{K}_r = \mathbf{T} \left( \mathbf{W}_v^\top \mathbf{K} \mathbf{V}_p \right), \\ \mathbf{F}_r &= \mathbf{T} \left( \mathbf{W}_v^\top \mathbf{F} \right), \quad \mathbf{G}_r = \mathbf{G} \mathbf{V}_p, \end{aligned} \quad (3.28)$$

with  $\mathbf{T} = \mathbf{W}_p^\top \mathbf{J} \mathbf{V}_v$ . Other methods to compute the transformation matrices  $\mathbf{V}$ ,  $\mathbf{W}$  for second-order systems, some requiring only one singular value decomposition, have been proposed in Reis and Stykel [217] and summarized in [50, 226]. They are reproduced in table 3.1. The projection names refer to the types of Gramians being used. *v* and *p* stand for balancing regarding velocity and position Gramians and the combinations thereof, *fv* for free velocity balancing, and *so* for second-order balancing. Only for certain cases of projection the stability of the original second-order system is retained for the reduced model [217]. Given a symmetric second-order system, truncation using *pv* and *fv* preserves stability. The error bound (3.20) is also not valid for any of the second-order truncation formulas [74].

The balanced truncation can be considered a POD with Petrov-Galerkin projection applied to the impulse response of a system [11]. In turn, POD can be used to obtain approximations of the Gramians, as their computation is typically very demanding. Exciting a system with

**Table 3.1:** Second-order balanced truncation formulas. The \* denotes factors of the SVD not needed, and thus not accumulated in practical computations [50].

Type	SVD(s)	Truncation	Reference
<i>v</i>	$\mathbf{U}\Sigma\mathbf{S}^\top = \mathbf{L}_v^\top \mathbf{M} \mathbf{R}_v$	$\mathbf{W} = \mathbf{L}_v \mathbf{U}_1 \Sigma_1^{-\frac{1}{2}}, \mathbf{V} = \mathbf{R}_v \mathbf{S}_1 \Sigma_1^{-\frac{1}{2}}$	[217]
<i>fv</i>	$*\Sigma\mathbf{S}^\top = \mathbf{L}_p^\top \mathbf{R}_p$	$\mathbf{W} = \mathbf{V}, \mathbf{V} = \mathbf{R}_p \mathbf{S}_1 \Sigma_1^{-\frac{1}{2}}$	[183]
<i>pv</i>	$\mathbf{U}\Sigma\mathbf{S}^\top = \mathbf{L}_v^\top \mathbf{M} \mathbf{R}_p$	$\mathbf{W} = \mathbf{L}_v \mathbf{U}_1 \Sigma_1^{-\frac{1}{2}}, \mathbf{V} = \mathbf{R}_p \mathbf{S}_1 \Sigma_1^{-\frac{1}{2}}$	[217]
<i>vp</i>	$*\Sigma\mathbf{S}^\top = \mathbf{L}_p^\top \mathbf{R}_v,$ $\mathbf{U} ** = \mathbf{L}_v^\top \mathbf{M} \mathbf{R}_p$	$\mathbf{W} = \mathbf{L}_v \mathbf{U}_1 \Sigma_1^{-\frac{1}{2}}, \mathbf{V} = \mathbf{R}_v \mathbf{S}_1 \Sigma_1^{-\frac{1}{2}}$	[217]
<i>p</i>	$*\Sigma\mathbf{S}^\top = \mathbf{L}_p^\top \mathbf{R}_p,$ $\mathbf{U} ** = \mathbf{L}_v^\top \mathbf{M} \mathbf{R}_v$	$\mathbf{W} = \mathbf{L}_v \mathbf{U}_1 \Sigma_1^{-\frac{1}{2}}, \mathbf{V} = \mathbf{R}_p \mathbf{S}_1 \Sigma_1^{-\frac{1}{2}}$	[217]
<i>so</i>	$\mathbf{U}_p \Sigma_p \mathbf{S}_p^\top = \mathbf{L}_p^\top \mathbf{R}_p,$ $\mathbf{U}_v \Sigma_v \mathbf{S}_v = \mathbf{L}_v^\top \mathbf{M} \mathbf{R}_v$	$\mathbf{W}_p = \mathbf{L}_p \mathbf{U}_{p,1} \Sigma_{p,1}^{-\frac{1}{2}}, \mathbf{V}_p = \mathbf{R}_p \mathbf{S}_{p,1} \Sigma_{p,1}^{-\frac{1}{2}},$ $\mathbf{W}_v = \mathbf{L}_v \mathbf{U}_{v,1} \Sigma_{v,1}^{-\frac{1}{2}}, \mathbf{V}_v = \mathbf{R}_v \mathbf{S}_{v,1} \Sigma_{v,1}^{-\frac{1}{2}}$	[74]

impulses, the POD constructs the controllability Gramian and obtaining snapshots regarding system input and output and applying a POD results in approximation for both Gramians [264].

To illustrate the balanced truncation, the cantilever beam model described in section 2.5.1 is reduced using the truncation formulas from table 3.1 provided by the software package SOLBT [51]. The transfer functions of the reduced models as well as their relative errors are presented in fig. 3.4. The orders of the reduced models are determined by truncating the smallest singular values of the balanced Gramians which sum does not exceed a threshold of  $\varepsilon_{\text{tol}} = 1 \cdot 10^{-8}$ . While this is not an error bound for all employed formulas, it still provides a reasonable estimate [50]. Except from *pv*, which order is estimated to be lower than the other reduced models, all truncation formulas yield models with low relative errors for most of the considered frequency range.

### 3.6 Interpolatory methods

Interpolatory model order reduction methods find a reduced representation of a system's input output relation by computing an interpolant for its transfer function. An effective way to find such interpolants is to enforce interpolation at important locations  $s_0$  of the transfer

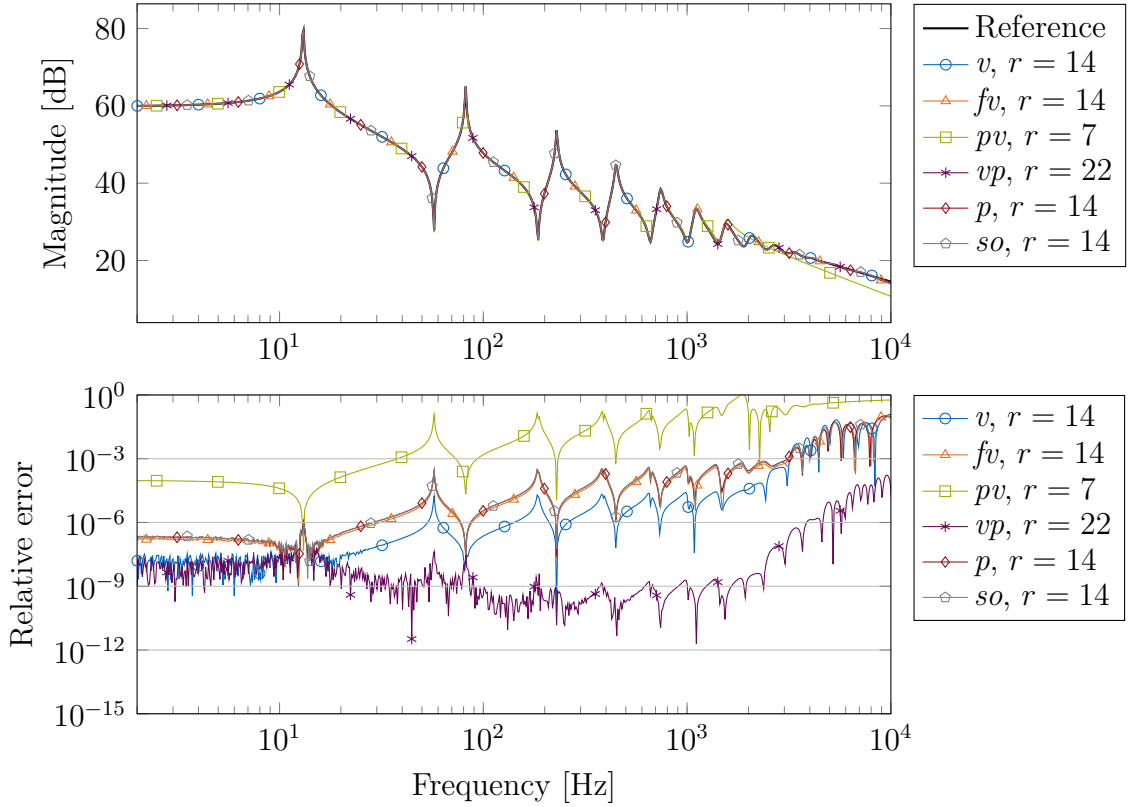


**Figure 3.4:** Transfer functions of the original and reduced models obtained from a balanced truncation using different balancing formulas from table 3.1 applied to the cantilever beam and their relative errors. The reduced orders are determined by truncating the columns of the Gramians corresponding to the smallest singular values which sum is smaller than  $1 \cdot 10^{-8}$ .

function, for example its moments, and possibly some of its derivatives and approximate the original rational function by a power series. This technique is termed moment matching. If  $s_0 = 0$  is chosen as only expansion point, moment matching is equivalent to a Padé approximation of the transfer function. The underlying problem of approximating the moments of the original transfer function  $\mathbf{H}$  by a reduced representation  $\mathbf{H}_r$ , given  $k$  interpolation points  $s_{0,i}$  each with an approximation order  $l_i$  is of the form

$$\frac{d^{j_i}}{ds^{j_i}} \mathbf{H}(s_{0,i}) = \frac{d^{j_i}}{ds^{j_i}} \mathbf{H}_r(s_{0,i}), \quad (3.29)$$

where  $i = 0, \dots, k$  and with orders of the derivative  $0 \leq j_i \leq l_i$ . The choice of the interpolation points is crucial for an accurate and compact representation of the original function. This interpolation can be achieved by projecting the original system onto a suitable reduction space [12, 124]. Although the moments in eq. (3.29) are given explicitly by eqs. (2.19) and (2.20), their direct computation is not efficient and prone to numerical problems. Using projection bases  $\mathbf{V}$ ,  $\mathbf{W}$  implicitly matching the desired moments is therefore a classic

approach to the interpolation problem.

In case of a SISO system,  $r$  interpolation points suffice to match up to  $2r$  moments of the original transfer function. However, tangentially matching moments of a MIMO system additionally requires tangent directions in which the original system is approximated, which also affect the quality of the resulting interpolant. The requirements for an successful interpolation can be derived for first and second-order systems using the generalized coprime realization of the considered system [12, 37, 268]. For this, the transfer function is rewritten in the general form

$$\mathbf{H}(s) = \mathbf{G}(s) \mathbf{K}(s)^{-1} \mathbf{F}(s), \quad (3.30)$$

with  $\mathbf{K}(s) \in \mathbb{C}^{n \times n}$ ,  $\mathbf{F}(s) \in \mathbb{C}^{n \times m}$ , and  $\mathbf{G}(s) \in \mathbb{C}^{p \times n}$ . Equation (3.30) can be used to represent a wide range of different system types, not only limited to first and second-order systems but also parametric models and is valid for SISO and MIMO systems. A first-order descriptor system can be represented by setting  $\mathbf{K}(s) = s\mathbf{E} - \mathbf{A}$ ,  $\mathbf{F}(s) = \mathbf{F}$ , and  $\mathbf{G}(s) = \mathbf{G}$ ; a second-order system fits by setting  $\mathbf{K}(s) = s^2\mathbf{M} + s\mathbf{C} + \mathbf{K}$ ,  $\mathbf{F}(s) = \mathbf{F}$ , and  $\mathbf{G}(s) = \mathbf{G}$ . Using this description, the quantities of a reduced order model obtained from projection with bases  $\mathbf{V}$ ,  $\mathbf{W}$  is given by

$$\begin{aligned} \mathbf{K}_r(s) &= \mathbf{W}^H \mathbf{K}(s) \mathbf{V}, \\ \mathbf{F}_r(s) &= \mathbf{W}^H \mathbf{F}(s), \quad \mathbf{G}_r(s) = \mathbf{G}(s) \mathbf{V}. \end{aligned} \quad (3.31)$$

To achieve interpolation of a SISO system, a reduced order model  $H_r(s)$  is required to fulfill

$$H_r(s_{0,i}) = H(s_{0,i}) \quad \text{and} \quad H_r^H(s_{0,i}) = H^H(s_{0,i}) \quad \forall i = 1, \dots, r. \quad (3.32)$$

In the case of MIMO systems, which transfer functions are matrix-valued, an interpolation of the full matrix function might be inefficient [12]. Therefore, instead of enforcing interpolation at specific points in every direction, interpolation is required only for specific directions at these points. This concept is known as tangential interpolation [113]. Tangential interpolation of the transfer function  $\mathbf{H}(s)$  of a MIMO system regarding several expansion points is then given by

$$\mathbf{H}_r(s_{0,i}) \mathbf{f}_i = \mathbf{H}(s_{0,i}) \mathbf{f}_i \quad \text{and} \quad \mathbf{g}_j^T \mathbf{H}_r(\sigma_{0,j}) = \mathbf{g}_j^T \mathbf{H}(\sigma_{0,j}) \quad \forall i, j = 1, \dots, r, \quad (3.33)$$

with sets of right and left tangential directions  $\{\mathbf{f}_i\}_{i=1}^r \subset \mathbb{C}^m$  respectively  $\{\mathbf{g}_i\}_{i=1}^r \subset \mathbb{C}^p$  and the corresponding sets of right and left interpolation points  $\{s_{0,i}\}_{i=1}^r$ ,  $\{\sigma_{0,i}\}_{i=1}^r \subset \mathbb{C}$ .

Two-sided or bitangential interpolation at  $s_{0,i}$  is achieved, if

$$\mathbf{g}_i^T \mathbf{H}_r^H(s_{0,i}) \mathbf{f}_i = \mathbf{g}_i^T \mathbf{H}^H(s_{0,i}) \mathbf{f}_i. \quad (3.34)$$

The requirements for interpolation (3.29) at a distinct expansion point for SISO and MIMO systems can thus be summarized as follows:

$$\begin{aligned} \text{If} \quad & \left[ \frac{d^j}{ds^j} \left( \mathcal{K}(s_0)^{-1} \mathcal{F}(s_0) \right) \right] \mathbf{f} \in \text{span}(\mathbf{V}) \quad \forall j = 0, \dots, k, \\ \text{then} \quad & \frac{d^j}{ds^j} \mathbf{H}_r(s_0) \mathbf{f} = \frac{d^j}{ds^j} \mathbf{H}(s_0) \mathbf{f} \quad \forall j = 0, \dots, k. \end{aligned} \quad (3.35)$$

$$\begin{aligned} \text{If} \quad & \left[ \frac{d^j}{ds^j} \left( \mathcal{K}(\sigma_0)^{-H} \mathcal{G}(\sigma_0)^H \right) \right] \mathbf{g} \in \text{span}(\mathbf{W}) \quad \forall j = 0, \dots, l, \\ \text{then} \quad & \mathbf{g}^T \frac{d^j}{ds^j} \mathbf{H}_r(\sigma_0) = \mathbf{g}^T \frac{d^j}{ds^j} \mathbf{H}(\sigma_0) \quad \forall j = 0, \dots, l. \end{aligned} \quad (3.36)$$

If (3.35) and (3.36) hold and  $s_0 = \sigma_0$ ,

$$\text{then} \quad \mathbf{g}^T \frac{d^j}{ds^j} \mathbf{H}_r(s_0) \mathbf{f} = \mathbf{g}^T \frac{d^j}{ds^j} \mathbf{H}(s_0) \mathbf{f} \quad \forall j = 0, \dots, k + l + 1. \quad (3.37)$$

Here,  $k$  and  $l$  are the derivative orders regarding left and right interpolation basis and the matrix functions are assumed to be analytic at their respective evaluation points. A proof is given in the book by Antoulas, Beattie, and Gugercin [12]. Note that the tangential directions in the above relations collapse to 1 in case of a SISO system, i.e.  $p = m = 1$ .

Given  $r$  interpolation points  $s_{0,i}$ ,  $i = 1, \dots, r$ , with interpolation order  $j_i = 1$  each, the corresponding projection matrices ensuring interpolation are constructed as

$$\mathbf{V} = \left[ \mathcal{K}(s_{0,1})^{-1} \mathcal{F}(s_{0,1}) \mathbf{f}_1 \quad \cdots \quad \mathcal{K}(s_{0,r})^{-1} \mathcal{F}(s_{0,r}) \mathbf{f}_r \right], \quad (3.38)$$

$$\mathbf{W} = \left[ \mathcal{K}(s_{0,1})^{-H} \mathcal{G}(s_{0,1})^H \mathbf{g}_1 \quad \cdots \quad \mathcal{K}(s_{0,r})^{-H} \mathcal{G}(s_{0,r})^H \mathbf{g}_r \right]. \quad (3.39)$$

After deflation, they can be used in the projection framework (3.31) in order to obtain a reduced model interpolating the frequency response of the original system. Equations (3.35) to (3.37) show that only linear equation systems of order  $n$  need to be solved to compute a structure-preserving reduced model; recall, that constructing a reduced model from balanced truncation requires the solution of Lyapunov equations, which is computationally more demanding. If series expansion factors of the transfer function are known, the reduction bases  $\mathbf{V}$ ,  $\mathbf{W}$  can be obtained using a recursive formulation proposed in [37]. For this, the system

shifted about  $s_0$  needs to be described as a power expansion of the form

$$\mathcal{K}(s_0 + s) = \sum_{i=0} s^i \mathcal{K}_i, \quad \mathcal{F}(s_0 + s) = \sum_{i=0} s^i \mathcal{F}_i, \quad \mathcal{G}(s_0 + s) = \sum_{i=0} s^i \mathcal{G}_i. \quad (3.40)$$

Then, the recursion for right and left projection vectors  $\mathbf{v}$ ,  $\mathbf{w}$ , which form the projection bases  $\mathbf{V} = [\mathbf{v}_1 \ \dots \ \mathbf{v}_k]$  and  $\mathbf{W} = [\mathbf{w}_1 \ \dots \ \mathbf{w}_l]$  is given by

$$\begin{aligned} \mathcal{K}_0 \mathbf{v}_0 &= \mathcal{F}_0 \mathbf{f} & \mathbf{w}_0^H \mathcal{K}_0 &= \mathbf{g}^H \mathcal{G}_0 \\ \mathcal{K}_0 \mathbf{v}_1 &= \mathcal{F}_1 \mathbf{f} - \mathcal{K}_1 \mathbf{v}_0 & \mathbf{w}_1^H \mathcal{K}_0 &= \mathbf{g}^H \mathcal{G}_1 - \mathbf{w}_0^H \mathcal{K}_1 \\ \mathcal{K}_0 \mathbf{v}_2 &= \mathcal{F}_2 \mathbf{f} - \mathcal{K}_1 \mathbf{v}_1 - \mathcal{K}_2 \mathbf{v}_0 & \mathbf{w}_2^H \mathcal{K}_0 &= \mathbf{g}^H \mathcal{G}_2 - \mathbf{w}_1^H \mathcal{K}_1 - \mathbf{w}_0^H \mathcal{K}_2 \\ &\vdots & & \\ \mathcal{K}_0 \mathbf{v}_k &= \mathcal{F}_k \mathbf{f} - \sum_{i=0}^k \mathcal{K}_i \mathbf{v}_{k-i} & \mathbf{w}_l^H \mathcal{K}_0 &= \mathbf{g}^H \mathcal{G}_l - \sum_{i=0}^l \mathbf{w}_{l-i}^H \mathcal{K}_i. \end{aligned} \quad (3.41)$$

A second-order system directly fits into the above framework and yields a three term recurrence with  $\mathcal{K}_0(s_0) = s_0^2 \mathbf{M} + s_0 \mathbf{C} + \mathbf{K}$ ,  $\mathcal{K}_1(s_0) = 2s_0 \mathbf{M} + \mathbf{C}$ ,  $\mathcal{K}_2(s_0) = \mathbf{M}$ ,  $\mathcal{F}(s_0) = \mathbf{F}$ , and  $\mathcal{G}(s_0) = \mathbf{G}$ . It is possible to compute the projection vectors  $\mathbf{v}$ ,  $\mathbf{w}$  up to an arbitrary interpolation order and to combine vectors based on different expansion points  $s_0$  in a single projection basis. Additionally, any transfer function which can be expressed as a polynomial of order  $p$  yields a similar recurrence with  $p + 1$  terms.

### 3.6.1 Second-order Krylov subspaces

Krylov subspaces are a classical choice to be used for projection based model order reduction and have been successfully applied to various kinds of problems, first mainly for first-order state space systems [28, 124]. Su and Craig [241] introduced a generalized Krylov subspace for second-order systems exploiting a similar recurrence as shown in eq. (3.41), for which Arnoldi methods for efficient computation have been established some years later [29, 171]. In the following, the second-order Krylov subspace will be outlined; for analogous techniques for first-order systems see, for example, Antoulas [11]. Only SISO systems will be considered in the following, but the approach can be extended for use with MIMO systems [64, 82, 256].

Given a matrix  $\mathbf{Z} \in \mathbb{R}^{n \times n}$  and a vector  $\mathbf{q} \in \mathbb{R}^n$ , the corresponding Krylov subspace of size  $r$  is spanned by a vector sequence of the form

$$\mathcal{G}_r(\mathbf{Z}, \mathbf{q}) = \text{span} \{ \mathbf{q}, \mathbf{Z}\mathbf{q}, \mathbf{Z}^2\mathbf{q}, \dots, \mathbf{Z}^{r-1}\mathbf{q} \}. \quad (3.42)$$

A Krylov subspace contains all vectors  $\mathbf{x}$  which are the solution to  $\mathbf{x} = p(\mathbf{Z})\mathbf{q}$ , with a

polynomial function  $p$  of degree smaller  $r - 1$  [224]. Apart from being used in moment matching methods, Krylov sequences also have other uses in linear algebra. They are used for the iterative solution of a linear system of equations  $\mathbf{Z}\mathbf{x} = \mathbf{q}$  or the iterative approximation of the eigenvalues of matrix  $\mathbf{Z}$  [11].

A Krylov space of the form eq. (3.42) is a suitable projection subspace for the dimension reduction of a first-order systems given by eq. (2.1). Its transfer function is rewritten as

$$H(s) = \mathbf{c} \left( \mathbf{I} - s\mathbf{A}^{-1}\mathbf{E} \right)^{-1} \mathbf{A}^{-1}\mathbf{b} \quad (3.43)$$

and the matrix and vector forming the Krylov sequence are identified as  $\mathbf{Z} = -\mathbf{A}^{-1}\mathbf{E}$  and  $\mathbf{q} = \mathbf{A}^{-1}\mathbf{b}$ . In order to arrive at a generalization of this Krylov sequence for second-order systems as introduced in Su and Craig [241], the following linearization of a second-order system is considered:

$$\mathbf{A}^{(1)} = \begin{bmatrix} \mathbf{K} & \mathbf{0} \\ \mathbf{0} & \mathbf{I} \end{bmatrix}, \quad \mathbf{E}^{(1)} = \begin{bmatrix} \mathbf{C} & \mathbf{M} \\ -\mathbf{I} & \mathbf{0} \end{bmatrix}, \quad \mathbf{b}^{(1)} = \begin{bmatrix} \mathbf{f} \\ \mathbf{0} \end{bmatrix}, \quad \mathbf{c}^{(1)} = [\mathbf{g} \quad \mathbf{0}], \quad (3.44)$$

where  $\mathbf{K}, \mathbf{C}, \mathbf{M} \in \mathbb{R}^{n \times n}$ ,  $\mathbf{f}, \mathbf{g} \in \mathbb{R}^n$ ,  $\mathbf{A}^{(1)}, \mathbf{E}^{(1)} \in \mathbb{R}^{2n \times 2n}$ , and  $\mathbf{b}^{(1)}, \mathbf{c}^{(1)} \in \mathbb{R}^{2n}$ . Introducing the linearization in the Krylov sequence yields

$$\mathbf{Z} = -\mathbf{A}^{(1)-1}\mathbf{E}^{(1)} = \begin{bmatrix} -\mathbf{K}^{-1}\mathbf{C} & -\mathbf{K}^{-1}\mathbf{M} \\ \mathbf{I} & \mathbf{0} \end{bmatrix} = \begin{bmatrix} \mathbf{Z}_1 & \mathbf{Z}_2 \\ \mathbf{I} & \mathbf{0} \end{bmatrix} \quad \text{and} \quad \mathbf{q} = -\mathbf{A}^{(1)-1}\mathbf{b}^{(1)} = \begin{bmatrix} \mathbf{K}^{-1}\mathbf{f} \\ \mathbf{0} \end{bmatrix}.$$

The resulting Krylov vectors  $\mathbf{Z}^i\mathbf{q}$  are of dimension  $2n$  and are related by

$$\mathbf{Z}^i\mathbf{q} = \begin{bmatrix} \mathbf{r}_i \\ \mathbf{r}_{i-1} \end{bmatrix}, \quad \text{for } i \geq 1. \quad (3.45)$$

The vectors  $\mathbf{r}_i$  are thus given recursively by

$$\begin{aligned} \mathbf{r}_0 &= \mathbf{q}, \\ \mathbf{r}_1 &= \mathbf{Z}_1\mathbf{r}_0, \\ \mathbf{r}_i &= \mathbf{Z}_1\mathbf{r}_{i-1} + \mathbf{Z}_2\mathbf{r}_{i-2}, \quad \text{for } i \geq 2, \end{aligned} \quad (3.46)$$

and consequently the  $r$ th generalized second-order Krylov subspace defined by the two matrices  $\mathbf{Z}_1, \mathbf{Z}_2$  and the starting vector  $\mathbf{q}$  spanned by the corresponding Krylov vectors  $\mathbf{r}_i, i = 0, \dots, r - 1$  is defined as

$$\mathcal{S}_r(\mathbf{Z}_1, \mathbf{Z}_2, \mathbf{v}_0) = \text{span} \{ \mathbf{r}_0, \mathbf{r}_1, \dots, \mathbf{r}_{r-1} \}. \quad (3.47)$$

The moment matching, i.e. expansion about  $s_0 = 0$ , of a second-order system is thus performed setting  $\mathbf{Z}_1 = -\mathbf{K}^{-1}\mathbf{C}$ ,  $\mathbf{Z}_2 = -\mathbf{K}^{-1}\mathbf{M}$  and  $\mathbf{q} = \mathbf{K}^{-1}\mathbf{f}$  [29]. If an approximation about the zero frequency is not optimal for the reduction task, the transfer function is shifted by a frequency  $s_0 \neq 0$ , yielding the shifted second-order transfer function

$$H(s) = \mathbf{g} \left( (s - s_0)^2 \mathbf{M} + (s - s_0) \widehat{\mathbf{C}} + \widehat{\mathbf{K}} \right)^{-1} \mathbf{f}, \quad (3.48)$$

with  $\widehat{\mathbf{C}} = 2s_0\mathbf{M} + \mathbf{C}$  and  $\widehat{\mathbf{K}} = s_0^2\mathbf{M} + s_0\mathbf{C} + \mathbf{K}$ . The corresponding second-order Krylov subspace is given analogously by the matrices  $\mathbf{Z}_1 = -\widehat{\mathbf{K}}^{-1}\widehat{\mathbf{C}}$ ,  $\mathbf{Z}_2 = -\widehat{\mathbf{K}}^{-1}\mathbf{M}$  and the vector  $\mathbf{q} = \widehat{\mathbf{K}}^{-1}\mathbf{f}$ . Note, that the structure-preserving method shown above is equivalent to the second-order Krylov subspace method, if a single expansion point is chosen for the structure-preserving scheme [37].

An orthonormal basis of  $\mathcal{S}_r(\mathbf{Z}_1, \mathbf{Z}_2, \mathbf{v}_0)$  can be found using, for example, the second-order Arnoldi (SOAR) procedure [29, 30] or its extended version TOAR (two-level orthogonal Arnoldi procedure), which provides increased numerical stability [171]. Again, bases for subspaces corresponding to different expansion points and with different sizes can be combined to create a single reduction basis. All basis vectors are concatenated into a single matrix, which, after deflating and thus removing possible overlapping basis vectors, spans the corresponding reduction space. This potentially increases the frequency range of good approximation of the reduced model while allowing a smaller reduced order. Additionally, a certain frequency range, not necessarily starting at  $s = 0$ , can be approximated by a reduced model given a suitable choice of expansion points. It must, however, be taken into account, that establishing a Krylov subspace about a shift  $s_0$  involves the factorization of a matrix of order  $n$ , while increasing the size of an already available Krylov subspace only involves matrix vector multiplications. In a computational implementation, the inverses of  $\mathbf{K}$ , respective  $\widehat{\mathbf{K}}$ , are not directly computed but factorizations are used.

In the following, the performance of model order reduction using a second-order Krylov subspace is shown using the cantilever beam model described in section 2.5.1. Two configurations which lead to reduced models of the same size are considered: a single expansion point with interpolation order  $r_0 = 20$  and  $n_s = 20$  expansion points with interpolation order  $r_0 = 1$  each. The 20 interpolation points are logarithmically distributed in the frequency range of interest, the single expansion point is located at  $s_0 = 2\pi i \cdot 400$  Hz. The orthonormal subspace of the experiment with  $n_s = 1$  is computed with TOAR. For the projection space with  $n_s = 20$ , the projection vectors for the first moment at each expansion point are obtained according to eq. (3.41). The projection basis in this case is obtained from an orthogonalization of the matrix containing all projection vectors. The transfer functions as well as the relative errors of the respective reduced models are given in fig. 3.5. Both models can

approximate the full model in a wide frequency range. However, the approximation quality of the model with  $n_s = 1$  is very sensitive to the location of the expansion point, which has been manually adjusted for this example. A reasonable placement of the expansion points will be discussed in the next section.

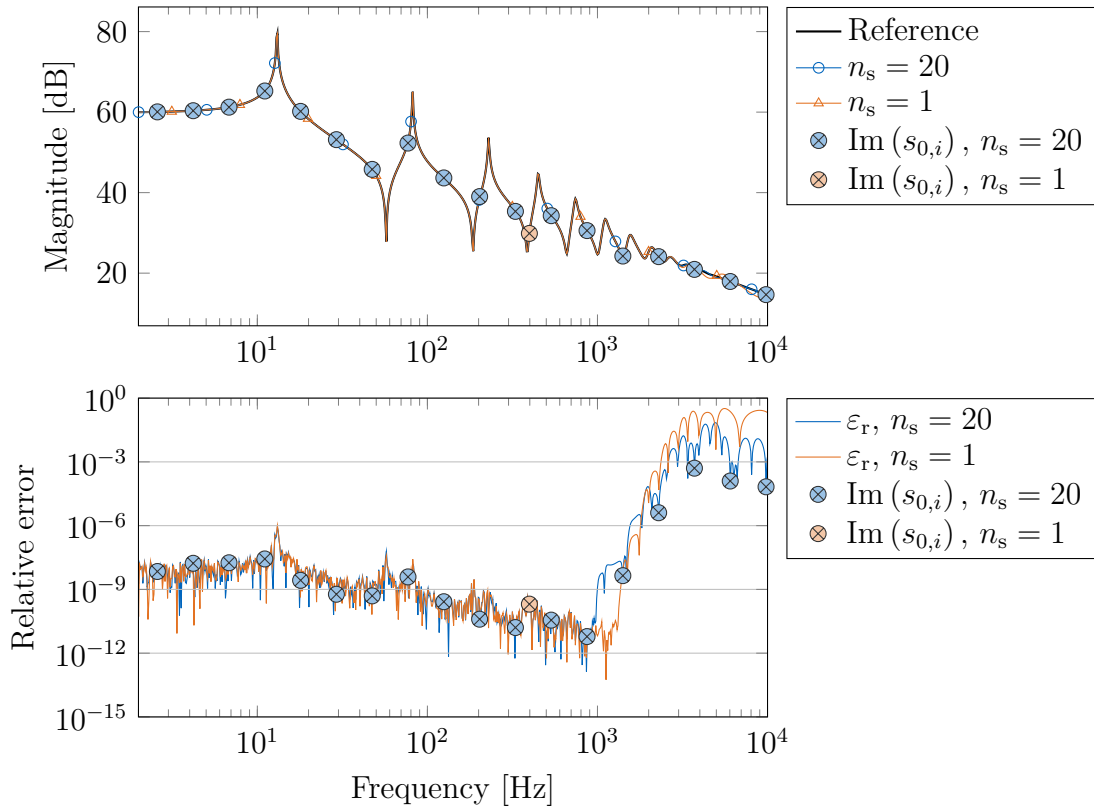


**Figure 3.5:** Transfer functions of the original and reduced models of order  $r = 20$  obtained from moment matching using TOAR applied to the cantilever beam and their relative errors. The reduction bases are obtained using one expansion point  $n_s = 1$  with interpolation order  $r_0 = 20$  and  $n_s = 20$  interpolation points of order  $r_0 = 1$  each. The locations of the expansion points are marked by circles.

### 3.6.2 Expansion point selection

The location of expansion points as well as their respective interpolation orders has a large influence on the performance of interpolatory reduction methods and is unique for every model. Contrary to balancing methods, it is not generally possible to make an uninformed a-priori choice, that yields high quality reduced models. A classical starting point is to choose linearly or logarithmically spaced expansion points in the frequency range of interest. However, there is not always incidence on how many expansion points should be used or how high their respective interpolation order should be. This may result in either not accurate

or unnecessarily large reduced models. Iterative and adaptive methods on the one hand and averaging methods on the other hand have therefore been introduced to automatically find locations and/or interpolation orders and to ensure reasonably sized reduced models.

A widely used iterative method is the iterative rational Krylov algorithm (IRKA), originally presented by Gugercin, Antoulas, and Beattie [126]. Given a fixed number of initial interpolation points, this method computes a reduced model which is optimal regarding the  $\mathcal{H}_2$  error of the approximation. Originally introduced for first-order systems, it was extended to be used with second-order systems as SO-IRKA, however losing some of its optimality claims [246, 268]. Another variant, TF-IRKA, is independent of the original system's realization by relying on the transfer function evaluation of the reduced model [38, 238]. The general IRKA procedure can be summarized as follows: Given initial expansion points closed under complex conjugation, compute a reduced model by projection, considering an interpolation order of one at each frequency shift. Then compute an eigenvalue decomposition of the reduced system; for MIMO systems, additionally compute the pole-residue expansion of the reduced transfer function as, for example, given in [225]. The eigenvalues mirrored along the imaginary axis are considered as expansion points for the next iteration. If the change of the expansion points between iterations diminishes, convergence is reached and optimal locations for the frequency shifts, and thus an optimal reduced model, has been found. The algorithm for first-order MIMO systems is summarized in algorithm 3.1; the variant for second order systems will be outlined more precisely in section 4.3. Given complex conjugate pairs of interpolation points, the projection bases obtained from IRKA can be kept real-valued. Here, the projection bases are built from the real and imaginary parts of the original reduction bases computed in algorithm 3.1 line 2. Only the matrix columns referring to one expansion point of each complex conjugate pair are considered, so the size of the projection basis does not change. IRKA can be computationally demanding, as each iteration involves the solution of  $r$  linear systems of order  $n$ . This cost can be leveraged by using intermediate-sized reduced models, as proposed in [46, 71], on which the optimization iterations are preformed. It can be shown, that the converged expansion points of the intermediate system are also valid for the full model. Another caveat is that IRKA does not provide an error bound for the reduced model, but finds the optimal reduced model given a user-provided reduced order  $r$ . If this is chosen too low, a good approximation of the full system response is not guaranteed. The approximation error of a model reduced by IRKA can only be assessed, if the full model's solution is known.

IRKA is now applied to find an optimal distribution of expansion points for the cantilever beam model described in section 2.5.1. The implementation from [103] is used in the following. To be applicable, the model is rewritten as a first-order system using the first companion form given by eq. (A.1).  $n_s = 20$  initial expansion points in the frequency

---

**Algorithm 3.1** The iterative rational Krylov algorithm for tangential interpolation

---

**Require:** Original system  $\mathbf{A}, \mathbf{E}, \mathbf{B}, \mathbf{C}$ ,  $r$  initial expansion points  $\mathbf{s}_0 = [s_{0,1} \ \cdots \ s_{0,r}] \in \mathbb{C}^r$ , two sets of initial tangent directions  $\mathbf{b}_1, \dots, \mathbf{b}_r$  and  $\mathbf{c}_1, \dots, \mathbf{c}_r$ . Expansion points and tangent directions must be closed under complex conjugation.

**Ensure:**  $\mathbf{A}_r, \mathbf{B}_r, \mathbf{C}_r, \mathbf{E}_r$

- 1: **while** no convergence **do**
- 2:   Compute left and right interpolation bases

$$\mathbf{V} = \left[ (s_{0,1}\mathbf{E} - \mathbf{A})^{-1} \mathbf{B} \mathbf{b}_1 \ \cdots \ (s_{0,r}\mathbf{E} - \mathbf{A})^{-1} \mathbf{B} \mathbf{b}_r \right]$$

$$\mathbf{W} = \left[ (s_{0,1}\mathbf{E}^\top - \mathbf{A}^\top)^{-1} \mathbf{C}^\top \mathbf{c}_1 \ \cdots \ (s_{0,r}\mathbf{E}^\top - \mathbf{A}^\top)^{-1} \mathbf{C}^\top \mathbf{c}_r \right]$$

- 3:   Orthogonalize bases
- 4:    $\mathbf{A}_r = \mathbf{W}^\mathbf{H} \mathbf{A} \mathbf{V}$ ,  $\mathbf{E}_r = \mathbf{W}^\mathbf{H} \mathbf{E} \mathbf{V}$ ,  $\mathbf{B}_r = \mathbf{W}^\mathbf{H} \mathbf{B}$ ,  $\mathbf{C}_r = \mathbf{C} \mathbf{V}$
- 5:   Compute pole-residue expansion of  $\mathbf{H}_r(s)$ :

$$\mathbf{H}_r(s) = \mathbf{C}_r (s\mathbf{E}_r - \mathbf{A}_r)^{-1} \mathbf{B}_r = \sum_{i=1}^r \frac{\hat{\mathbf{c}}_i \hat{\mathbf{b}}_i^\top}{s - \lambda_i}$$

- 6:   Update expansion points and tangent directions  $\mathbf{s}_0 \leftarrow -\boldsymbol{\lambda}$ ,  $\mathbf{b} \leftarrow \hat{\mathbf{b}}$ ,  $\mathbf{c} \leftarrow \hat{\mathbf{c}}$
  - 7: **end while**
  - 8: Project system  $\mathbf{A}_r = \mathbf{W}^\mathbf{H} \mathbf{A} \mathbf{V}$ ,  $\mathbf{E}_r = \mathbf{W}^\mathbf{H} \mathbf{E} \mathbf{V}$ ,  $\mathbf{B}_r = \mathbf{W}^\mathbf{H} \mathbf{B}$ ,  $\mathbf{C}_r = \mathbf{C} \mathbf{V}$
- 

range  $2\pi i[1, \dots, 16\,000]$  Hz are used to start the iteration, which converged after 36 iterations under a tolerance of  $\varepsilon_{\text{tol}} = 1 \cdot 10^{-2}$ . Figure 3.6 shows the transfer functions of the original and reduced model and the relative approximation error. It can be seen, that the expansion points converge to the locations of the peaks in the transfer function, leading to a good approximation over nearly the complete considered frequency range.

To alleviate the issue of defining the reduced order a-priori, adaptive methods based on estimating the reduction error have been developed [63, 64, 81, 102, 109, 135, 221, 272]. The resulting reduced order is not predefined for these methods and they can therefore be used in settings, where the solution of the full system is not available. Error estimation methods are used in these iterative algorithms to measure the approximation quality of the current reduced model and either increase the interpolation order at an already established expansion point or add a new frequency shift to the global reduction basis. Typically, the only inputs required for such algorithms are a frequency range in which the resulting reduced model should be accurate as well as a desired error tolerance. A variety of error estimators has been established for different kinds of problems [80, 100, 108, 124, 202] which are often used in combination with a greedy scheme to find appropriate locations for expansion points. Here, the next interpolation point is chosen at the location where the approximation error

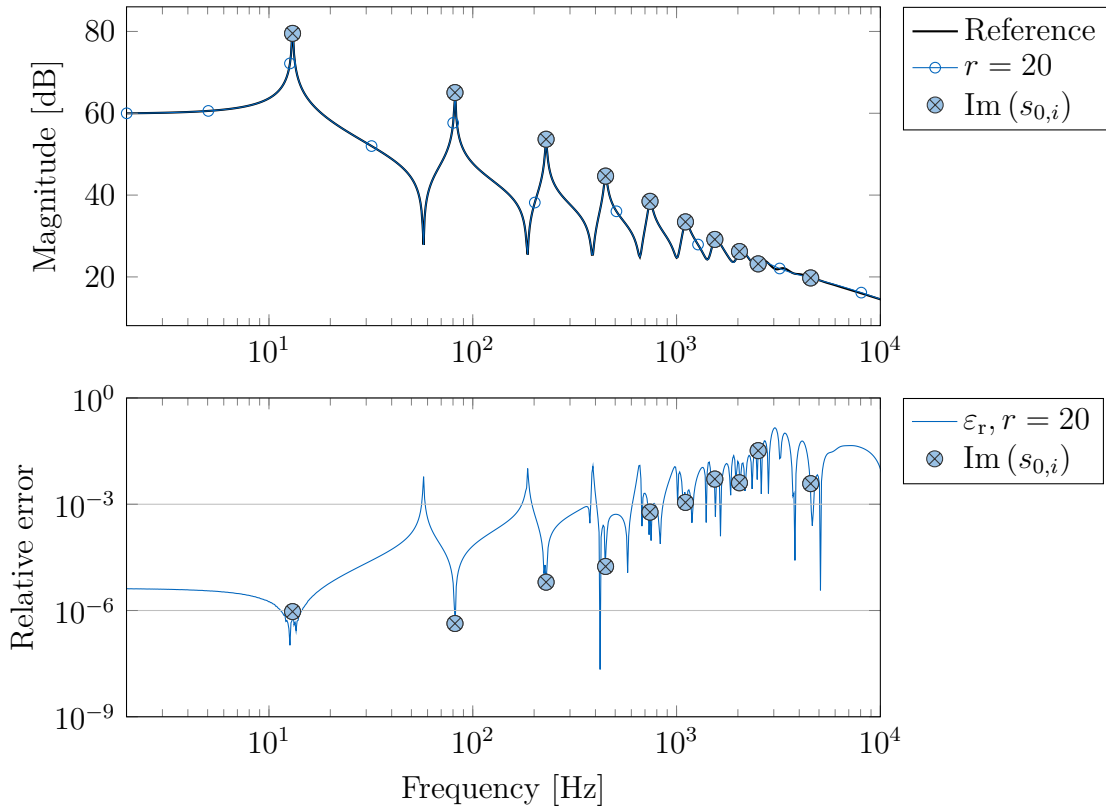


**Figure 3.6:** Transfer functions of the original and reduced models of order  $r = 20$  obtained from IRKA applied to the cantilever beam and the relative error. Convergence under a tolerance of  $\varepsilon_{\text{tol}} = 1 \cdot 10^{-2}$  was reached after 36 iterations. The locations of the expansion points are marked by circles.

is estimated to be maximal in a specific frequency range. Estimation methods suitable for second-order vibro-acoustic systems as well as adaptive algorithms relying on error estimation will be presented in detail in section 4.4.

A different take on ensuring a good approximation quality is based on oversampling. Here, the initial reduction basis is of intermediate size  $q > r$ , which is then reduced to the finally desired order  $r$ . This procedure relies on the estimation, that all important characteristics of the full model are captured in the intermediate model. Averaging this basis, for example using a pivoted QR decomposition, and then truncating it yields a reduced model of the desired size. It is also possible to recover representations of the controllability and observability subspaces from this larger subspace and thus finding a minimal realization of the original system [44]. The intermediate subspace can also be used to estimate the error of the reduced model. Computing the larger subspace yields transfer function evaluations at all considered frequency shifts. This result can be compared to the transfer function of a reduced model of desirable size and additional basis vectors can be added to the finalized reduction basis

using a greedy scheme. Here, the basis vectors corresponding to the shifts with the highest difference between the intermediate model's transfer function and the resulting model's transfer function are chosen to augment the reduction basis [4, 41]. Examples for strategies based on oversampling will be given in section 4.1.

### 3.6.3 Data-driven interpolatory model reduction

The Loewner framework is a data-driven method constructing a rational interpolant of a system's transfer function. The reduced model is computed solely utilizing system inputs and outputs, from which a Petrov-Galerkin projection as of eqs. (3.1) and (3.3) is obtained. As for POD or DMD, no realization of the original system is required; the method can be described as matrix-free. For a complete overview over the underlying theory, see e.g. [10, 12]; in the following, only the general procedure for data obtained from a SISO system will be outlined.

The basis of the technique is the Loewner matrix [180], which arranges two pairs of complex numbers  $(s_{0,i}, y_i)$ ,  $i = 1, \dots, k$  and  $(\sigma_{0,j}, z_j)$ ,  $j = 1, \dots, q$ , where all  $s_0$  and  $\sigma_0$  are distinct, in the Loewner matrix  $\mathbb{L} \in \mathbb{C}^{q \times r}$ . In this setting, given an underlying function  $\phi(s)$ , it holds  $y_i = \phi(s_{0,i})$  and  $z_j = \phi(\sigma_{0,j})$ . The Loewner matrix is given by

$$\mathbb{L} = \begin{bmatrix} \frac{z_1 - y_1}{\sigma_{0,1} - s_{0,1}} & \dots & \frac{z_1 - y_k}{\sigma_{0,1} - s_{0,k}} \\ \vdots & \ddots & \vdots \\ \frac{z_q - y_1}{\sigma_{0,q} - s_{0,1}} & \dots & \frac{z_q - y_k}{\sigma_{0,q} - s_{0,k}} \end{bmatrix}. \quad (3.49)$$

In the interpolatory model reduction context, the entries in the Loewner matrix are defined from sets  $\{s_{0,i}\}_{i=1}^r \subset \mathbb{C}$  and  $\{\sigma_{0,j}\}_{j=1}^q \subset \mathbb{C}$  of right and left interpolation frequencies producing right and left responses  $\{y_i\}_{i=1}^r \subset \mathbb{C}^m$  and  $\{z_j\}_{j=1}^q \subset \mathbb{C}^p$ . In a MIMO system, tangential directions  $\{f_i\}_{i=1}^r \subset \mathbb{C}^m$  respectively  $\{g_j\}_{j=1}^q \subset \mathbb{C}^p$  are again used to achieve tangential interpolation. The problem to be solved is to obtain a representation for the unknown underlying function  $\phi(s)$ , in this case the transfer function of the original system. In the Loewner framework the rational barycentric form

$$\phi(s) = \sum_{i=1}^k \frac{\alpha_i y_i}{s - s_{0,i}} \bigg/ \sum_{i=1}^k \frac{\alpha_i}{s - s_{0,i}} \quad (3.50)$$

is used because of its numerical stability. The unknown parameters  $\boldsymbol{\alpha} = [\alpha_1 \ \dots \ \alpha_r]$  are obtained from the null space of  $\mathbb{L}$ : due to the construction of the Loewner matrix, the equation  $\mathbb{L}\boldsymbol{\alpha} = 0$  has a nontrivial solution, yielding the unknown factors. Given enough

samples of the original transfer function, the rank of  $\mathbb{L}$  is equal to the McMillan degree of the interpolated function. This means, that the rank of  $\mathbb{L}$  encodes the minimal order of a surrogate representation interpolating the complete data used in the Loewner framework.

Instead of directly using the barycentric form (3.50), a realization of the interpolated system in terms of a state-space model in descriptor form can be obtained. It is given by

$$\mathbf{E} = -\mathbb{L}, \mathbf{A} = -\mathbb{L}_s, \mathbf{B} = \mathbf{z}, \mathbf{C} = \mathbf{y}, \quad (3.51)$$

where  $\mathbb{L}_s$  is the shifted Loewner matrix introduced by Mayo and Antoulas [180] and given by

$$\mathbb{L}_s = \begin{bmatrix} \frac{\sigma_{0,1}z_1 - y_1s_{0,1}}{\sigma_{0,1} - s_{0,1}} & \dots & \frac{\sigma_{0,1}z_1 - y_k s_{0,k}}{\sigma_{0,1} - s_{0,k}} \\ \vdots & \ddots & \vdots \\ \frac{\sigma_{0,q}z_q - y_1s_{0,1}}{\sigma_{0,q} - s_{0,1}} & \dots & \frac{\sigma_{0,q}z_q - y_k s_{0,k}}{\sigma_{0,q} - s_{0,k}} \end{bmatrix}. \quad (3.52)$$

No additional computations other than the partitioning in the Loewner matrices are required to obtain this realization. However, the Loewner matrix might be large, depending on the source and quantity of the data and also the McMillan degree of the underlying function might be too high to obtain a reasonably-sized reduced model. In this case, the extraction of the most relevant data might be necessary to obtain an efficient surrogate. Similarly to the POD, this can be performed using a singular value decomposition of the Loewner matrix and afterwards truncating all matrix columns associated to small singular values.

It is also possible to find structure-preserving realizations of systems with a higher order polynomial transfer function using Loewner matrices [233, 234]. This is especially interesting in cases where data is being continuously measured from a built structure. This data can be utilized to find a system representation of the original structure, which is typically second-order [3, 121]. As measurement data may be heavily influenced by noise, recent works propose methods to handle noisy input data in the Loewner framework [95, 122].

As an example, the Loewner framework is now used to find a realization of the beam model from section 2.5.1 given 800 measurements of its transfer function at discrete locations. As the data is coming from numerical evaluation of the transfer function, no noise has to be considered in this case. The reduced order  $r = 27$  is obtained by performing the SVD of the Loewner matrix eq. (3.49) and truncating all of its columns corresponding to singular values  $\sigma < 1 \cdot 10^{-8}$ . The resulting reduced model is able to approximate the original model over a wide frequency range containing most poles visible in the transfer function. In comparison a realization based on the McMillan degree obtained from  $\text{rank}(\mathbb{L}) = 357$  interpolates the

original transfer function in the complete frequency range and therefore shows a very low approximation error.

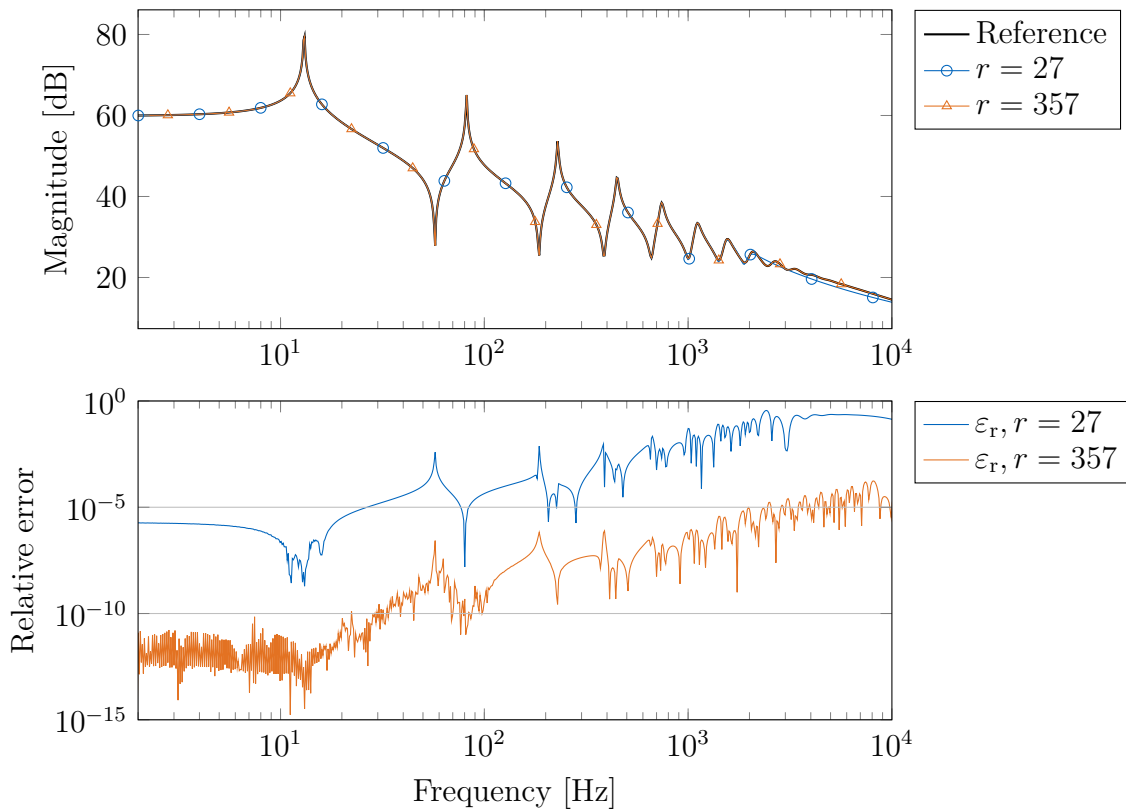


**Figure 3.7:** Transfer functions of the original and reduced models of order  $r = 27$  and  $r = 357$  obtained from the Loewner framework applied to the cantilever beam and the relative error.

### 3.7 Parametric model order reduction

For many problems in optimization, design, and control, multiple parameters need to be varied during the simulation process. Such parameters include, for example, material or geometrical properties or types of excitation. Standard reduced order models, as discussed in the preceding sections, are only valid for a specific set of parameters, so the reduction basis would need to be recomputed for every new parameter realization, which is typically not feasible. Therefore, methods for parametric model order reduction (PMOR) have been established, which preserve the dependency on chosen parameters in reduced space. A review over many methods used for PMOR is given by Benner, Gugercin, and Willcox [47]. A certain range of variation of these parameters is thus being represented by a single reduced model without the need to recompute the reduction basis. A second-order system depending on  $d$

parameters  $\mathbf{p} = [p_1 \ \cdots \ p_d]^\top$  is given by

$$\Sigma: \begin{cases} \mathbf{M}(\mathbf{p}) \ddot{\mathbf{x}}(t, \mathbf{p}) + \mathbf{C}(\mathbf{p}) \dot{\mathbf{x}}(t, \mathbf{p}) + \mathbf{K}(\mathbf{p}) \mathbf{x}(t, \mathbf{p}) = \mathbf{F}(\mathbf{p}) \check{\mathbf{u}}(t, \mathbf{p}), \\ \check{\mathbf{y}}(t, \mathbf{p}) = \mathbf{G}(\mathbf{p}) \mathbf{x}(t, \mathbf{p}), \end{cases} \quad (3.53)$$

for which a reduced system of the same shape is sought. To generalize the following considerations for different types of dynamical systems, we extend the generalized coprime factorization (3.30) to include a parameter dependence:

$$\mathbf{H}(s, \mathbf{p}) = \mathcal{G}(s, \mathbf{p}) \mathcal{K}(s, \mathbf{p})^{-1} \mathcal{F}(s, \mathbf{p}). \quad (3.54)$$

Consequently, the matrices for a second-order system are given by  $\mathcal{K}(s, \mathbf{p}) = s^2 \mathbf{K}(\mathbf{p}) + s \mathbf{C}(\mathbf{p}) + \mathbf{K}(\mathbf{p})$ ,  $\mathcal{F}(s, \mathbf{p}) = \mathbf{F}(\mathbf{p})$ , and  $\mathcal{G}(s, \mathbf{p}) = \mathbf{G}(\mathbf{p})$ . Again, we focus on projection based model order reduction, so a reduced system regarding the two reduction bases  $\mathbf{V}$ ,  $\mathbf{W}$  is obtained from

$$\mathcal{K}_r(s, \mathbf{p}) = \mathbf{W}^H \mathcal{K}(s, \mathbf{p}) \mathbf{V}, \quad \mathcal{F}_r(s, \mathbf{p}) = \mathbf{W}^H \mathcal{F}(s, \mathbf{p}), \quad \mathcal{G}_r(s, \mathbf{p}) = \mathcal{G}(s, \mathbf{p}) \mathbf{V}. \quad (3.55)$$

In order to obtain a reduced model for a specific parameter realization  $\mathbf{p}$ , the full order system matrices are required for this specific  $\mathbf{p}$  in the projection framework. This can be difficult to compute and may require a large amount of memory, so it is favorable to obtain an affine representation of the full order model. This describes the system with a combination of constant matrices and possibly nonlinear functions depending on the parameters

$$\begin{aligned} \mathcal{K}(s, \mathbf{p}) &= \mathcal{K}_0(s) + k_1(\mathbf{p}) \mathcal{K}_1(s) + \cdots + k_q(\mathbf{p}) \mathcal{K}_q(s), \\ \mathcal{F}(s, \mathbf{p}) &= \mathcal{F}_0(s) + f_1(\mathbf{p}) \mathcal{F}_1(s) + \cdots + f_q(\mathbf{p}) \mathcal{F}_q(s), \\ \mathcal{G}(s, \mathbf{p}) &= \mathcal{G}_0(s) + g_1(\mathbf{p}) \mathcal{G}_1(s) + \cdots + g_q(\mathbf{p}) \mathcal{G}_q(s). \end{aligned} \quad (3.56)$$

Here,  $k_i(\mathbf{p})$ ,  $f_i(\mathbf{p})$ ,  $g_i(\mathbf{p})$ ,  $i = 1, \dots, q$  are scalar valued, possibly nonlinear functions. Using such representation enables the computation of reduced quantities independent from  $\mathbf{p}$ . In order to build the parameter dependent matrices in reduced space only the scalar functions need to be evaluated and multiplied to the constant matrices. Consequently, the full scale matrices do not need to be assembled in the online phase and the reduced matrices can be reused for each new parameter. Although theoretically such an affine representation can be found for any system, a too large number  $q$  of affine parts is not efficient. In this case, the parameter dependence has to be considered as a black-box. The empirical interpolation method (EIM) [32] and its discrete form (DEIM) [75] can be applied here and find a parameter dependent reduced model [8]. Snapshots of the original system at certain realizations

of the parameters are required for the method. Subsequently, DEIM chooses which snapshots to include in the projection basis using a greedy method. The gappy POD, originally proposed for nonlinear model order reduction [97, 263], is also frequently used for black-box parametric model order reduction [47].

The considered methods to compute the reduction bases  $\mathbf{V}$ ,  $\mathbf{W}$  originate in some of the methods presented in the previous chapters and start by computing individual bases for each parameter sample. The parameter sampling performed in this step is crucial for the performance of the model order reduction. Full grid or Latin hypercube sampling is a classical choice for systems with a small or medium numbers of parameters but the computational costs can grow fast. If the parameter dependence is known to be smooth, sparse grids may be employed [118]. For more complex situations or a large parameter space ( $d > 10$ ), more sophisticated methods including adaptive schemes or techniques based on local sensitivity analysis have been proposed [70, 76, 140, 248]. Additionally, methods not depending on parameter sampling have been proposed. Here, the parameter dependent system is reformulated to a non-parametric system where the parameter influence is modeled as additional inputs to the system [34, 39, 255].

The individual projection subspaces obtained from parameter sampling can be either combined to one global basis or used in a local basis approach. For a global basis, the individual projection matrices are collected in global left and right projection matrices. As the individual bases might contain redundant information, an orthogonalization procedure is applied. The size of this basis and thus the reduced model can grow fast if many parameters need to be considered. In case an interpolative method has been used to construct the individual bases, the resulting reduced model interpolates the full solution at all combinations of frequency and parameter values which were used for the sampling process. PMOR procedures following this global approach have been presented, for example, in [35, 43, 89]. A global basis can also be computed by concatenating individual bases obtained from a balancing method. The resulting reduced model is, however, not necessarily balanced, even for the parameter values used for generating the individual bases [47]. A related approach is to interpolate between the local bases, respectively on a manifold of their subspaces [7, 65]. Here, the resulting projection basis has the same size as the original basis. Using both local and global methods requires the projection step to be computed for each new parameter realization, if no affine parameter decomposition is available. To overcome this, methods to directly interpolate the reduced matrices, rather than the projection bases, have been established [93, 201]. If large amounts of transfer function measurements of a parametric system are available, directly interpolating these transfer functions yields surrogates for the full order model. Ionita and Antoulas [143] introduced an extension to the Loewner framework being able to interpolate parametrized transfer functions. This method will be outlined in more detail in section 5.1.

Combining reduced parametric models with different fidelity, so called multifidelity approaches can be an efficient way to evaluate parametric systems, especially in settings where uncertain parameters have to be considered. Peherstorfer, Willcox, and Gunzburger [206] give an overview over techniques applicable for such cases.

---

## 4 Model order reduction for vibro-acoustic systems

The model order reduction methods presented in the previous chapter are directly applicable to a wide range of vibro-acoustic problems, if their transfer function has a standard second-order structure. A modification of the methods is, however, required if frequency dependent input or system matrices have to be considered. Additionally, strategies to choose appropriate locations for expansion points and to determine a reasonable size for the reduced models are required, especially if the solution of the full order system is not known prior to the reduction process. The following chapter addresses some open issues in model order reduction of vibro-acoustic systems. After giving an overview over the applicability of the state-of-the-art methods described in chapter 3 to different types of vibro-acoustic systems in section 4.1, a method to compute reduced models for systems with frequency dependent system matrices is presented in section 4.2. Techniques to obtain surrogate models only valid in a specific frequency region, which is often desirable in vibro-acoustics, are presented in section 4.3. Section 4.4 concludes the chapter with strategies assessing the reduction error and automatically finding reduced order models requiring as less a-priori knowledge as possible.

### 4.1 Applicability of model order reduction methods

The performance of the model order reduction methods described in chapter 3 is in the following assessed using the MORscore presented in section 3.2. The model problems defined in section 2.5 are used as application examples, so the applicability of the reduction methods to various types of vibro-acoustic problems is discussed. The following section is based on Aumann and Werner: “Structured model order reduction for vibro-acoustic problems using interpolation and balancing methods” (2022) [25]. Alternative surveys assessing the applicability of model order reduction methods to vibrating structural systems are, for example, available in [41, 57, 226]. Hetmaniuk, Tezaur, and Farhat [134] presented a survey specifically targeting vibro-acoustic systems, where the structure-preserving method

from section 3.6 has been used to reduce a system with frequency dependent input. Modal based reduction methods for vibro-acoustic problems with frequency dependent system matrices, including, for example, complex damping measures or radiating boundary conditions are summarized in [220]. The authors of [254, 270, 272] employ Krylov subspace methods for these kinds of problems. A different approach to moment matching is the so called well-conditioned asymptotic waveform evaluation (WCAWE) introduced by Slone, Lee, and Lee [239], which matches moments of polynomial systems without the need for a linearization. The methodology is similar to the moment matching strategy based on the generalized coprime realization shown in section 3.6. The WCAWE has been applied to vibro-acoustic problems including radiating boundary conditions in [162] and poroelastic models in [221, 223].

In the following study, we use the models presented in section 2.5 and compare their applicability and performance regarding the following structure preserving methods:

- *equi*: Structure preserving interpolation without considering derivatives of the moments, i.e. an interpolation order of  $r_0 = 1$  at each expansion point. The interpolation points are distributed linearly along the imaginary axis between  $i\omega_{min}$  and  $i\omega_{max}$ .  $\omega_{min}$  and  $\omega_{max}$  denote the frequency range of interest, which is specified for each model individually. If required, the initial distribution is augmented by interpolation points at locations having a large impact on the system's frequency response.
- *avg*: An intermediate basis with order  $q > r$  is precomputed and orthogonalized for this method. This medium sized interpolation basis is then truncated to the desired order  $r$ , averaging the large reduction space to obtain the reduction space of desired size. The expansion points for the large space are distributed linearly in the frequency range of interest but can be modified similar to *equi*.
- $\mathcal{L}_\infty$ : This algorithm chooses a subset of interpolation points from a larger presampled database in order to minimize the approximation error of the resulting reduced model in the frequency range of interest. Expansion points are subsequently added during the procedure at the location where the difference between the original transfer function and the transfer function of the current reduced model is at a maximum. For this, the transfer function evaluations at each interpolation point in present in the presampling basis is saved to be able to perform the optimization step with reasonable computational effort. The method is described in detail in [41].
- *minrel*: This method follows [44] and aims at computing a minimal realization of the original dynamical system. Again, an intermediate reduction basis of order  $q > r$  is

computed in a first step. The dominant subspaces of this reduction space are determined using a singular value decomposition. Subsequently, the parts of the intermediate basis with less dominance are truncated to obtain the final projection space of order  $r$ .

- *SO-BT*: The balanced truncation methods as presented in section 3.5 with the according truncation formulas given in table 3.1.
- *POD*: A proper orthogonal decomposition according to section 3.4. The snapshot matrix is filled with  $q$  samples of the frequency response of the corresponding system obtained at linearly distributed locations in the frequency range of interest.

The methods *avg*,  $\mathcal{L}_\infty$ , *minrel*, and *POD* require a presampling step in which a reduction basis of order  $q > r$  and the evaluation of the transfer function at the expansion points are computed before applying the reduction method. The locations of the expansion points are linearly distributed in the frequency range of interest for all following methods and additional shifts may be introduced in order to capture the original system's behavior for the complete transfer function. We apply three different approaches to compute this database for *avg*,  $\mathcal{L}_\infty$ , and *minrel* in the following experiments:

- For the standard method, no derivatives at the expansion points are considered and the presampling basis is computed in the same way as described for *equi*; this basis is also used for *POD*. The transfer function evaluations required for  $\mathcal{L}_\infty$  can be computed in the same step. Thus,  $q$  solutions of a linear equation system of order  $n$  are required for each presampling basis  $\mathbf{V}$  and  $\mathbf{W}$ .
- *sp*: This presampling method is based on the structure preserving interpolation scheme summarized in section 3.6 and considers the series expansion factors of the transfer function as presented in [37]. It computes multiple columns of the presampling basis in the same step, so less than  $q$  linear systems of equations have to be solved for a basis of order  $q$ . For each expansion point the recursive formulation (3.41) is used with an interpolation order  $r_0 = 3$  at each frequency shift. This is the lowest interpolation order allowing a recursion for a second-order system without dropping any polynomial terms.
- *soa*: This method uses higher interpolation orders  $r_0$ , individually set for each model problem. The method's name refers to the second-order Arnoldi method from [171], summarized in section 3.6.1, which is used to obtain the projection bases. Again, less than  $q$  linear systems of equations have to be solved for each projection basis, as multiple columns are computed from the same matrix decomposition.

The presampling methods *sp* and *soa* leverage the computational costs of computing the initial basis, as only  $\frac{q}{r_0}$  factorizations of the full order system are required. This may of course also lead to an intermediate basis containing less information about the dynamic behavior of the original system. Note, that the order of models reduced with  $\mathcal{L}_\infty$  is always a factor of  $r_0$  as all columns associated with the chosen shift are selected for the reduction basis. The nonlinear frequency dependent contributions arising in *Case C* systems, for example the coupled poroacoustic system, cannot straightforwardly be treated in *sp* and *soa*, as the required expansion factors cannot directly be obtained. Therefore, these presampling strategies are not considered for now. A strategy to include also non-polynomial frequency dependencies is introduced in section 4.2. *sp* and *soa* are not applicable to compute a presampling basis for *POD*.

We compare different projections to assess the controllability and observability of the various systems. Apart from the double-sided projection, we also consider one-sided projections regarding the system input and output respectively. The input projection is obtained by setting  $\mathbf{W} = \mathbf{V}$ , the output projection by setting  $\mathbf{V} = \mathbf{W}$ . Where applicable, we also compare complex and real valued projection bases. A real valued basis is obtained from the initial complex valued basis by  $\mathbf{V} = [\text{Re}(\mathbf{V}), \text{Im}(\mathbf{V})]$  and  $\mathbf{W} = [\text{Re}(\mathbf{W}), \text{Im}(\mathbf{W})]$ , thus having a dimension of  $2r$ . The considered projections are:

- *tsimag*: Double-sided projection  $\mathbf{W} \neq \mathbf{V}$  with  $\mathbf{V}, \mathbf{W} \in \mathbb{C}^{n \times r}$
- *tsreal*: Double-sided projection  $\mathbf{W} \neq \mathbf{V}$  with  $\mathbf{V}, \mathbf{W} \in \mathbb{R}^{n \times 2r}$
- *osimaginput*: Single-sided projection  $\mathbf{W} = \mathbf{V}$  with  $\mathbf{V}, \mathbf{W} \in \mathbb{C}^{n \times r}$
- *osrealinput*: Single-sided projection  $\mathbf{W} = \mathbf{V}$  with  $\mathbf{V}, \mathbf{W} \in \mathbb{R}^{n \times 2r}$
- *osimagoutput*: Single-sided projection  $\mathbf{V} = \mathbf{W}$  with  $\mathbf{V}, \mathbf{W} \in \mathbb{C}^{n \times r}$
- *osrealoutput*: Single-sided projection  $\mathbf{V} = \mathbf{W}$  with  $\mathbf{V}, \mathbf{W} \in \mathbb{R}^{n \times 2r}$

To allow a one-sided projection regarding the system input for *SO-BT*, only the controllability Gramian is computed and is used as the left and right projection matrices in orthogonalized and truncated form. A one-sided projection regarding the system output is analogously possible by computing the observability Gramian. No real valued bases are considered for *SO-BT*. Only *osimaginput* is applicable for *POD*, as the snapshots are obtained from measurements of the transfer function given a specific input.

For the following computations of the MORscore, we approximate the relative error under

the  $\mathcal{L}_\infty$ -norm via

$$\varepsilon(r) = \frac{\max_{\omega \in [\omega_{\min}, \omega_{\max}]} \|H(\omega \mathbf{i}) - H_r(\omega \mathbf{i})\|_2}{\max_{\omega \in [\omega_{\min}, \omega_{\max}]} \|H(\omega \mathbf{i})\|_2} \approx \frac{\|H - H_r\|_{\mathcal{L}_\infty}}{\|H\|_{\mathcal{L}_\infty}}, \quad (4.1)$$

where  $H_r$  is the transfer function of a reduced-order model of size  $r$ . For simplicity, the errors are denoted with the  $\mathcal{L}_\infty$ -norm in the plots.

### 4.1.1 Structural vibration

The vibrating plate equipped with tuned vibration absorbers (TVA) described in section 2.5.2 is considered in the following. Two models using proportional damping respectively hysteretic damping are reduced using the methods described above. *SO-BT* is not applicable to the hysteretically damped model, because  $\mathbf{C} = 0$  in this system. The standard presampling for *minrel*, *avg*, and  $\mathcal{L}_\infty$  is conducted with  $n_s = 250$  frequency shifts distributed linearly in  $s = 2\pi \mathbf{i} [1, \dots, 250]$ . As the models are described by standard second-order transfer functions, *sp* yields three columns for each shift. Using  $n_s = 80$  shifts linearly distributed in the same range and augmented by shifts at  $s = 2\pi \mathbf{i} [46, 47, 48, 50]$  results in the intermediate reduction basis with  $r = 252$ . The additional shifts were introduced because the behavior near the tuning frequency of the TVAs is very local and can only be captured by shifts in this frequency region. For *soa* presampling a local order of  $r_0 = 10$  is chosen for each of the  $n_s = 21$  shifts linearly distributed in  $s = 2\pi \mathbf{i} [1, \dots, 250]$  and four additional shifts at  $s = 2\pi \mathbf{i} [46, 47, 48, 50]$ . This again yields an intermediate reduction basis of order  $r = 250$ . Because of the high impact of the TVA on the transfer function near its tuning frequency the expansion points sampling for *equi* is modified similarly to the presampling methods. The shifts at  $s = 2\pi \mathbf{i} [46, 47, 48, 49, 50]$  are always considered, the location of the remaining shifts are linearly distributed in the frequency range of interest. For orders  $r < 5$  only the first  $r$  extra shifts are considered.

All methods are able to compute reasonably accurate models of the hysteretically damped model, their MORscore referenced to  $\varepsilon_{\text{ref}} = 1 \cdot 10^{-6}$  is given in fig. 4.1. The tolerance is chosen higher than  $\varepsilon_{\text{ref}} = 1 \cdot 10^{-16}$  because the relative approximation error does not drop below  $1 \cdot 10^{-3}$  for any employed method and the MORscore for the individual methods would therefore be too close to each other to allow proper comparisons. The projections with complex valued bases yield very good results for all reduction methods, only  $\mathcal{L}_\infty$  *soa* falls short. It has to be noted, that all reduced models computed from a *soa* presampling need a higher reduced order  $r$  to be as accurate as the other presampling methods. This is because only 25 shifts and their derivatives are present in the reduction basis, as opposed to 250 and

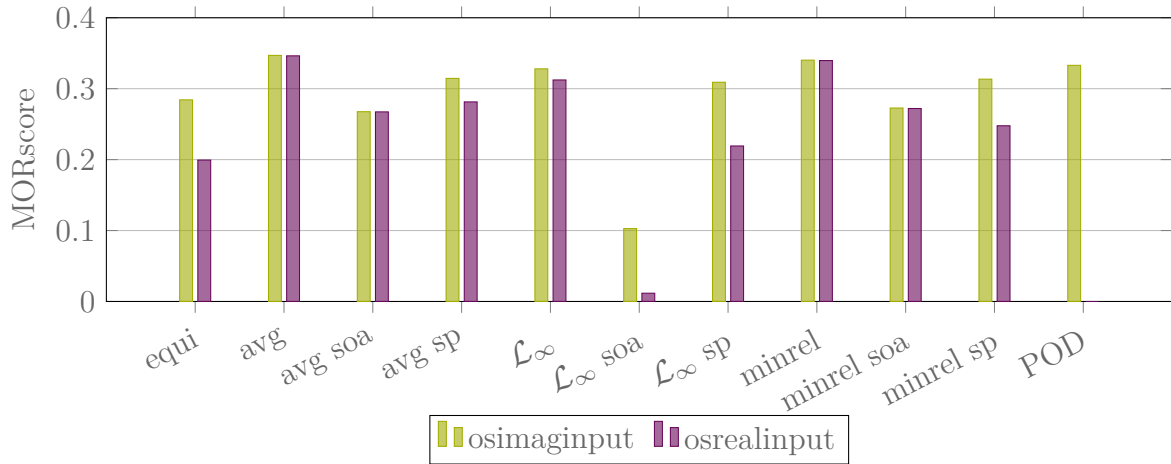


**Figure 4.1:** MORscore  $\mu(250; 10^{-6})$  of all employed reduction and projection methods for the plate with hysteretic damping.

84 respectively.

Using  $\mathcal{L}_\infty$  in combination with *soa*, the order of the reduced models is increased in steps of 10, which is the chosen size of the second-order Krylov subspaces employed. Therefore, a larger reduced model is constructed as compared to the other methods, but less computational effort is required in the presampling process. Figure 4.2 shows the  $\mathcal{H}_\infty$  norm of the relative errors plotted over the reduced order  $r$ . It can be seen, that all methods including  $\mathcal{L}_\infty$  *soa* are able to compute reduced models with the same accuracy given a large enough reduced order  $r$ . A characteristic drop in the error norm can be observed for most methods. This originates from the effect of the employed TVAs which have a local but considerable influence on the transfer function at their specific tuning frequency of  $f = 48$  Hz. A good approximation quality can only be achieved, if this behavior is depicted accurately by the reduced model.

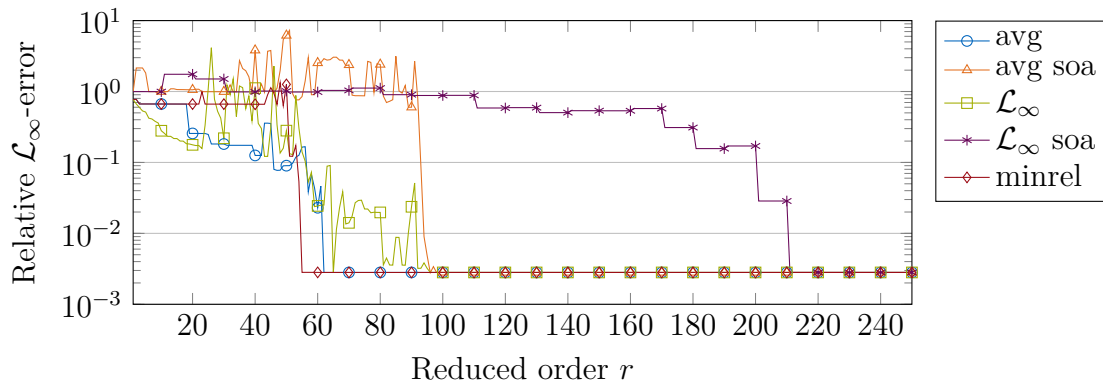


**Figure 4.2:** Relative  $\mathcal{L}_\infty$ -error for reduced models of the plate model with hysteretic damping computed by several reduction methods and *osimagination* projection.

Applying the reduction methods on the proportionally damped model yields models with

on overall better accuracy compared to the model with hysteretic damping, as there are less only slightly damped poles in the transfer function. Because of this, the tolerance for computing the MORscore is not modified and set to  $\varepsilon_{\text{ref}} = 1 \cdot 10^{-16}$ . The MORscore for each employed method is given in fig. 4.3. Especially *avg*,  $\mathcal{L}_\infty$ , and *minrel* using the standard presampling method yield good results, while the models computed from *soa* and *sp* presampling have a slightly lower MORscore. Given the lower computational cost for computing the presampling basis, especially for *soa*, the accuracy is still acceptable. Only  $\mathcal{L}_\infty$  *soa* yields considerably less accurate models.

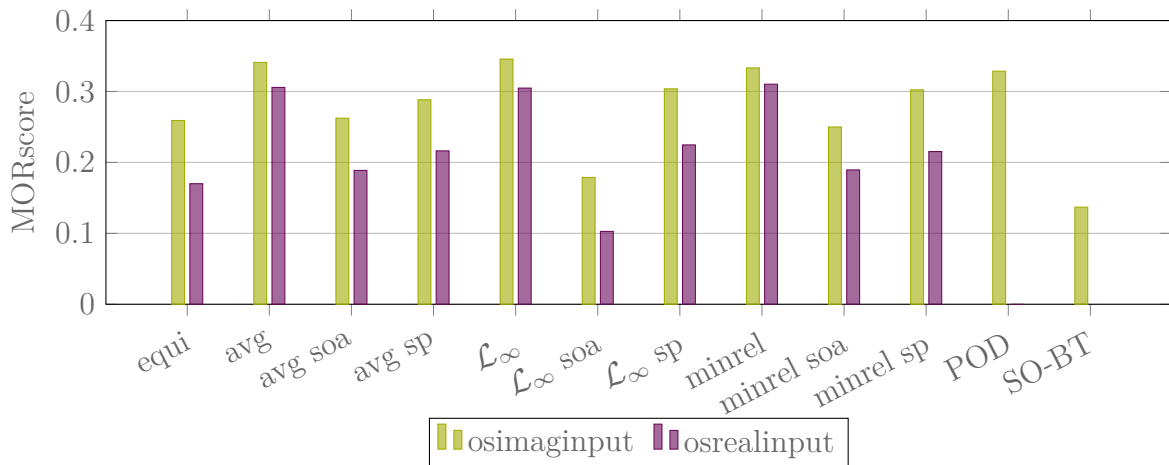


**Figure 4.3:** MORscore  $\mu(250; 10^{-16})$  of all employed reduction and projection methods for the proportionally damped plate.

It can be seen in the error-over-order plot fig. 4.4, that the reduced model computed by  $\mathcal{L}_\infty$  *soa* reaches the error level of the other methods for a reduced order  $r = 250$ . The lower MORscore is thus also influenced by the fact, that the order  $r$  is incremented in steps of  $r_0 = 10$  for  $\mathcal{L}_\infty$  *soa*. It is also observable, that *avg*,  $\mathcal{L}_\infty$ , and *minrel* show a very similar behavior depending on their presampling method. Using the classic presampling, the best achievable accuracy can be reached with reduced models of order around  $r = 60$ , models computed from *sp* presampling require  $r = 90$ , and using *soa* yields comparable accuracy for models larger than  $r = 100$ . Of course  $\mathcal{L}_\infty$  *soa* required a larger reduced order  $r$ , because  $r$  is a multiple of  $r_0 = 10$  for this model. The other two models computed with *soa*, however, are comparable to *equi*, so the presampling subspace computed by *soa* is able to capture the most important features of the original system's transfer function. The reduced model computed with the one-sided *SO-BT* does not reach the accuracy of the other methods and stagnates for  $r \geq 160$ .

The reason for the stagnation of the approximation error of reduced models computed by  $\mathcal{L}_\infty$  *soa* can be observed in the error plot fig. 4.5. The relatively high error in the region of the tuning frequency of the TVA at  $f = 48$  Hz is present up to models with  $r = 240$ . At

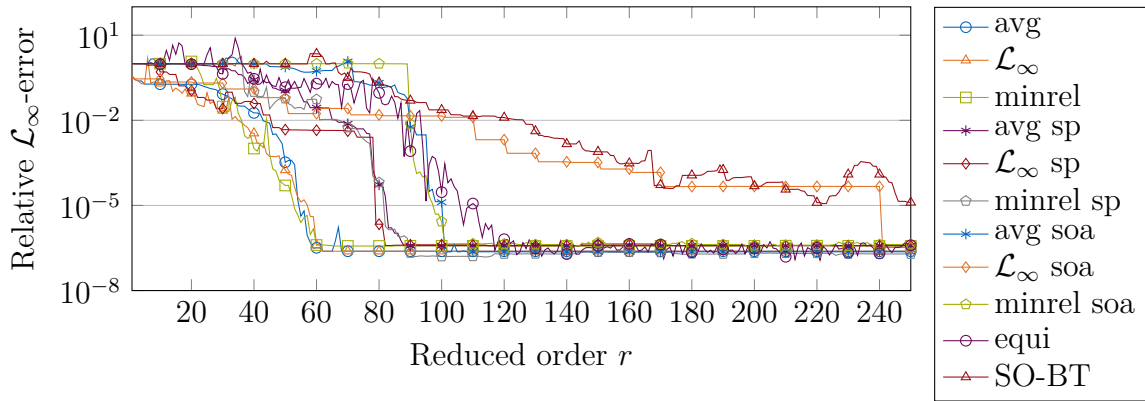


**Figure 4.4:** Relative  $\mathcal{L}_\infty$ -error for reduced models of the plate model with proportional damping computed by several reduction methods with *osimainput* projection. Note the similar performance of *avg*,  $\mathcal{L}_\infty$ , and *minrel* based on the employed presampling method.

$r = 250$ ,  $\mathcal{L}_\infty$  selects the shift and corresponding subspace, which contains enough information to approximate the original transfer function also in the region around  $f = 48$  Hz and the error drops to the level of the models computed using the other reduction methods.

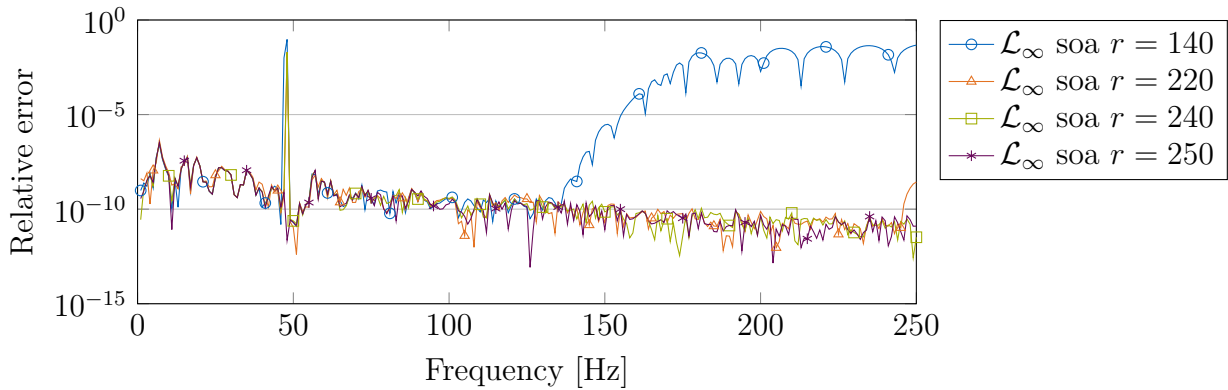


**Figure 4.5:** Comparison of original and reduced transfer functions as well as relative errors for reduced models of the proportionally damped plate computed by  $\mathcal{L}_\infty$  *soa*. The error peak near the tuning frequency of the TVA at  $f = 48$  Hz is clearly visible.

In order to compare the different formulas for *SO-BT* given in table 3.1, a slightly modified model of the proportionally damped plate is considered. Here, the displacement at the loading point is evaluated rather than the mean displacement at the surface of the plate. The result is obtained with a vector  $\mathbf{g} \in \mathbb{R}^n$  instead of a matrix, allowing the computation of a left projection basis  $\mathbf{W}$  in reasonable time. The corresponding transfer function is given in fig. 4.6. Additionally, the transfer functions of the reduced models computed using *SO-BT* and its various truncation formulas and the corresponding relative errors are reported therein. All formulas presented in table 3.1 yield reasonably accurate reduced models. Similar to the results above, the very local effect of the TVAs around  $f = 48$  Hz cannot easily be captured by the reduction method, resulting in a relatively high error in this frequency region even

for a reduced order of  $r = 250$ . *SO-BT so* produces a model with slightly higher error than the other formulas.

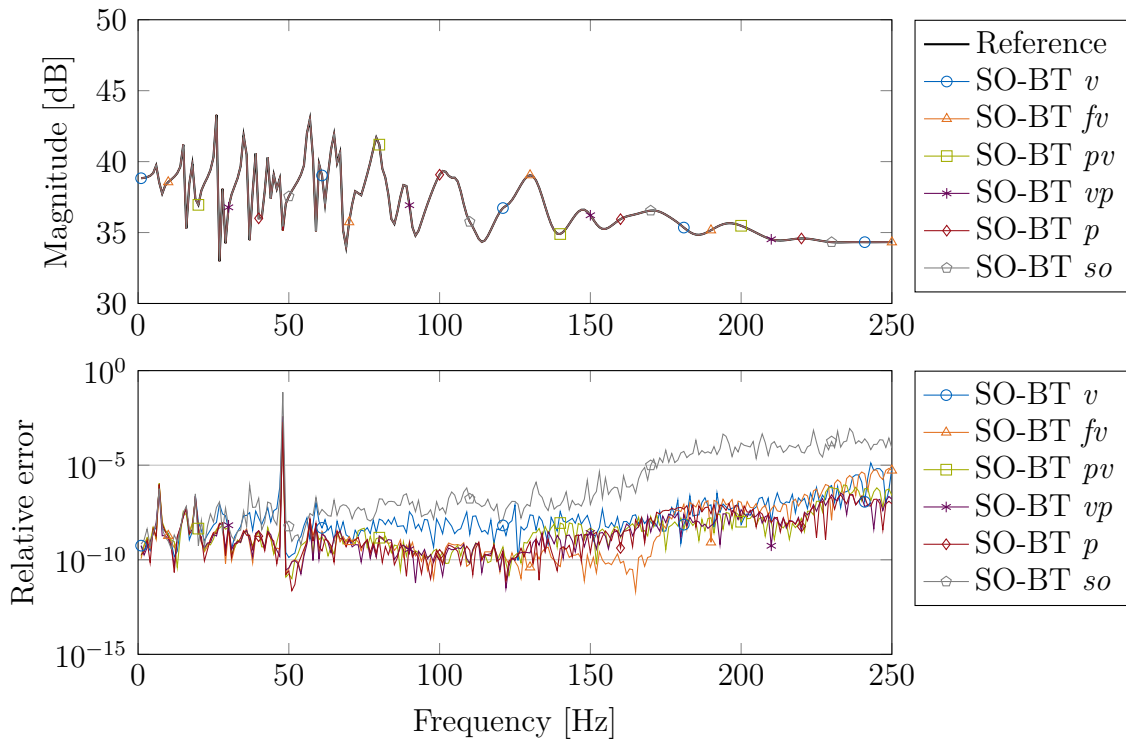


**Figure 4.6:** Original and reduced transfer functions as well as relative errors for the proportionally damped plate with a single output and order  $r = 250$ . Comparison of the *SO-BT* formulas. All reduced models have their approximation error maximum around the tuning frequency of the TVA ( $f = 48$  Hz).

Additionally, all other methods have been used to compute reduced models and their MORscore is given in fig. 4.7. The results are very similar to the ones reported above: all methods produce accurate reduced models. However,  $\mathcal{L}_\infty soa$  has a lower MORscore, as the  $r$  is incremented in steps of  $r_0 = 10$ . All reduced models capture the transfer function in the critical region around  $f = 48$  Hz for large enough reduced orders. As the displacement at the loading point is evaluated in the transfer function, i.e. input and output vectors are identical, a two-sided projection does not yield a benefit and *tsimag*, *osimaginput*, and *osimagoutput* show nearly the same MORscore for each reduction method. It has to be noted, that *avg* and *minrel* with classical presampling yield very similar results for complex and real valued projection bases.

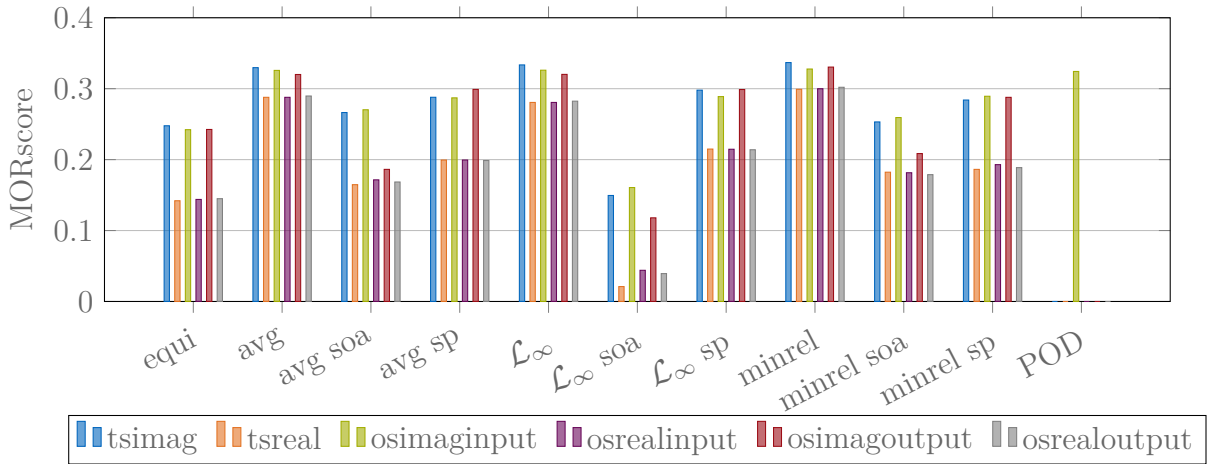


**Figure 4.7:** MORscore  $\mu(250; 10^{-16})$  of all employed reduction and projection methods for the proportionally damped plate with a single output.

### 4.1.2 Sound transmission

The sound transmission problem described in section 2.5.3 is assessed regarding the applicability of the reduction techniques described at the beginning of the section. The presampling for *minrel*, *avg*, and  $\mathcal{L}_\infty$  was conducted with  $n_s = 200$  frequency shifts distributed linearly in  $s = 2\pi i [1, \dots, 1000]$ . As the quadratic frequency associated with the mass matrix is the highest order of  $s$  in the transfer function, each shift computed by *sp* contributes three columns to the presampling basis.  $n_s = 67$  shifts, also linearly distributed in the frequency range, are chosen such that the global reduction basis is of size  $r = 201$ . For *soa*, a local order  $r_0 = 10$  along with  $n_s = 20$  is chosen, yielding an intermediate reduction basis of order  $r = 200$ . Because the numerical model has unstable eigenvalues, the required Gramians for *SO-BT* could not be computed.

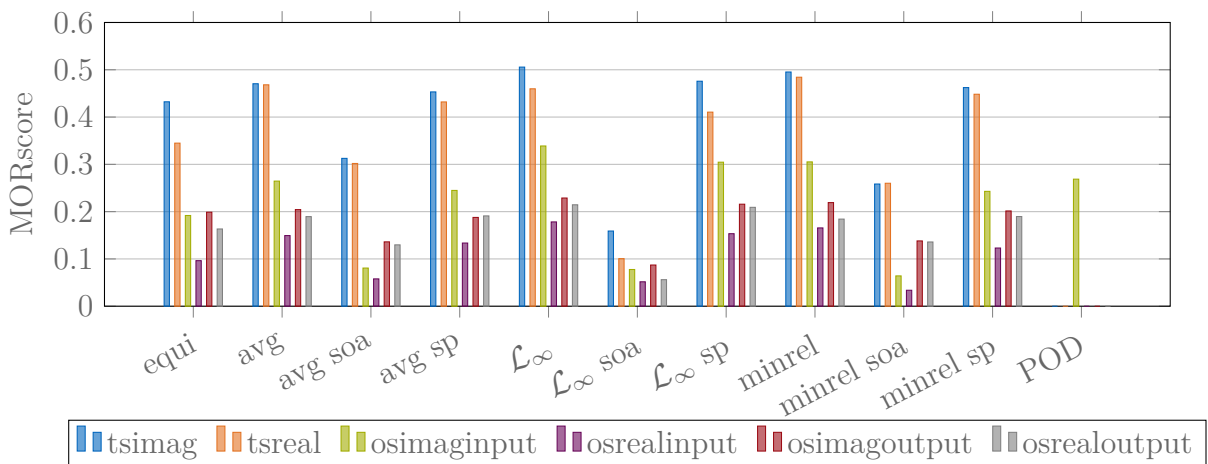


**Figure 4.8:** MORscore  $\mu(100; 10^{-16})$  of all employed reduction and projection methods for the sound transmission problem.

The MORscore given in fig. 4.8 shows, that especially the two-sided projections yield very good results with the highest MORscore observed in all experiments reported in this study. As expected,  $\mathcal{L}_\infty$  *soa* falls a bit short due to the reduced order being incremented in steps of 10. But also *avg soa* and *minrel soa* perform not as good as the other methods, while still showing a MORscore  $\mu > 0.3$  referenced to  $\varepsilon_{\text{ref}} = 1 \cdot 10^{-16}$ , which is comparable to the other models. It can be seen, that using only input or output based projection has a significant impact on approximation quality. The error comparisons in fig. 4.9 show, that the approximation error of the one-sided projections stagnates at around  $1 \cdot 10^{-5}$ , while the two-sided projections yield models with much better accuracy. As expected, the real valued projection requires a higher reduced order  $r$  but also results in models of comparable accuracy for higher  $r$ .

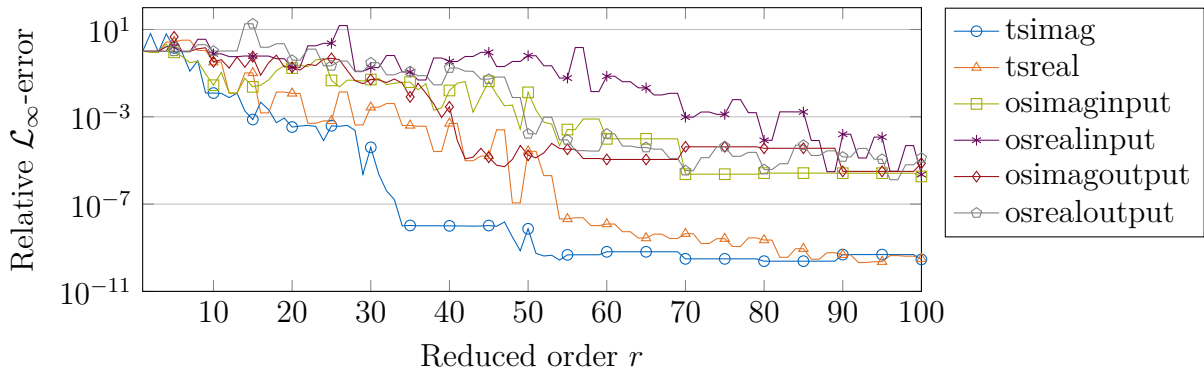


**Figure 4.9:** Comparison of the relative  $\mathcal{L}_\infty$ -error for reduced models of the sound transmission problem computed by *equi* using different projections. While the two-sided projections reach very low approximation errors, the approximation error of the models computed with one-sided projection stagnates at a higher level.

### 4.1.3 Acoustic scattering

The acoustic scattering problem described in section 2.5.4 is considered a *Case B* problem because of its excitation and is in the following assessed regarding the applicability of the reduction methods. The presampling was conducted with  $n_s = 200$  frequency shifts distributed linearly in  $s = 2\pi i [1, \dots, 600]$ . Again, *sp* yields three columns for the intermediate reduction basis, so  $n_s = 67$  linearly distributed shifts are chosen to obtain a basis of size  $r = 201$ . For *soa*, a local order  $r_0 = 5$  is chosen, so the  $n_s = 40$  expansion points yield again a presampling basis with order  $r = 200$ . *SO-BT* is not applicable to this problem because of its frequency dependent input vector.

The MORscore for each applied reduction method is given in fig. 4.10 and it can be seen, that again a two-sided interpolation with complex valued bases outperforms the other projection methods. Also in line with the observations from the other models is the lower

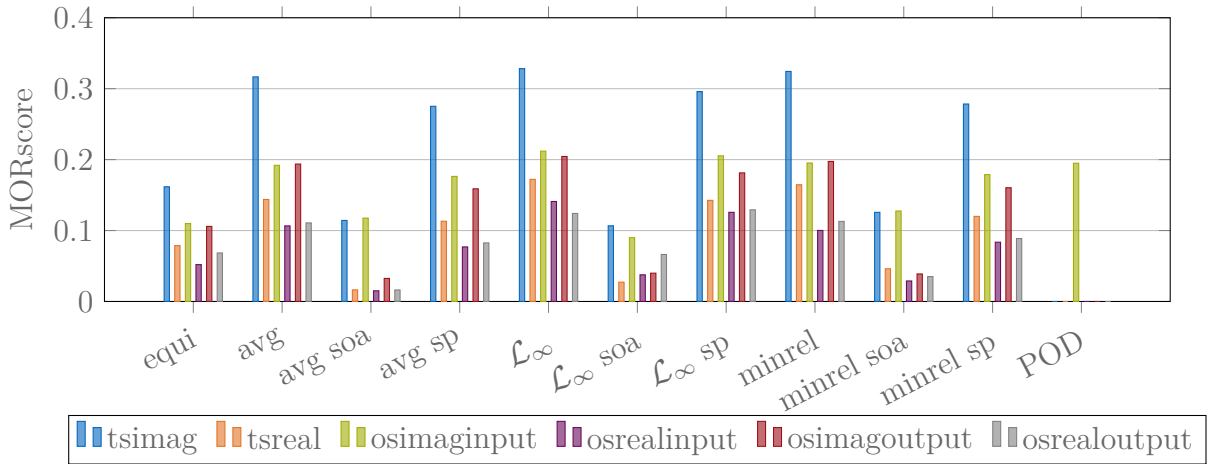


**Figure 4.10:** MORscore  $\mu(200; 10^{-16})$  of all employed reduction and projection methods for the scattering problem.

rate of approximation when using *soa*. Additionally, the local order  $k$  of the second-order Krylov space employed in *soa* was reduced compared to the other experiments, as there are many individual modes present in the transfer function. *equi* shows also a worse performance than the other methods. It can be seen in the error-over-order plot fig. 4.11, that the error stagnates until approximately  $r = 140$  before it drops to the same level as the other methods. This suggests, that important feature of the system response have not been captured by the smaller reduction bases. The oscillating behavior of the relative error in the region of  $150 < r < 190$  is a sign that crucial parts of the transfer function are missed by sampling with equidistantly distributed expansion points. This is supported by the relative errors in fig. 4.12. Here, the error over frequency for reduced models computed by *equi* with order  $r = 140$  and  $r = 200$  are plotted. While the larger reduced model shows a very low error over the complete frequency range, more information from the frequency region above 450 Hz than is available in the smaller model is required in the reduction basis for a proper approximation of the original system. It is, however, also apparent, that the approximation quality for all methods is better in the lower frequency range, presumably because of a large number of modes in the higher frequency region. If this is known a-priori, the locations of the expansion points can be altered appropriately. If this is not possible, the methods *avg*,  $\mathcal{L}_\infty$ , and *minrel* show their benefit. At the cost of computing a larger intermediate reduction basis, the most relevant information from this basis is chosen, allowing smaller reduced models with better accuracy.

The error graph for *avg soa tsimag* in fig. 4.12 shows characteristic spikes at the locations of the expansion points in the presampling basis. This suggests that the employed second-order Krylov subspace does not contain enough information to enable an as accurate approximation as the other presampling methods. A remedy would be to increase the local

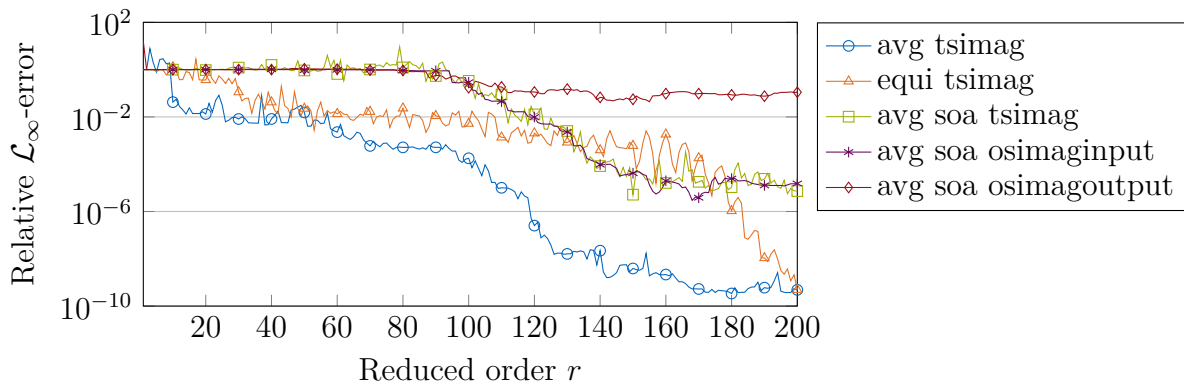


**Figure 4.11:** Relative  $\mathcal{L}_\infty$ -error for reduced models of the acoustic scattering problem computed by several reduction methods. *equi* requires many expansion points until it reaches a comparable error level as *avg*, which performs best, at around  $r = 200$ . The presampling basis for *soa* does not contain enough information to allow a comparable relative error.

order  $k$ , which would in turn increase the size of the presampling subspace. Increasing  $k$  is up to a certain bound less computationally expensive than establishing a completely new shift. Projection regarding the system output using a *soa* presampling, however, does not yield a good approximation of the original system at all.

#### 4.1.4 Coupled poroacoustic system

The system modeling the acoustic cavity equipped with two poroelastic materials described in section 2.5.5 is considered in the following. Because of the frequency dependency in the system matrices, the presampling methods *sp* and *soa* are not applicable; neither is *SO-BT*. The presampling for *minrel*, *avg*, and  $\mathcal{L}_\infty$  is conducted with  $n_s = 200$  frequency shifts distributed linearly in the frequency region  $s = 2\pi i [1, \dots, 800]$ . The snapshot matrix for *POD* consists out of frequency responses at  $n_s = 200$  frequency locations distributed linearly in the same frequency region.

The MORscore reported for all employed methods in fig. 4.13 shows a high approximation quality for all reduction methods with a MORscore  $\mu > 0.4$  for many methods. *equi* converges a bit slower thus showing a lower MORscore; it reaches a similar error level as the presampling methods for reduced orders higher than  $r = 180$ , suggesting that this is an appropriate size for the presampling basis. The corresponding relative  $\mathcal{H}_\infty$  errors over the reduced order for all employed reduction methods is given in fig. 4.14. The oscillations in the errors for *minrel*, *avg*, and  $\mathcal{L}_\infty$  at higher reduced orders are the result of an ill-conditioning of the reduced models. Ill-conditioned matrices have also been observed for *equi* for reduced orders  $r > 140$ . The errors for *POD* are slightly higher than the other methods, as only input information is available in the snapshot basis. Comparing the MORscore for all *osimainput*

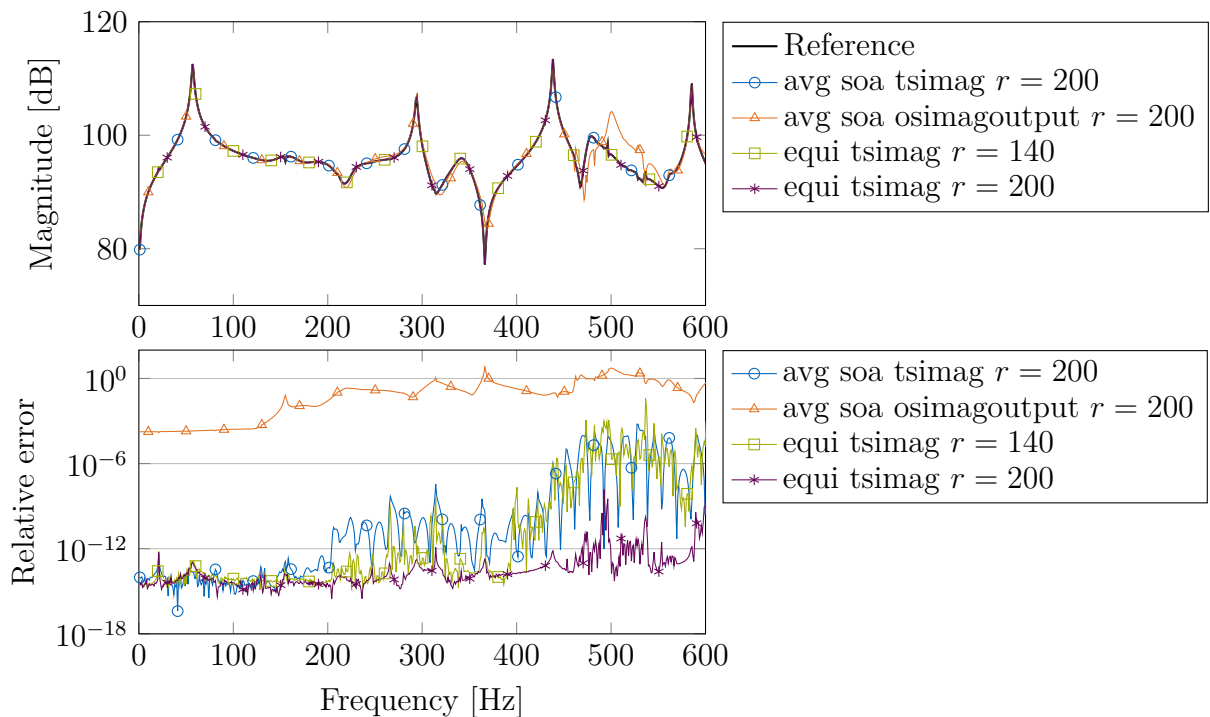


**Figure 4.12:** Original and reduced transfer functions as well as relative errors for the scattering problem reduced with different methods. The lack of information in the higher frequency range for *equi tsmag* with  $r = 140$  and *avg soa tsmag* with  $r = 200$  is clearly visible.

however shows, that its results are comparable to the other reduction methods.

#### 4.1.5 Conclusive remarks

The model order reduction methods described in chapter 3 have been applied on typical vibro-acoustic systems and have been assessed regarding their performance and applicability. All methods are able to compute reasonably sized reduced models which are much smaller than the original models. No a-priori knowledge about the original systems' responses are required, but the majority of the methods require a time consuming presampling procedure. Therefore these methods are especially suited to find small reduced models in settings where the offline cost is not decisive. However, the naive sampling approach *equi* is based on is not applicable well if the reduced order required for the desired accuracy is not known. This approach is used as a reference in the above experiments showing how large the presampling basis needs to be to contain enough information for a good performance of the other methods. Strategies to automatically find locations and interpolation orders without a-priori knowledge of the system response will be presented in section 4.4. Considering derivatives in the presampling bases has the potential to save computational resources in the computation of

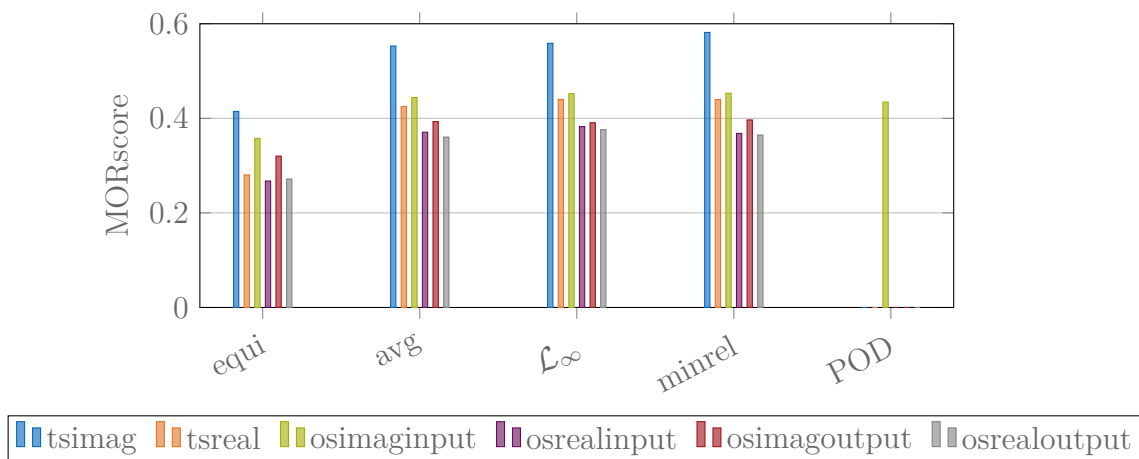


**Figure 4.13:** MORscore  $\mu(1e-16; 200)$  of all employed reduction and projection methods for the poroacoustic system.

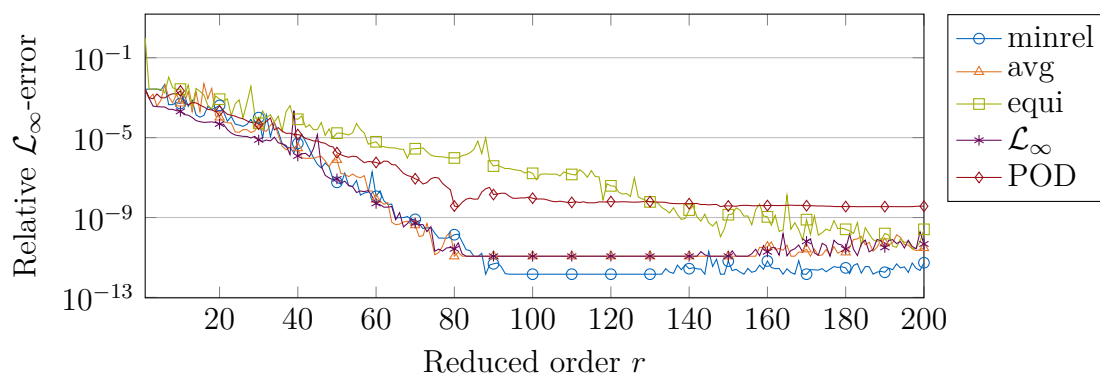


**Figure 4.14:** Relative  $\mathcal{L}_\infty$ -error for reduced models of the poroacoustic system computed by several reduction methods. A two-sided projection with complex valued bases, i.e. *tsimag*, is considered for all cases except *POD*. *minrel* performs best and also *equi* yields acceptable results for a high reduced order  $r$ . The oscillations for higher  $r$  are the result of an ill-conditioning of the reduced systems' matrices.

the basis. The results often show only a small difference regarding the choice of presampling method. It has to be noted, that if the original model—like the hysteretically damped plate—has many undamped modes, also the size of the reduced model needs to grow in order to obtain a reasonably accurate reduced model. Here, it could be beneficial to compute reduced models valid in a specific frequency region only, if the desired application allows this. Methods considering such strategies will be presented in section 4.3.

All reduction methods are applicable to basic vibro-acoustic problems from structural vibration and also fluid-structure-interaction. Only the hysteretically damped plate cannot be reduced with *SO-BT*, as no viscous damping matrix is present in this system. *SO-BT* is theoretically applicable to the sound transmission problem, but due to unstable eigenvalues the method did not converge in this specific case. *equi* and all presampling based methods can be used with all system types, making them a very flexible choice for structure preserving

model order reduction. For *Case C*, where a complex frequency dependency is present in the system matrices, derivatives cannot be considered without additional measures; so *soa* and *sp* are not applicable for the poroacoustic system. Methods to obtain the required factors for the derivatives will be presented in section 4.2.

## 4.2 Reduction of systems with nonlinear frequency dependent terms

The following section is based on Aumann et al.: “Automatic model order reduction for systems with frequency dependent material properties” (2021) [19]. Dissipation mechanisms in vibro-acoustic systems are often depending on the excitation frequency and are, if analyzed in the frequency domain, described by frequency dependent material properties [96]. Such material models exist, for example, for constrained layer damping [6, 250] and poro-elastic materials described by the Biot theory [5, 58, 59, 222]. A perfectly matched layer (PML), which is often used to model radiation problems, can also be formulated as a frequency dependent dissipative material [203, 259, 274]. A discretization with finite elements results in dynamical systems with nonlinear and non-polynomial frequency dependency, so many classic model order reduction techniques described in chapter 3 cannot directly be applied. Especially if higher interpolation orders at certain frequency shifts are desired, specialized methods need to be employed.

We consider a  $q$ -th order polynomial system with corresponding constant matrices  $\mathbf{A}_j$ ,  $j = 0, \dots, q$ , where nonlinear effects are introduced by  $l$  scalar functions  $\phi_i(s)$ ,  $i = 1, \dots, l$  which are applied to the system according to  $l$  corresponding constant matrices  $\mathbf{B}_i$ . Such systems with one input and one output are given by

$$\Sigma: \begin{cases} \left( \sum_{j=0}^q s^j \mathbf{A}_j + \sum_{i=1}^l \phi_i(s) \mathbf{B}_i \right) \mathbf{x}(s) = \mathbf{f}u(s), \\ y(s) = \mathbf{g}\mathbf{x}(s), \end{cases} \quad (4.2)$$

and are described by their transfer function

$$H(s) = \mathbf{g} \left( \sum_{j=0}^q s^j \mathbf{A}_j + \sum_{i=1}^l \phi_i(s) \mathbf{B}_i \right)^{-1} \mathbf{f}. \quad (4.3)$$

An example for such systems are models containing poroelastic materials described by the Biot theory and discretized with the finite element method. An affine formulation of such systems which can directly be transformed to the form of eq. (4.3) is, for example, given in

eq. (A.3). For efficient computation a reduced system of order  $r \ll n$  with the same structure and transfer function is sought. Due to the nonlinearity in  $\phi_i(s)$  many standard reduction methods cannot be employed directly. If the functions governing the dissipation mechanism are given as polynomial functions, the structure preserving moment matching framework relying on the generalized coprime factorization (3.30) can be applied, because the required series expansion factors can directly be obtained. This has been applied to vibro-acoustic systems by, for example, Hetmaniuk, Tezaur, and Farhat [134], where a quadratic term in the system excitation has been considered. Given general differentiable functions describing the frequency dependency, the analytic derivatives can be used in the well-conditioned asymptotic waveform evaluation (WCAWE) method to retain the frequency dependency in reduced space [162, 221, 223]. A similar approach has been shown in [269, 270, 272], where a truncated Taylor series has been used to approximate the frequency dependency. This yields a second-order system, which can be reduced using standard model order reduction methods.

The general idea in this strategy is to approximate the nonlinearity with a polynomial of degree  $d = 2$ , thus yielding a standard second-order system being directly compatible to many established model order reduction methods. The strategy is briefly outlined: First, each function  $\phi_i(s)$  is expanded about the same frequency shift  $s_0$ :

$$\tilde{\phi}_i(s) = \phi_i(s_0) + \phi_i'(s_0)(s - s_0) + \frac{\phi_i''(s_0)}{2}(s - s_0)^2 + \dots \quad (4.4)$$

Inserting all terms up to second order depending on  $s$  into eq. (4.3) and shifting about  $s_0$  yields a standard second-order system

$$H(s) = \mathbf{g} \left( (s - s_0)^2 \widehat{\mathbf{M}} + (s - s_0) \widehat{\mathbf{C}} + \widehat{\mathbf{K}} \right)^{-1} \mathbf{f}, \quad (4.5)$$

with

$$\begin{aligned} \widehat{\mathbf{M}} &= \mathcal{A}_2 + \sum_{i=1}^l \frac{\phi_i''(s_0)}{2} \mathcal{B}_i, \\ \widehat{\mathbf{C}} &= 2s_0 \mathcal{A}_2 + \mathcal{A}_1 + \sum_{i=1}^l \phi_i'(s_0) \mathcal{B}_i, \\ \widehat{\mathbf{K}} &= s_0^2 \mathcal{A}_2 + s_0 \mathcal{A}_1 + \mathcal{A}_0 + \sum_{i=1}^l \phi_i(s_0) \mathcal{B}_i. \end{aligned} \quad (4.6)$$

The above representation can now be used with, for example, the generalized coprime factorization eq. (3.41) or the second-order Krylov subspace eq. (3.47) to compute a projection basis for model order reduction. However, approximating the nonlinear frequency depen-

dependency using a Taylor series requires analytic expressions of the nonlinear functions  $\phi_i(s)$ , at least for some frequency ranges, where the series is computed. As each set of Taylor approximations is only valid for a certain physical problem, applying the method to new problems always requires the solution of multiple differentiation problems. Additionally, the Taylor series is truncated after the quadratic term to fit the second-order structure of the model order reduction strategies. This potentially leads to a decrease of approximation quality with increasing distance from the frequency shift.

In the following, we present a technique to compute reduced order models for systems with nonlinear frequency dependency, which is automatically approximated by a polynomial of order  $d > 2$ . The resulting system's transfer function (4.3) is thus approximated by

$$H(s) \approx \hat{H}(s) = \mathbf{g} \left( \sum_{j=0}^q s^j \mathcal{A}_j + \sum_{i=0}^d s^i \hat{\mathcal{B}}_i \right)^{-1} \mathbf{f}. \quad (4.7)$$

The matrices  $\hat{\mathcal{B}}_i$  incorporate the factors obtained from the approximation of  $\phi_i$ ; these factors can, as in eq. (4.6), be obtained from a Taylor series, for example. The key aspects of the proposed method are the employment of higher order Krylov subspaces and the automatic consideration of nonlinear frequency dependent functions without the need for analytic derivatives. The method considers higher order terms with  $d > 2$  of the frequency dependent functions by employing a Krylov space of order  $k = \max(q, d)$  acquired by an Arnoldi method, similar to the method for second-order systems described in section 3.6.1. This allows a better representation of the nonlinear effects in the reduced space. Instead of a Taylor expansion, the adaptive Antoulas-Anderson (AAA) algorithm introduced by Nakatsukasa, Sète, and Trefethen [190] is used to approximate the nonlinear functions and find a polynomial representation of the system given by eq. (4.7), which is required for the Arnoldi method. Because AAA only requires function evaluations to find a rational approximate, neither analytic expressions nor derivatives of the nonlinear functions describing the frequency dependent behavior are required. Therefore, damping effects solely described by data points obtained, for example, from measurements, can be used in this procedure.

Alternative methods to compute reduced order models for systems with nonlinear frequency dependency have been established in the past: The mode displacement method, typically used for classically damped systems, has been extended to vibro-acoustic systems with nonlinear damping behavior as presented in [220]. In extension to the iterative rational Krylov algorithm IRKA [38], general forms of nonlinearity have been considered in [238]. The optimal expansion points for a rational interpolation of the system's transfer function are iteratively found using the Loewner framework [180]. Thus, no analytic derivatives are required, as the algorithm solely relies on transfer function evaluations in the reduced space.

Most techniques mentioned above and also the following method require an affine representation of the frequency dependency. In cases where such a form is not available, the concept of recycling Krylov subspaces for varying values of the frequency dependent function may be employed to obtain a reduced order model [197].

### 4.2.1 Automatic approximation of frequency dependent nonlinearities

In the following, we outline a strategy to automatically find approximations to the scalar functions  $\phi_i(s)$  in eq. (4.3) and add them to the original dynamical system in order to arrive at eq. (4.7). AAA is used to find a representation for  $\phi_i(s)$  in a frequency range of interest, given data points rather than an analytic function. It has been successfully applied to solve nonlinear eigenvalue problems [166] and to linearize dynamical systems with nonlinear frequency dependency [165]. Such linearization allows the direct use of standard model order reduction methods, but the system's structure is changed and the order is increased from  $n$  to  $n(d+1)$  prior to the reduction,  $d$  being the maximum polynomial order of the nonlinear terms. In the following approach the nonlinear functions are approximated up to an arbitrary order  $d \geq q$  and a Krylov subspace of order  $d$  is subsequently used to find a suitable reduction basis. An enlargement of the original system matrices is not necessary and the reduced system retains the shape of the original system. In the following, the AAA algorithm as well as the reformulation of the system to a polynomial system using the AAA approximation are described. The higher order Krylov subspace employed to reduce the size of the resulting system is presented in section 4.2.2.

AAA automatically finds a rational approximation  $r_i(s)$  of  $\phi_i(s)$  in barycentric form

$$\phi_i(s) \approx r_i(s) = \frac{n(s)}{d(s)} = \frac{\sum_{j=1}^m \frac{w_j f_j}{s - s_j}}{\sum_{j=1}^m \frac{w_j}{s - s_j}}, \quad (4.8)$$

where  $m \geq 1$  is the order of approximation,  $w_j$  are weights,  $f_j$  are data points, and  $s_j$  are support points. At the expansion points, it holds  $r(s_j) = f_j$  for each  $j$ . The barycentric form of the interpolant is potentially better conditioned than, for example, a quotient of polynomials [190]. As the interpolation is performed based on data points, no analytic description of the underlying function is required and the  $M \gg 1$  data points  $\mathfrak{s} \subseteq \mathbb{C}$  with their corresponding function values  $\mathfrak{f} \subseteq \mathbb{C}$  are, along with an approximation tolerance, the only required input to the algorithm, which is summarized in the following. The AAA algorithm is an iterative process automatically choosing the expansion point locations  $s_j$  along with their function values  $f_j$  in eq. (4.8) in a greedy way, i.e. new expansion points are chosen where the difference between the original function and the current approximation is maximal. An intermediate interpolant is computed in each iteration and the difference to

the data points to be interpolated is computed. If the difference between the two functions is too large, a new support point  $s_j$  is chosen at the location where this difference is the largest. The weights  $w_j$ ,  $j = 1, \dots, m$  required to obtain the interpolant in form of eq. (4.8) are computed solving a least-squares problem over the set of sample points  $\mathfrak{s}^{(m)} \setminus \{s_1, \dots, s_m\}$  which have not yet been selected as support points. The least-squares problem is given by

$$\text{minimize } \|fd - n\|_{\mathfrak{s}^{(m)}}, \quad \|w\|_m = 1, \quad (4.9)$$

where  $\|\square\|_{\mathfrak{s}^{(m)}}$  is the discrete 2-norm over the set of not selected data points  $\mathfrak{s}^{(m)}$  and  $\|\square\|_m$  is the discrete 2-norm on vectors containing the weights. Nakatsukasa, Sète, and Trefethen [190] recommend reformulating eq. (4.9) to the matrix problem

$$\text{minimize } \|\mathbb{L}^{(m)}w\|_{M-m}, \quad \|w\|_m = 1, \quad (4.10)$$

with the  $(M - m) \times m$  Loewner matrix  $\mathbb{L}$  relating the selected expansion points to the non-selected data points (c.f. section 3.6.3). It is given by

$$\mathbb{L}^{(m)} = \begin{bmatrix} \frac{f_1^{(m)} - f_1}{s_1^{(m)} - s_1} & \dots & \frac{f_1^{(m)} - f_m}{s_1^{(m)} - s_m} \\ \vdots & \ddots & \vdots \\ \frac{f_{M-m}^{(m)} - f_1}{s_{M-m}^{(m)} - s_1} & \dots & \frac{f_{M-m}^{(m)} - f_m}{s_{M-m}^{(m)} - s_m} \end{bmatrix}, \quad (4.11)$$

and the weights are obtained from the right vector of the singular value decomposition of  $\mathbb{L}$ . An implementation example of the algorithm is given in [190]. The implementation used in the following is based on this example. Following [166], the barycentric form of  $r(s)$  in eq. (4.8) can be written in matrix notation as

$$r_i(s) = \mathbf{a}_i (\mathcal{D}_i + s\mathcal{E})^{-1} \mathbf{b} \quad (4.12)$$

with

$$\mathbf{a}_i = [w_{i,1}f_{i,1} \quad \dots \quad w_{i,m}f_{i,m}], \quad \mathbf{b} = [1 \quad 0 \quad \dots \quad 0]^T,$$

$$\mathcal{D}_i = \begin{bmatrix} w_{i,1} & w_{i,2} & \dots & w_{i,m-1} & w_{i,m} \\ -s_{i,1} & s_{i,2} & & & \\ & -s_{i,2} & \ddots & & \\ & & \ddots & s_{i,m-1} & \\ & & & -s_{i,m-1} & s_{i,m} \end{bmatrix}, \quad \mathcal{E} = \begin{bmatrix} 0 & 0 & \dots & 0 & 0 \\ 1 & -1 & & & \\ & 1 & \ddots & & \\ & & \ddots & -1 & \\ & & & 1 & -1 \end{bmatrix}.$$

Shifting the system about  $s_0$  results in

$$r_i(s) = \mathbf{a}_i \left( \mathbf{I} - (s - s_0) \widehat{\mathcal{D}}_i \right)^{-1} \tilde{\mathbf{b}}_i, \quad (4.13)$$

with  $\widehat{\mathcal{D}}_i = -(\mathcal{D}_i + s_0 \mathcal{E})^{-1} \mathcal{E}$ ,  $\hat{\mathbf{b}}_i = (\mathcal{D}_i + s_0 \mathcal{E})^{-1} \mathbf{b}$ , and identity  $\mathbf{I}$ . As  $m$  is typically small, the computational cost of the matrix operations required for shifting the system can be neglected. In the vicinity of  $s_0$ , the matrix inverse in (4.13) can be approximated with a Neumann series

$$r_i(s) = \mathbf{a}_i \hat{\mathbf{b}}_i + \mathbf{a}_i \left( (s - s_0) \widehat{\mathcal{D}}_i \right) \hat{\mathbf{b}}_i + \mathbf{a}_i \left( (s - s_0) \widehat{\mathcal{D}}_i \right)^2 \hat{\mathbf{b}}_i + \dots \quad (4.14)$$

We now consider the approximations  $r_i(s)$  in matrix notation instead of the original functions  $\phi_i(s)$  in the dynamical system's transfer function (4.3). After shifting about  $s_0$  and truncating the Neumann series after the  $d$ -th term, we arrive at the shifted version of eq. (4.7)

$$H(s) = \mathbf{g} \left( \sum_{j=0}^q (s - s_0)^j \widehat{\mathcal{A}}_j + \sum_{i=0}^d (s - s_0)^i \widehat{\mathcal{B}}_i \right)^{-1} \mathbf{f}, \quad (4.15)$$

where

$$\begin{aligned} \widehat{\mathcal{A}}_i &= \sum_{j=i}^q \binom{j}{i} s_0^{j-i} \mathcal{A}_j, \\ \widehat{\mathcal{B}}_i &= \sum_{j=1}^l \mathbf{a}_j \widehat{\mathcal{D}}_j^i \hat{\mathbf{b}}_j \mathcal{B}_j \end{aligned}$$

Here,  $\binom{j}{i} = \frac{j!}{i!(j-i)!}$  is the binomial coefficient regarding  $j$  and  $i$ ,  $q$  is the number of constant matrices corresponding to powers of  $s$  in the original transfer function, and  $l$  is the number of constant matrices corresponding to the nonlinear functions  $\phi(s)$ . Contrary to approximating the nonlinear frequency contributions with, for example, a Taylor series, this method can be employed automatically without the need for analytic derivatives. Therefore it can be applied to different kinds of problems with an affine representation of frequency dependent behavior without the need of problem-specific changes. A  $k$ -th order Krylov subspace for systems with a transfer function of shape (4.15) has been proposed in [168], which is equivalent to the recurrence in the coprime factorization presented in eq. (3.41). In the following, we will briefly outline a method to compute an orthogonal basis for a  $k$ -th order Krylov subspace.

## 4.2.2 Model order reduction with higher order Krylov subspaces

Lin, Bao, and Wei [168] proposed a generalization of the second-order Krylov subspace for projection based model order reduction of systems with a higher order polynomial transfer function. For establishing a definition of the higher order Krylov space, we consider the system with approximated frequency dependency (4.15) in the general form

$$H(s) = \mathcal{G}(s) \mathcal{K}(s)^{-1} \mathcal{F}(s), \quad (3.30)$$

with  $\mathcal{G}(s) = \mathbf{g}$ ,  $\mathcal{F}(s) = \mathbf{f}$ , and the polynomials  $\mathcal{K}(s) = \sum_{j=0}^q s^j \mathcal{A}_j + \sum_{i=0}^d s^i \hat{\mathcal{B}}_i$ , which are combined to matrices  $\mathcal{C}_i$  for  $j = i$ . It follows  $\mathcal{K}(s) = \sum_{i=0}^k s^i \mathcal{C}_i$  with  $k = \max(q, d)$ . The resulting system's transfer function can be expressed in linear form as

$$H(s) = \mathbf{g}^{(k)} (\mathcal{M}_0 + s\mathcal{M}_1)^{-1} \mathbf{f}^{(k)} = \mathbf{g}^{(k)} (\mathbf{I} - \mathcal{M}_0^{-1} \mathcal{M}_1)^{-1} \mathcal{M}_0^{-1} \mathbf{f}^{(k)}, \quad (4.16)$$

with

$$\mathcal{M}_0 = \begin{bmatrix} \mathcal{C}_0 & 0 & \cdots & 0 \\ 0 & \mathbf{I} & \cdots & 0 \\ \vdots & \ddots & \ddots & \vdots \\ 0 & \cdots & 0 & \mathbf{I} \end{bmatrix}, \quad \mathcal{M}_1 = \begin{bmatrix} \mathcal{C}_1 & \mathcal{C}_2 & \cdots & \mathcal{C}_q \\ -\mathbf{I} & 0 & \cdots & 0 \\ \vdots & \ddots & \ddots & \vdots \\ 0 & \cdots & -\mathbf{I} & 0 \end{bmatrix}, \quad \mathbf{f}^{(k)} = \begin{bmatrix} \mathbf{f} \\ 0 \\ \vdots \\ 0 \end{bmatrix}, \quad \mathbf{g}^{(k)} = [\mathbf{g} \ 0 \ \cdots \ 0].$$

Similar as described in section 3.6.1 for the second-order Krylov subspace, the  $k$  matrices  $\mathbf{Z}_i$ ,  $i = 1, \dots, k$  and the starting vector  $\mathbf{q}$ , which define the  $k$ -th order Krylov subspace, are obtained from this representation as

$$\begin{aligned} \mathbf{Z}_1 &= -\mathcal{C}_0^{-1} \mathcal{C}_1, \\ \mathbf{Z}_2 &= -\mathcal{C}_0^{-1} \mathcal{C}_2, \\ &\vdots \\ \mathbf{Z}_k &= -\mathcal{C}_0^{-1} \mathcal{C}_k, \\ \mathbf{q} &= -\mathcal{C}_0^{-1} \mathbf{f}. \end{aligned} \quad (4.17)$$

The resulting Krylov vectors  $\mathbf{Z}^i \mathbf{q}$  of dimension  $qn$  are related by

$$\mathbf{Z}^i \mathbf{q} = \begin{bmatrix} \mathbf{r}_i \\ \mathbf{r}_{i-1} \\ \vdots \\ \mathbf{r}_{i-k+1} \end{bmatrix}, \quad \text{for } i \geq k+1. \quad (4.18)$$

Again, the vectors  $\mathbf{r}_i$  are given recursively as

$$\begin{aligned}
\mathbf{r}_0 &= \mathbf{v}_0 \\
\mathbf{r}_1 &= \mathbf{Z}_1 \mathbf{r}_0 \\
\mathbf{r}_2 &= \mathbf{Z}_1 \mathbf{r}_1 + \mathbf{Z}_2 \mathbf{r}_0 \\
&\vdots \\
\mathbf{r}_{i-1} &= \mathbf{Z}_1 \mathbf{r}_{i-2} + \mathbf{Z}_2 \mathbf{r}_{i-3} + \cdots + \mathbf{Z}_k \mathbf{r}_{i-k-1}.
\end{aligned} \tag{4.19}$$

The resulting space

$$\mathcal{S}_r^{(k)}(\mathbf{Z}_1, \dots, \mathbf{Z}_k, \mathbf{q}) = \text{span}(\mathbf{r}_0, \mathbf{r}_1, \dots, \mathbf{r}_{r-1}). \tag{4.20}$$

is called the  $r$ -th Krylov subspace of order  $k$  [168]. An orthonormal basis  $\mathbf{V}$  of the Krylov space  $\mathcal{S}_r^{(k)}$  is found using, for example, an Arnoldi procedure similar to [30, 171]. Wang, Jiang, and Kong [262] proposed a specialized variant of the Arnoldi algorithm for the  $q$ -th order Krylov subspace having less requirements on the amount of available memory. The subspace for basis  $\mathbf{W}$  is found similarly by solving the adjoint problem. Both bases can now be employed in a projection framework as of eq. (3.31). The same procedure is possible for a system shifted about a frequency  $s_0$ . Here, the quantities  $\tilde{\mathcal{A}}_i$  and  $\tilde{\mathcal{B}}_i$  from section 4.2.1 are used to build matrices  $\tilde{\mathcal{C}}_i$  such that the shift is included in the transfer function

$$H(s) = \mathbf{g} \left( \sum_{i=0}^k (s - s_0)^i \tilde{\mathcal{C}}_i \right)^{-1} \mathbf{f}, \tag{4.21}$$

with  $\tilde{\mathcal{C}}_i = \sum_{j=i}^k \binom{j}{i} \tilde{\mathcal{C}}_j s_0^{j-i}$ . The choice of subspace size  $r$  and location of the shift has a large influence on the approximation quality of a reduced model. To increase the reduced model's accuracy for a wide range of frequencies, it can be beneficial to not only increase the size of the Krylov subspace, but to combine multiple subspaces with different shifts  $s_0$  in a global basis [36, 124]. For each shift added to the projection basis, the solution of up to two linear systems of order  $n$  is required. Increasing the order at an already established shift only requires matrix vector products if the factorization of  $\mathbf{Z}_0$  is stored for each shift and a suitable Arnoldi strategy is chosen [30].

### 4.2.3 Numerical experiments

The effectiveness of the proposed strategy is evaluated in some numerical experiments. The following numerical experiments were conducted on nodes of LRZ's Cool-MUC-2 cluster. Each node is equipped with a 28 core Intel® Haswell based CPU and 56 GB RAM are

available per job. The algorithms have been implemented and run using Matlab® R2020a.

### Coupled poro-acoustic system

As first example we consider the three-dimensional interior acoustic problem coupled to two poroelastic materials shown in section 2.5.5. The evaluation of a frequency sweep in steps of 1 Hz in the considered frequency range from 1 to 800 Hz takes  $t_c \approx 7.8 \cdot 10^4 \text{ s} \approx 21.7 \text{ h}$  on the employed machine. Viscous drag  $\tilde{b}(s)$  and effective bulk modulus of the fluid phase  $\tilde{K}_f(s)$  are governing the dissipation mechanism in the poroelastic material and are described by the complex valued functions

$$\tilde{b}(s) = \sigma \phi^2 \sqrt{1 + \frac{4i \operatorname{Im}(s) \alpha_\infty^2 \mu \rho_f}{\sigma^2 \Lambda^2 \phi^2}}, \quad (2.62)$$

$$\tilde{K}_f(s) = \frac{\gamma P_0}{\gamma - (\gamma - 1) \left[ 1 + \frac{8\mu}{i \operatorname{Im}(s) Pr \Lambda'^2 \rho_f} \sqrt{1 + \frac{i \operatorname{Im}(s) Pr \Lambda'^2 \rho_f}{16\mu}} \right]^{-1}}. \quad (2.54)$$

Their real and imaginary parts in the frequency range  $[1, \dots, 800] \text{ Hz}$  are given in fig. 4.15 for a poroelastic material with the parameters  $\phi = 0.93$ ,  $\sigma = 80 \cdot 10^3 \text{ kg m}^{-3} \text{ s}^{-1}$ ,  $\alpha_\infty = 2.5$ ,  $\Lambda = 10 \cdot 10^{-6} \text{ m}$ ,  $\Lambda' = 100 \cdot 10^{-6} \text{ m}$ ,  $\rho_f = 1.205 \text{ kg m}^{-3}$ ,  $\mu = 1.8208 \cdot 10^{-5} \text{ N s m}^{-2}$ ,  $\gamma = 1.4$ ,  $P_0 = 1.0128 \cdot 10^5 \text{ Pa}$ ,  $Pr = 0.712$ , which is given as Material 1 in table 2.3. The nonlinear behavior of both functions is clearly visible.

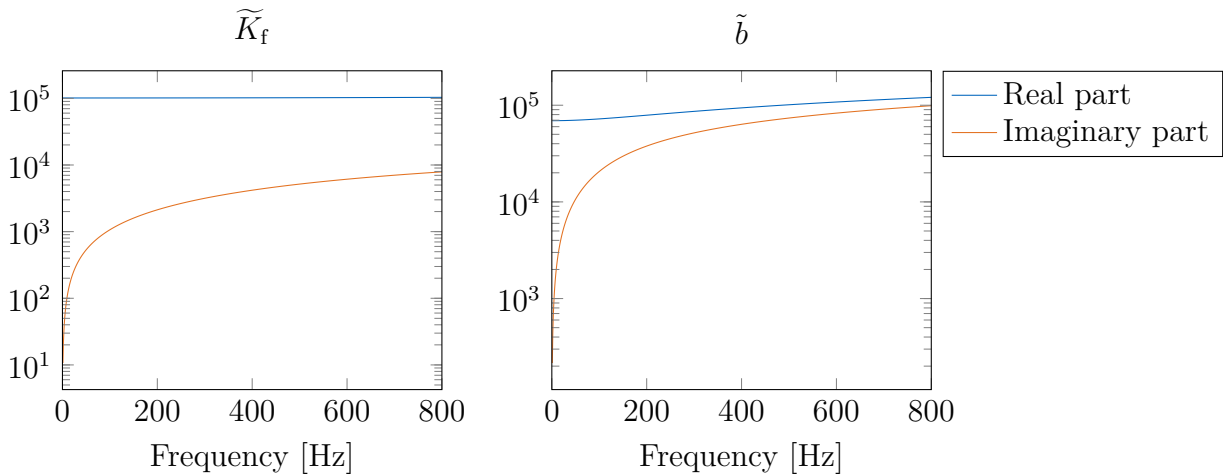


**Figure 4.15:** Real and imaginary parts of effective bulk modulus  $\tilde{K}_f$  and viscous drag  $\tilde{b}(s)$  for a polyurethane foam. The material parameters are given in tables 2.2 and 2.3. Material 1 is considered in this figure.

**Automatic approximation of the frequency dependent functions** All frequency dependent functions introduced in the transfer function can be approximated by AAA under a tolerance of  $1 \cdot 10^{-14}$  in the frequency range in which the models are evaluated. The complex-valued projection bases used in the following experiments are obtained by *osimaginput*, i.e. single-sided projection with complex-valued projection matrices regarding the system input and setting  $\mathbf{W} = \mathbf{V}$ . The coupling functions in eq. (A.3) introduce  $\frac{1}{s^2}$  terms, which cannot be represented well by a polynomial, so the AAA approximation is accurate only in a relatively narrow band around the expansion point. To overcome this, all functions are multiplied by  $s^2$ , which only slightly increases the required order of AAA for some functions but greatly increases the range of accuracy for the approximated coupling functions. The effect is illustrated in fig. 4.16: the relative approximation errors of two reduced models, one using the original and one using the modified formulation, are compared. Both models are projected using a Krylov space of order  $k = 5$  with a single expansion point at  $s_0 = 2\pi i \cdot 400$  and have an order of  $r = 200$ . The AAA approximation in combination with a Krylov subspace yields reduced models which are accurate in nearly the complete frequency range. Additionally it can be seen, that the modified model has a lower relative error, especially in the higher frequency region. Given the fact, that the computational complexity of both models is the same, the modified version is used for the following numerical examples.

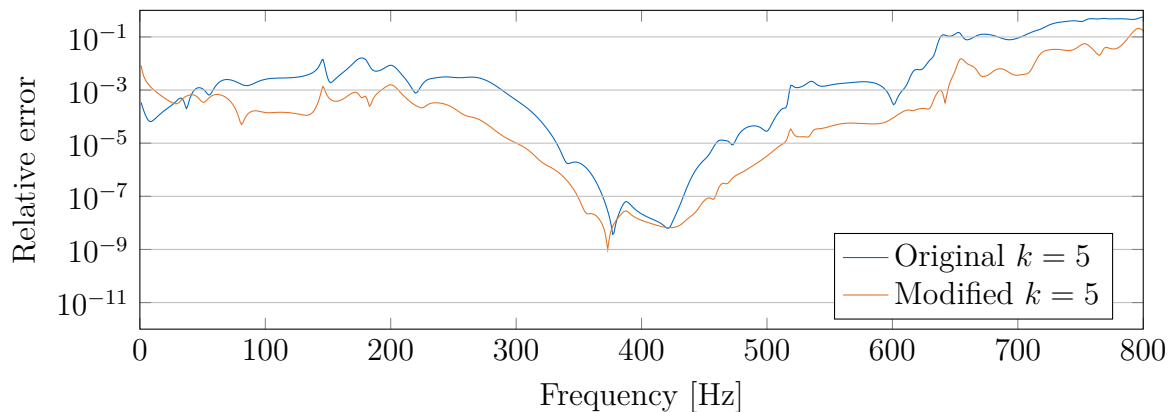


**Figure 4.16:** Approximation error of the original and modified poroacoustic models. A single Krylov subspace of order  $k = 5$  with expansion point  $s_0 = 2\pi i \cdot 400$  is considered. The reduced model has an order of  $r = 200$ .

The influence of the approximation of the matrix inverse in eq. (4.13) by a Neumann series expansion is examined in the following. The relative error  $\varepsilon_e(i\omega)$  considering the expanded approximation and the original function is identical to the error of a Taylor series expansion with same shift and order. It can be seen, that the approximation can become unstable for  $s$  far away from the shift  $s_0$ . However, the approximation error of the reduced model can

still be acceptable in these regions, as it is shown in fig. 4.17. Here, the relative errors  $\varepsilon_r(i\omega)$  of reduced models shifted about  $s_0 = 2\pi i \cdot 400$  with  $r = 400$  and different Krylov subspace orders  $k$  are compared. Additionally, the highest approximation error of the Neumann series compared to the respective original function is given for each  $k$ . The function with the highest error  $\varepsilon_e$  is chosen from the ten frequency dependent functions considered in the model. It can be seen, that increasing the subspace order  $k$  also widens the frequency range around the chosen shift, where the reduced model is accurate (solid lines in fig. 4.17). Note, that the size of the reduced models is the same in all cases. Accordingly, the accuracy of the series expansion increases with increasing order  $k$  (dashed lines in fig. 4.17). However, this expansion has very high relative errors for low frequencies. This does not impair the approximation quality of the reduced model, as the influence of the function is apparently low in this frequency region. However, an approximation based on an expansion point located in this frequency region might have a large influence on the approximation quality of the reduced model in the higher frequency region. As this is problem dependent, the employed series expansions should be examined prior to the reduction process in order to avoid placing expansion points in such regions.

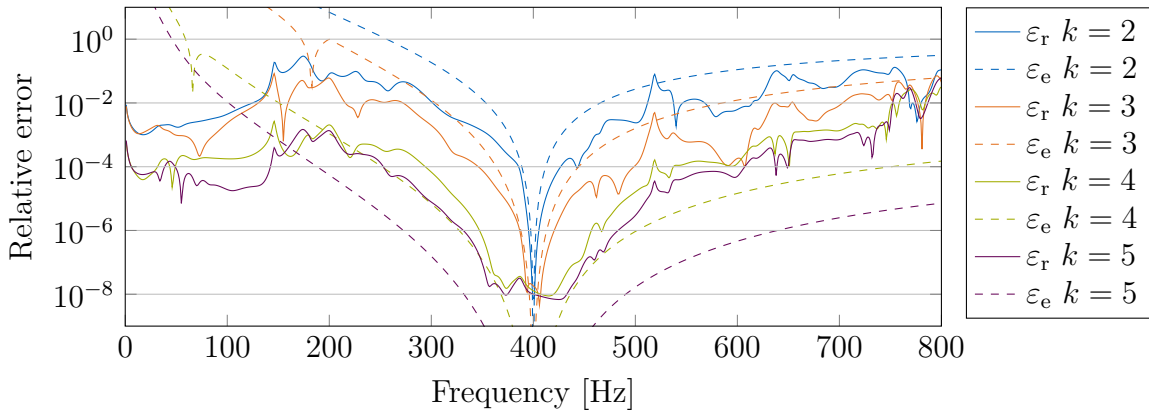


**Figure 4.17:** Approximation errors for different Krylov space orders  $k$  and the Neumann expansion error for the respective function with the highest error regarding the poroacoustic model. The reduced models are expanded about  $s_0 = 2\pi i \cdot 400$  with  $r = 400$ .

**Influence of subspace order on the accuracy** We now investigate the influence of higher orders  $k$  of the Krylov subspace on the approximation quality of reduced models with different sizes  $r$ . The reduced models are computed using reduction bases with a single expansion point at  $s_0 = 2\pi i \cdot 400$ . The maximum absolute relative errors according to eq. (4.1) for all combinations of  $r$  and  $k$  are given in fig. 4.18. It can be seen, that a higher order  $k$  leads to more accurate reduced models if the reduced order  $r$  is kept constant. The error of

the models based on subspaces with  $k = 2$  and  $k = 3$  is nearly one magnitude higher than the other reduced models', especially for higher reduced orders  $r$ . This suggests, that by truncating after the quadratic or cubic terms of the AAA approximation, important parts of the frequency dependent functions are neglected. However, the effect of increasing the subspace order further has a smaller effect in terms of accuracy, suggesting that all functions are sufficiently approximated.

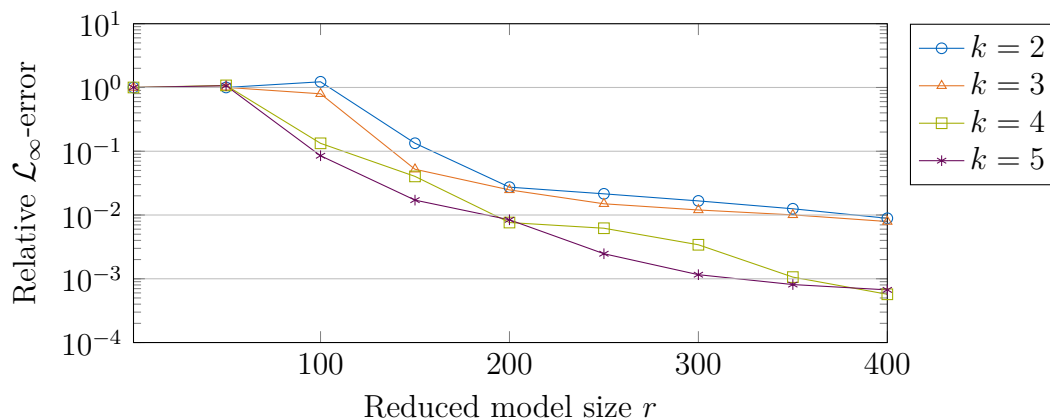


**Figure 4.18:** The maximum relative error in the frequency range  $[1, \dots, 800]$  Hz of reduced models of different sizes  $r$  and Krylov subspace orders  $k$ . All subspaces are expanded around  $s_0 = 2\pi i \cdot 400$ .

The better accuracy of the higher order Krylov subspace comes with increased computational cost. Figure 4.19 plots the required computation times for the same models as above with increasing  $r$  against their maximum relative errors. The curves begin at  $r = 1$  at their leftmost points, while the rightmost data points correspond to  $r = 400$ . While increasing  $k$  leads to lower maximum errors, the computation time is also increased. It can be seen, that using lower orders of  $k$  in combination with a higher reduced order  $r$  has the potential to yield more accurate reduced models in the same time than employing a higher  $k$  in combination with a lower  $r$ . In this example, the reduced order  $r$  is the limiting factor regarding accuracy, as it has a higher influence on the transfer function of the reduced models than the accurate representation of the frequency dependent functions. The results suggest, that the benefit of higher orders  $k$  is small if the computation times are crucial for the application. However, the computation times for all models are still much lower than the time required for the evaluation of the full model.

**Multi-point moment matching** In order to obtain a reduced model of reasonable size with high accuracy over a wide frequency range, we combine multiple Krylov spaces to a single projection basis. We again consider different orders  $k$  of the employed Krylov spaces while

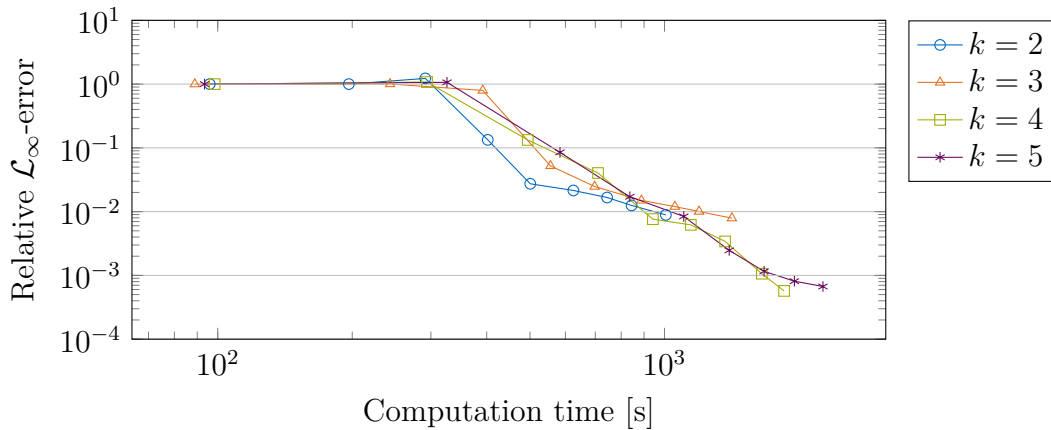


**Figure 4.19:** The maximum relative error in the frequency range  $[1, \dots, 800]$  Hz of reduced models of different sizes  $r$  and Krylov subspace orders  $k$  over the required computation time. All models are computed using a single expansion point  $s_0 = 2\pi i \cdot 400$ . The curves begin at  $r = 1$  at their leftmost points, each mark represents an increased order of 50, and the rightmost data point corresponds to  $r = 400$ .

their size  $r$  remains constant. We start with a model computed from four expansion points  $s_{0,i} = 2\pi i [100, 300, 500, 700]$  in the frequency range of interest. An order  $r_0 = 100$  is considered for each subspace, thus the resulting reduced model has an order of  $r = 400$ . Their relative errors are given in fig. 4.20.

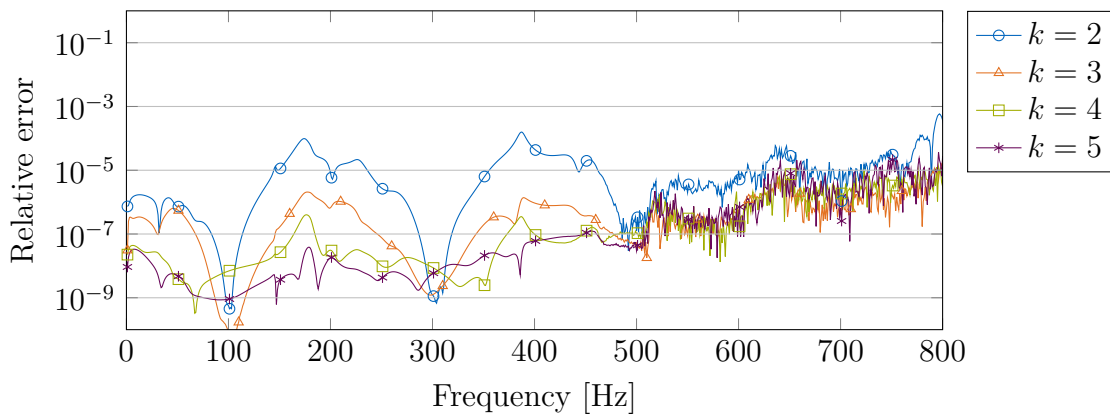


**Figure 4.20:** Approximation error of a reduced model approximating the poroacoustic system. Approximation with different orders  $k$  of the Krylov spaces around  $s_{0,i} = 2\pi i [100, 300, 500, 700]$  with reduced orders  $r_0 = 100$ . The resulting model is of order  $r = 400$ .

Again, the influence of higher orders  $k$  can be observed in an increased accuracy between the expansion points. Comparing the relative errors to the reduced models computed from a single expansion point reported in fig. 4.17, the benefit of multiple expansion points is obvious. Despite having the same reduced order, the relative error is lower for a wider

frequency range if more than one expansion point is chosen. An uninformed a-priori choice of expansion point locations and reduced order may, however, not be ideal and result in too large or inaccurate reduced models. Therefore, a method to obtain a reduced model under a certain accuracy automatically without requiring a-priori knowledge about expansion point locations or a reasonable reduced order is presented in the following section 4.4.

### Viscoelastic sandwich beam model

We now consider a system with only one frequency dependent function. It models a symmetric sandwich beam with length  $l = 0.21$  m, consisting out of two layers of cold rolled steel surrounding a viscoelastic ethylene-propylene-diene core [250]. The beam is clamped at one side, a sketch is given in fig. 4.21. The system is discretized using finite elements and

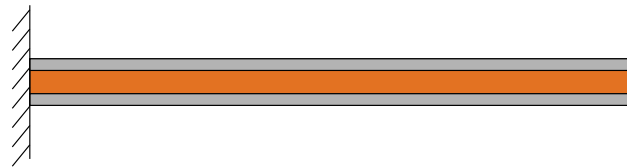


**Figure 4.21:** A sketch of the sandwich beam with viscoelastic core. The steel face sheets are depicted gray, the viscoelastic core orange.

has an order of  $n = 3360$ ; the matrices have been taken from [136]. Due to the relatively small size of the original model, the computation times are not considered in this example. The beam is excited by a single load at its free end and the displacement is measured at the same location; the frequency response function is given in fig. 4.23. The dissipation behavior of the constrained layer damping can be described by a fractional derivative model (c.f. eq. (2.53)), and is added by a nonlinear function depending on  $s$  [6, 229]. The resulting system's transfer function is given by

$$H(s) = \mathbf{g} \left( s^2 \mathbf{A}_2 + \mathbf{A}_0 + \frac{G_0 + G_\infty (\mathbf{i} \operatorname{Im}(s) \tau)^\alpha}{1 + (\mathbf{i} \operatorname{Im}(s) \tau)^\alpha} \mathbf{B}_1 \right)^{-1} \mathbf{f}, \quad (4.22)$$

where  $\mathbf{A}_0$ ,  $\mathbf{B}_1$  are the stiffness matrices corresponding to the elastic and viscoelastic parts and  $\mathbf{A}_2$  is the mass matrix of the system. The parameters for the fractional derivative model are  $G_0 = 350.4$  kPa,  $G_\infty = 3.062$  MPa,  $\tau = 8.230$  ns, and  $\alpha = 0.675$ . The model is evaluated in the frequency range  $[10, \dots, 10\,000]$  rad s<sup>-1</sup>. A AAA approximation of order 12 is able to approximate the fractional derivative model function in this frequency range under a tolerance of  $1 \cdot 10^{-14}$ .

The full order model is reduced using a Krylov subspace with a single expansion point  $s_0 = 5005\mathbf{i}$  in the middle of the considered frequency range. Figure 4.22 shows the maximum

relative errors for reduced models of different sizes  $r$  compared to the order of the respective Krylov subspace  $r$ . All reduced models achieve a good approximation quality in the desired frequency range, suggesting that the automatic approximation of the fractional derivative model function in eq. (4.22) is successful. Choosing a higher subspace order  $k$  leads to an earlier drop in the maximum relative error, showing the potentially higher accuracy of models based on a higher  $k$  given a certain size of the reduced order model  $r$ . The observation that all models reach a similar accuracy regardless of their subspace order  $k$  shows that the damping introduced by the FD model can be approximated well by a second-order function.

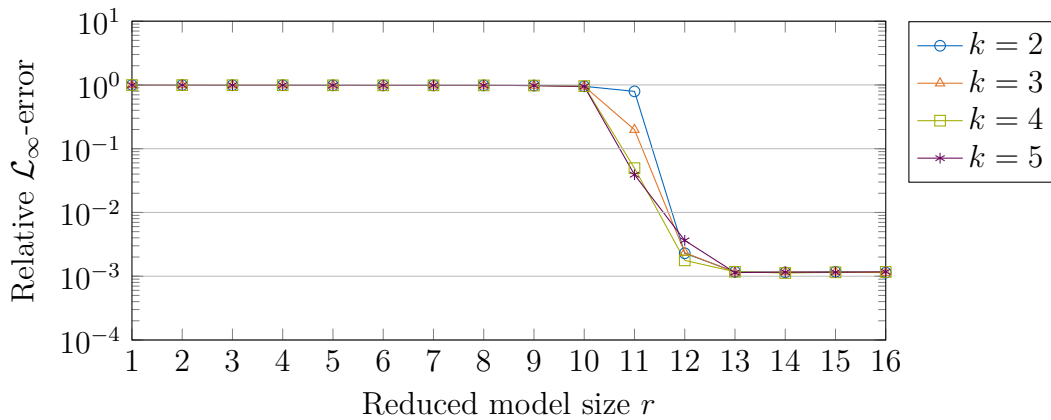


**Figure 4.22:** The maximum relative error in the frequency range  $[10, \dots, 10\,000]$  rad s<sup>-1</sup> of reduced models of the sandwich beam regarding different sizes  $r$  and Krylov subspace orders  $k$ . All subspaces are expanded around  $s_0 = 5005i$ .

The benefit of higher subspace orders  $k$  can also be observed in fig. 4.23. Again, the original model is reduced to  $r = 11$  using Krylov spaces of different orders  $k$  expanded about  $s_0 = 5005i$ . The relative errors of all models are very low in the direct vicinity of the expansion point, while the approximation quality of the reduced models based on  $k = 2$  and  $k = 3$  deteriorates in the lower frequency region. Especially the location of the first mode in the transfer function cannot be exactly approximated by these models, which is observable in the models' transfer functions. However, increasing the reduced order  $r$  yields reduced models being accurate for all values of  $k$ .

#### 4.2.4 Conclusive remarks

The presented method is able to compute reduced models for systems with frequency dependent material properties. The reduction method automatically adds frequency dependent contributions up to a specified order and computes the  $k$ -th order Krylov subspace. Thus,

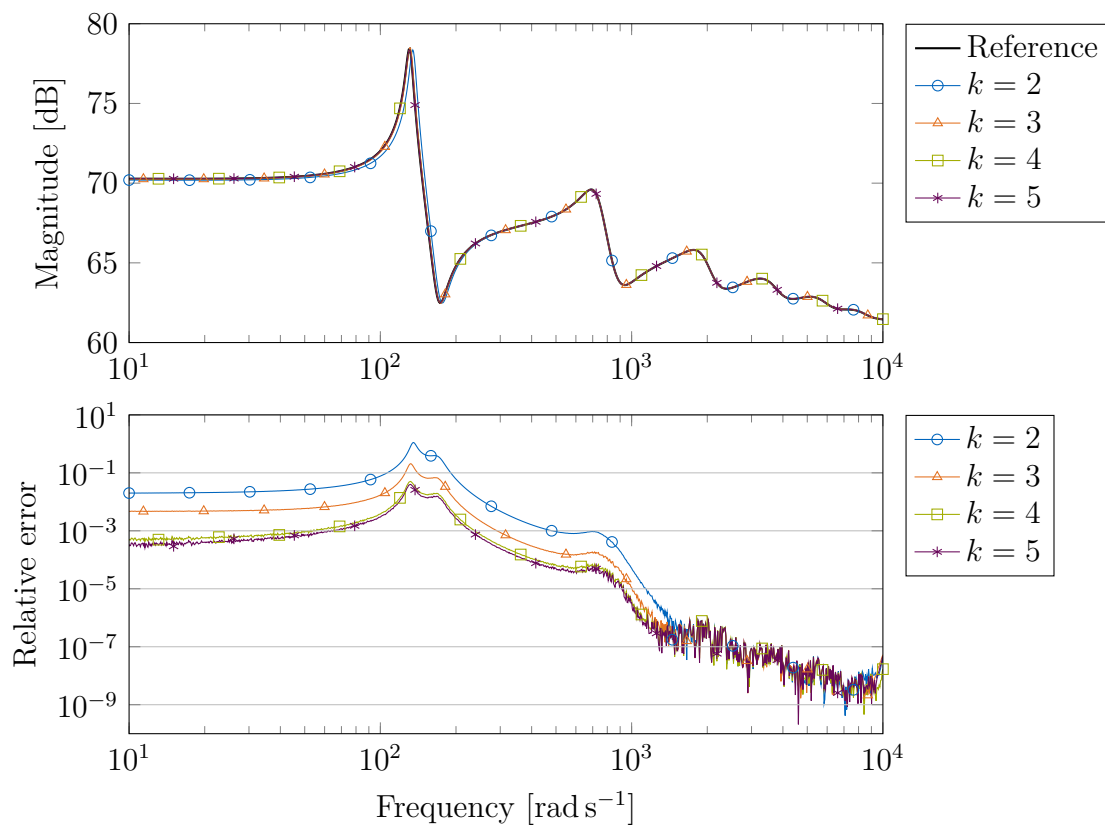


**Figure 4.23:** Transfer functions and approximation errors of reduced models of the sandwich beam. Approximation with different orders  $k$  of the Krylov subspace around  $s_0 = 5005i$  with reduced order  $r = 11$ .

it can be used, without modification, for systems with any form of frequency dependent material, which can be written in an affine form. No analytic form of the frequency dependent functions is required, as the incorporated AAA algorithm works on data points only. The higher order Krylov subspaces have shown to be beneficial, as the range of highly accurate approximation around the expansion point grows for increasing values of  $k$ , while the size of the reduced model stays the same. This is especially interesting, if small reduced models are required.

## 4.3 Frequency-limited approximation of vibro-acoustic systems

For many application cases, the response of vibro-acoustic systems in predefined frequency ranges is of special interest. For example, locally resonant materials need to be designed in a way their dissipative effect reaches a maximum at certain frequencies at which vibration

of the host structure is to be prevented. The design process of such structures often involves many iterations to obtain an optimal design, so it is beneficial to use efficient surrogate models for evaluating the frequency response. Specially adapted model order reduction methods allow the computation of such surrogates being only valid in a specified frequency range, thus further reducing the size of the surrogate. Frequency limited balanced truncation is often employed in this case. Here, the controllability and observability Gramians eqs. (2.6) and (2.7) are obtained from an integral expression defined in the desired frequency range rather than for frequencies from  $-\infty$  to  $\infty$  [48, 115]. The method has recently been extended for second-order systems [50, 129]. An alternative approach for frequency limited moment matching is based on IRKA and also utilizes the frequency limited Gramians [211]. In this case, only one Krylov space is computed directly, the other projection basis is obtained using one frequency limited Gramian. Instead of  $2r$  solutions of the original system, only  $r$  solutions are required per iteration, the required Gramian is only computed once. Compared to IRKA, the stability of the original model is always retained. Several algorithms have been proposed for this use-case, for overviews see [210, 261].

A special case of frequency limited approximation can be considered if second-order systems are reduced using SO-IRKA. Proposed by Wyatt [268], it extends the applicability of IRKA to second-order systems while losing some optimality conditions. However, some of its features can be exploited in order to compute reduced models of second-order systems. As standard IRKA (algorithm 3.1), the algorithm starts at arbitrary initial expansion points  $s_i$  and builds a reduced model matching the original system around these points. The mirror images of the reduced system's eigenvalues are used as updated expansion points in the next iteration, until convergence is reached. The algorithm for a SISO second-order system is sketched in algorithm 4.1. Contrary to first order IRKA, the intermediate reduced second order systems in SO-IRKA yield  $2r$  eigenvalues  $\lambda_{2r}$ . If all eigenvalues would be chosen as expansion points for the next iteration, the reduced model's size would double each iteration. Therefore, only a subset of eigenvalues is chosen as updated expansion points in algorithm 4.1 line 6. This choice is arbitrary and choosing  $r$  of the mirror images of  $\lambda_{2r}$  closest to the imaginary axis leads to a reduced model valid around  $s = 0$ . This strategy can be extended to choose  $r$  of the  $2r$  eigenvalues lying in a specified frequency region. Doing so, a reduced model matching the original system in this frequency range can be computed [22].

The following numerical experiment shows the different approaches; all experiments were conducted on a workstation with an Intel® Xeon® Gold 6136 @ 3.0 GHz and 256 GB RAM using Matlab® R2020a. The sound transmission model described in section 2.5.3 is reduced to two models of each  $r = 20$ . One model is computed to match the moments starting at  $f = 0$  Hz, for the second model a convergence interval  $\zeta_c = 2\pi i [300, \dots, 600]$  is chosen. In

---

**Algorithm 4.1** The iterative rational Krylov algorithm for second order SISO systems, SO-IRKA

---

**Require:** Original system  $\Sigma$ ,  $r$  initial expansion points  $\mathbf{s}_0 = [s_{0,1} \ \cdots \ s_{0,r}] \in \mathbb{C}^r$  closed under complex conjugation

**Ensure:** Reduced system  $\Sigma_r$

- 1: **while** no convergence **do**
- 2:     Compute projection bases

$$\mathbf{V} = \left[ \left( s_{0,1}^2 \mathbf{M} + s_{0,1} \mathbf{C} + \mathbf{K} \right)^{-1} \mathbf{f} \ \cdots \ \left( s_{0,r}^2 \mathbf{M} + s_{0,r} \mathbf{C} + \mathbf{K} \right)^{-1} \mathbf{f} \right]$$

$$\mathbf{W} = \left[ \left( s_{0,1}^2 \mathbf{M} + s_{0,1} \mathbf{C} + \mathbf{K} \right)^{-H} \mathbf{g}^\top \ \cdots \ \left( s_{0,r}^2 \mathbf{M} + s_{0,r} \mathbf{C} + \mathbf{K} \right)^{-H} \mathbf{g}^\top \right]$$

- 3:     Orthogonalize bases  $\mathbf{V} = \text{orth}(\mathbf{V})$ ,  $\mathbf{W} = \text{orth}(\mathbf{W})$
  - 4:      $\mathbf{M}_r = \mathbf{W}^H \mathbf{M} \mathbf{V}$ ,  $\mathbf{C}_r = \mathbf{W}^H \mathbf{C} \mathbf{V}$ ,  $\mathbf{K}_r = \mathbf{W}^H \mathbf{K} \mathbf{V}$
  - 5:     Solve the quadratic eigenvalue problem  $(\mathbf{M}_r \lambda^2 + \mathbf{C}_r \lambda + \mathbf{K}_r) \mathbf{x} = 0$
  - 6:     Choose  $r$  eigenvalues  $\lambda_r$  from  $\lambda_{2r}$
  - 7:     Update expansion points  $\mathbf{s}_0 \leftarrow -\lambda_r$
  - 8: **end while**
  - 9: Project  $\Sigma$  using  $\mathbf{V}$ ,  $\mathbf{W}$  to obtain  $\Sigma_r$
- 

the first model, the mirror images of eigenvalues closest to the imaginary axis are considered as expansion points for the following iteration and the complex conjugate pairs of initial expansion points are distributed linearly in the range  $\mathbf{s}_0 = \pm 2\pi i [1, \dots, 300]$ . For the second model, all mirror images of eigenvalues inside the convergence interval are considered. If less than  $r$  eigenvalues lie in this interval, the remaining expansion points are obtained from the eigenvalues with the lowest distance to the interval. This also ensures a good approximation at the borders of the interval, as shifts lying outside the interval can also have an impact on the solution inside the interval. Here, 10 complex conjugate pairs in the range  $\mathbf{s}_0 = \pm 2\pi i [300, \dots, 600]$  are chosen as initial expansion points. *tsreal* is used for projection in both experiments. The results are given in figs. 4.24 and 4.25. Both models match the original system response in different frequency ranges and show the applicability of both approaches. The influence of the distribution of the expansion points at convergence on the approximation quality of the reduced model is clearly visible in both results. While the reduced models approximate the original transfer function well in vicinity of the shifts, the approximation deteriorates with increasing distance. This can be used as an indicator of the range in which the reduced models are valid, as the reduced order has to be fixed before starting IRKA.

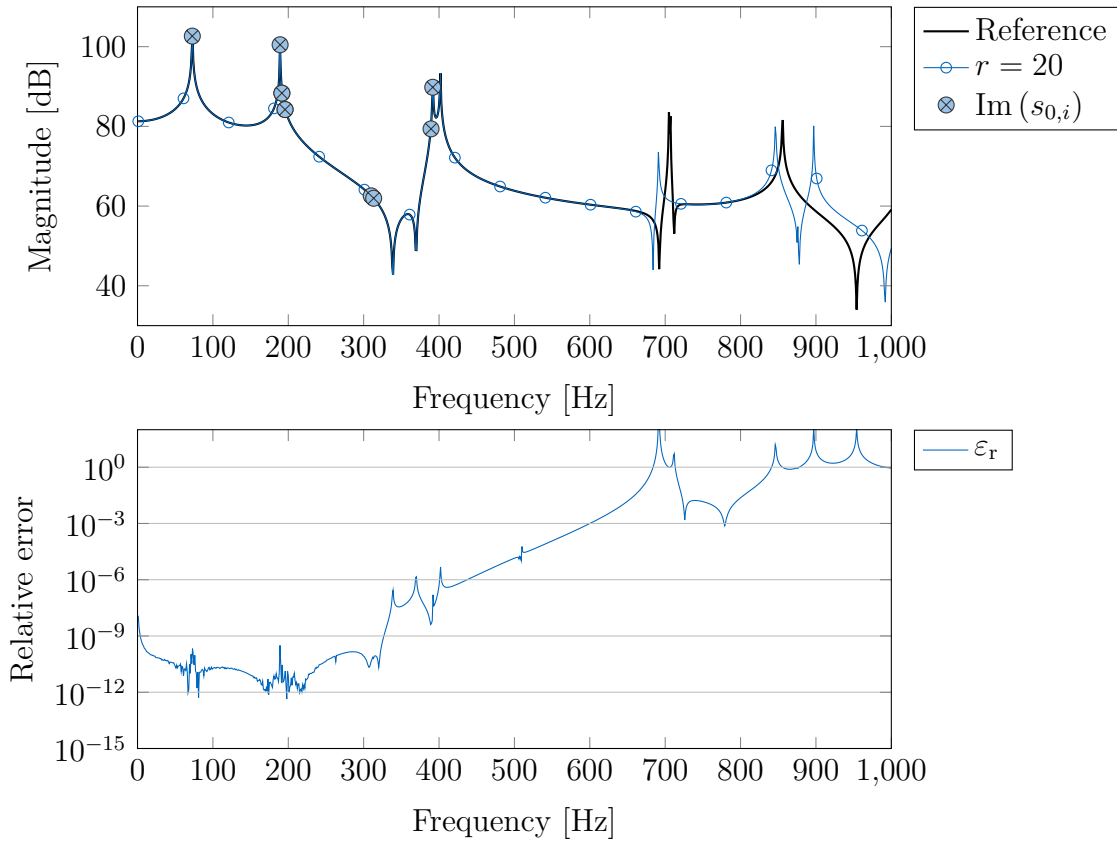


**Figure 4.24:** Transfer functions of the sound transmission model and the model reduced with SO-IRKA as well as relative error. The sound transmission problem is reduced to  $r = 20$  and the mirror images of the  $r$  eigenvalues closest to the imaginary axis are chosen as expansion points for the consecutive iteration. Filled blue circles mark the imaginary parts of the expansion points.

### 4.3.1 Optimization using intermediate models

A drawback of IRKA are its computational costs. During each iteration,  $2r$  linear equation systems of order  $n$  need to be evaluated. This can be prohibitive, especially for large models. In the following, two strategies are presented which aim at reducing this computational cost or speeding up the iteration process. Given an original system with a large order  $n$ , the by far most computationally expensive part in SO-IRKA is the repeated computation of the reduction bases in algorithm 4.1 line 2. In order to reduce this cost, Castagnotto and Lohmann [71] proposed the confined iterative rational Krylov algorithm (CIRKA) as an extension to standard first-order IRKA (algorithm 3.1). The main idea is to perform the costly optimization steps on an intermediate reduced model with order  $q > r$ , while still  $q \ll n$ . Their approach is sketched in algorithm 4.2 and can be outlined as follows: First, the intermediate model  $\Sigma_m$  is computed via projection using initial expansion points and interpolation orders. SO-IRKA is now applied on the resulting model to obtain  $\Sigma_r$ . After

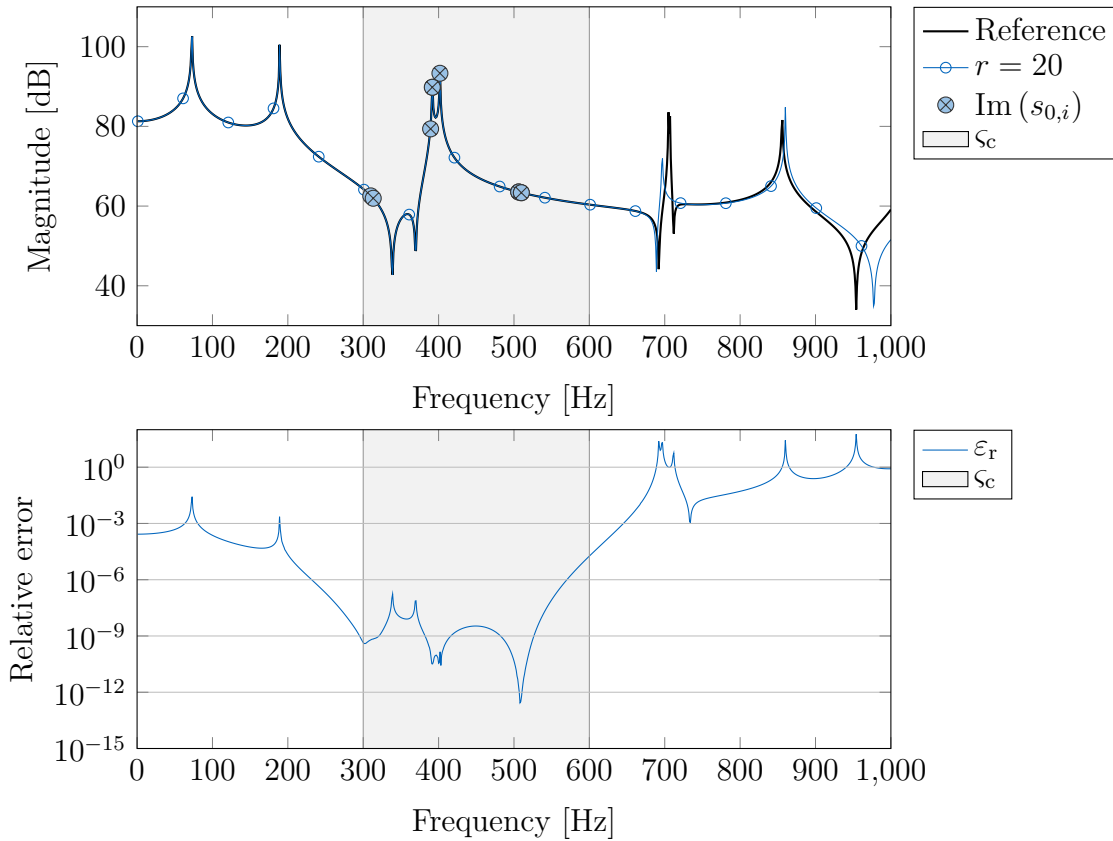


**Figure 4.25:** Transfer functions of the original and a reduced model valid in the range  $\varsigma_c = 2\pi i [300, \dots, 600]$  as well as relative error. The sound transmission problem is reduced to  $r = 20$ , the mirror images of the  $r$  eigenvalues closest to the defined frequency range are considered as expansion points in the next iteration. The convergence interval is marked in gray, filled blue circles mark the imaginary parts of the expansion points.

convergence, new expansion points for  $\Sigma$  with interpolation order  $r_0 = 1$  are established at the locations of the converged interpolation points regarding  $\Sigma_m$  obtained from SO-IRKA. This ensures that all important information from  $\Sigma$  is available in  $\Sigma_m$  and ultimately ensures that the optimal expansion points regarding  $\Sigma_m$  are also optimal regarding  $\Sigma$ . The algorithm terminates if the expansion points obtained from SO-IRKA converge.

The initial intermediate model  $\Sigma_m^0$  computed in algorithm 4.2 line 2 can be obtained using different strategies. One is to use an Arnoldi method to compute also some derivatives of the moments at the initial expansion points  $\mathbf{s}_0$ . The approximation quality is improved near the chosen shifts and although the initial  $\Sigma_m$  is likely to not approximate the original system well, enough information for the SO-IRKA optimization steps is present in the model. Another approach is to perform moment matching around an arbitrary shift  $s_0$  with a large enough interpolation order  $q$ . This is likely to be less computational expensive, but the approximation quality might be acceptable for a smaller frequency range only. The updating

**Algorithm 4.2** Confined IRKA for second order SISO systems, SO-CIRKA

**Require:** Original system  $\Sigma$ ,  $r$  initial expansion points  $\mathbf{s}_0 = [s_{0,1} \ \cdots \ s_{0,r}] \in \mathbb{C}^r$  closed under complex conjugation

**Ensure:** Reduced system  $\Sigma_r$ , error estimation  $\hat{\epsilon}_{\text{CIRKA}}$

- 1:  $i \leftarrow 0$ ,  $\mathbf{s}_0^i \leftarrow \mathbf{s}_0$
- 2: Compute intermediate model  $\Sigma_m^i$
- 3: **while** no convergence **do**
- 4:    $i \leftarrow i + 1$
- 5:    $[\Sigma_r^i, \mathbf{s}_0^i] \leftarrow \text{SO-IRKA}(\Sigma_m^{i-1}, \mathbf{s}_0^{i-1})$
- 6:   Compute  $\hat{\epsilon}_{\text{CIRKA}}$
- 7:   Update intermediate model  $\Sigma_m^i$  with shifts at  $\mathbf{s}_0^i$  regarding  $\Sigma$
- 8: **end while**

of  $\Sigma_m$  in algorithm 4.2 line 7 can be conducted by adding all newly obtained shifts from SO-IRKA to the basis of the intermediate model. Doing so increases the size of  $\Sigma_m$  by  $r$  in each iteration. Typically it is beneficial to add only new shifts in order to keep  $q$  low. Alternatively,  $\Sigma_m$  can be reinitialized using only the newly found interpolation points. This ensures a constant size  $q$  but the approximation quality might decrease for some locations. As the reinitialization based on  $r$  interpolation points must yield a basis of order  $q$ , again derivatives of the moments at the considered shifts need to be considered. An estimation of the approximation error can be obtained in the final step of the algorithm by relating the frequency responses of  $\Sigma_m$  and  $\Sigma_r$  by

$$\hat{\epsilon}_{\text{CIRKA}}(s) = \frac{|H_m(s) - H_r(s)|}{|H_m(s)|}, \quad (4.23)$$

where  $H_m(s)$  is the transfer function of the intermediate model  $\Sigma_m$  and  $H_r$  the reduced model's transfer function [71].

Contrary to the original algorithm, we employ the frequency limited variant of SO-IRKA. Here, the call to SO-IRKA in algorithm 4.2 line 5 also includes the frequency range in which the model should be valid. As described above, the mirror images of the  $r$  eigenvalues closest to the defined range are chosen as new interpolation points, ensuring a good approximation in this frequency range. The initial intermediate model is computed using an Arnoldi method considering the  $r$  initial expansion points  $\mathbf{s}_0$  with an interpolation order  $d$  each, i.e.  $q = rd$ . Updating is performed by augmenting  $\Sigma_m$  by the newly found shifts only.

The performance of the algorithm is presented in a numerical experiment. The sound transmission problem from section 2.5.3 is considered and reduced to  $r = 20$ . The reduced model should be valid in the range  $\zeta_c = 2\pi i [300, \dots, 600]$  and an initial interpolation order  $d = 5$  is chosen. The 10 initial expansion points are distributed linearly in the range

$\mathbf{s}_0 = \pm 2\pi i [300, \dots, 600]$ . The projection is performed using *tsreal*. The results are presented in fig. 4.26. Contrary to standard SO-IRKA tuned to be valid in the same frequency range in fig. 4.25, considerably less decompositions of the full-order matrices are required. Standard SO-IRKA performed 100 decompositions of size  $n$  matrices until convergence to obtain the reduced model presented in fig. 4.25, which has a relative error norm  $\|\varepsilon_r\| = 1.73 \cdot 10^{-8}$  in the desired range of approximation. The confined algorithm only required the solution of 40 full-order systems, while the relative error norm  $\|\varepsilon_r\| = 1.74 \cdot 10^{-8}$  is comparable. Additionally, the error estimation  $\hat{\varepsilon}_{\text{CIRKA}}$  automatically obtained during CIRKA iterations shows a good accordance to the actual relative approximation error  $\varepsilon_r$ .

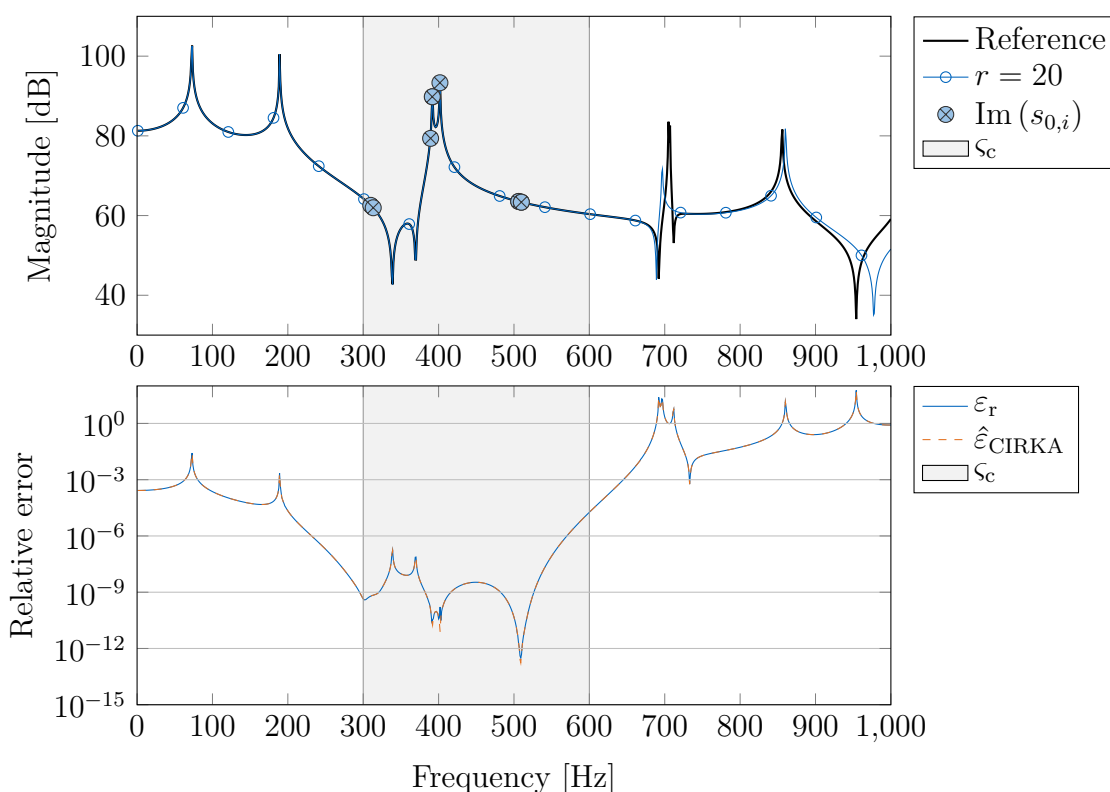


**Figure 4.26:** Transfer functions of the original and a reduced model obtained from algorithm 4.2 as well as relative error  $\varepsilon_r$  and its estimation  $\hat{\varepsilon}_{\text{CIRKA}}$ . The original system is reduced to  $r = 20$ , the mirror images of the  $r$  eigenvalues closest to the frequency range  $\mathcal{S}_c = \pm 2\pi i [300, \dots, 600]$  are considered as expansion points in the next SO-IRKA iteration inside the CIRKA algorithm. The convergence interval is marked in gray, filled blue circles mark the imaginary parts of the expansion points.

### 4.3.2 Choice of initial expansion points

Another way to reduce the computational cost of IRKA or its variants is to make an educated guess regarding the initial expansion points. If, for example, similar systems have been

evaluated before, important features of the transfer function may be known and the initial expansion points can be put in regions with large influence on the dynamic response. This is believed to ensure a fast convergence, as the mirror images of the system poles coincide with optimal expansion points for IRKA. Additionally, the mode count can be a hint for a reasonable size of the reduced model, which needs to be defined before starting the reduction process. The following idea, originally presented in Aumann and Müller: “A-priori pole selection for reduced models in vibro-acoustics” (2019) [22], can be applied to vibro-acoustic systems and utilizes analytic considerations about the number and location of modes. The number of mode shapes, i.e. how many wave lengths  $\lambda$  fit into a specific part of a system’s geometry, can be deduced from geometrical and material properties of the considered system. From this number, the amount of modes in a frequency band can be determined, which can be an educated guess for initial expansion points used in an IRKA framework. For a one-dimensional system of length  $l$ , the wavelength of the  $N$ th mode is given by

$$\lambda_N = \frac{2l}{N + \delta_{BC}}, \quad (4.24)$$

where the term  $\delta_{BC}$  incorporates the effects of boundary conditions. The mode count function relating number of modes to wave number  $k = \frac{2\pi}{\lambda}$  is thus given by

$$N(k)^{1d} = \frac{kl}{\pi} + \delta_{BC}. \quad (4.25)$$

The superscript  $1d$  indicates the problem dimension. For a simply supported 1d system,  $\delta_{BC,s} = 0$ , for a system clamped at one end and no constraint at the other end,  $\delta_{BC,c} \approx \frac{(2N-1)\pi}{2} - N$  [62]. Similar relations for various types of systems can be derived and are found, for example, in [87, 172].

A procedure to obtain an educated guess for initial expansion points used in combination with SO-IRKA or its frequency limited variant presented in the preceding sections is sketched in the following: We first choose the frequency range  $[f_{\min}, f_{\max}]$  in which the reduced model should be valid. Now the mode count in this frequency region  $\Delta N$  is evaluated as

$$\Delta N = N(f_{\max}) - N(f_{\min}), \quad (4.26)$$

where the specific functions for  $N$  are chosen according to the system’s geometry. As many expansion points as computed modes are then distributed linearly within the frequency range and SO-IRKA is started to match the original system’s moments in the specified frequency range.

The strategy is now applied to the sound transmission problem described in section 2.5.3

in order to find a reasonable reduced order  $r$ . The model consists out of two acoustic cavities and two elastic plates, so the mode count functions for these subsystems need to be evaluated. For clamped plates, the bending mode count is given by

$$N(f) = \frac{k(f)^2 A}{4\pi} + 1, \quad \text{with } k(f) = \left( \frac{48\rho(1-\nu^2)\pi^2 f^2}{Eh^2} \right)^{1/4}, \quad (4.27)$$

where  $A$  is the area of the plate,  $\rho$  material density,  $\nu$  Poisson's ratio,  $E$  Young's modulus, and  $h$  plate thickness (c.f. eq. (2.47)). Other types of modes are not present in the considered frequency range and are thus omitted. The mode count for an acoustic cavity of volume  $V$  is obtained from

$$N(f) = \frac{4\pi f^3 V}{3(K/\rho)^{1.5}}, \quad (4.28)$$

where  $K$  is the acoustic fluid's bulk modulus and  $\rho$  its density. We aim for a reduced model valid up to 1000 Hz and obtain a mode count for the complete system of  $N = 46$ . SO-IRKA is started with 46 initial expansion points in complex conjugate pairs distributed linearly in the range  $\mathbf{s}_0 = \pm 2\pi i [1, \dots, 1000]$ . Convergence was reached after six iterations, the transfer functions of the reduced model and the corresponding relative error are given in fig. 4.27. The error is sufficiently low in the desired frequency range having a norm of  $\|\varepsilon_r\| = 3.60 \cdot 10^{-5}$ , indicating that the mode count was a good a-priori measure to estimate the required reduced order. Additionally, no expansion points lie outside of the desired frequency range, so the reduced order is not overestimated. Note, that adding a tolerance to the computed mode count might help increasing the accuracy near the boundaries of the frequency range. Again, the distribution of the expansion points is directly related to the frequency range in which the reduced model is accurate. This can also be used as a corrective measure to check if the mode count did underestimate the required number of expansion points.

### 4.3.3 Conclusive remarks

We presented specializations of the general IRKA framework making it a valuable tool for the reduction of vibro-acoustic systems. The frequency limited approximation possible with the SO-IRKA variant is especially interesting for systems with very local effects, for example local resonances. Rather than choosing the new expansion points only based on their location, the approach could be extended to consider also the dominance of the respective poles. Doing so would consider the expansion points with potentially the highest impact in the desired frequency range rather than all expansion points lying inside this region. As the iterations inside IRKA can become computationally costly, the CIRKA approach from [71]

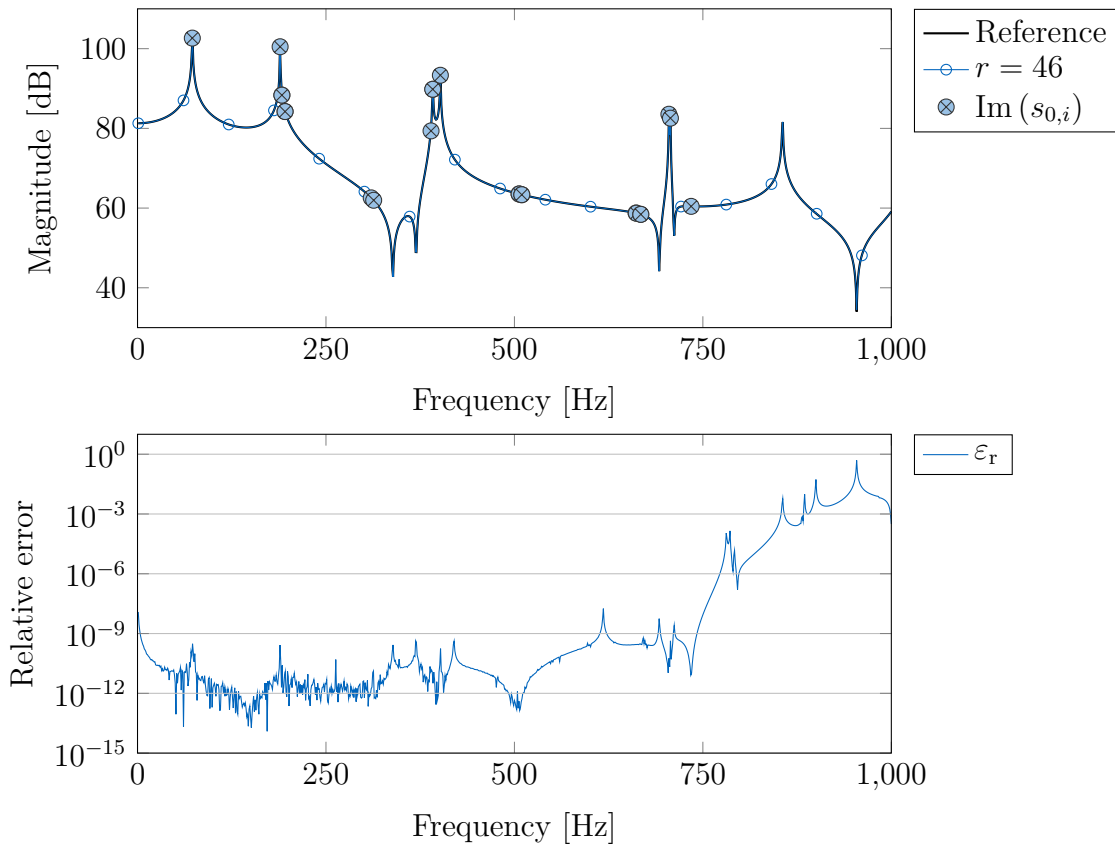


**Figure 4.27:** Transfer functions of the original and a reduced model obtained from algorithm 4.1 as well as relative error. According to the computed mode count, the sound transmission problem is reduced to  $r = 46$ , the mirror images of the  $r$  eigenvalues closest to the imaginary axis are considered as expansion points in the next iteration.

has been extended to be used with second-order systems, leading to a considerably lower computational cost. Again, the strategies for matching moments in a specific frequency range only can be applied here.

Another issue was to obtain a reasonable estimate for the required reduced order of a system which should be valid for certain frequencies. Although being a rather specialized method, the mode count provided an appropriate estimate for the reduced order of vibro-acoustic systems. For more complex systems, this measure is not applicable anymore, so other methods need to be employed. The following section presents automatic reduction methods applicable to more general systems.

## 4.4 Automatic model order reduction for vibro-acoustic systems

Rules regarding a reasonable reduced order and optimal placement of the expansion points for moment matching model order reduction methods are typically only valid for very specific cases. Therefore, considerable effort has been put in the design of adaptive algorithms enabling an automatic generation of high quality reduced models given as few input parameters as possible, in the best case only the frequency range, in which the surrogate should be valid. If such algorithms are employed during the design phase of structures, another goal is that they should be computationally less expensive than solving the full model, as this solution would make the exact approximation error (3.5) available and an estimation of it would not be necessary anymore. A variety of such adaptive methods has been proposed [63, 64, 81, 102, 109, 135, 221, 272]. They rely on estimating the reduction error  $\varepsilon(s)$  which is given for a SISO system by

$$\hat{\varepsilon}(s) \approx \varepsilon(s) = (H(s) - H_r(s))u(s). \quad (4.29)$$

The correct and efficient estimation of the approximation error is still an open issue and a variety of error estimators has been established for different kinds of problems. Grimme [124] introduced two heuristic methods to estimate the approximation error of reduced models. One is based on comparing different reduced models of the same original system. If both reduced models exhibit the same behavior, it is argued that both models appropriately approximate the full system's response. This method has been used, for example, in [130, 270, 272]. The second approach is using the residuals of the reduced system to estimate the exact residual. Both methods are independent of the employed model order reduction method and can be applied in a variety of cases. Additional error estimators based on residual expressions of the reduced system applicable to any projection-based reduction method have been presented by Feng and Benner [108]. If a Krylov subspace is used for reduction, an analytic expression for the approximation error of the reduced system at the location of matched moments can be derived [63, 64, 81]. The location of modes of structural dynamical systems has been used to define an error estimator in [155]. The modes of the reduced system are partitioned into modes located in a frequency range of interest and modes lying outside this range. Using only the modes inside the frequency range of interest and transforming the reduced model to modal coordinates (c.f. section 2.4.2), an estimation for the approximation error can be derived [101, 105, 156].

Contrary to estimating the approximation error, bounds for this error can be derived for some cases. An error bound  $\tilde{\varepsilon}(s)$  ensures, that the approximation error is always below that

bound, i.e.  $\varepsilon \leq \tilde{\varepsilon}$ . While this is desirable as it is always on the safe side, many error bounds for moment matching model order reduction are difficult to obtain or lack tightness [252]. This means, that the actual error may be overestimated and leads to potentially inefficient reduced models. Some error bounds not depending on a certain reduction method have been proposed in [106]. An error bound for second order systems is presented in [202], but the system has to be transformed into a strictly dissipative state space realization destroying its second order structure. Another error bound for second-order systems is proposed in [101]; however, the—at least approximate—computation of Gramians is required here. Note that error bounds are always available if balanced truncation methods are employed. This comes, however, at the cost of explicitly computing the Gramians, which is computationally demanding [199]. In the following section 4.4.1, different methods for estimating the error of vibro-acoustic systems are presented. It is assumed, that the solution of the full order model is not available. The potential of the estimation methods lies in using them in an adaptive procedure. In an adaptive multi-point reduction scheme, the interpolation order of expansion points lying near a region where a high error is estimated are increased, or a new expansion point is introduced inside this region to get a better approximation of the full system.

Examples for such algorithms are presented in sections 4.4.2 and 4.4.3. Alternative approaches for automatic model order reduction based on SO-IRKA and truncation of Krylov vectors are presented in sections 4.4.3 and 4.4.4. Sections 4.4.1 and 4.4.2 are mainly based on Aumann and Müller: “Robust error assessment for reduced order vibro-acoustic problems” (2020) [23]. All following numerical experiments are implemented in Matlab® R2020a and performed on a machine equipped with an Intel® Xeon®Gold 6136 CPU @ 3.0 GHz and 256 GB RAM.

### 4.4.1 Estimation of the approximation error

#### Residual approach

A classical method estimating the error of a reduced system utilizes the right and left residuals. For a second-order system, they are given by

$$\begin{aligned} \mathbf{r}_f(s) &= \mathbf{f} - \mathcal{K}(s) \mathbf{V}_{\mathbf{x}_r}(s), \\ \mathbf{r}_g(s) &= \mathbf{g}^\top - \mathcal{K}(s)^\mathbf{H} \mathbf{W}_{\mathbf{x}_r}(s), \end{aligned} \tag{4.30}$$

with  $\mathcal{K}(s) = s^2\mathbf{M} + s\mathbf{C} + \mathbf{K}$ . They can be computed without large costs using matrix-vector products. Using the residuals, the exact approximation error  $\varepsilon$  can be expressed as

$$\varepsilon(s) = \mathbf{r}_g^H \mathcal{K}(s)^{-1} \mathbf{r}_f. \quad (4.31)$$

Due to the matrix inverse in eq. (4.31), the error cannot be computed for large systems, but the residuals normalized by system input and output respectively can be used as an error estimate following

$$\begin{aligned} \hat{\varepsilon}_{r,f}(s) &= \frac{\|\mathbf{r}_f(s)\|}{\|\mathbf{f}\|}, \\ \hat{\varepsilon}_{r,g}(s) &= \frac{\|\mathbf{r}_g(s)\|}{\|\mathbf{g}^T\|}, \end{aligned} \quad (4.32)$$

where  $\|\square\|$  is a suitable norm. A small residual at a certain frequency  $s_i$  typically implies a good approximation around  $s_i$ . However, this is not valid, if  $s_i$  is near a pole of the system, as the values of  $\mathcal{K}(s)^{-1}$  get very high and a small residual can still correspond to a large model error [124]. Practically, using the residual as an error estimator in a vibro-acoustic setting can yield very promising results [135]. In an adaptive scheme, a new expansion point for a multi-point moment-matching scheme is added at the location with the highest relative residual  $\hat{\varepsilon}_r$  until the residual at all evaluation points lies beneath a specified threshold.

An analytic expression for the moment error  $\varepsilon$  at the expansion point of an Arnoldi method has been derived in [81] and has been adapted for second order systems with proportional damping by [64]. The expression can be computed cheaply during an Arnoldi method iteratively increasing the order of the reduced model and it shows the exact error of the reduced model at the expansion point for the next iteration. Motivated by this expression, an error estimator which can be computed by matrix vector products and the solution of one linear system of order  $r$  has been proposed by Bodendiek and Bollhöfer [63] and is outlined in the following. The norm of the approximation error (4.29) is bounded by

$$\|\mathbf{y}(s) - \mathbf{y}_r(s)\| \leq \tilde{\varepsilon}_m(s) = \left\| \mathbf{g} \mathcal{K}(s)^{-1} \right\| \|\mathbf{r}_m(s)\|, \quad (4.33)$$

with  $\mathcal{K}(s) = s^2\mathbf{M} + s\mathbf{C} + \mathbf{K}$  and  $\mathbf{r}_m(s) = \mathbf{f} - \mathbf{H}(s) \mathbf{V} \mathcal{K}_r(s)^{-1} \mathbf{W}^H \mathbf{f}$ , where  $\mathcal{K}_r(s) = s^2\mathbf{M}_r + s\mathbf{C}_r + \mathbf{K}_r$ . For a proof see [63]. Instead of computing the bound (4.33) with the full system  $\mathcal{K}(s)$ , using the reduced system  $\mathcal{K}_r(s)$ , as in

$$\|\mathbf{y}(s) - \mathbf{y}_r(s)\| \approx \hat{\varepsilon}_m(s) = \left\| \mathbf{g}_r \mathcal{K}_r(s)^{-1} \right\| \|\mathbf{r}_m(s)\|, \quad (4.34)$$

yields an estimate of the model error  $\hat{\varepsilon}_m(s)$ . This expression is no bound for the error, but it

highlights regions with a potentially high approximation error, if the reduced model captures the most important characteristics of the original system.

### Complementary approximations

An alternative way for estimating the model error is given by the difference of the transfer functions of two different reduced SISO models  $H_{r,1}(s)$  and  $H_{r,2}(s)$ :

$$\hat{\varepsilon}_c(s) = H_{r,1}(s) - H_{r,2}(s). \quad (4.35)$$

The reduced models do not have to be computed by the same reduction method. The estimate is based on the assumption that if  $H_{r,1}(s)$  and  $H_{r,2}(s)$  differ, at least one of the two reduced model does not approximate the original system well. If both reduced models converge to the same transfer function,  $\hat{\varepsilon}_c$  diminishes and it is argued that both approximate the transfer function of the original system. As the method is heuristic, it may be possible, that both reduced models miss important features of the full system's response but still converge to the same transfer function. This cannot be detected without knowledge of the original system response and results in an incorrect estimation of the approximation error.

Instead of comparing two completely different reduced models, Grimme [124] proposed to compare  $H_{r,1}(s)$  to the transfer function  $H_{r,12}(s)$  of a reduced model built combining the reduction bases of the two complementary models. The combination of both bases results in a better approximation of the full system, so the comparison (4.35) is assumed to be nearer to the true error. Another modification is to compare not two completely different reduced models but two models of different reduced order, based on the same expansion points [40]. This has lower computational costs, as increasing the order of a Krylov subspace does not necessarily involve full system decompositions. This approach can easily be used in an iterative method to find the appropriate size of a reduced order model. If the difference between the transfer functions of two models sharing the same expansion points but having different orders diminishes, it is assumed that further increasing the order does not increase the approximation quality and the reduced model is sufficiently accurate in the vicinity of the matched poles. However, it cannot be ruled out, that some features of the full system are missing in the reduced model, making the estimate incorrect. To minimize this risk, both strategies can be combined: two independent models are created at interlaced expansion points and their order is increased iteratively. The reduced model is considered accurate in a specific frequency region, if both models converge to the same frequency response under a certain tolerance [272].

### 4.4.2 A greedy algorithm for automatic model order reduction

The error estimators presented above can be employed in automatic model reduction approaches. In the following, we present an iterative algorithm, which finds new expansion points in a greedy way in order to create a reduced model valid in a predefined frequency region  $\varsigma_c = [s_{\min}, s_{\max}]$ , similar to the methods from [63, 252]. Greedy methods are heuristic approaches aiming at finding a local optimum for the posed problem at each step. This means they do not always find the best solution to a problem, in global sense, but are typically quicker than global approaches [61]. In the scope of automatic model order reduction, the greedy aspect of many algorithms is to establish a new interpolation point at the location where the estimated approximation error is maximal. Such algorithms typically consist out of the following steps: Starting with an initial expansion point, the interpolation order is iteratively increased. Between the iterations, one of the error estimation methods presented above is employed to detect convergence or stagnation. In the case of stagnation, i.e. the estimated approximation error does not change if the reduced order is increased, a new expansion point is chosen at the location, where the maximum error is estimated. Iteration is stopped, if a defined maximal reduced order is reached or the error is estimated to be sufficiently low. Algorithm 4.3 sketches the procedure. Here, the two-level orthogonal Arnoldi (TOAR) procedure [171] is employed to compute the Krylov bases. Algorithm 4.3 can also be modified in order to start with multiple initial expansion points. In this case, initial projection bases have to be computed before starting the optimization loop in algorithm 4.3 line 2.

We apply the algorithm in combination with different error estimation methods described above to evaluate it regarding its efficiency to create reduced models of vibro-acoustic systems. We consider the vibrating beam from section 2.5.1 as an academic example and the sound transmission problem from section 2.5.3 as a more applied example. The error estimators  $\hat{\epsilon}_c$  based on complementary approximations eq. (4.35),  $\hat{\epsilon}_{r,f}$  based on the right residual 4.32, and  $\hat{\epsilon}_m$  inspired by the moment error eq. (4.34) are employed. Each reduced model is computed to be valid in a predefined frequency range  $\varsigma_c = [s_{\min}, s_{\max}]$  and the initial expansion point is chosen as  $s_0 = \sqrt{s_{\min}s_{\max}}$  as recommended in [63]. This range is directly fed into algorithm 4.3 and the error estimators are evaluated at 100 linearly distributed frequencies in  $\varsigma_c = [s_{\min}, s_{\max}]$ .

**Vibrating beam** We consider a system modeling the vibrating beam described in section 2.5.1. A full order of  $n = 600$  is chosen for the following experiments. The convergence interval is set to  $\varsigma_c = 2\pi i [0, 1600]$ ; the greedy algorithm starts with order  $r_0 = 2$  and increases to  $r_m = 10$  in steps of 4. The convergence tolerance of all methods is set to  $\epsilon_{\text{tol}} = 1 \cdot 10^{-8}$ .

**Algorithm 4.3** Greedy method for expansion point selection

**Require:** Original system  $\Sigma$ , initial expansion point  $s_{0,0}$ , frequency range  $\varsigma_c = [s_{\min}, s_{\max}]$ , tolerance  $\varepsilon_{\text{tol}}$ , minimum and maximum interpolation orders  $r_0$  and  $r_m$ , maximum global reduced order  $r_{\max}$

**Ensure:** Reduced system  $\Sigma_r$ , error estimation  $\hat{\varepsilon}$

```

1:  $i \leftarrow 0$ ,  $\hat{\varepsilon}_r \leftarrow 1$ ,  $r_i \leftarrow r_0$ 
2: while  $\hat{\varepsilon} > \varepsilon_{\text{tol}}$  do
3:    $[\mathbf{V}_i, \mathbf{W}_i] \leftarrow \text{TOAR}(\Sigma, s_{0,i}, r_i)$ 
4:    $\mathbf{V} \leftarrow \text{orth}(\mathbf{V}_0, \dots, \mathbf{V}_i)$ ,  $\mathbf{W} \leftarrow \text{orth}(\mathbf{W}_0, \dots, \mathbf{W}_i)$ 
5:   Compute error estimator  $\hat{\varepsilon}$  in range  $[s_{\min}, s_{\max}]$ 
6:   if  $r_i < r_m$  then
7:     Increase  $r_i$ 
8:   else
9:      $s_{i+1} \leftarrow \arg \max_{s \in \varsigma_c} \hat{\varepsilon}_r$ 
10:     $r_{i+1} \leftarrow r_m$ 
11:     $i \leftarrow i + 1$ 
12:   end if
13:   if  $\sum_{j=0}^i r_j > r_{\max}$  then
14:     break
15:   end if
16: end while
17: Project  $\Sigma$  using  $\mathbf{V}$ ,  $\mathbf{W}$  to obtain  $\Sigma_r$ 

```

The projection is performed following *osrealinput*, thus a real-valued basis is considered and by setting  $\mathbf{W} = \mathbf{V}$ , the symmetry of the original system is retained in the reduced space. Table 4.1 compares the different reduction methods according to the reduced order necessary to achieve convergence in the proposed interval  $r$ , norm of the relative approximation error  $\|\varepsilon_r(s)\|$  in the convergence interval  $\varsigma_c$ , and computation time  $t_c$ .

**Table 4.1:** Comparison of reduced models for the vibrating beam computed with algorithm 4.3 and different error estimators. Order of the reduced model  $r$ , norm of the approximation error  $\|\varepsilon_r(s)\|$  in the convergence interval  $\varsigma_c = 2\pi i [0, 1600]$ , and computation time  $t_c$ .

Method	$r$	$\ \varepsilon_r(s)\ $	$t_c$ [s]
$\hat{\varepsilon}_c$	22	$5.91 \cdot 10^{-7}$	0.06
$\hat{\varepsilon}_{r,f}$	32	$8.49 \cdot 10^{-7}$	0.75
$\hat{\varepsilon}_m$	16	$8.49 \cdot 10^{-7}$	0.19

All methods converge and create reduced models achieving a sufficiently low approximation error in the frequency range of interest. The transfer function and approximation errors are given in fig. 4.28. The greedy method employing  $\hat{\varepsilon}_m$  converges to the smallest reduced model of order  $r = 16$ , while the model created with  $\hat{\varepsilon}_c$  has order  $r = 22$  but the computation time

is the lowest.  $\hat{\varepsilon}_{r,f}$  needs more iterations to reach convergence, resulting in a larger reduced model and a longer computation time.  $\hat{\varepsilon}_c$  only requires the solution of a linear system of order  $r$  for error assessment, while  $\hat{\varepsilon}_{r,f}$  and  $\hat{\varepsilon}_m$  perform additional matrix vector products of order  $n$ . Given that all reduced models have a comparable accuracy, no benefit of the residual based error bounds compared to complementary approximations can be observed for this model.

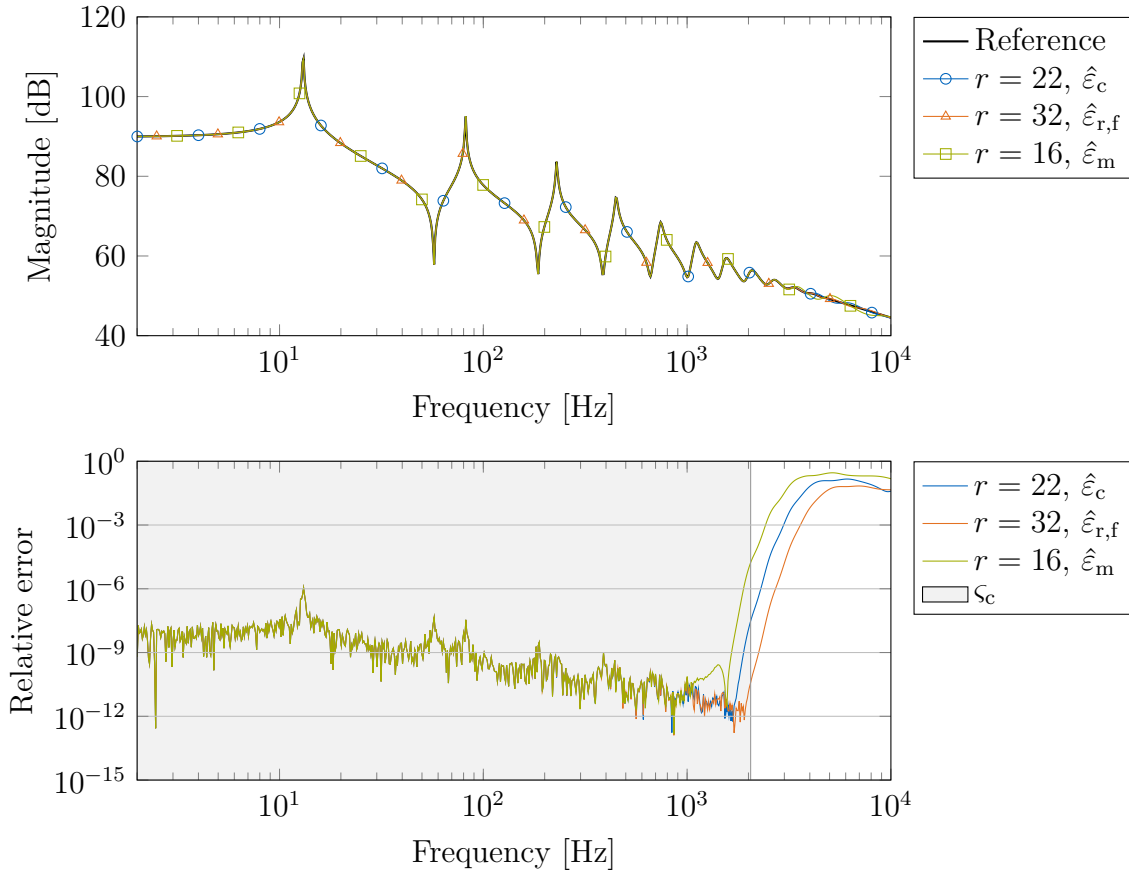


**Figure 4.28:** Transfer functions and relative errors of reduced models for the beam model computed with algorithm 4.3 employing the error estimators  $\hat{\varepsilon}_c$ ,  $\hat{\varepsilon}_{r,f}$ , and  $\hat{\varepsilon}_m$ . The convergence interval is set to  $S_c = 2\pi i [0, \dots, 1600]$ .

**Sound transmission problem** We now consider the sound transmission problem from section 2.5.3. In the first example, the convergence interval is chosen to be  $S_c = 2\pi i [0, \dots, 500]$ ; the evaluation of the full order model in this frequency range takes  $t_c = 6.79 \cdot 10^4 \text{ s} \approx 18.9 \text{ h}$ . The projection is performed following *tsreal*, retaining the realness of the original system. A two-sided interpolation is chosen because the original system is non-symmetric. The greedy algorithm 4.3 starts with order  $r_0 = 6$  and increases it to  $r_n = 18$  in steps of 4. The convergence tolerance the method employing the complementary approximations  $\hat{\varepsilon}_c$  is set to

$\varepsilon_{\text{tol}} = 1 \cdot 10^{-5}$ ; the other methods' tolerances are set to  $\varepsilon_{\text{tol}} = 1 \cdot 10^{-3}$ , as they have been found to overestimate the actual reduction error. Table 4.2 compares the different reduction methods according to reduced order necessary to achieve convergence in the proposed interval  $r$ , norm of the relative approximation error  $\|\varepsilon_r(s)\|$ , and computation time  $t_c$ .

**Table 4.2:** Comparison of reduced models for the sound transmission problem computed with algorithm 4.3 and different error estimators. Order of the reduced model  $r$ , norm of the relative approximation error  $\|\varepsilon\|$  in convergence interval  $\varsigma_c = 2\pi i [0, \dots, 500]$ , and computation time  $t_c$ .

Method	$r$	$\ \varepsilon_r(s)\ $	$t_c$ [s]
$\hat{\varepsilon}_c$	32	$3.05 \cdot 10^{-4}$	647
$\hat{\varepsilon}_{r,f}$	42	$4.06 \cdot 10^{-10}$	1013
$\hat{\varepsilon}_m$	54	$4.07 \cdot 10^{-10}$	1124

All methods yield accurate reduced models at convergence capturing the important features of the original transfer function. However,  $\hat{\varepsilon}_c$  underestimates the actual approximation error and yields a reduced model with a higher error norm than required. The error plots in fig. 4.29 show, that the double peak around 400 Hz is not approximated as accurate by this reduced model as by the other two models. The greedy algorithm employing error estimator  $\hat{\varepsilon}_c$  computes its reduced model in the shortest time with the lowest order  $r = 32$ , but has the highest error. Both error estimators  $\hat{\varepsilon}_{r,f}$  and  $\hat{\varepsilon}_m$  take longer to converge and result in larger reduced models of orders  $r = 42$  and  $r = 54$  respectively. Both models have much lower errors than the required tolerance. This is the result of an overestimation of the actual approximation error by these estimators. Additionally to requiring more iterations until convergence, the computation of the more computationally demanding error estimator at 100 sampling points in the frequency region of interest in each iteration adds to the longer computation times compared to  $\hat{\varepsilon}_c$ .

The same system is now reduced to a model which should be valid in the frequency range  $\varsigma_c = 2\pi i [300, \dots, 600]$  also using *tsreal*. The evaluation of the full order model in this frequency range takes  $t_c = 6.33 \cdot 10^4 \text{ s} \approx 17.6 \text{ h}$ . Again, algorithm 4.3 starts with order  $r_0 = 6$  and increases the interpolation order to  $r_n = 18$  in steps of 4 before establishing a new shift. The convergence tolerance for the algorithm employing  $\hat{\varepsilon}_c$  is set to  $\varepsilon_{\text{tol}} = 1 \cdot 10^{-5}$  respectively to  $\varepsilon_{\text{tol}} = 1 \cdot 10^{-3}$  for the other two methods. Table 4.3 compares the different reduction methods according to reduced order necessary to achieve convergence in the proposed interval  $r$ , norm of relative approximation error  $\|\varepsilon_r(s)\|$  in the range  $\varsigma_c = 2\pi i [300, \dots, 600]$ , and computation time  $t_c$ .

All methods create reduced models with sufficient accuracy, the error plot is presented in fig. 4.30. Again, the error estimation based on complementary approximations creates a small

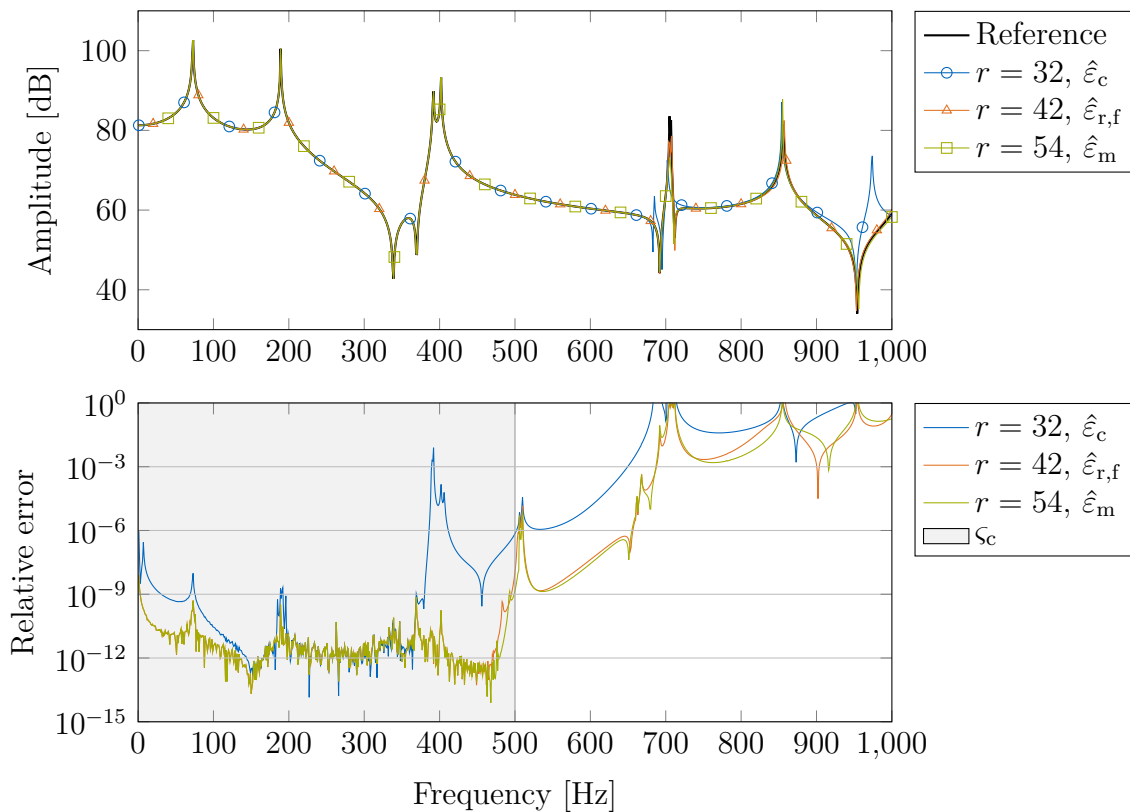


**Figure 4.29:** Transfer functions and relative errors of reduced models for the sound transmission model computed with algorithm 4.3 employing the error estimators  $\hat{\epsilon}_c$ ,  $\hat{\epsilon}_{r,f}$ , and  $\hat{\epsilon}_m$ . The convergence interval is set to  $\zeta_c = 2\pi i [0, \dots, 500]$ .

reduced model with  $r = 32$  in the fastest time compared to the other estimation methods. All features of the transfer function could be captured and the actual approximation error is below the specified tolerance in the convergence region. The models created using  $\hat{\epsilon}_{r,f}$  and  $\hat{\epsilon}_m$  have higher orders of  $r = 60$  while their approximation error is not considerably lower. All error estimation methods overestimate the actual error in the specified frequency range.

#### 4.4.3 Frequency windowing for automatic model order reduction

We now present an alternative method to automatically compute reduced models valid in a specified frequency range. Here, the range is divided in frequency windows, each associated with a corresponding expansion point at the center frequency. The procedure is outlined in algorithm 4.4 and is based on Aumann et al.: “Automatic model order reduction for systems with frequency dependent material properties” (2021) [19]. It can be summarized as follows: One or more locations for initial expansion points are defined and intermediate reduced models are obtained which are used to compute the error estimation. For each expansion point, a local subspace and the corresponding reduced model is computed. For each pair of adjacent

**Table 4.3:** Comparison of reduced models of the sound transmission problem valid in  $\varsigma_c = 2\pi i [300, \dots, 600]$  computed with algorithm 4.3 and different error estimators. Order of the reduced model  $r$ , norm of the relative approximation error  $\|\varepsilon_r(s)\|$  in the convergence interval, and computation time  $t_c$ .

Method	$r$	$\ \varepsilon_r(s)\ $	$t_c$ [s]
$\hat{\varepsilon}_c$	32	$3.84 \cdot 10^{-10}$	677
$\hat{\varepsilon}_{r,f}$	60	$1.67 \cdot 10^{-10}$	1444
$\hat{\varepsilon}_m$	60	$1.67 \cdot 10^{-10}$	1411

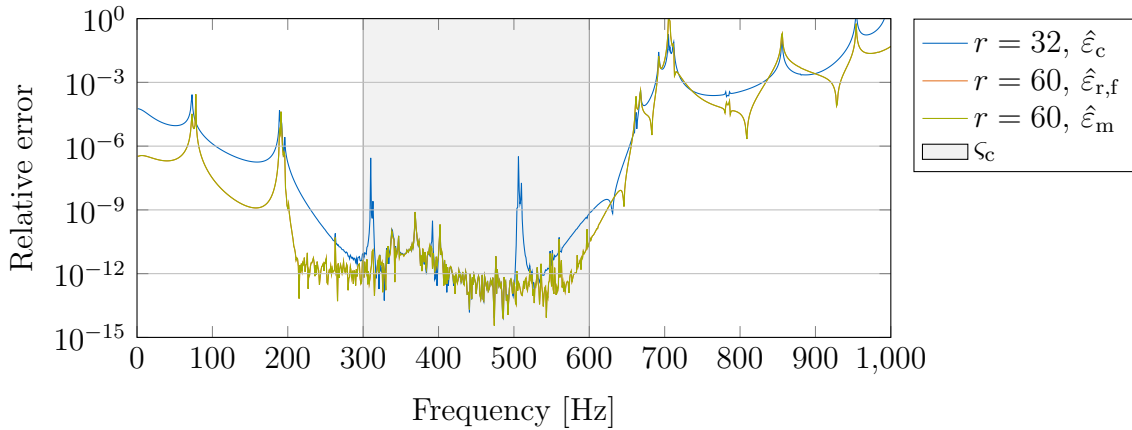


**Figure 4.30:** Relative errors of the reduced models for the sound transmission model computed with algorithm 4.3 employing the error estimators  $\hat{\varepsilon}_c$ ,  $\hat{\varepsilon}_{r,f}$ , and  $\hat{\varepsilon}_m$ . The convergence interval is set to  $\varsigma_c = 2\pi i [300, \dots, 600]$ .

expansion points, the corresponding intermediate reduced models are used to estimate the approximation error in the frequency range between the two expansion points according to  $\hat{\varepsilon}_c(s)$  given by eq. (4.35). If both reduced models have, under a specified tolerance, similar transfer functions in this frequency region, this region is considered sufficiently accurate and both local subspaces are combined in an orthonormal subspace. The involved subspaces are flagged as inactive, meaning the orders of the respective expansion points are not increased anymore, as this would not lead to a higher accuracy in the area between them. If the estimated error between the two shifts is not below the specified tolerance, the interpolation order at both shifts is increased. After all individual subspaces have been processed, a global reduction basis is computed from all local subspaces and the global error estimator  $\hat{\varepsilon}_{c,g}(s)$  is evaluated. If the estimated error is higher than the specified tolerance, the order of the subspace with the corresponding expansion point located next to the highest estimated error is increased. If the maximum estimated approximation error is located next to the same expansion point for consecutive iterations and is not improving, a stagnation is assumed. In this case, a new expansion point is established, rather than increasing the order  $r$  of the

respective subspace. Additionally, the order at a specific expansion point is increased up to a defined maximal order only. If the highest estimated error is between two expansion points with maximal order or between one expansion point with maximal order and a boundary of the frequency range, a new shift is introduced between these locations. Also if all local subspaces are combined and flagged as inactive and the estimated error is higher than the specified tolerance, a new expansion point is established at the location where  $\hat{\varepsilon}_{c,g}(s)$  has its maximum value. If the estimated error is below the defined tolerance or the maximum number of iterations has been reached, the final reduced model is computed using the current global basis.

The presented adaptive procedure is used to automatically compute reduced models of the poroacoustic system described in section 2.5.5. The reduced model is computed to be valid in  $s = 2\pi i [1, \dots, 800]$ . The algorithm is tested with Krylov space orders from  $k = 2$  to  $k = 8$  and three configurations of initial expansion points are considered. The expansion points are distributed linearly in the frequency range  $s = 2\pi i [100, \dots, 800]$  and  $n_s = 4$ ,  $n_s = 5$ , and  $n_s = 6$  initial shifts are considered. The frequency range is chosen to start at 100 Hz rather than at 1 Hz, because approximating the frequency dependent functions with a shift in the low frequency region leads to an unstable representation in the higher frequency region (c.f. fig. 4.17). In order to obtain this information, only AAA evaluations are required, which can be computed without large computational costs. The initial order of each shift is  $r_0 = 50$ . The interpolation order at the shifts is increased in steps of  $r_{\text{incr}} = 10$  up to a maximum of  $r_{\text{max}} = 100$ . New shifts are established with an initial order of  $r_{\text{min}} = 10$ . The tolerance of the algorithm is set to  $\varepsilon_{\text{tol}} = 1 \cdot 10^{-5}$  and the algorithm terminates after 25 iterations.

The results for the numerical experiments are reported in table 4.4, where the size of the resulting reduced order models  $r$ , the maximum error  $\varepsilon$  and its estimation  $\hat{\varepsilon}_1$  in the considered frequency range, the overall computation time  $t_c$ , and the required iterations are given for the three starting configurations and different orders of employed Krylov spaces  $k$ . The results are also given in graphical form in figs. 4.31 to 4.33, where the required computation time and reduced order are compared to the obtained maximum relative error for each considered order of the employed Krylov subspace  $k$ .

Most configurations yield reduced models with a maximum error lower than the defined threshold, only the configurations  $n_s = 4$ ,  $k = 3$  and  $n_s = 5$ ,  $k = 2$  did not converge in less than 25 iterations and thus yield models with a higher maximum error. The error estimation also performs acceptable. Although the estimator tends to underestimate the exact approximation error, they are in the same order of magnitude. A higher increment  $r_{\text{incr}}$  of interpolation order potentially leads to a better error estimation at the cost of larger reduced order models. The benefit of a higher order  $k$  of the employed Krylov spaces lies in the smaller size of the resulting reduced models. These models have approximation errors

**Algorithm 4.4** Adaptive subspace computation.

**Require:** Original system  $\Sigma$ , initial expansion points  $s_{0,i}$ ,  $i = 1, \dots, p$  with corresponding initial orders  $r_{0,i}$ , frequency range  $\varsigma_c = [s_{\min}, s_{\max}]$ , minimum and maximum expansion point order  $r_{\min}$ ,  $r_{\max}$ , order increment  $r_{\text{incr}}$ , tolerance  $\varepsilon_{\text{tol}}$

**Ensure:** Reduced system  $\Sigma_r$

```

1: while  $\max(\hat{\varepsilon}_{c,g}(s)) > \varepsilon_{\text{tol}}$  do
2:   Compute  $\Sigma_{r,i}$  for each  $s_{0,i}$  and corresponding  $r_i$ 
3:   Compute  $\hat{\varepsilon}_{c,ij}(s)$  for each pair of adjacent  $s_{0,i}$  and  $s_{0,j}$ 
4:   if  $\hat{\varepsilon}_{c,ij}(s) < \varepsilon_{\text{tol}}$  then
5:     Combine subspaces for  $\Sigma_{r,i}$  and  $\Sigma_{r,j}$ 
6:     Flag combined subspaces inactive
7:   else
8:      $r_i \leftarrow r_i + r_{\text{incr}}$ ,  $r_j \leftarrow r_j + r_{\text{incr}}$ 
9:   end if
10:  Compute global subspace from all active local subspaces and reduce  $\Sigma$ 
11:  Compute global error estimator  $\hat{\varepsilon}_{c,g}(s)$  in  $\varsigma_c$ 
12:  Find  $s_{0,j}$  which location is next to  $\max \hat{\varepsilon}_{c,g}(s)$ 
13:  if  $r_j < r_{\max}$  then
14:    if Stagnation then
15:      Add new expansion point at  $\max \hat{\varepsilon}_{c,g}(s)$ 
16:    else
17:       $r_j \leftarrow r_j + r_{\text{incr}}$ 
18:    end if
19:  else
20:    Find  $s_{0,k}$  which location is on the opposite side of  $\max \hat{\varepsilon}$  regarding  $s_{0,j}$ 
21:    if  $r_k < r_{\max}$  then
22:       $r_k \leftarrow r_k + r_{\text{incr}}$ 
23:    else
24:      Add new expansion point at  $\max \hat{\varepsilon}_{c,g}(s)$ 
25:    end if
26:  end if
27:  if All local subspaces are flagged inactive then
28:    Add new expansion point at  $\max \hat{\varepsilon}_{c,g}(s)$ 
29:  end if
30: end while
31: Compute  $\Sigma_r$  with the global subspace

```

in a similar range than larger reduced models obtained using Krylov spaces with  $k = 2$  or  $k = 3$ . The computation times, however, tend to be higher with increasing  $k$ , even if the resulting reduced model is smaller. The choice for either a higher subspace order  $k$  or lower computation time should be motivated from the actual application case of the reduced model. The initial configurations also have an influence on the resulting reduced models, again depending on the order  $k$  of the employed Krylov spaces. Starting with four expansion

**Table 4.4:** Results of the adaptive algorithm applied to the poroacoustic model regarding the three initial configurations and different Krylov space orders  $k$ . Reported are the order of the resulting reduced order models  $r$ , the maximum error  $\varepsilon$  and its estimate  $\hat{\varepsilon}_1$  in the considered frequency range, the overall computation time  $t_c$ , and the number of iterations.

$n_s$	$k$	$r$	$\max \varepsilon$	$\max \hat{\varepsilon}_1$	$t_c$ [s]	Iterations
4	2	500	$4.16 \cdot 10^{-4}$	$9.08 \cdot 10^{-6}$	2143.1	16
	3	590	$2.80 \cdot 10^{-3}$	$2.76 \cdot 10^{-3}$	3134.2	25
	4	370	$5.08 \cdot 10^{-6}$	$3.51 \cdot 10^{-6}$	2217.7	8
	5	290	$2.71 \cdot 10^{-5}$	$9.24 \cdot 10^{-6}$	1996.6	8
	6	330	$4.25 \cdot 10^{-6}$	$3.28 \cdot 10^{-6}$	2602.3	8
	7	280	$8.83 \cdot 10^{-7}$	$2.73 \cdot 10^{-6}$	2501.7	8
	8	280	$1.65 \cdot 10^{-6}$	$1.38 \cdot 10^{-6}$	2752.5	8
	5	2	690	$2.31 \cdot 10^{-2}$	$4.82 \cdot 10^{-3}$	3391.7
3		470	$1.32 \cdot 10^{-5}$	$7.72 \cdot 10^{-6}$	2321.9	8
4		380	$4.18 \cdot 10^{-4}$	$7.91 \cdot 10^{-6}$	2288.9	6
5		290	$2.44 \cdot 10^{-7}$	$3.80 \cdot 10^{-7}$	2011.8	4
6		330	$9.14 \cdot 10^{-7}$	$3.68 \cdot 10^{-7}$	2632.7	8
7		330	$5.81 \cdot 10^{-7}$	$4.52 \cdot 10^{-7}$	2926.9	8
8		330	$1.05 \cdot 10^{-6}$	$1.88 \cdot 10^{-7}$	3235.2	8
6		2	600	$2.34 \cdot 10^{-5}$	$5.87 \cdot 10^{-6}$	2094.1
	3	460	$1.26 \cdot 10^{-5}$	$8.09 \cdot 10^{-6}$	2067.5	4
	4	360	$3.80 \cdot 10^{-7}$	$1.83 \cdot 10^{-7}$	2210.3	5
	5	330	$7.50 \cdot 10^{-7}$	$4.57 \cdot 10^{-7}$	2241.8	3
	6	330	$9.71 \cdot 10^{-7}$	$4.85 \cdot 10^{-7}$	2508.8	3
	7	350	$6.28 \cdot 10^{-7}$	$2.48 \cdot 10^{-7}$	3102.6	5
	8	330	$6.56 \cdot 10^{-7}$	$3.41 \cdot 10^{-7}$	3106.8	3

points distributed in the frequency range of interest yields the smallest reduced models, apart from the not converged experiment  $n_s = 4$ ,  $k = 3$ . For  $k > 3$ . For the configuration with  $n_s = 6$ , only a few iterations are required to achieve convergence. Here, the initial condition is already a reasonably accurate model for higher orders  $k$ .

#### 4.4.4 Automatic approximation in a frequency range using SO-IRKA

An alternative approach to automatically find an appropriate size for a reduced model is based on an extension of SO-IRKA. This approach is presented in the following section and is based on Aumann and Müller: “An adaptive method for reducing second-order dynamical systems” (2021) [21]. It is based on the fact, that an eigenvalue decomposition of a second-order system yields twice as many eigenvalues as the size of the system. By choosing a

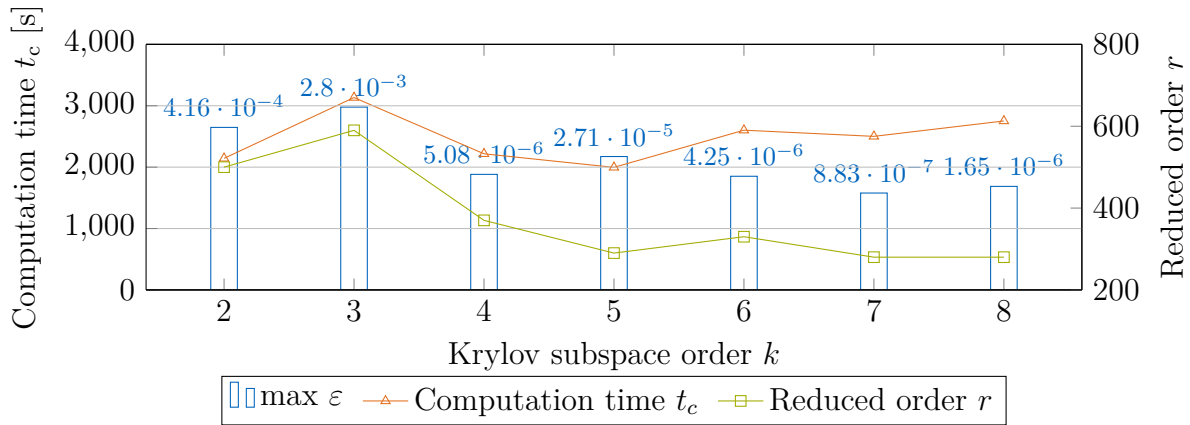


**Figure 4.31:** Comparison of required computation time  $t_c$  and resulting reduced order  $r$  to the obtained maximum relative errors for the starting configuration with  $n_s = 4$  expansion points.

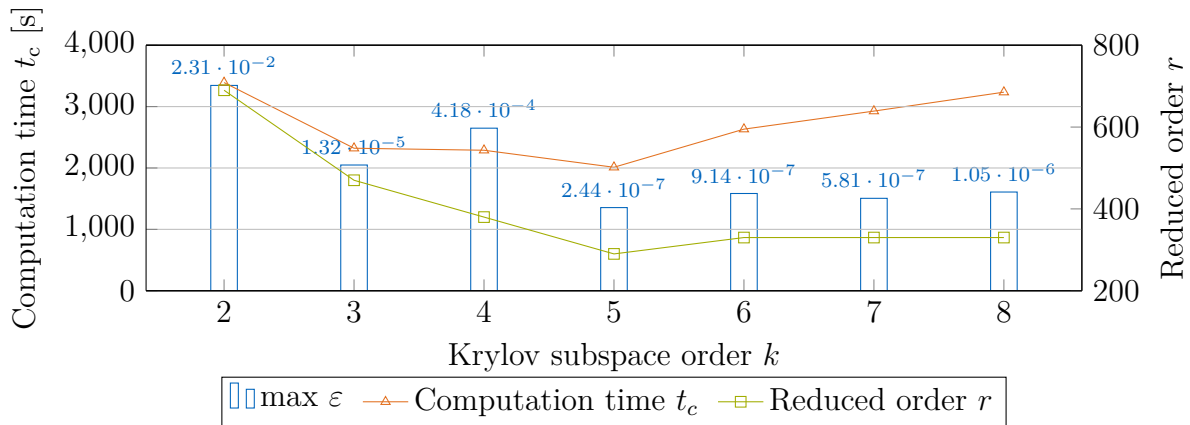


**Figure 4.32:** Comparison of required computation time  $t_c$  and resulting reduced order  $r$  to the obtained maximum relative errors for the starting configuration with  $n_s = 5$  expansion points.

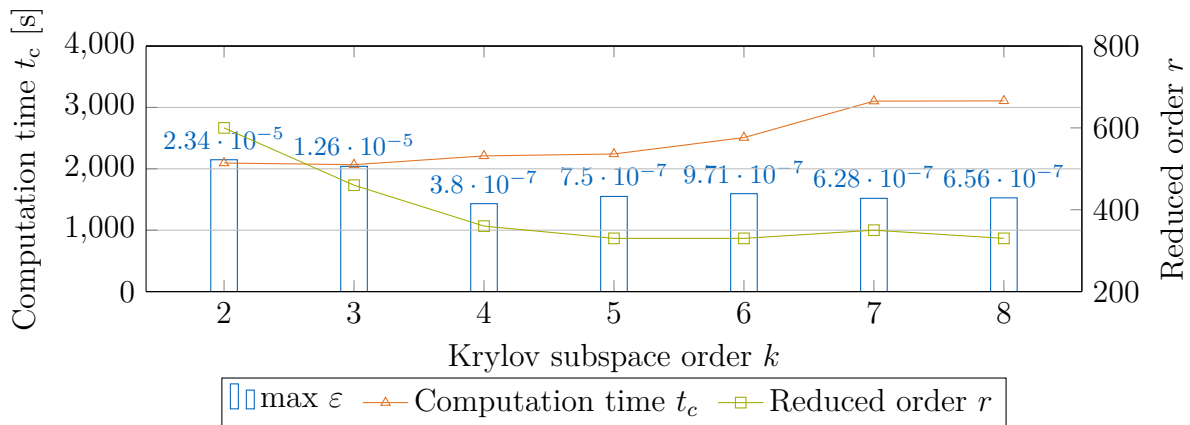


**Figure 4.33:** Comparison of required computation time  $t_c$  and resulting reduced order  $r$  to the obtained maximum relative errors for the starting configuration with  $n_s = 6$  expansion points.

suitable subset during each iteration, the required order of the reduced model to be accurate

in a specific frequency region can be found in an adaptive way. As IRKA's optimization steps to obtain reasonable expansion point locations for the reduced order model involve the solution of linear equation systems of the size of the full-order model, its computational cost is often high. To reduce these costs, we apply SO-CIRKA given in algorithm 4.2. The only input to the proposed model order reduction method apart from the original system is a frequency range  $\varsigma_c = [\omega_{\min}, \omega_{\max}]$ , making the algorithm applicable without requiring a-priori knowledge about the full order model.

The frequency-limiting of the reduced model regarding a frequency range not necessarily starting at zero is achieved as follows: Extending the idea from Aumann and Müller [22], we choose such pairs of eigenvalues for updating the expansion points in each iteration of SO-IRKA which mirror images lie in  $\varsigma_c$ . This can be achieved by adapting SO-IRKA (c.f. algorithm 4.1) as shown in algorithm 4.5. At convergence, this modified variant of SO-IRKA yields a reduced model being valid in this specified frequency range, as it was shown in section 4.3. Rather than choosing  $r$  updated expansion points during each iteration, we now determine a suitable size for the reduced order model by considering the locations of all  $2r$  eigenvalues  $\lambda_{2r}$ . This is motivated by the argument, that a reduced model is not likely to be able to approximate a system in a complete specified frequency range, if all its eigenvalues lie inside this range. So instead of selecting a subset of  $\lambda_{2r}$  with fixed size  $r$  as potential locations for new expansion points, all mirror images of eigenvalues lying in the frequency range of interest are considered for the next iteration. Doing so increases the size of the reduced model and this is repeated until at least one pair of eigenvalues lies outside  $\varsigma_c$ . It is argued that the reduced model is now large enough to capture all important dynamics of the original model in the desired frequency range. After having obtained this reduced order  $r$ , again only  $r$  eigenvalues from  $\lambda_{2r}$  are considered as locations for expansion points during the next iterations until convergence is reached.

The frequency-limiting behavior is revisited by the following numerical example. The model of the cantilevered beam from section 2.5.1 with modified cross section width and height  $a = 0.001$  m is reduced using algorithm 4.1 to obtain a model valid in the frequency range  $\varsigma_c = 2\pi [1000, 2000]$ . The algorithm finds two pairs of eigenvalues lying in the specified frequency range and thus yields a reduced model of order  $r = 4$ . Its transfer function and the corresponding approximation error are given in fig. 4.34. It can be seen, that the reduced model approximates the original system in the specified frequency range, but the approximation quality deteriorates near the boundaries of  $\varsigma_c$ . Therefore, another reduced model is computed where not only the shifts located inside of  $\varsigma_c$  are considered but also the two pairs lying left and right of the interval. This yields a reduced model of order  $r = 8$  which approximates the full order model in  $\varsigma_c$  with higher accuracy than the model with  $r = 4$ .

**Algorithm 4.5** Adaptive variant of SO-IRKA

**Require:** Original system  $\Sigma$ ,  $r_0$  initial expansion points  $\mathbf{s}_0 = [s_{0,1} \ \cdots \ s_{0,r}] \in \mathbb{C}^r$  closed under complex conjugation, frequency range  $\varsigma_c = [s_{\min}, s_{\max}]$

**Ensure:** Reduced system  $\Sigma_r$

1: **while** no convergence **do**

2:   Compute projection bases

$$\mathbf{V} = \left[ \left( s_{0,1}^2 \mathbf{M} + s_{0,1} \mathbf{C} + \mathbf{K} \right)^{-1} \mathbf{f} \ \cdots \ \left( s_{0,r}^2 \mathbf{M} + s_{0,r} \mathbf{C} + \mathbf{K} \right)^{-1} \mathbf{f} \right]$$

$$\mathbf{W} = \left[ \left( s_{0,1}^2 \mathbf{M} + s_{0,1} \mathbf{C} + \mathbf{K} \right)^{-H} \mathbf{g}^H \ \cdots \ \left( s_{0,r}^2 \mathbf{M} + s_{0,r} \mathbf{C} + \mathbf{K} \right)^{-H} \mathbf{g}^H \right]$$

3:   Orthogonalize bases  $\mathbf{V} = \text{orth}(\mathbf{V})$ ,  $\mathbf{W} = \text{orth}(\mathbf{W})$

4:    $\mathbf{M}_r = \mathbf{W}^H \mathbf{M} \mathbf{V}$ ,  $\mathbf{C}_r = \mathbf{W}^H \mathbf{C} \mathbf{V}$ ,  $\mathbf{K}_r = \mathbf{W}^H \mathbf{K} \mathbf{V}$

5:   Solve the quadratic eigenvalue problem  $(\mathbf{M}_r \lambda^2 + \mathbf{C}_r \lambda + \mathbf{K}_r) \mathbf{x} = 0$

6:   Choose  $\boldsymbol{\lambda}_{\text{new}}$  from  $\boldsymbol{\lambda}_{2r}$  such that  $\boldsymbol{\lambda}_{\text{new}} \leftarrow \|\boldsymbol{\lambda}_{2r}\| \subset [s_{\min}, s_{\max}]$

7:   Update expansion points  $\mathbf{s}_0 \leftarrow -\boldsymbol{\lambda}_{\text{new}}$

8: **end while**

9: Project  $\Sigma$  using  $\mathbf{V}$ ,  $\mathbf{W}$  to obtain  $\Sigma_r$

Considering the observations from fig. 4.34, the two pairs of eigenvalues lying left and right of the frequency range of interest are also considered in algorithm 4.5 to compute the projection basis. This increases the approximation quality near the boundaries of  $\varsigma_c$  and should provide a safe estimation for  $r$ . If an estimate for the required order of the reduced model is available, the algorithm can be provided with it to speed up convergence. Otherwise, it is started with two pairs of expansion points located at  $[\pm i\omega_{\min}, \pm i\omega_{\max}]$ . Additionally, we make use of CIRKA to be able to perform the optimization loop on a reduced model of intermediate size. Algorithm 4.2 can directly be employed but instead of standard SO-IRKA, the adaptive and frequency-limited variant algorithm 4.5 is called inside CIRKA. In the following, the initial intermediate model is computed using TOAR. At each initial expansion point  $s_{0,i}$ , with  $i = 1, \dots, r$ , a local Krylov space with interpolation order  $d$  is computed and their bases are concatenated to obtain the global projection matrices  $\mathbf{V}, \mathbf{W} \in \mathbb{C}^{n \times rd}$ . After the adaptive SO-IRKA converges, the error estimator eq. (4.23) is evaluated in the frequency range of interest  $\varsigma_c$ . This estimate is used as a measure for convergence of the outer CIRKA iterations and the algorithm is stopped, if it falls under a certain threshold for all points inside  $\varsigma_c$ . If no convergence is reached, both schemes to update the intermediate basis described in section 4.3.1 can be employed.

In the following, we evaluate the effectiveness of the adaptive variant of SO-IRKA by computing reduced models valid in a specific frequency range without pre-defining a reduced order  $r$ . Additionally, its computational cost is compared to employing CIRKA in

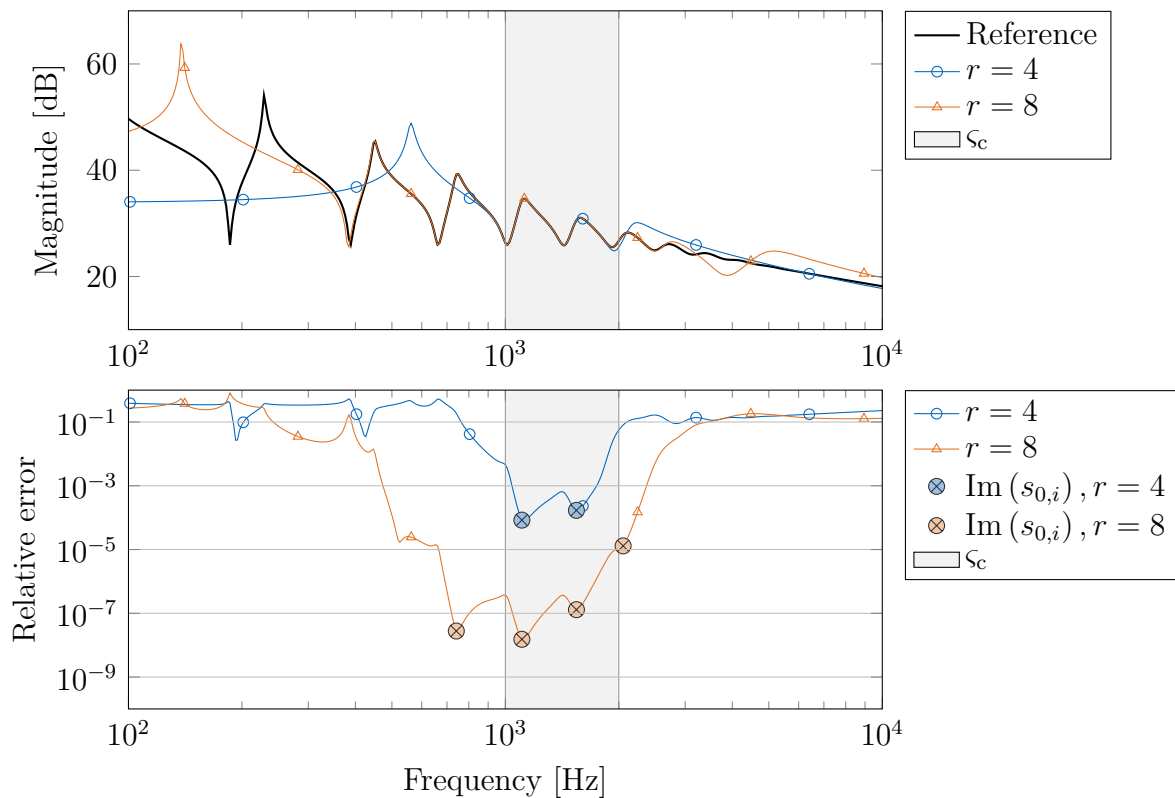


**Figure 4.34:** Transfer functions and relative errors of two reduced models of the cantilevered beam obtained from algorithm 4.5 with the locations of the expansion points and the frequency range of interest  $\zeta_c$ .

combination with adaptive SO-IRKA. All following numerical experiments are conducted on a workstation with an Intel<sup>®</sup> Xeon<sup>®</sup> CPU E5-2620 v3 @ 2.4 GHz and 96 GB RAM using Matlab<sup>®</sup> R2020a. The only parameter provided to the algorithms is the frequency range  $\zeta_c = [\omega_{\min}, \omega_{\max}]$ , the order is automatically obtained during the procedures. The initial expansion points are chosen as  $[\pm i\omega_{\min}, \pm i\omega_{\max}]$  and CIRKA is considered converged if the estimated error eq. (4.23) is smaller than  $\tau = 1 \cdot 10^{-3}$  in  $\zeta_c$ .

We start by considering the frequency range between  $\omega_{\min} = 2\pi \cdot 1 \text{ rad s}^{-1}$  and  $\omega_{\max} = 2\pi \cdot 500 \text{ rad s}^{-1}$ . The transfer functions and corresponding relative errors of the reduced models obtained from CIRKA employing the adaptive SO-IRKA and adaptive SO-IRKA alone are reported in fig. 4.35. The reduced models obtained from SO-IRKA and CIRKA with augmenting the intermediate-sized model's basis after each run of SO-IRKA (marked by CIRKA aug.) show comparable relative errors which are low over the complete frequency range of interest. The reduced model computed with CIRKA using the update strategy re-initializing the intermediate bases after each inner run of SO-IRKA (marked by CIRKA res.) has a lower overall approximation quality. The relative error is especially high near the

double peak in the transfer function at 400 Hz.

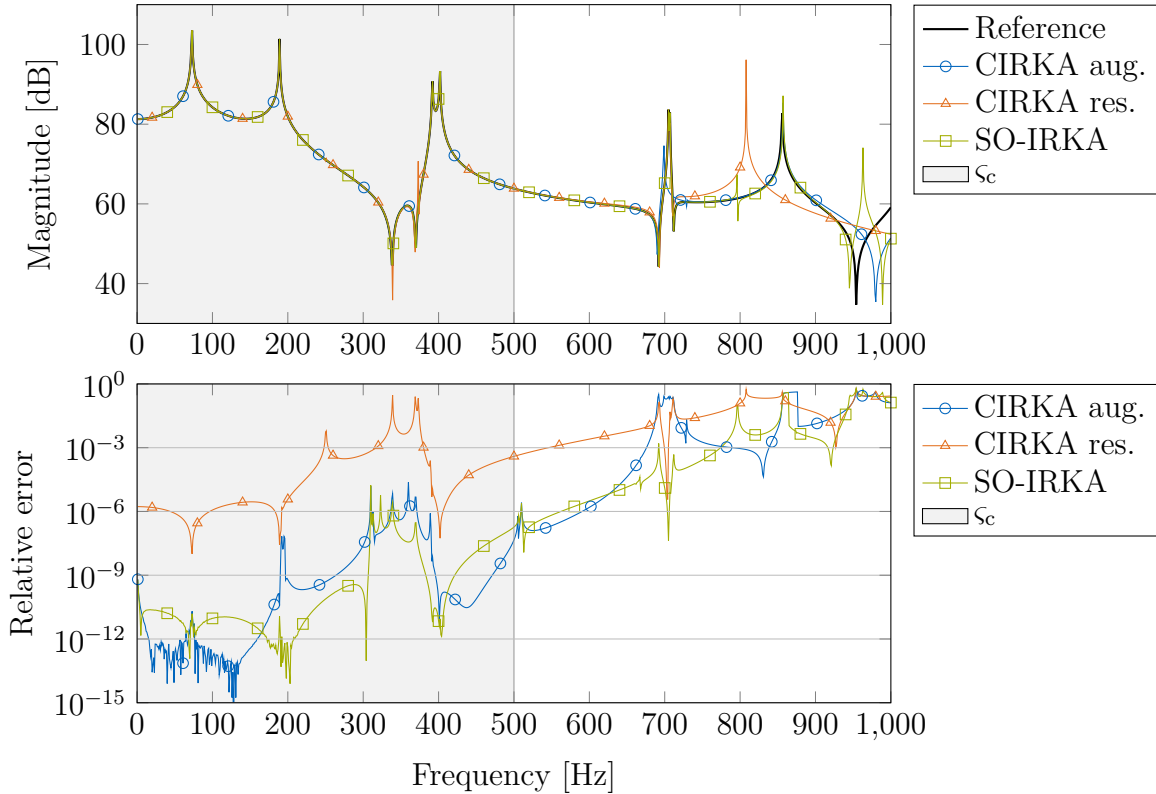


**Figure 4.35:** Transfer functions and relative errors of reduced models of the sound transmission problem valid in  $\varsigma_c = 2\pi [1, 500]$  obtained from the adaptive algorithms.

The resulting reduced orders  $r$ , maximal relative errors in the frequency range of interest  $\max \varepsilon_r$ , and the number of required decompositions of matrices of order  $n$ ,  $n_{LU}$ , are given in table 4.5. While SO-IRKA and CIRKA aug. yield models with similar accuracy and reduced orders  $r$ , the re-initialization of the intermediate model's basis after each inner run of SO-IRKA leads to a smaller reduced order  $r$  but also the maximal error is magnitudes higher than for the other models. SO-IRKA requires  $n_{LU} = 186$  decompositions of full order matrices until convergence is reached, more than ten times as many as the methods based on CIRKA.

**Table 4.5:** Comparison of the different reduced models valid in  $\varsigma_c = 2\pi [1, 500]$ .

Method	$r$	$\max \varepsilon_r$	$n_{LU}$
CIRKA aug.	22	$2.37 \cdot 10^{-5}$	14
CIRKA res.	10	$2.97 \cdot 10^{-1}$	14
SO-IRKA	24	$1.73 \cdot 10^{-5}$	186

In a second example we apply the same algorithms to obtain a model valid in the range

$\varsigma_c = 2\pi [700, 1000]$ . A double peak in the transfer function is located near the lower bound of the range, so the benefit of including the two nearest outlying pairs of eigenvalues as locations for expansion points can be evaluated. All three algorithms yield models approximating the original transfer function in  $\varsigma_c$  and their transfer functions as well as relative errors are given in fig. 4.36. Again, CIRKA aug. performs well with low errors in the desired frequency range. SO-IRKA alone and CIRKA res. yield similar results having both a peak in the relative error near the anti-resonance at 950 Hz.

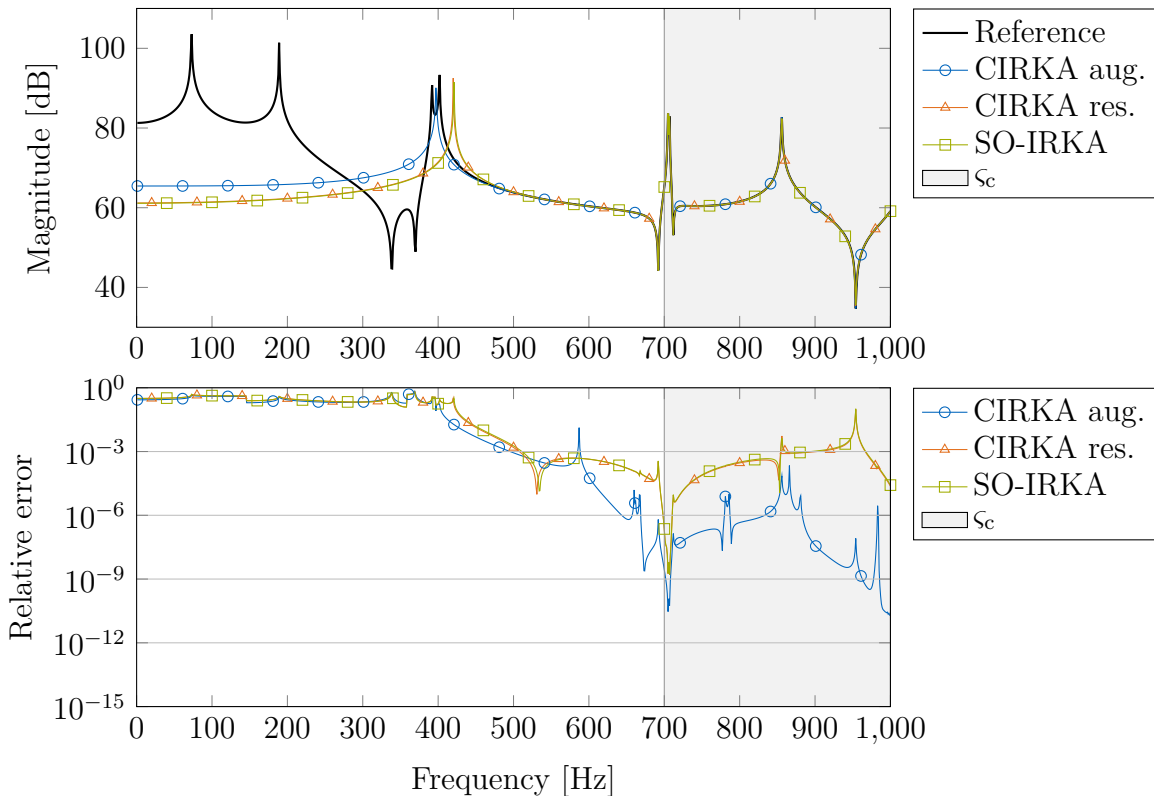


**Figure 4.36:** Transfer functions and relative errors of reduced models of the sound transmission problem valid in  $\varsigma_c = 2\pi [700, 1000]$  obtained from the adaptive algorithms.

The reduced orders and maximal relative errors of the three resulting models are reported in table 4.6. Both SO-IRKA and CIRKA res. yield models with a reduced order  $r = 10$ , while the model obtained from CIRKA aug. has an order of  $r = 28$ . However, the maximal error is much lower in this case while still requiring less matrix decompositions than SO-IRKA without CIRKA. The overall higher errors compared to the previous example can be explained by the fact, that less modes are located in this frequency range, requiring the individual shifts to approximate a wider frequency range.

**Table 4.6:** Comparison of the different reduced models valid in  $\varsigma_c = 2\pi [700, 1000]$ .

Method	$r$	$\max \varepsilon_r$	$n_{LU}$
CIRKA aug.	28	$2.19 \cdot 10^{-4}$	28
CIRKA res.	10	$9.51 \cdot 10^{-2}$	14
SO-IRKA	10	$1.03 \cdot 10^{-1}$	40

#### 4.4.5 Conclusive remarks

Different algorithms to automatically compute reduced order models relying on as few a-priori information as possible have been presented in the preceding section. First, we presented some techniques to assess the approximation error of reduced order models and a greedy algorithm to use them in an automatic reduction framework, which does not need many inputs from the user. Only by specifying the convergence interval, in which the reduced model should be valid, reduced models of vibro-acoustic systems can be created automatically with high accuracy in a reasonable time. All presented error estimators were able to guide the greedy algorithm towards reasonable expansion points, also resulting in accurate reduced models. However, the estimators based on moment error and residual lack tightness and the models created with these estimators tend to be larger. Comparing complementary approximations of two reduced models with increasing order was found to provide the best trade-off between model accuracy and computation time. Important features of the transfer functions of all considered models could properly be reproduced by this method. Instead of a greedy method, a windowing approach can be more suited for models where a high accuracy is required for a wide frequency range. High quality reduced models incorporating frequency dependent material properties could be computed using this approach. Additionally, the number and location of eigenvalues of a reduced system computed during SO-IRKA can provide a measure for an appropriate reduced order. Only specifying the range, reduced models of the beam and the sound transmission problem could be obtained with high accuracy. The use of CIRKA succeeded at decreasing the computational cost required by the adaptive variant of SO-IRKA.

## 5 Parametric model order reduction for vibro-acoustic systems

Many vibro-acoustic systems depend on a set of parameters which is subject to optimization during the design phase of engineering structures. This optimization regarding, for example, the noise and vibration of vehicles towards a high level of comfort for the passengers, requires many repeated evaluations of high fidelity models under varying parameters. Such parameters can include material properties, locations of excitation, or variations in the model geometry. The transfer function of a SISO second-order parametric system is given by

$$H(s, \mathbf{p}) = \mathbf{g}(\mathbf{p}) \left( s^2 \mathbf{M}(\mathbf{p}) + s \mathbf{C}(\mathbf{p}) + \mathbf{K}(\mathbf{p}) \right)^{-1} \mathbf{f}(\mathbf{p}), \quad (5.1)$$

where all system matrices, the input, and the output vector are depending on a set of parameters  $\mathbf{p}$ . Because of the high computational costs of the high fidelity models and the need of their repeated evaluation, low dimensional representations retaining the dominant features of the original model are required.

Parametric model order reduction methods achieve this by, for example, combining the projection bases obtained for different parameter realizations of the full model [47]. Many of these methods require an affine representation of the parametric system, i.e. the parameter dependence can be expressed by functions which are multiplied with constant matrices (c.f. eq. (3.56)). Such representations can often be acquired if the parameters are material constants, but are typically hard or inefficient to obtain for geometric parameters. Data-driven methods do not require insight in the structure of the dynamical system at all and compute parametric reduced models solely based on system output data [68, 143, 190, 218]. However, these methods seldom preserve the structure of the original system. However, specialized methods that obtain also the structure of the original system from data have been proposed [69, 234]. The sampling of the parameter space has a large influence on the quality of the parametric reduced model. Beattie, Gugercin, and Tomljanović [39] proposed a data-driven method retaining the dependence on parameters in reduced space without the need of sampling the parameter space. However, this method requires an affine representation of the original system.

Parametric model order reduction is an important tool enabling an efficient design process of vibro-acoustic systems and its value has frequently been shown: Parametric models of vibrating structures with a radiation boundary condition were computed by van Ophem, Deckers, and Desmet [255] using Krylov subspaces. Here, the original system's parametric dependence is rewritten as additional inputs to the system, allowing the computation of the reduced model without requiring a sampling of the parameter space. A classic parametric reduction method employing quasi-random sampling in the parameter space has been employed in [271] to obtain reduced models of vibrating plates with spatially differing damping properties. Lappano et al. [161] computed reduced models of poroelastic systems using a POD. The method presented in Ullmann, Sicklinger, and Müller [248] combines a Krylov method with adaptive sampling in the parameter space and is therefore able to compute efficient reduced models of systems with a high-dimensional parameter space. Purely data-driven methods based on regression algorithms have been used by Melo Filho et al. [181] to compute a parametric model of a locally resonant structure.

In the following chapter, we will present two strategies to compute reduced models retaining the dependence on one or more parameters from the full order model. The first method utilizes the Loewner framework and its extension to parametric systems. This data-driven method relies on a database of system evaluations, which are obtained from a presampling performed by models reduced with SO-IRKA. Convergence of the algorithm is enhanced by using the converged, i.e. somewhat optimal, expansion points of one parameter combination as starting point for the next IRKA run performed for a model with similar parameters as it is believed to have a similar frequency response. The method is described in section 5.1 along with numerical examples. The second method is also based on SO-IRKA, but can also be used with any moment-matching technique. Here, a regression model is trained to map model parameters to near-optimal locations of expansion points for moment-matching. The method is further outlined in section 5.2 and applied to two parametric models.

## 5.1 Parametric model order reduction using the Loewner framework

This section is based on Aumann, Miksch, and Müller: “Parametric model order reduction for acoustic metamaterials based on local thickness variations” (2019) [20]. The Loewner framework discussed in section 3.6.3 and has already been successfully applied to reduce dynamic and vibro-acoustic systems [120, 165, 208]. In the following, its extension for parametric systems, the parametric Loewner framework, is employed to compute reduced models of vibro-acoustic systems while retaining the dependence on a specified set of parameters

[143]. Transfer function evaluations of the original system under varying parameters are required, which are computationally costly to obtain. We therefore follow an idea from Benner and Grundel [45] to alleviate the computational burden. The main idea is to compute reduced models for a set of parameters using SO-IRKA and use the reduced models to compute the frequency response for each parameter. The obtained data are then used as input for the parametric Loewner framework. The convergence for the different SO-IRKA runs can be accelerated, if the expansion points used at convergence for one parameter are reused as starting point for the following parameters. Often, the overall system response does not change drastically, if a parameter is changed. This is illustrated with an example using the beam model from section 2.5.1. Figure 5.1 shows transfer function evaluations of beams with length  $l = 0.8$  m and quadratic cross sections of different heights  $a_i = [0.005, \dots, 0.05]$  m. It can be observed, that the transfer function peaks of systems based on only slightly varying parameters lie in a similar region. So even while the best IRKA expansion points for one parameter are not necessarily the best for a second parameter, the reused expansion points are a good start for the following iterations and the algorithm probably converges faster.

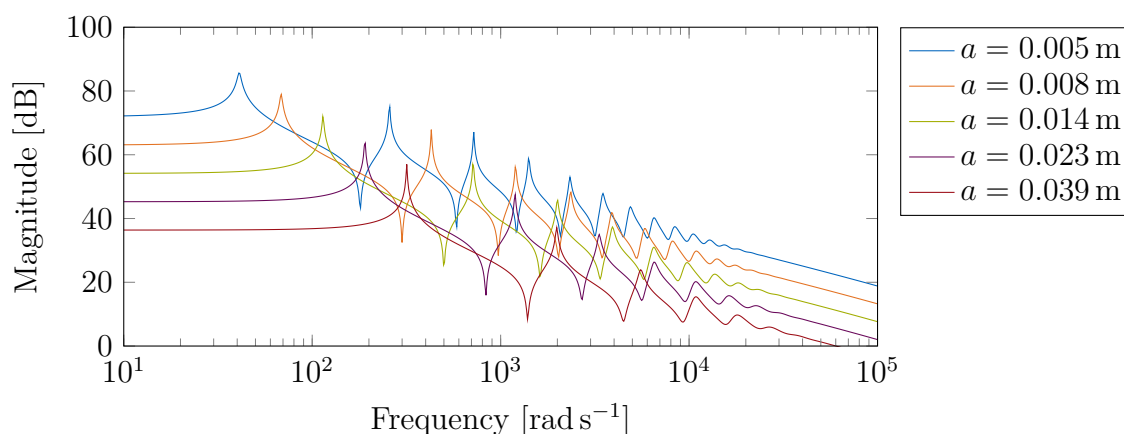


**Figure 5.1:** The frequency response functions of a parametric beam evaluated at different cross section heights  $a$ .

The parametric Loewner framework is the base of the employed model order reduction method and is shortly summarized in the following. The barycentric interpolation formula (3.50) is extended to include not only frequency  $s$  with corresponding expansion points  $s_{0,i}$ , but also parameters  $p$  with expansion points  $\pi_j$ . The two-variable case reads:

$$\phi(s,p) = \sum_{i=1}^{k+1} \sum_{j=1}^{q+1} \frac{\alpha_{ij} y_{ij}}{(s - s_{0,i})(p - \pi_j)} \bigg/ \sum_{i=1}^{k+1} \sum_{j=1}^{q+1} \frac{\alpha_{ij}}{(s - s_{0,i})(p - \pi_j)}, \quad \alpha_{ij} \neq 0, \quad (5.2)$$

where  $k$  and  $q$  are the order in frequency and parameter respectively [9]. The parameters  $\alpha_{ij}$  are obtained as follows: First, transfer function measurements for a set of parameters

$p_j, j = 1, \dots, M$  at frequencies  $s_i, i = 1, \dots, N$  are computed as of eq. (5.1) and partitioned into a matrix  $\Phi$  with entries  $\phi_{ij} = H(s_i, p_j)$ . The partitioning is performed according to

$$\begin{aligned} [s_1, \dots, s_N] &= [s_{0,1}, \dots, s_{0,\bar{n}}] \cup [\sigma_{0,1}, \dots, \sigma_{0,\underline{n}}], \\ [p_1, \dots, p_M] &= [\pi_1, \dots, \pi_{\bar{m}}] \cup [\nu_1, \dots, \nu_{\underline{m}}], \end{aligned} \quad (5.3)$$

where  $\underline{n} + \bar{n} = N$  and  $\underline{n} = \lfloor N/2 \rfloor$  and  $\underline{m} + \bar{m} = M$  and  $\underline{m} = \lfloor M/2 \rfloor$ . The resulting matrix is given by

$$\Phi = \left[ \begin{array}{ccc|ccc} y_{11} & \cdots & y_{1\bar{m}} & \phi_{1,\bar{m}+1} & \cdots & \phi_{1M} \\ \vdots & \ddots & \vdots & \vdots & \ddots & \vdots \\ y_{\bar{n}1} & \cdots & y_{\bar{n}\bar{m}} & \phi_{\bar{n},\bar{m}+1} & \cdots & \phi_{\bar{n}M} \\ \hline \phi_{\bar{n}+1,1} & \cdots & \phi_{\bar{n}+1,\bar{m}} & z_{11} & \cdots & z_{1\underline{m}} \\ \vdots & \ddots & \vdots & \vdots & \ddots & \vdots \\ \phi_{N,1} & \cdots & \phi_{N\bar{m}} & z_{\underline{n}1} & \cdots & z_{\underline{n}\underline{m}} \end{array} \right]. \quad (5.4)$$

The entries in block  $\Phi_{11}$  are the measurements  $y_{ij} = H(s_{0,i}, \pi_j)$ , block  $\Phi_{22}$  contains the measurements  $z_{ij} = H(\sigma_{0,i}, \nu_j)$ . The transfer function samples  $H_{ij}$  can have various origins: results from numerical simulations can be used as well as experimental measurement data or a combination of both. The resulting two-variable Loewner matrix [143] is given by

$$\mathbb{L}_2 = \left[ \begin{array}{cc|cc} \frac{z_{11} - y_{11}}{(\sigma_{0,1} - s_{0,1})(\nu_1 - \pi_1)} & \cdots & \frac{z_{11} - y_{1\bar{m}}}{(\sigma_{0,1} - s_{0,1})(\nu_1 - \pi_{\bar{m}})} & \cdots \\ & & \vdots & \\ \frac{z_{\underline{n}\underline{m}} - y_{11}}{(\sigma_{0,\underline{n}} - s_{0,1})(\nu_{\underline{m}} - \pi_1)} & \cdots & \frac{z_{\underline{n}\underline{m}} - y_{1\bar{m}}}{(\sigma_{0,\underline{n}} - s_{0,1})(\nu_{\underline{m}} - \pi_{\bar{m}})} & \cdots \\ \cdots & \left[ \begin{array}{cc|cc} \frac{z_{11} - y_{\bar{n}1}}{(\sigma_{0,1} - s_{0,\bar{n}})(\nu_1 - \pi_1)} & \cdots & \frac{z_{11} - y_{\bar{n}\bar{m}}}{(\sigma_{0,1} - s_{0,\bar{n}})(\nu_1 - \pi_{\bar{m}})} & \cdots \\ & & \vdots & \\ \frac{z_{\underline{n}\underline{m}} - y_{\bar{n}1}}{(\sigma_{0,\underline{n}} - s_{0,\bar{n}})(\nu_{\underline{m}} - \pi_1)} & \cdots & \frac{z_{\underline{n}\underline{m}} - y_{\bar{n}\bar{m}}}{(\sigma_{0,\underline{n}} - s_{0,\bar{n}})(\nu_{\underline{m}} - \pi_{\bar{m}})} & \cdots \end{array} \right] & \end{array} \right]. \quad (5.5)$$

Analogously to the single-variable case, the coefficients  $\alpha_{ij}$  are obtained from the null space of this matrix, i.e. solving  $\mathbb{L}_2 \alpha = 0$ .

In order to approximate the full order system, from which the measurements in  $\Phi$  are obtained, rather than interpolate its response, Ionita and Antoulas [143] presented  $\widehat{\mathbb{L}}_2$  as a generalization of eq. (5.5). A main idea of this framework is that the required orders to interpolate the underlying data are encoded in  $\mathbb{L}_2$ . For this the order  $k$  associated with

frequency is determined by  $k = \max_j \text{rank } \mathbb{L}_{p_j}$  from the Loewner matrices  $\mathbb{L}_{p_j}$ , which are the  $j$  Loewner matrices obtained from the  $j$  columns of  $\Phi$ . Analogously, order  $q$  in the parameter variable is computed as  $q = \max_i \text{rank } \mathbb{L}_{s_i}$  from the  $i$  Loewner matrices  $\mathbb{L}_{s_i}$  associated with the  $i$  rows of  $\Phi$ . The generalized version  $\widehat{\mathbb{L}}_2$  of eq. (5.5) relying on the partitioning based on  $k$  and  $q$  is given by

$$\widehat{\mathbb{L}}_2 = \left[ \widehat{\mathbb{L}}_\sigma^\top \quad \widehat{\mathbb{L}}_\pi^\top \quad \mathbb{L}_2^\top \right]^\top, \quad (5.6)$$

where

$$\widehat{\mathbb{L}}_\sigma = \begin{bmatrix} \mathbb{L}_{\sigma_1} & & \\ & \ddots & \\ & & \mathbb{L}_{\sigma_{k+1}} \end{bmatrix}, \quad \mathbb{L}_{\sigma_i} = \begin{bmatrix} \frac{\Phi_{12}(i,1) - y_{i1}}{\nu_1 - \pi_1} & \dots & \frac{\Phi_{12}(i,1) - y_{i,q+1}}{\nu_1 - \pi_{q+1}} \\ \vdots & \ddots & \vdots \\ \frac{\Phi_{12}(i,m) - y_{i1}}{\nu_m - \pi_1} & \dots & \frac{\Phi_{12}(i,m) - y_{i,q+1}}{\nu_m - \pi_{q+1}} \end{bmatrix}, \quad (5.7)$$

and

$$\widehat{\mathbb{L}}_\pi = \left[ \begin{array}{c|c|c} \mathbb{L}_{\pi_1}(:,1) & & \mathbb{L}_{\pi_1}(:,k+1) \\ & \ddots & \\ & & \mathbb{L}_{\pi_{q+1}}(:,k+1) \end{array} \right], \quad (5.8)$$

$$\mathbb{L}_{\pi_j} = \begin{bmatrix} \frac{\Phi_{21}(1,j) - y_{1j}}{\sigma_{0,1} - s_{0,1}} & \dots & \frac{\Phi_{21}(1,j) - y_{k+1,j}}{\sigma_{0,1} - s_{0,k+1}} \\ \vdots & \ddots & \vdots \\ \frac{\Phi_{21}(n,j) - y_{1j}}{\sigma_{0,n} - s_{0,1}} & \dots & \frac{\Phi_{21}(n,j) - y_{k+1,j}}{\sigma_{0,n} - s_{0,k+1}} \end{bmatrix}.$$

The notation  $\square(:, i)$  in eqs. (5.7) and (5.8) refers to the  $i$ th column of a matrix. It is shown, that a function of shape (5.2) with orders  $k+1$ ,  $q+1$  interpolates all data given in  $\Phi$  and that the required coefficients  $\alpha$  can be obtained from the null space of the generalized two-variable Loewner matrix  $\widehat{\mathbb{L}}_2$ . If no null space is found for  $\widehat{\mathbb{L}}_2$ , coefficients for an approximation of the original function can be obtained from a singular value decomposition of  $\widehat{\mathbb{L}}_2$ . In this case, the reduced model approximates the measurements and the approximation error is proportional to the smallest singular value of  $\widehat{\mathbb{L}}_2$  [143].

A natural limitation of the method is that only data contained in the measurements can be interpolated and a too coarse sampling in either frequency or parameter domain results in reduced models of bad quality compared to the full system response. A reasonable number of transfer function measurements  $N$  and  $M$  cannot be directly related to the order of the full model  $n$ , but can be adjusted using the ranks  $k$  and  $q$  of the Loewner matrices. If  $k+1 = \bar{n}$

(respective  $q + 1 = \overline{m}$ ), not all features of the transfer function can be kept in the reduced model and a finer grind in frequency (respective parameter) space should be considered.

### 5.1.1 The parametric model order reduction algorithm

We now combine the parametric Loewner approach described in the previous section with SO-IRKA, presented in algorithm 4.1. The transfer function measurements required for populating the Loewner matrix are obtained from numerical models being first reduced with SO-IRKA to save computational resources. To enable faster convergence of IRKA, the converged expansion points for one parameter combination are considered as the initial expansion points for the neighboring parameter. The procedure is sketched in algorithm 5.1.

---

#### Algorithm 5.1 Parametric model reduction using IRKA and the Loewner framework

---

**Require:** Original parametric system  $\Sigma(p)$ ,  $r$  initial expansion points for SO-IRKA  $\mathfrak{s}_0 \in \mathbb{C}^r$  closed under complex conjugation, set of evaluation frequencies  $\mathbf{s}_n$ ,  $n = 1, \dots, N$ , set of parameters  $\mathbf{p}_m$ ,  $m = 1, \dots, M$

**Ensure:** Coefficients for the two-variable rational barycentric formula  $\alpha_{ij}, y_{ij}, s_{0,i}, \pi_j$

- 1: **for**  $m = 1 : M$  **do**
  - 2:     Compute  $\mathbf{M}_m \leftarrow \mathbf{M}(p_m)$ ,  $\mathbf{C}_m \leftarrow \mathbf{C}(p_m)$ ,  $\mathbf{K}_m \leftarrow \mathbf{K}(p_m)$  constituting  $\Sigma^m$
  - 3:      $[\Sigma_r^m, \mathfrak{s}_0^m] \leftarrow \text{SO-IRKA}(\Sigma^m, \mathfrak{s}_0^{m-1})$
  - 4:     Compute the frequency response of  $\Sigma_r^m$  for  $\mathbf{s}_n$  and save it in  $\Phi_{nm}$
  - 5: **end for**
  - 6: Obtain orders  $k$  and  $q$  from  $\mathbb{L}_2$
  - 7: Partition  $\mathbf{s}$  and  $\mathbf{p}$  accordingly
  - 8: Construct the parametric Loewner matrix  $\widehat{\mathbb{L}}_2$  from eq. (5.6)
  - 9: Compute  $\boldsymbol{\alpha}$  such that  $\widehat{\mathbb{L}}_2 \boldsymbol{\alpha} = 0$
- 

While SO-IRKA is structure preserving, the parametric model resulting from the Loewner framework can only be represented by a state-space model. Realizations for higher order systems are available for the single-variable case [234], but have not been established for the parametric case.

### 5.1.2 Numerical examples

In the following, we will present numerical experiments showing the effectiveness of the proposed strategy. It is applied to a parametrized version of the clamped beam from section 2.5.1 and a more complex system modeling the response of a vibrating plate with local thickness variations and a constrained layer damping. All experiments have been conducted on a computer equipped with an Intel® Xeon® W-2135 3.70 GHz and 32 GB RAM. All codes are implemented with MATLAB® R2018a.

First, the parametric Loewner framework without the application of SO-IRKA is evaluated using the beam model. It is parametrized with respect to the cross section height  $a$ , all other parameters remain constant. Frequency responses for a set of 12 linearly distributed cross-section sizes  $a_i = [0.005, \dots, 0.05]$  m evaluated at 400 frequencies logarithmically distributed in the range  $[10, \dots, 1 \cdot 10^5]$  rad s<sup>-1</sup> are given as input to the parametric Loewner framework. The framework returns the coefficients for eq. (5.2), which can be evaluated for any frequency and parameter value in range of the snapshot data. The reduced model has dimensions of  $k = 66$  in the frequency space and  $q = 5$  in the parameter space. The frequency response of the reduced model is now evaluated for a cross section height of  $a = 0.0425$  m, which is exactly in the middle between two parameters in the set the reduced model is built upon. The frequency response and approximation error evaluated regarding  $a = 0.0425$  m are given in fig. 5.2. The corresponding error norm  $\|\varepsilon_r\| = 1.538 \cdot 10^{-6}$  in the frequency range of interest is low. Due to the fact, that the transfer function for each parameter  $a_i$  has to be computed to populate the Loewner matrix, the computation time for the offline phase  $t_o = 3.966$  s is significantly higher than the evaluation of one specific transfer function  $t_f = 0.244$  s. After computing the reduced order model, the evaluation time of the transfer function for any parameter  $a_i$  in the parameter space reduces to  $t_e = 0.065$  s. In order to reduce the computational effort in the offline phase, the method presented in algorithm 5.1 obtains the transfer functions from already reduced models. Its application is presented in the following.

We are now considering the numerical model of an aluminum plate with material parameters  $E = 69$  GPa,  $\nu = 0.22$ ,  $\rho = 2650$  kg m<sup>-3</sup> and dimensions  $0.6 \times 0.5 \times 0.003$  m. The plate has a circular thickness variation with diameter  $d = 0.2$  m. The remaining plate thickness in the middle of the circle is  $h = 0.001$  m. In the circular region, a damping material is applied on the opposite side of the plate and clamped by a layer of aluminum, as shown in fig. 5.3. Such localized structures can have a beneficial effect on the host structure regarding vibration and structure-borne noise [86, 235]. The main idea is that waves entering the zone with reduced thickness are slowed while their amplitude increases. This increased amount of vibration energy is then dissipated by the damping material applied in this region. In order to prevent reflections of waves at the beginning of the zones with reduced thickness, a smooth transition of the plate thickness needs to be ensured. Optimal coefficients for the geometry of these zones have been established [186, 187]. Different damping coefficients are applied to the aluminum and the damping material. The discretized model has a dimension of  $n = 61\,671$ . To test the capabilities of algorithm 5.1, we parametrize the model regarding different damping materials.

A model reduced to  $r = 30$  using SO-IRKA can approximate the full system up to  $5000$  rad s<sup>-1</sup> with good accuracy with an error norm  $\|\varepsilon_r\| = 4.289 \cdot 10^{-6}$ . The computation time to generate one reduced model using SO-IRKA is  $t_c = 43.6$  s and the evaluation

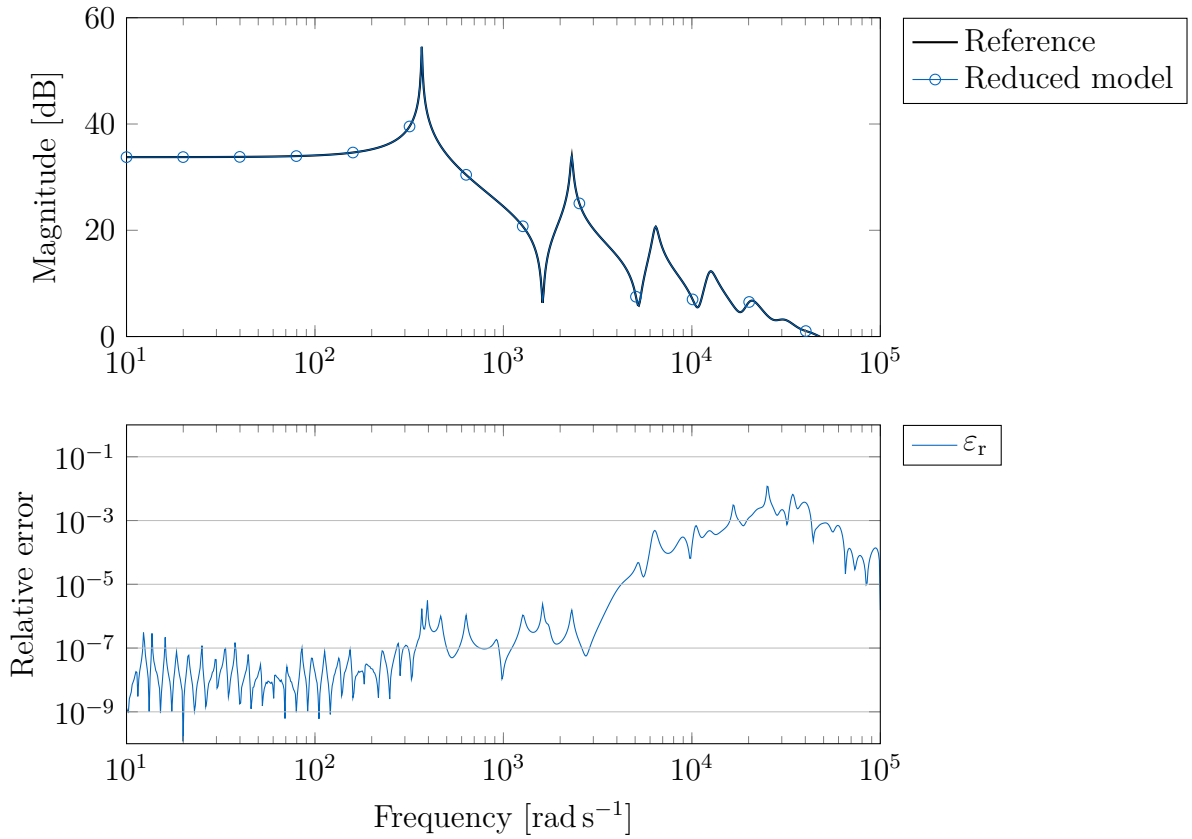


**Figure 5.2:** Beam model reduced with the parametric Loewner framework evaluated at  $a = 0.0425$  m. Frequency response at the cantilever tip of the full and the reduced model and approximation error with respect to the direct solution.

time of the reduced model in the frequency range of interest is  $t_e = 0.119$  s. This is an improvement compared to the direct solution time of the full system taking  $t_f = 838.5$  s. A parametrized reduced model is now generated using algorithm 5.1. 50 different damping materials are used in the offline presampling with damping-to-stiffness ratios between  $\mathbf{p} = [9.0 \cdot 10^{-9}, \dots, 4.098 \cdot 10^{-6}]$ . Due to the constant update of the initial expansion points, SO-IRKA converges fast, usually already after the second iteration. The frequency response of the reduced model evaluated at  $p = 2.1 \cdot 10^{-8}$  is shown in fig. 5.4. This parameter lies in the middle between two parameters of the original evaluation set  $p_i$ .

The resulting parametric model has the dimensions  $k = 47$  in the frequency space and  $q = 26$  in the parameter space, which indicates, that snapshots for more parameters are required to interpolate the measurement data, rather than approximate it. Nevertheless, the reduced model is able to approximate the full model up to a frequency of  $5000 \text{ rad s}^{-1}$ . The resulting error norm  $\|\varepsilon_r\| = 6.377 \cdot 10^{-4}$  shows, that the reduced model is accurate in the frequency range  $s = [10, \dots, 1 \cdot 10^5] \text{ rad s}^{-1}$ . The reduced parametric model is generated

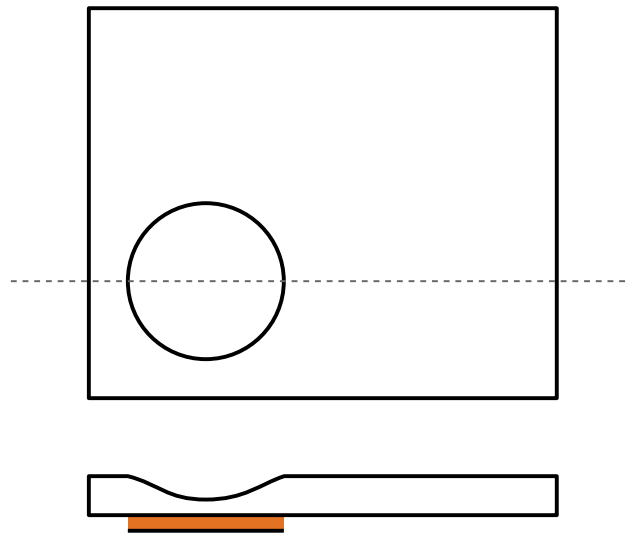


Figure 5.3: Plate with ABH and applied constrained layer damping (orange).

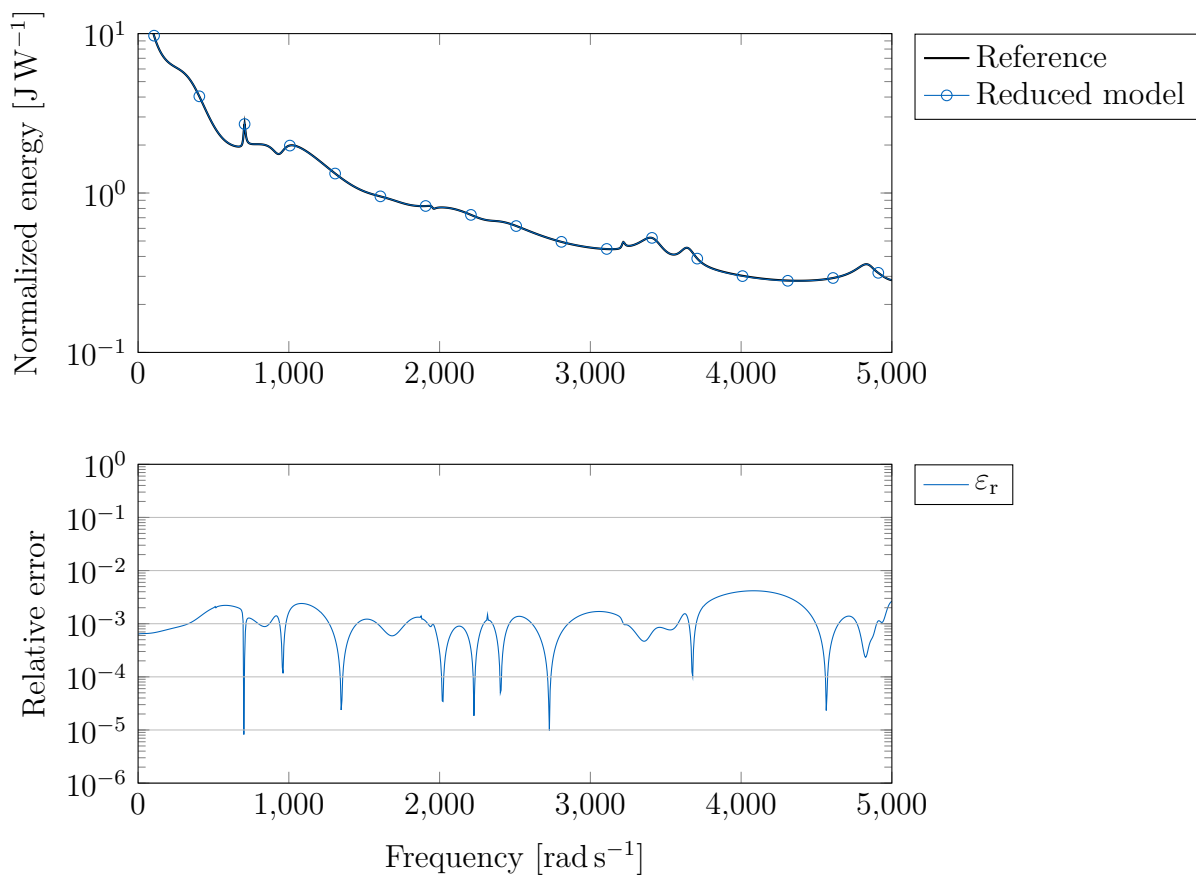


Figure 5.4: Frequency response function of the parametric reduced plate model evaluated at  $p = 2.1 \cdot 10^{-8}$ . Total energy normalized with input power compared to direct solution on the left, error plot on the right.

within  $t_c = 14.7$  s, the evaluation of the reduced model for a parameter takes  $t_e = 0.23$  s. It is clear, that the generation of the transfer function snapshots for 50 parameters results in a longer computation time than solving the system for one distinct parameter. But if the reduced model is to be evaluated for many parameters, for example in an optimization study, the initial overhead of generating the reduced model is compensated.

### 5.1.3 Concluding remarks

Algorithm 5.1 exploits the fact, that poles of parametric models evaluated at similar parameters lie in a similar frequency region and reuses the expansion points at convergence of one IRKA run as starting point for the next. The a-priori selection of nearly optimal poles, as discussed in section 4.3.2, has the potential to speed up convergence also in the first IRKA run. An alternative approach to obtain near optimal expansion points for a moment matching method is presented in the following section.

Regarding the Loewner framework part in algorithm 5.1, it is crucial to provide an appropriate sampling in frequency and parameter space. The rank for the parameter space encoded in the Loewner matrix only has a valid meaning, if all features of the original models have been captured in the frequency response function snapshots. Without prior knowledge of the system response, valid parametric models can only be created using a rather dense parameter space. An adaptive greedy procedure to detect optimal sampling points in the parameter space could, for example, be used.

## 5.2 Prediction of near optimal interpolation points for parametric model order reduction

We now show a strategy combining moment matching methods and data driven regression methods to a physics informed strategy for parametric model order reduction of vibro-acoustic systems, presented in Aumann and Müller: “Predicting near optimal interpolation points for parametric model order reduction using regression models” (2021) [24]. The main idea is linked to the observation, that parametric systems with similar parameters also have similar optimal pole locations (c.f. fig. 5.1). Rather than computing a reduced model directly yielding the approximated frequency response, we try to find a relation between parameters of the full order model and the locations of appropriate frequency shifts. Using these shifts, a reduced model of good quality can be computed without the need of optimizing the shift locations. Similar approaches have been studied in [46, 273]. Our strategy is outlined as follows: Firstly, we iteratively compute the optimal frequency locations for a moment match-

ing method for different parameter realizations, for example using SO-IRKA. Secondly, the locations are processed such that each snapshot location resembles a physical pole of the transfer function. Following, we train a data-driven model to learn the map between the model parameters and the optimal frequency shifts. We consider regression models, which are outlined in section 5.2.1. Querying the trained model with a yet unknown combination of parameters now yields a good approximation for the optimal locations, which are used to project the system onto the lower dimensional subspace.

By characterizing the resulting system by appropriate expansion points, rather than the actual system output, the result space of the learned model stays low-dimensional while containing the most important features of the physical model. Additionally, the model's physical behavior is included in the learning framework and the resulting reduced model preserves the original system structure. Learning strategies not solely relying on data are often termed physics informed machine learning [68, 214]. In an engineering context, machine learning methods have been combined with model order reduction for example to find coefficients for proper orthogonal decomposition (POD) in [243]; a neural network was trained in [181] to predict the vibration behavior of resonant substructures used to control structural vibrations; Ibañez et al. [141] reconstructed constitutive laws for finite element simulations from data.

The quality of the reduced model greatly depends on the choice of the expansion points  $s_0$ , which are not known a-priori. A valid choice are the mirror images of the full system's eigenvalues, reflected at the imaginary axis. However, a full eigenvalue decomposition is not always available or feasible in the scope of an efficient reduction algorithm. The iterative rational Krylov algorithm (IRKA) and its extension to second-order systems SO-IRKA [268] is therefore used to find optimal interpolation (or expansion) points. Upon convergence, the reduced system's eigenvalues are the mirror images of the used interpolation points. In each iteration, IRKA needs to solve  $2r$  linear systems of equations of order  $n$  (respectively  $r$  linear systems of equations, if the system is symmetric), making the method computationally rather expensive. So if a set of nearly optimal expansion points is known a-priori, the number of iterations until convergence can be reduced, while the quality of the resulting reduced model is not affected.

### 5.2.1 Regression methods

The proposed parametric reduction strategy can be used with different data-driven interpolation or "machine learning" methods. In the following and for the numerical experiments, a nearest neighbors regression, a multivariate polynomial regression, and a support vector machine regression model are considered. The strategies are summarized in the following.

### Nearest neighbors regression

A  $k$ -nearest neighbor ( $k$ NN) model fits the predicted value  $\hat{s}_{0,i}(\mathbf{p})$  given a parameter set  $\mathbf{p}$  not present in the training data based on the  $k$  data points in the training dataset having the shortest distance in a defined metric. The fit is defined as

$$\hat{s}_{0,i}(\mathbf{p}) = \frac{1}{k} \sum_{\mathbf{p}_j \in N_k(\mathbf{p})} w_j s_{0,ij}, \quad (5.9)$$

where  $\mathbf{p}_j$  are the  $k$  closest points to the new parameter set  $\mathbf{p}$ ,  $N_k(\mathbf{p})$  defines the neighborhood of  $\mathbf{p}$  according to a metric,  $w_j$  is a weighting factor, and  $s_{0,ij}$  is the  $i$ -th expansion point regarding the  $j$ -th neighbor of the queried value. So the value of the approximation  $\hat{s}_{0,i}(\mathbf{p})$  is defined as the weighted mean between the  $k$  values  $\hat{s}_{0,i}(\mathbf{p}_j)$  with the smallest distance between  $\mathbf{p}$  and  $\mathbf{p}_j$  in parameter space [133]. We choose the Euclidean distance as metric and the inverse of the distance as weighting function. This assigns a higher weight to a point from the training data with a smaller distance, allowing a smoother approximation of the original solution space. For the numerical experiments covered in the following, the  $k$ NN models were found to be able to approximate also higher dimensional solution spaces with good accuracy.

### Multivariate polynomial regression

In the context of multivariate polynomial regression (MPR), the function  $s_{0,i}(\mathbf{p})$  of the location of the  $i$ th expansion point can be approximated by a polynomial of order  $q$  of the form

$$\begin{aligned} \hat{s}_{0,i}(\mathbf{p}) = & \alpha_0 + \sum_{j_1=1}^l \alpha_{j_1} p_{j_1} + \sum_{j_1=1}^l \sum_{j_2=j_1}^l \alpha_{j_1 j_2} p_{j_1} p_{j_2} + \dots \\ & + \sum_{j_1=1}^l \sum_{j_2=j_1}^l \dots \sum_{j_q=j_{q-1}}^l \alpha_{j_1 \dots j_q} p_{j_1} p_{j_2} \dots p_{j_q}, \end{aligned} \quad (5.10)$$

with coefficients  $\alpha_{j_0}, \alpha_{j_1}, \dots, \alpha_{j_1 \dots j_q}$  [72, 249]. The coefficients are obtained by solving an overdetermined equation system and minimizing the mean squared residual error, also known as least squares fitting. If the individual parameter values in  $\mathbf{p}$  greatly differ in size, the parameters should be scaled to have a similar magnitude before fitting the polynomial. Otherwise, the least squares problem is likely to be ill-conditioned. Also a high order  $q$  might lead to an ill-conditioning of the least squares problem. However, in the considered models, the functions  $s_{0,i}(\mathbf{p})$  are relatively smooth, so a sufficient accuracy can be achieved with a relatively low  $q$ . Compared to the local approach of the  $k$ NN regression, the MPR

is fitted to the global parameter space allowing a better generalization if the solution space is smooth, but being not as accurate regarding jumps or discontinuities in the solution space. Increasing the polynomial order to approximate this behavior is very likely to lead to a numerically ill-conditioned least squares problem. MPR therefore has the potential to perform better in approximating smooth functions.

### Support vector regression

A support vector machine (SVM) finds an  $n$ -dimensional tube with a certain width  $\varepsilon$  containing most samples from a set of training data [26, 257]. This tube is found by solving an optimization problem regarding the given error tolerance  $\varepsilon$  and weighting all samples lying outside this tube by a loss function. The resulting manifold is described by the so called support vectors, which can be used for regression analyses. This methodology is a generalization of a SVM and termed support vector regression (SVR). Predictions for new input parameters are found by

$$\hat{s}_{0,i}(\mathbf{p}) = \sum_{j=1}^l (\alpha_j - \alpha_j^*) \mathbf{G}(\mathbf{p}_n, \mathbf{p}) + b, \quad (5.11)$$

where the parameters  $\alpha$ ,  $\alpha^*$  are found by solving a minimization problem,  $b$  is the intercept of the regression, and  $\mathbf{G}(\cdot)$  is a Gram matrix built using a kernel function. This function can be a radial basis function  $\mathbf{G}(\mathbf{p}_i, \mathbf{p}_j) = \exp(-\|\mathbf{p}_i - \mathbf{p}_j\|_{\mathbb{F}}^2)$ , for example.

### 5.2.2 Parametric model order reduction algorithm

We now combine the regression models with a moment matching method based on SO-IRKA to obtain an algorithm for parametric model order reduction. Similar to the other model order reduction methods, it is split in an offline and an online phase. The map  $\sigma : \mathcal{P} \rightarrow \mathcal{S}$  between the realizations of the parameter set  $\mathbf{p} \in \mathcal{P}$  and the corresponding optimal expansion points  $\sigma(\mathbf{p}) \in \mathcal{S}$  obtained from SO-IRKA is sought during the algorithm's offline phase. The vector valued function  $\sigma(\mathbf{p})$  returns a set of optimal expansion points for a model under parameters  $\mathbf{p}$ . It can be seen as the result of SO-IRKA. Full order models with different parameter realizations  $\mathbf{p}$  are used to fill a database of optimal expansion points  $\sigma(\mathbf{p})$ . The gathered data will be termed training data. We then use a regression method to learn the map from the parameter input  $\mathbf{p}$  to the interpolation points  $\sigma(\mathbf{p})$ . In the online phase, appropriate interpolation points for a new parameter set  $\mathbf{p}_{\text{new}}$  are retrieved from this map and used to compute the reduction bases  $\mathbf{V}$ ,  $\mathbf{W}$  without the need for iterations in SO-IRKA. Projecting the full model onto this basis yields a new reduced model which is not optimal

in the sense of the  $\mathcal{H}_2$ -norm, but is expected to approximate the full order system with a comparable level of accuracy.

Up to  $2r$  linear systems of equations of size  $n$  have to be solved during the online phase for each reduced model, which can be of considerable computational cost. Benner, Grundel, and Hornung [46] suggest using intermediate models of moderate size but not necessarily optimal quality to compute the actual reduced model. Here, the projection matrices computed in the training phase are reused to compute projection matrices  $\mathbf{V}$ ,  $\mathbf{W}$ , which project the full system onto a subspace of order  $q > r$ . This intermediate model is then used to compute the projection matrices for an unknown set of parameters during the online phase. However, the original system matrices are required to be in affine form, which is not applicable for all cases, especially if the geometric location of parts of the model is parametrized. In the following, we will assume the computational costs of solving  $r$  equation systems of size  $n$  to be affordable during the online phase. To speed up the creation of the dataset, it is advisable to reuse the expansion points at convergence of a model with a similar parameter configuration as initial expansion points as outlined in section 5.1.

Rather than interpolating the complete set valued function  $\boldsymbol{\sigma}(\mathbf{p})$  at once, we learn  $r$  independent models, one for each interpolation point. By doing so, we obtain  $r$  scalar valued functions  $\sigma_i(\mathbf{p})$ ,  $i = 1, \dots, r$ . For vibro-acoustic systems, these functions can be considered smooth and do not exhibit jumps or discontinuities. They can therefore be approximated with high accuracy by interpolation methods. For each model in the training dataset, the expansion points are ordered by their absolute value before training the data-driven model. This means, there will be one model for the “first” expansion point (i.e. with the lowest absolute value), another for the “second”, and so on. To illustrate this, fig. 5.5 plots the absolute value of the first expansion point for a model of a cantilevered beam over different parameter values for the beam length and its Young’s modulus. It can be seen, that the function surface is smooth and no jumps are present, as the number of modes per frequency band changes smoothly depending on geometric or material properties of the model. This is the case for many vibro-acoustic systems [172]. After querying each model, the obtained interpolated expansion points are combined to a new set  $\boldsymbol{\sigma}_{\text{new}}$  and the corresponding projection matrices  $\mathbf{V}$ ,  $\mathbf{W}$  are computed using the full order model.

If the expansion points are matched one by one, i.e. the order of the reduced systems in the training data is not constant, it is necessary to determine a reasonable order of the reduced model for a new parameter set  $\mathbf{p}$ . For this, an additional model is trained, which maps the parameter sets in the training data to the acquired reduced orders. Again, the required orders change relatively smoothly with varying parameters, so a reasonable interpolation quality can be achieved. Figure 5.6 plots the required orders for the beam model, if a frequency range from zero to 10 kHz is to be matched.

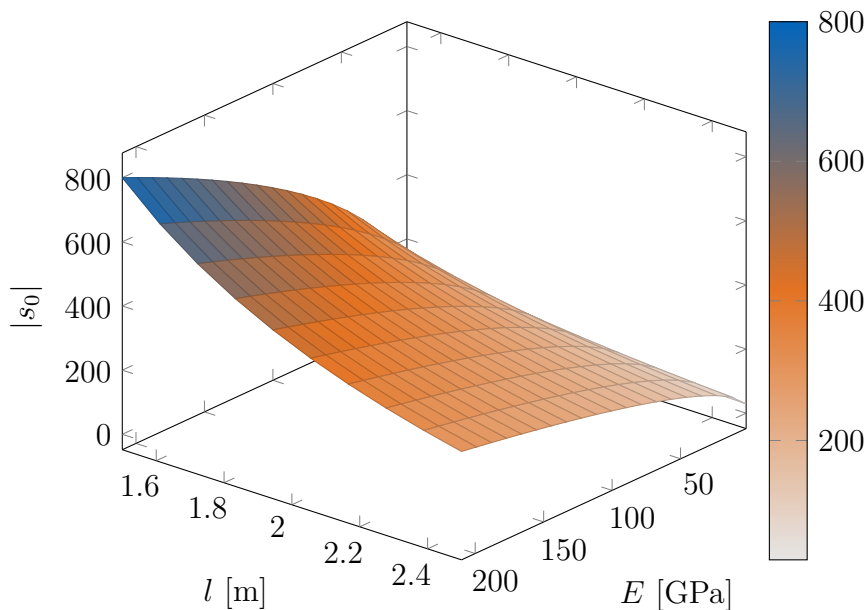


**Figure 5.5:** The absolute value of the first expansion point  $|s_0|$  of a cantilevered beam excited by a point force at the free end. Parameters are the beam length  $l$  and Young's modulus  $E$ .

Not all optimal interpolation points obtained from SO-IRKA are necessarily mirror images of poles of the corresponding transfer function [12, p. 87]. This means, that SO-IRKA can yield multiple interpolation points around one physical pole for one set of parameters but not for the neighboring set, for example. Therefore, the interpolation points need to be processed in a way, that the “first” point in the sense of fig. 5.5 resembles the “first” pole, and so on. We achieve this by converting the reduced model’s transfer function into the pole residual form

$$H_r(s) = \sum_{i=1}^r \frac{R_i}{s - \lambda_i}, \quad (5.12)$$

with the reduced system’s eigenvalues  $\lambda_i$ , which are, up to the convergence tolerance, identical to the mirror images of the interpolation points obtained from IRKA, and the corresponding residuals  $R_i$ . The residuals can be computed from an eigenvalue decomposition of the reduced system [225, 226], which is computationally cheap to perform. The higher the absolute value of a residual, the higher the corresponding pole’s dominance in the transfer function; so removing expansion points with a small residual does not affect the system’s transfer function considerably. Because we only want to use expansion points corresponding to physical poles to train the regression models, we only use the expansion points  $\lambda_i$  with a residual  $R_i$  larger than a certain threshold to compute the projection bases  $\mathbf{V}$ ,  $\mathbf{W}$ . As well as removing these residuals from the transfer function, removing the corresponding expansion points from the projection bases has only little effect on the transfer function of the

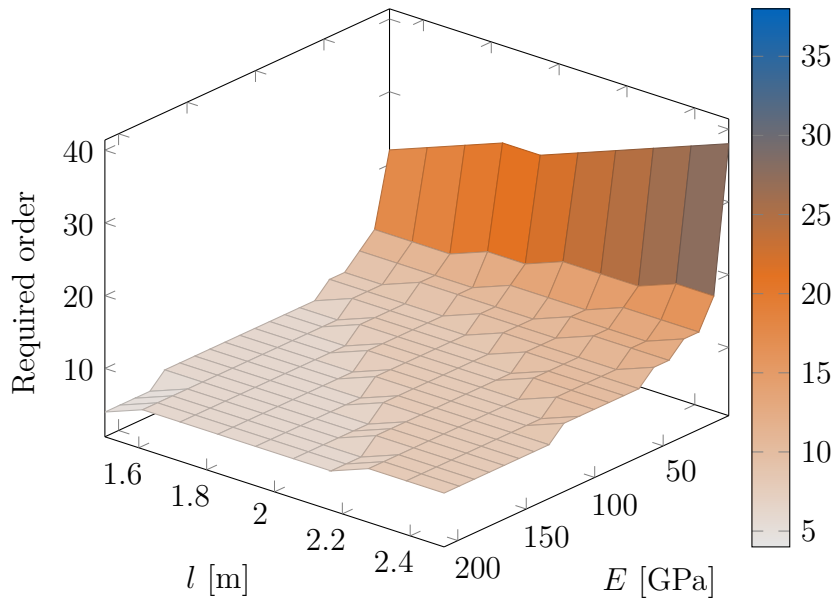


**Figure 5.6:** The required orders for IRKA to compute a reduced model of a cantilevered beam valid up to 10 kHz.

reduced system. The resulting sets of interpolation points for different parameters can now be ordered in a way, that the first entry in the set corresponds to the first physical pole and so on.

The resulting algorithm's offline phase is given in algorithm 5.2. The postprocessing step in algorithm 5.2 line 5 includes the computation of the expansion points' residuals and discarding expansion points which residuals have low values as described above. Any of the methods overviewed in section 5.2.1 can be used to learn the map in algorithm 5.2 line 8.

---

#### Algorithm 5.2 Offline phase

---

**Require:** Parametrized model  $\Sigma(\mathbf{p})$ , parameter samples  $\mathbf{P} = [\mathbf{p}_1, \dots, \mathbf{p}_k]$

**Ensure:** A trained regression model representing map  $\sigma : \mathbf{p} \rightarrow \sigma(\mathbf{p})$

- 1: Initialize  $\mathbf{S}$
  - 2: **for**  $i = 1, \dots, k$  **do**
  - 3:     Build full model  $\Sigma(\mathbf{p}_i)$
  - 4:     Compute optimal expansion points  $\sigma_i$  using SO-IRKA
  - 5:     Postprocess  $\sigma_i$
  - 6:      $\mathbf{S}(:, i) = \sigma_i$
  - 7: **end for**
  - 8: Use  $\mathbf{P}$  and  $\mathbf{S}$  to train a regression model to find map  $\sigma : \mathbf{p} \rightarrow \sigma(\mathbf{p})$
- 

The following online phase is summarized in algorithm 5.3. The projection matrices  $\mathbf{V}$ ,  $\mathbf{W}$  computed in algorithm 5.3 line 3 are obtained from multi-point moment matching while considering an interpolation order of 1.

---

**Algorithm 5.3** Online phase

---

**Require:** Map  $\sigma : \mathbf{p} \rightarrow \sigma(\mathbf{p})$  as trained regression model, parameter set  $\mathbf{p}_{\text{new}}$ **Ensure:** Reduced model  $\Sigma_r(\mathbf{p}_{\text{new}})$ 

- 1: Build full model  $\Sigma(\mathbf{p}_{\text{new}})$
  - 2: Query regression model to obtain  $\sigma(\mathbf{p}_{\text{new}})$
  - 3: Compute projection matrices  $\mathbf{V}$ ,  $\mathbf{W}$  using  $\sigma(\mathbf{p}_{\text{new}})$
  - 4: Obtain  $\Sigma_r(\mathbf{p}_{\text{new}})$  by projection
- 

### 5.2.3 Numerical experiments

To assess the performance of the different regression models employed in the algorithm, two parametrized models of vibro-acoustic systems are considered: the clamped beam from section 2.5.1 and an acoustic cavity, excited by a vibrating membrane attached to a boundary of the cavity. Due to the vibro-acoustic coupling, the cavity model's system matrices are not symmetric and the damping behavior is spatially varying, making it an interesting experiment to assess the methods in a vibro-acoustic context.

The performance of the parametric reduced order models regarding the different regression models and underlying reduction procedures is measured using the normalized root mean square error (NRMSE)

$$\varepsilon_{\text{NRMSE}} = \frac{\|\mathbf{y} - \mathbf{y}_r\|}{\sqrt{n_f} (\max(|\mathbf{y}|) - \min(|\mathbf{y}|))}, \quad (5.13)$$

where  $\mathbf{y}$  is the frequency response of the full order model in the considered frequency range,  $\mathbf{y}_r$  the response of the reduced model obtained with predicted expansion points, and  $n_f$  the number of frequency samples in the response. All computations have been performed on a workstation with an Intel® Xeon® Gold 6136 CPU @ 3.0 GHz with 256 GB RAM.

#### Beam model

We model the vibration of two sets of clamped Euler-Bernoulli beams with square cross sections  $A = 1 \cdot 10^{-6} \text{ m}^2$  subjected to a harmonic load at the free end using a finite element model of order  $n = 300$ . Proportional Rayleigh damping is applied, such that  $\mathbf{C} = \alpha \mathbf{M} + \beta \mathbf{K}$ . Set  $\mathcal{P}_1$  is parametrized regarding length  $l$  and Young's modulus  $E$ , set  $\mathcal{P}_2$  additionally regarding material density  $\rho$  and proportional damping parameters  $\alpha$ ,  $\beta$ . The parameter sampling for both datasets is summarized in Table 5.1.

**Table 5.1:** Parameter ranges, number of samples, and sample distribution for the two beam datasets.

Parameter	Range	$n$ samples		Distribution
		$\mathcal{P}_1$	$\mathcal{P}_2$	
$l$	$[1.5, \dots, 2.5]$ m	10	5	linear
$E$	$[2.1 \cdot 10^9, \dots, 2.1 \cdot 10^{11}]$ Pa	20	5	linear
$\rho$	$[6000, \dots, 8000]$ kg m <sup>-3</sup>	-	5	linear
$\alpha$	$[1.64 \cdot 10^{-4}, \dots, 1.64 \cdot 10^{-2}]$ s <sup>-1</sup>	-	3	logarithmic
$\beta$	$[9.1 \cdot 10^{-8}, \dots, 9.1 \cdot 10^{-6}]$ s	-	3	logarithmic

Each combination of the parameters is present in the dataset, resulting in 200 samples for  $\mathcal{P}_1$  and 1125 samples for  $\mathcal{P}_2$ . The training data for both sets contain every third parameter combination of the complete dataset, the rest of the dataset is used for testing the approximation. The training set for  $\mathcal{P}_1$  contains 67 samples and the resulting models are tested with the remaining 133 samples; the training set for  $\mathcal{P}_2$  contains 375 samples, its test set contains 750 samples. For each set of models  $\mathcal{P}_1, \mathcal{P}_2$ , two datasets are computed: one with SO-IRKA, reducing the original model to a fixed size of  $r = 20$ , and one using the adaptive SO-IRKA strategy described in section 4.4.4 for a frequency range of  $s = [0, \dots, 10\,000]$  rad s<sup>-1</sup>.

Increasing  $l$  and  $\rho$  shifts the transfer function peaks towards lower frequencies, increasing  $E$  shifts them towards higher frequencies. Increasing  $\alpha$  or  $\beta$  decreases the amplitude of the transfer function but has little effect on the location of the peaks. The effect of the parameters on the transfer function is shown in fig. 5.7. Comparing the model with the most response peaks to the one with the fewest, it is obvious that different reduced orders are required to reduce these two models efficiently and setting a fixed reduced order for all samples in the dataset would either lead to a poor approximation for some parameter sets or to an overestimation of the required order for the other parameter sets, thus reducing the efficiency of the reduced model.

For each sample, the expansion points are predicted according to the chosen regression method. The according reduced model is computed and the NRMSE over the frequency range  $s = [0, \dots, 10\,000]$  rad s<sup>-1</sup> is computed. Fig. 5.8 shows the NRMS of the approximation error for all models created with  $k$ NN, MPR, and SVR with the training data from  $\mathcal{P}_1$ , Fig. 5.9 for the training data from  $\mathcal{P}_2$ . The boxes mark the lower and upper quartile, the horizontal lines in the boxes show the median error, and the whiskers reach to the maximum and minimum values of the NRMSE. The  $k$ NN model is fit for  $k = 3$  neighbors and a Gaussian kernel function  $G(\mathbf{p}_i, \mathbf{p}_j) = \exp(-\|\mathbf{p}_i - \mathbf{p}_j\|_F^2)$  is used in the SVR. MPR is employed using a quadratic polynomial ( $q = 2$ ) as well as a polynomial of order  $q = 8$ . The least squares problem is well-conditioned for all considered cases.

The computation times to fit the different models for the two parameter case are  $t_{kNN} = 0.076$  s for the  $k$ NN model,  $t_{MPR,2} = 0.057$  s and  $t_{MPR,8} = 0.063$  s for the MPRs, and  $t_{SVR} =$

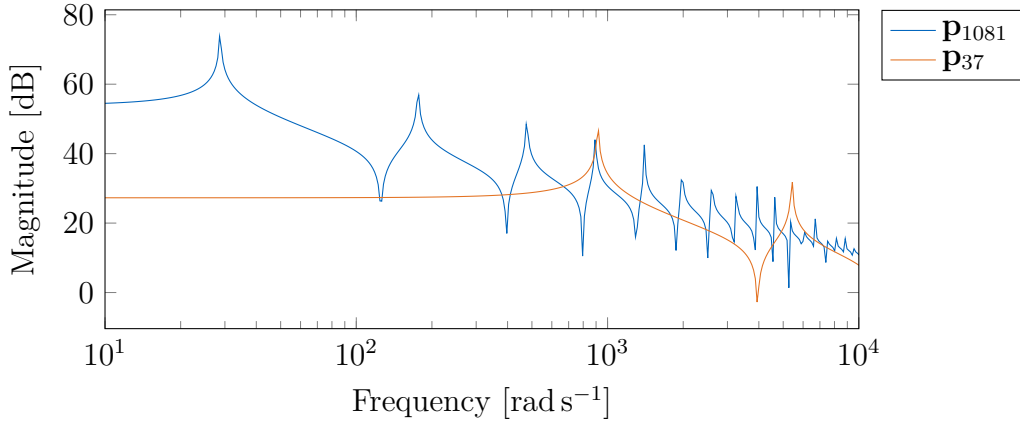


**Figure 5.7:** Transfer functions of two beam models from  $\mathcal{P}_2$  at different parameter samples.  $\mathbf{p}_{1081}$  is the sample with the highest number of response peaks in the considered frequency range,  $\mathbf{p}_{37}$  the sample where the peaks are at locations furthest away from zero.

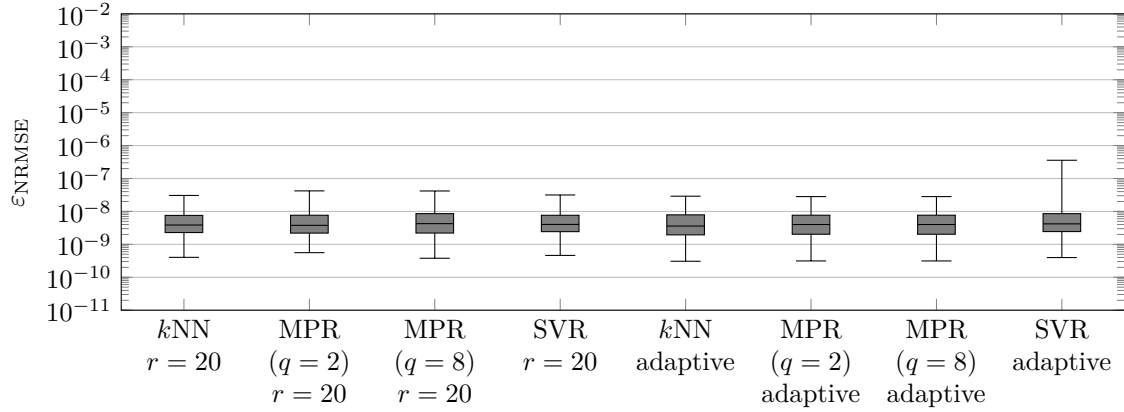


**Figure 5.8:** NRMSE for the reduced models obtained with expansion points from  $k$ NN, MPR, and SVR models with parameters from test data from  $\mathcal{P}_1$ .

4.358 s for the SVR; for the five parameter case the models take  $t_{kNN} = 0.351$  s,  $t_{MPR,2} = 0.133$  s,  $t_{MPR,8} = 4.428$  s, and  $t_{SVR} = 28.485$  s to be fitted. The SVR did not succeed in robustly approximating the location of expansion points for projection in the five parameter setting, possibly due to a too small set of training data.  $k$ NN and MPR yield good results, even for the high dimensional parameter space of  $\mathcal{P}_2$ . For the two parameter case  $\mathcal{P}_1$ , all methods performed similarly with comparable median errors. Using SO-IRKA with an adaptive order and learning an additional model with this order does not have a large influence on the median approximation error for  $\mathcal{P}_1$ . However, learning the required reduced order for  $\mathcal{P}_2$  using a MPR yields a model prone to underestimating the required order for parameter combinations at the boundaries of the sampled region. In this case, the local approach of  $k$ NN outperforms the global approach of the MPR. The resulting outliers have very high errors compared to the  $k$ NN models. The actual approximation quality of the

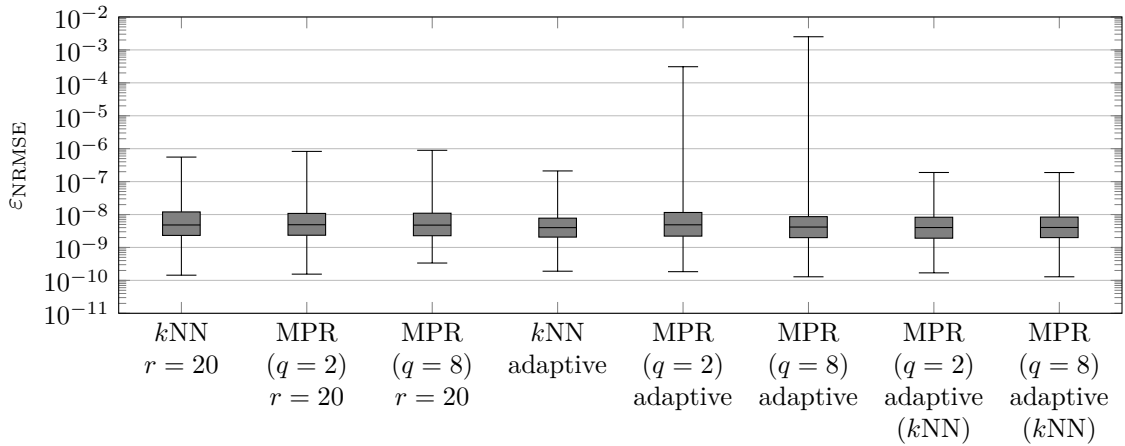


**Figure 5.9:** NRMSE for the reduced models obtained with expansion points from  $kNN$  and MPR models with parameters from test data from  $\mathcal{P}_2$ . The SVR does not succeed in approximating the expansion point locations due to a too small set of training data. The last two data points plot the errors of reduced models where the order is obtained from a  $kNN$  model and the expansion points are interpolated by a MPR.

sampling point locations is of comparable quality for  $kNN$  and MPR, so combining a  $kNN$  model for the required order with a MPR approximation for the sampling point locations yields better results. The SVR with adaptive order also produced some outliers originating from an underestimated required order of the reduced system. The order of the polynomial employed in the MPR does not have a large influence on the approximation quality. Despite the rather sparse parameter sampling in  $\mathcal{P}_2$ , the models fit with  $kNN$  and MPR perform well. The average order of all considered models is  $r = 10.4$  for  $\mathcal{P}_1$  and  $r = 12.9$  for  $\mathcal{P}_2$ , compared to the fixed order of  $r = 20$ . By fitting also the reduced orders, the computational cost of computing the projection basis can therefore be potentially decreased by around 40 % in this case. The  $kNN$  method showed better results for fitting the required order of the reduced model. Here, the NRMSE is in the same order of magnitude than for the fixed order experiments. A global fitting using MPR is, however, not as suited for estimating the required reduced order.

To show the validity of the approach to use near-optimal expansion point locations fig. 5.10 exemplary plots the transfer functions for one parameter realization. The full model's transfer function is compared to the transfer functions of the reduced model computed with SO-IRKA and the reduced model computed with interpolated expansion points obtained from a  $kNN$  model. It can be seen that the approximation errors of both reduced models are nearly the same.

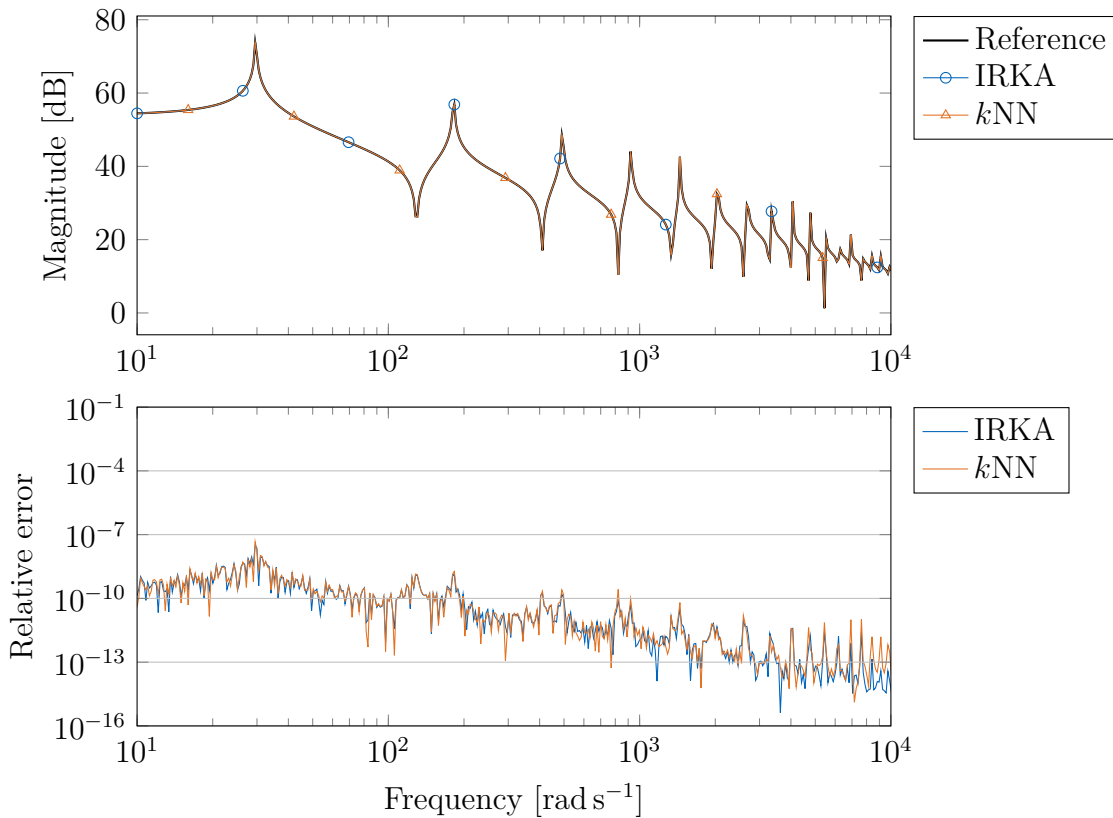


**Figure 5.10:** Transfer functions and relative errors for dataset  $p_{1038}$ , which has the highest  $\varepsilon_{\text{NRMSE}}$  in the training data from  $\mathcal{P}_2$ . Adaptive SO-IRKA converges to a reduced order  $r = 42$ , approximating the full model's transfer function well in the frequency range of interest. The  $k$ NN model to determine the required order also predicted  $r = 42$ , the reduced model based on the interpolated expansion points also shows a very low relative error.

### Acoustic cavity model

The second considered example consists out of a two-dimensional rectangular acoustic cavity with rigid walls parallel to the coordinate axes. At the wall along  $x = 0$ , a vibrating beam-like structure of height  $a$  attached to an aperture in the middle of the wall is excited by a harmonic pressure load and radiates into the acoustic fluid of the cavity. For the structure, the material parameters  $E = 69 \text{ GPa}$ ,  $\rho = 2650 \text{ kg m}^{-3}$ , and  $\nu = 0.22$  and proportional damping with  $\alpha = 1.64 \cdot 10^{-2} \text{ s}^{-1}$  and  $\beta = 9.1 \cdot 10^{-8} \text{ s}$  are considered. The cavity is filled with air which compression wave speed is set to  $c_a = 343.5 \text{ m s}^{-1}$ . The acoustic pressure resulting from the excitation of the structure is measured at a location near the middle of the cavity. Figure 5.11 sketches the system. The system is discretized using a finite element model of order  $n = 3000$ , which is parametrized regarding the size of the vibrating membrane  $a = [0.05, \dots, 0.2] \text{ m}$  and the cavity length in  $x$ -direction  $l = [0.4, \dots, 0.7] \text{ m}$ . The parameter space is sampled with 10 linearly distributed membrane sizes  $a_i$  and 20 linearly distributed

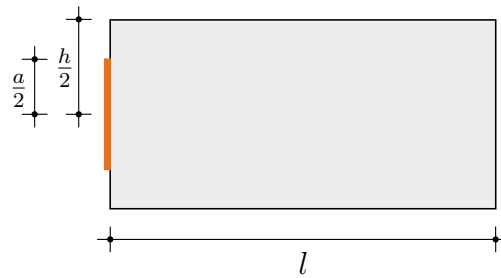


**Figure 5.11:** Sketch of the 2d acoustic cavity with length  $l$ , height  $h$  and membrane size  $a$ . The black walls are reflecting, the orange membrane is flexible.

cavity lengths  $l_i$ , so the complete dataset contains 200 samples. The training dataset contains 67 samples, the remaining 133 samples represent the test dataset. The parameters are sampled according to a linear distribution between the respective minima and maxima and the training data is chosen to be every third parameter combination. Contrary to the beam model, increasing parameter  $a$  does not shift the peaks of the transfer function in whole, but changes the distribution of the peaks, as plotted in fig. 5.12. Because of the parametrization of the model's shape in  $a$ , it is not trivial to find an affine parameter representation of the model, which is a prerequisite for many parametric model order reduction methods.

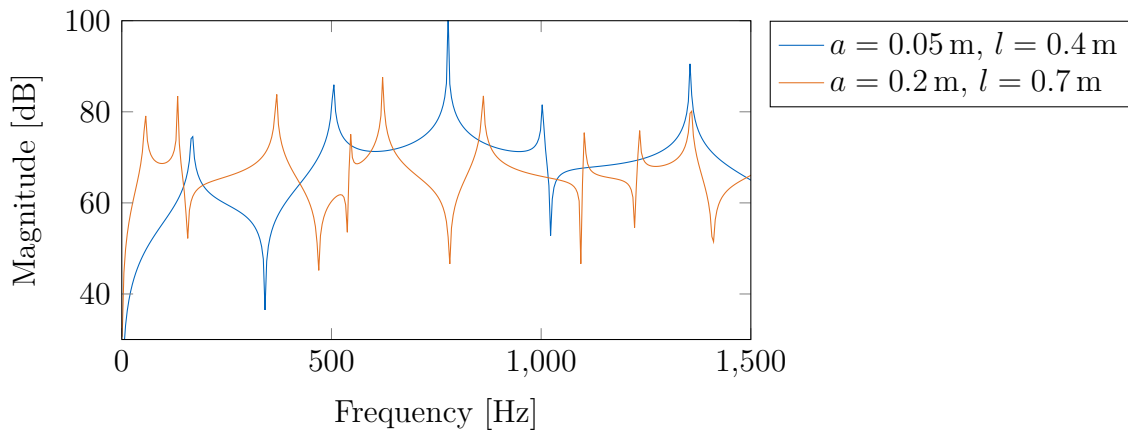


**Figure 5.12:** Transfer functions of two cavity models at different parameters.

Figure 5.13 compares the NRMS approximation errors of the reduced models using the parameters from the test dataset regarding the different regression models. All learning methods yield reduced models of comparable quality with acceptable accuracy. The median errors are slightly higher than those present in the beam model and outliers with errors of some magnitudes higher than the median can be observed. The models based on fixed and adaptive order IRKA again perform similarly. Contrary to the beam models, not all moments in the transfer function are well separated and some modes may overlay each other. This results in locations of the expansion points lying on a not as smooth surface as it is the case for

the beam model (see figs. 5.5 and 5.6) and thus a higher overall error. Additionally, a mode being overlaid by other modes for a certain parameter combination might be required for a good approximation of a model with similar parameters. In this case, the interpolation misses this expansion point location, again resulting in a higher approximation error. Nevertheless, all errors are in an acceptable range and no reduced model fails to approximate the full system response completely. The computation times to fit the different models for the two parameter case are  $t_{kNN} = 0.063\text{ s}$  for the  $kNN$  model,  $t_{MPR,2} = 0.054\text{ s}$  and  $t_{MPR,8} = 0.082\text{ s}$  for the MPRs, and  $t_{SVR} = 1.767\text{ s}$  for the SVR. This shows, compared to the two-parameter beam model, that the time to fit the models is independent of the full model order  $n$ .

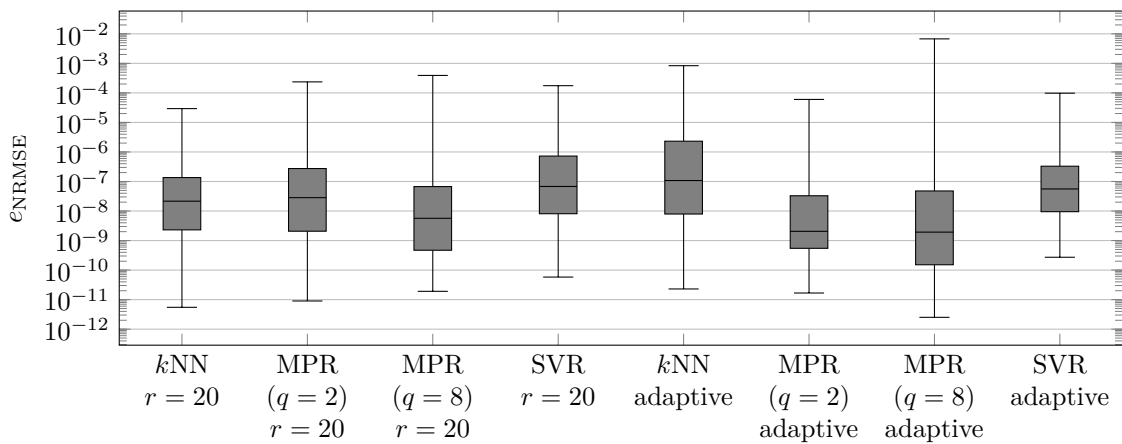


**Figure 5.13:** NRMSE for the cavity reduced models obtained with expansion points from  $kNN$ , MPR, and SVR models with parameters from the test dataset.

### 5.2.4 Conclusive remarks

We presented a strategy for parametric model order reduction of vibro-acoustic systems using regression models. The regression model yields expansion point locations for a moment matching MOR method which ensure a reduced model of good approximation quality without the need for iterations. After having obtained the database with optimal expansion points for a number of parameter samples, the main computational cost lies in projecting the full order model onto the reduced space, requiring at most  $2r$  decompositions of a matrix of order  $n$ . Especially the  $kNN$  regression model is able to robustly predict valid locations for the expansion points. The computational cost of fitting the  $kNN$  model from the previously obtained data is low compared to the computations necessary to find the expansion point locations using the full order model. The MPR also performs well, also for a high number of parameters, if the parameters vary smoothly over their considered range. The SVR yields good results for smooth solution spaces, but could not be fit for a larger number of parameters

given a dataset of limited size in the presented experiment. However, fitting the SVR has a substantially higher computational cost than the other two methods. It should be noted that the fitting of all models is independent of the full model order  $n$  and is only affected by the number of parameters and the amount of training data.

The algorithm is invasive, as it requires access to the original model and the system needs to be assembled for each chosen parameter before the reduction. To obtain a non-invasive parametric reduced model independent from the original model, the parametric Loewner framework discussed in section 5.1 can be employed in a postprocessing step. In this setting, the regression method computes reduced models of the original system for various parameter realizations. Their transfer function evaluations are then used in the parametric Loewner framework to obtain a parametric reduced model independent of the full order system. The use of the regression method decreases the high computational cost of obtaining all necessary transfer function data. As the rank of the Loewner matrix is related to the amount of data necessary for an accurate approximation of the original system, additional data for yet not considered parameter sets can be added to the Loewner database with relatively low computational effort.

## 6 Conclusions and Outlook

In order to design and optimize vibro-acoustic structures regarding their radiated noise or general vibration behavior, engineers rely on mathematical models describing the encountered physical phenomena. The numerical representation of these models, however, often leads to very large models which cannot be evaluated with appropriate efforts regarding time and computational resources. Therefore, strategies to reduce the computational complexity of such models are inevitable in engineering practice. The main goal of this work was to investigate efficient and robust strategies to compute reduced models for complex vibro-acoustic systems and establish frameworks for model order reduction applicable to a wide range of problems. Appropriate reduced models are much less computationally demanding regarding memory and storage requirements and can be used as sufficiently accurate surrogates for the original models. A prerequisite for their application in engineering practice is, however, an efficient and robust generation process.

Such robust model order reduction processes are required to meet certain criteria: Firstly, it is important to have reduction methods which are able to depict the input/output relation of the original system as accurate as possible. Another important factor in assessing if a method is applicable in engineering practice is its robustness and usability. Here, a lower accuracy is often acceptable as long as it stays in certain bounds; it is more important, that the algorithms require only few input parameters and still yield acceptable results if some of these parameters are not optimally chosen. Additionally, the cost of obtaining the result is often a very important factor in engineering practice. As many engineering tasks involve the optimization of systems regarding model parameters, efficient surrogate models should be valid for a certain range of model parameters. The works presented in this thesis are aimed at providing approaches to these different fields in order to help establishing efficient evaluation techniques applicable in engineering practice.

### 6.1 Assessment of research objectives

The research objectives stated in the beginning of the thesis are now assessed regarding the achievements presented throughout the work:

**Accurate and reliable representation of complex vibro-acoustic systems in reduced space, especially for systems with frequency dependent material properties**

A main objective in successful model order reduction is to obtain models which approximate the original system using a surrogate model with an as low as possible order. In section 4.1, established model order reduction methods were assessed regarding their applicability to vibro-acoustic systems. The considered systems showed different properties, for example symmetry or frequency dependency of the system matrices, which lead to differently shaped transfer functions. Most methods were found to be applicable and the resulting reduced models reached acceptable to very good accuracy. Limitations of the methods were identified, as original models with a too high amount of undamped modes cannot be represented well by low order reduced models. Additionally, very localized effects in the transfer function may easily be missed, if the methods are applied without taking the original system's response into account. This results in inaccurately reduced models.

The complex frequency dependent damping mechanisms encountered in various vibro-acoustic applications, such as poroelastic systems or specific cases of viscoelastic damping, required a new reduction technique. The new method presented in section 4.2 extended a standard moment matching method by automatically approximating the frequency dependent terms, such that this dependency could be considered in reduced space. Compared to existing methods based on a Taylor approximation, this method can be applied automatically and also higher order derivatives can be considered without modifications. The consideration of higher order derivatives also showed the possibility to generate smaller reduced models while having a comparable accuracy. The proposed method is not limited to vibro-acoustic systems but can be applied to any form of transfer function containing non-polynomial terms.

Vibro-acoustic models are often required to be valid in a specific frequency region only. An extension to the iterative rational Krylov algorithm (IRKA) for second order systems being able to approximate an original system in a specific frequency region only was shown in section 4.3. This method relies on the second-order structure of the original system and a strategy to reduce the computational cost of the optimization iterations inside IRKA has been presented.

**Robust and reliable automatic model order reduction methods for the application to vibro-acoustic systems**

As observed for some models in the applicability study in section 4.1, an inappropriate choice of expansion points has a large influence on the approximation quality of moment matching methods. The other degree of freedom which has to be considered before reducing a system is a reasonable size of the reduced order model. While optimal locations for the expansion points can be obtained using iterative methods,

an appropriate choice for the required reduced order is not easy to obtain a-priori. Therefore, methods estimating the approximation error of reduced models need to be employed, if the original system's response is not available. Automatic algorithms finding an appropriate reduced order and valid locations for expansion points in an adaptive way have been investigated and compared in section 4.4.

Two algorithms combining Krylov subspace methods with techniques for error estimation have been applied to different vibro-acoustic systems and yielded reasonably sized reduced models showing a good accuracy. Most employed error estimators could also be successfully applied, with some having difficulties with ill-conditioned system matrices. The most promising method for estimating the approximation error was comparing the frequency response of two reduced models obtained using different reduction parameters and using this difference as error estimation. This is convenient, as it is straightforward to apply and the required reduced models are a byproduct of the proposed adaptive algorithms. The algorithms are independent of the employed moment matching method, so they could be applied to any kind of vibro-acoustic system.

Another investigated method was to use the location of a reduced system's eigenvalues computed during the application of IRKA as indicator whether the considered reduced order is large enough. The strategy increases the size of the reduced model adaptively by selecting all eigenvalues of the reduced system which lie in a specified frequency region as locations for new expansion points. While adaptive methods relying on error estimators are prone to overestimate the required reduced order, this modification of IRKA typically yields smaller reduced models but is also computationally more expensive. A combination with CIRKA was found to successfully reduce the computational cost while still ensuring accurate reduced order models.

**Model order reduction strategies for parametrized vibro-acoustic systems** Many vibro-acoustic structures are subject to exhaustive optimization studies regarding possibly large sets of parameters during their design phase. Reducing the computational cost of the required system evaluations has the potential to save a large amount of time and computational resources. Strategies to obtain reduced models retaining the dependence on a set of parameters have therefore been investigated in chapter 5. The possibility to compute a reduced model relying only on transfer function evaluations is especially interesting in a vibro-acoustic setting, as measurement data from real world structures is often available. This data can be used, for example, to create models for systems which cannot be fully described by mathematical models, for example because of uncertainties in the material properties.

Additionally, a method learning the map between model parameters and near optimal locations for expansion points for a moment matching method was proposed. Here, the

underlying physics of the model are used to obtain classifiers for the full scale model, which can be processed by data driven regression methods. Given enough input data, the obtained expansion point locations have a good quality and the resulting reduced models are accurate. At the same time, the data-driven regression models predicting the expansion points are of moderate size, as they only process distinct values. This is especially beneficial compared to classic parametric model order reduction methods, where each considered parameter significantly increases the size of the projection bases.

## 6.2 Suggestions for future work

By achieving the research results presented above, new questions regarding some of these topics emerged. They can be the basis of future work and are summarized in the following:

- The automatic method to include frequency dependent material properties in a Krylov subspace presented in section 4.2 can be applied to various other problems. An interesting choice would be to apply it to systems where a free radiation is modeled with a perfectly matched layer (PML). Using a standard formulation, a PML leads to frequency dependent and complex valued system matrices. Unlike the problems considered in this thesis, this frequency dependency cannot be easily written in an affine form. This means, that the system matrices need to be reassembled for every considered frequency step. Studies showed, that it is possible to use a PML tuned to a specific frequency also for a larger range of frequencies under an acceptable loss of accuracy [259]. The choice of this expansion frequency is, however, subject to optimization as no universal a-priori measure is available. Lenzi et al. [162] used an alternative formulation of a PML, which made it possible to write the frequency dependency as polynomial functions of higher order. This formulation could be used together with the method from section 4.2 in order to compute efficient models for radiation and scattering problems.
- In this thesis only standard second-order systems have been analyzed with iterative Krylov methods. While this leads to interesting possibilities regarding finding an appropriate order for the reduced model in an adaptive way or limiting the frequency range of approximation, the methods are not applicable to general vibroacoustic systems. The realization-independent variant of IRKA proposed by Beattie and Gugercin [38] could be used to find optimal locations for expansion points also for poroacoustic systems, for example. This, however, comes at the cost of losing the benefits of having twice as many eigenvalues as required for finding expansion point

locations. This fact was exploited for standard second-order systems throughout sections 4.3 and 4.4.

- It would also be interesting to investigate strategies to not only obtain expansion points for SO-IRKA considering the locations of the reduced system's eigenvalues, but to also take their corresponding dominance into account. It would be interesting to see, if it is possible to create even more compact reduced models if only the eigenvalues with a certain dominance lying in a specified frequency range are considered as locations for expansion points, instead of considering all eigenvalues located in this frequency range. As the transfer function of the intermediate reduced model inside the IRKA iterations can be obtained without high computational effort, an automatic procedure to determine which expansion points should be kept and which can be omitted can be employed. Here, the least dominant eigenvalues are successively truncated until the transfer function changes more than a defined tolerance.
- The error estimation methods and the resulting algorithms for automatic model order reduction presented in section 4.4 were found to result in accurate reduced order models. There is, however, still room for improvement, as the methods are sensitive to some parameters, which can only be determined heuristically. These include, for example, the increment size for the associated Krylov spaces. Also a stagnation of approximation quality is not always directly recognized by the algorithms, potentially leading to unnecessarily large reduced models. This "too large" reduced model could be reduced to a smaller model in a second step by employing a standard, non-iterative method. In this setting, the solution of the intermediate reduced model is available and can therefore be used for error assessment of the final reduced model. Additionally, other error estimators, as for example proposed by Feng et al. [106, 107, 108] may be assessed regarding their applicability and performance on vibro-acoustic systems.
- A combination of the two parametric model order reduction methods presented in sections 5.1 and 5.2 would be beneficial. The first step in generating the required data is the same for both methods and consists out of obtaining reduced models and their optimal expansion points using an iterative Krylov method. The transfer function measurements of the reduced models are then used to compute the parametric model using the Loewner framework and the expansion points are the basis to learn the map between input parameters and expansion point locations using a regression model. The parametric Loewner framework encodes the required amount of training data to obtain a good quality model; so if more data is required to obtain an accurate parametric model, additional training data can be generated using reduced models computed with

the interpolated expansion points resulting from the regression model.

- The possibility to use other methods than standard regression models in the parametric model order reduction method from section 5.2 should be investigated. This could include, for example, prediction based on polynomial chaos expansion [231]. Additionally, it could be investigated if it is beneficial to employ regression methods based on neural networks in the vibro-acoustic setting, similar to Swischuk et al. [243]. This could have the potential of allowing a sparse sampling of the parameter space while still being able to yield good predictions for near-optimal expansion points.

# A Appendix

## A.1 Equivalent first-order systems for second-order systems

Various formulations to rewrite second-order systems as equivalent first-order systems are available and can be found. Salimbahrami [228] gives an overview. The formulations referenced in this thesis are given in the following. Here, a matrix  $\mathbf{J}$  denotes an arbitrary invertible matrix of dimensions  $n \times n$ .

- First companion form. Note: If  $\mathbf{K}$  and  $\mathbf{M}$  are symmetric and invertible, choosing  $\mathbf{J} = -\mathbf{K}$  preserves the symmetry of the original second-order system:

$$\mathbf{A}^{(1)} = \begin{bmatrix} 0 & \mathbf{J} \\ -\mathbf{K} & -\mathbf{C} \end{bmatrix}, \mathbf{B}^{(1)} = \begin{bmatrix} 0 \\ \mathbf{F} \end{bmatrix}, \mathbf{C}^{(1)} = \begin{bmatrix} \mathbf{G}^\top \\ 0 \end{bmatrix}^\top, \mathbf{E}^{(1)} = \begin{bmatrix} \mathbf{J} & 0 \\ 0 & \mathbf{M} \end{bmatrix} \quad (\text{A.1})$$

- Second companion form:

$$\mathbf{A}^{(1)} = \begin{bmatrix} -\mathbf{K} & 0 \\ 0 & \mathbf{J} \end{bmatrix}, \mathbf{B}^{(1)} = \begin{bmatrix} \mathbf{F} \\ 0 \end{bmatrix}, \mathbf{C}^{(1)} = \begin{bmatrix} \mathbf{G}^\top \\ 0 \end{bmatrix}^\top, \mathbf{E}^{(1)} = \begin{bmatrix} \mathbf{C} & \mathbf{M} \\ \mathbf{J} & 0 \end{bmatrix} \quad (\text{A.2})$$

## A.2 A decomposed FE formulation for poroelastic materials

The weak formulation for poroelastic Biot materials eq. (2.102) can be decomposed into an affine representation of frequency dependent function  $\phi(s)$  and corresponding constant matrices  $\mathbf{A}$ . The individual parts of eq. (2.102) are reproduced for reference:

$$\mathbf{K}_{p,s} = \int_{\Omega} \mathbf{B}_s^\top \mathbf{D} \mathbf{B}_s \, d\Omega, \quad (2.103)$$

$$\widetilde{\mathbf{M}}_{p,s} = \tilde{\rho} \int_{\Omega} \mathbf{N}_s^\top \mathbf{N}_s \, d\Omega, \quad (2.104)$$

$$\widetilde{\mathbf{K}}_{p,f} = \frac{\phi^2}{\tilde{\rho}_f} \int_{\Omega} \nabla \mathbf{N}_f^\top \nabla \mathbf{N}_f \, d\Omega, \quad (2.105)$$

$$\widetilde{\mathbf{M}}_{p,f} = \frac{\phi^2}{\widetilde{R}} \int_{\Omega} \mathbf{N}_f^T \mathbf{N}_f \, d\Omega, \quad (2.106)$$

$$\widetilde{\mathbf{Z}}_{p,sf} = \left( \tilde{\gamma} + \phi \left( 1 + \frac{\widetilde{Q}}{\widetilde{R}} \right) \right) \int_{\Omega} \mathbf{N}_s^T \nabla \mathbf{N}_f \, d\Omega + \phi \left( 1 + \frac{\widetilde{Q}}{\widetilde{R}} \right) \int_{\Omega} \nabla \mathbf{N}_s^T \mathbf{N}_f \, d\Omega, \quad (2.107)$$

$$\mathbf{f}_{p,s} = \int_{\Gamma} \mathbf{N}_s^T \boldsymbol{\sigma}_{t,n,\Gamma} \, d\Gamma, \quad (2.108)$$

$$\mathbf{f}_{p,f} = \phi \int_{\Gamma} \mathbf{N}_f^T (\mathbf{u}_{f,n} - \mathbf{u}_{s,n}) \, d\Gamma. \quad (2.109)$$

Under the assumption  $\phi \left( 1 + \widetilde{Q}/\widetilde{R} \right) \cong 1$ , which is the case for the majority of porous materials used in a vibro-acoustic setting, a possible affine decomposition of eq. (2.102) into one constant matrix without a frequency dependent function and six constant matrices with a corresponding frequency dependent function  $\phi_i(s)$  is given by

$$\begin{aligned} \sum_{i=0}^6 \phi_i(s) \mathbf{A}_i &= \underbrace{\begin{bmatrix} \mathbf{K}_{p,s} & -\int_{\Omega} \mathbf{N}_s^T \nabla \mathbf{N}_f \, d\Omega - \int_{\Omega} \nabla \mathbf{N}_s^T \mathbf{N}_f \, d\Omega \\ 0 & 0 \end{bmatrix}}_{\mathbf{A}_0} + \underbrace{\tilde{\gamma}(s)}_{\phi_1(s)} \underbrace{\begin{bmatrix} 0 & -\int_{\Omega} \mathbf{N}_s^T \nabla \mathbf{N}_f \, d\Omega \\ 0 & 0 \end{bmatrix}}_{\mathbf{A}_1} \\ &+ \underbrace{\frac{\phi^2}{\tilde{\rho}_f(s)}}_{\phi_2(s)} \underbrace{\begin{bmatrix} 0 & 0 \\ 0 & \int_{\Omega} \nabla \mathbf{N}_f^T \nabla \mathbf{N}_f \, d\Omega \end{bmatrix}}_{\mathbf{A}_2} + \underbrace{\frac{s^2}{\phi_3(s)}}_{\phi_3(s)} \underbrace{\begin{bmatrix} 0 & 0 \\ \left( \int_{\Omega} \mathbf{N}_s^T \nabla \mathbf{N}_f \, d\Omega + \int_{\Omega} \nabla \mathbf{N}_s^T \mathbf{N}_f \, d\Omega \right)^T & 0 \end{bmatrix}}_{\mathbf{A}_3} \\ &+ \underbrace{s^2 \tilde{\gamma}(s)}_{\phi_4(s)} \underbrace{\begin{bmatrix} 0 & 0 \\ \left( \int_{\Omega} \mathbf{N}_s^T \nabla \mathbf{N}_f \, d\Omega \right)^T & 0 \end{bmatrix}}_{\mathbf{A}_4} + \underbrace{s^2 \tilde{\rho}(s)}_{\phi_5(s)} \underbrace{\begin{bmatrix} \int_{\Omega} \mathbf{N}_s^T \mathbf{N}_s \, d\Omega & 0 \\ 0 & 0 \end{bmatrix}}_{\mathbf{A}_5} + \underbrace{\frac{s^2 \phi^2}{\widetilde{R}(s)}}_{\phi_6(s)} \underbrace{\begin{bmatrix} 0 & 0 \\ 0 & \int_{\Omega} \mathbf{N}_f^T \mathbf{N}_f \, d\Omega \end{bmatrix}}_{\mathbf{A}_6}. \end{aligned} \quad (\text{A.3})$$

Here, 0 denotes a zero matrix of appropriate size.

## Bibliography

- [1] A. Abbad, N. Atalla, M. Ouisse, and O. Doutres. “Numerical and experimental investigations on the acoustic performances of membraned Helmholtz resonators embedded in a porous matrix”. In: *Journal of Sound and Vibration* 459 (2019), p. 114873. ISSN: 0022-460X. DOI: [10.1016/j.jsv.2019.114873](https://doi.org/10.1016/j.jsv.2019.114873).
- [2] S. Adhikari. “Damping models for structural vibration”. PhD thesis. University of Cambridge, 2001.
- [3] M. I. Albakri, V. V. Sriram Malladi, S. Gugercin, and P. A. Tarazaga. “Estimating dispersion curves from frequency response functions via vector-fitting”. In: *Mechanical Systems and Signal Processing* 140 (2020), p. 106597. ISSN: 08883270. DOI: [10.1016/j.ymsp.2019.106597](https://doi.org/10.1016/j.ymsp.2019.106597).
- [4] N. Aliyev, P. Benner, E. Mengi, and M. Voigt. “A subspace framework for  $\mathcal{H}_\infty$ -norm minimization”. In: *SIAM Journal on Matrix Analysis and Applications* 41.2 (2020), pp. 928–956. ISSN: 0895-4798. DOI: [10.1137/19M125892X](https://doi.org/10.1137/19M125892X).
- [5] J.-F. Allard and N. Atalla. *Propagation of sound in porous media: Modelling sound absorbing materials*. 2nd ed. Hoboken, NJ: Wiley, 2009. ISBN: 9780470747339. DOI: [10.1002/9780470747339](https://doi.org/10.1002/9780470747339). (Visited on 07/14/2021).
- [6] K. Amichi and N. Atalla. “A new 3d finite element for sandwich beams with a viscoelastic core”. In: *Journal of Vibration and Acoustics* 131.2 (2009). ISSN: 07393717. DOI: [10.1115/1.3025828](https://doi.org/10.1115/1.3025828).
- [7] D. Amsallem and C. Farhat. “Interpolation method for adapting reduced-order models and application to aeroelasticity”. In: *AIAA Journal* 46.7 (2008), pp. 1803–1813. ISSN: 0001-1452. DOI: [10.2514/1.35374](https://doi.org/10.2514/1.35374).
- [8] H. Antil, M. Heinkenschloss, and D. C. Sorensen. “Application of the discrete empirical interpolation method to reduced order modeling of nonlinear and parametric systems”. In: *Reduced Order Methods for Modeling and Computational Reduction*. Ed. by A. Quarteroni and G. Rozza. Modeling, Simulation and Applications. Cham: Springer, 2014, pp. 101–136. ISBN: 9783319020891. DOI: [10.1007/978-3-319-02090-7\\_4](https://doi.org/10.1007/978-3-319-02090-7_4).
- [9] A. C. Antoulas, A. C. Ionita, and S. Lefteriu. “On two-variable rational interpolation”. In: *Linear Algebra and its Applications* 436.8 (2012), pp. 2889–2915. ISSN: 00243795. DOI: [10.1016/j.laa.2011.07.017](https://doi.org/10.1016/j.laa.2011.07.017).
- [10] A. C. Antoulas, S. Lefteriu, and A. C. Ionita. “A Tutorial Introduction to the Loewner Framework for Model Reduction”. In: *Model Reduction and Approximation*. Ed. by P. Benner, M. Ohlberger, A. Cohen, and K. Willcox. Philadelphia: SIAM, 2017, pp. 335–376. ISBN: 978-1-61197-481-2. DOI: [10.1137/1.9781611974829.ch8](https://doi.org/10.1137/1.9781611974829.ch8).

- [11] A. C. Antoulas. *Approximation of large-scale dynamical systems*. Vol. 6. Advances in design and control. Philadelphia: SIAM, 2005. ISBN: 9780898716580. URL: [http://epubs.siam.org/ebooks/siam/advances\\_in\\_design\\_and\\_control/dc06](http://epubs.siam.org/ebooks/siam/advances_in_design_and_control/dc06).
- [12] A. C. Antoulas, C. A. Beattie, and S. Gugercin. *Interpolatory methods for model reduction*. Vol. 21. Computational science and engineering. Philadelphia: Society for Industrial and Applied Mathematics, 2020. ISBN: 978-1-61197-607-6. DOI: [10.1137/1.9781611976083](https://doi.org/10.1137/1.9781611976083).
- [13] P. J. Antsaklis and A. N. Michel. *Linear systems*. 2nd corr. printing. Boston, Mass.: Birkhäuser, 2006. ISBN: 978-0-8176-4435-2.
- [14] R. J. Astley. “Infinite elements for wave problems: a review of current formulations and an assessment of accuracy”. In: *International Journal for Numerical Methods in Engineering* 49.7 (2000), pp. 951–976. ISSN: 1097-0207. DOI: [10.1002/1097-0207\(20001110\)49:7<951::AID-NME989>3.0.CO;2-T](https://doi.org/10.1002/1097-0207(20001110)49:7<951::AID-NME989>3.0.CO;2-T).
- [15] R. J. Astley, G. J. Macaulay, J.-P. Coyette, and L. Cremers. “Three-dimensional wave-envelope elements of variable order for acoustic radiation and scattering. Part I. Formulation in the frequency domain”. In: *The Journal of the Acoustical Society of America* 103.1 (1998), pp. 49–63. ISSN: 0001-4966. DOI: [10.1121/1.421106](https://doi.org/10.1121/1.421106).
- [16] R. J. Astley. “Infinite elements”. In: *Computational Acoustics of Noise Propagation in Fluids - Finite and Boundary Element Methods*. Ed. by S. Marburg and B. Nolte. Berlin, Heidelberg: Springer Berlin Heidelberg, 2008, pp. 197–230. ISBN: 978-3-540-77447-1. DOI: [10.1007/978-3-540-77448-8\\_8](https://doi.org/10.1007/978-3-540-77448-8_8).
- [17] N. Atalla, M. A. Hamdi, and R. Panneton. “Enhanced weak integral formulation for the mixed  $(u,p)$  poroelastic equations”. In: *The Journal of the Acoustical Society of America* 109.6 (2001), pp. 3065–3068. ISSN: 0001-4966. DOI: [10.1121/1.1365423](https://doi.org/10.1121/1.1365423).
- [18] N. Atalla, R. Panneton, and P. Debergue. “A mixed displacement-pressure formulation for poroelastic materials”. In: *The Journal of the Acoustical Society of America* 104.3 (1998), pp. 1444–1452. ISSN: 0001-4966. DOI: [10.1121/1.424355](https://doi.org/10.1121/1.424355).
- [19] Q. Aumann, E. Deckers, S. Jonckheere, W. Desmet, and G. Müller. *Automatic model order reduction for systems with frequency dependent material properties*. Submitted to Computer Methods in Applied Mechanics and Engineering. 2021.
- [20] Q. Aumann, M. Miksch, and G. Müller. “Parametric model order reduction for acoustic metamaterials based on local thickness variations”. In: *Journal of Physics: Conference Series* 1264 (2019), p. 012014. ISSN: 1742-6588. DOI: [10.1088/1742-6588/1264/1/012014](https://doi.org/10.1088/1742-6588/1264/1/012014).
- [21] Q. Aumann and G. Müller. *An adaptive method for reducing second-order dynamical systems*. Submitted to IFAC-PapersOnLine. 2021.
- [22] Q. Aumann and G. Müller. “A-priori pole selection for reduced models in vibro-acoustics”. In: *PAMM* 19.1 (2019). ISSN: 16177061. DOI: [10.1002/pamm.201900205](https://doi.org/10.1002/pamm.201900205).
- [23] Q. Aumann and G. Müller. “Robust error assessment for reduced order vibro-acoustic problems”. In: *Proceedings of ISMA 2020*. KU Leuven - Department of Mechanical Engineering, 2020, pp. 1901–1914.

- [24] Q. Aumann and G. Müller. “Predicting near optimal interpolation points for parametric model order reduction using regression models”. In: *PAMM* 20.S1 (2021). ISSN: 16177061. DOI: [10.1002/pamm.202000352](https://doi.org/10.1002/pamm.202000352).
- [25] Q. Aumann and S. W. R. Werner. *Structured model order reduction for vibro-acoustic problems using interpolation and balancing methods*. 2022. URL: <http://arxiv.org/pdf/2201.06518v1>.
- [26] M. Awad and R. Khanna. “Support vector regression”. In: *Efficient Learning Machines*. Ed. by M. Awad and R. Khanna. Berkeley, CA: Apress, 2015, pp. 67–80. ISBN: 978-1-4302-5989-3. DOI: [10.1007/978-1-4302-5990-9\\_4](https://doi.org/10.1007/978-1-4302-5990-9_4).
- [27] R. L. Bagley and P. J. Torvik. “A theoretical basis for the application of fractional calculus to viscoelasticity”. In: *Journal of Rheology* 27.3 (1983), pp. 201–210. ISSN: 0148-6055. DOI: [10.1122/1.549724](https://doi.org/10.1122/1.549724).
- [28] Z. Bai. “Krylov subspace techniques for reduced-order modeling of large-scale dynamical systems”. In: *Applied Numerical Mathematics* 43.1-2 (2002), pp. 9–44. ISSN: 01689274. DOI: [10.1016/S0168-9274\(02\)00116-2](https://doi.org/10.1016/S0168-9274(02)00116-2).
- [29] Z. Bai and Y. Su. “Dimension reduction of large-scale second-order dynamical systems via a second-order arnoldi method”. In: *SIAM Journal on Scientific Computing* 26.5 (2005), pp. 1692–1709. ISSN: 1064-8275. DOI: [10.1137/040605552](https://doi.org/10.1137/040605552).
- [30] Z. Bai and Y. Su. “SOAR: a second-order Arnoldi method for the solution of the quadratic eigenvalue problem”. In: *SIAM Journal on Matrix Analysis and Applications* 26.3 (2005), pp. 640–659. ISSN: 0895-4798. DOI: [10.1137/S0895479803438523](https://doi.org/10.1137/S0895479803438523).
- [31] M. C. C. Bampton and R. R. Craig. “Coupling of substructures for dynamic analyses”. In: *AIAA Journal* 6.7 (1968), pp. 1313–1319. ISSN: 0001-1452. DOI: [10.2514/3.4741](https://doi.org/10.2514/3.4741).
- [32] M. Barrault, Y. Maday, N. C. Nguyen, and A. T. Patera. “An ‘empirical interpolation’ method: application to efficient reduced-basis discretization of partial differential equations”. In: *Comptes Rendus Mathématique* 339.9 (2004), pp. 667–672. ISSN: 1631073X. DOI: [10.1016/j.crma.2004.08.006](https://doi.org/10.1016/j.crma.2004.08.006).
- [33] K.-J. Bathe. *Finite element procedures*. Englewood Cliffs, NJ: Prentice Hall, 1996. ISBN: 0-13-301458-4.
- [34] U. Baur, C. Beattie, and P. Benner. “Mapping parameters across system boundaries: parameterized model reduction with low rank variability in dynamics”. In: *PAMM* 14.1 (2014), pp. 19–22. ISSN: 16177061. DOI: [10.1002/pamm.201410006](https://doi.org/10.1002/pamm.201410006).
- [35] U. Baur, C. Beattie, P. Benner, and S. Gugercin. “Interpolatory projection methods for parameterized model reduction”. In: *SIAM Journal on Scientific Computing* 33.5 (2011), pp. 2489–2518. ISSN: 1064-8275. DOI: [10.1137/090776925](https://doi.org/10.1137/090776925).
- [36] C. A. Beattie and S. Gugercin. “Krylov-based model reduction of second-order systems with proportional damping”. In: *2005 44th IEEE Conference on Decision and Control & European Control Conference*. Piscataway, N.J: Institute of Electrical and Electronics Engineers, 2005, pp. 2278–2283. ISBN: 0-7803-9567-0. DOI: [10.1109/CDC.2005.1582501](https://doi.org/10.1109/CDC.2005.1582501).

- [37] C. Beattie and S. Gugercin. “Interpolatory projection methods for structure-preserving model reduction”. In: *Systems & Control Letters* 58.3 (2009), pp. 225–232. ISSN: 01676911. DOI: [10.1016/j.sysconle.2008.10.016](https://doi.org/10.1016/j.sysconle.2008.10.016).
- [38] C. Beattie and S. Gugercin. “Realization-independent  $\mathcal{H}_2$ -approximation”. In: *2012 IEEE 51st IEEE Conference on Decision and Control (CDC)*. IEEE, 2012, pp. 4953–4958. ISBN: 978-1-4673-2066-5. DOI: [10.1109/CDC.2012.6426344](https://doi.org/10.1109/CDC.2012.6426344).
- [39] C. Beattie, S. Gugercin, and Z. Tomljanović. *Sampling-free parametric model reduction for structured systems*. 2019. URL: <http://arxiv.org/pdf/1912.11382v1>.
- [40] T. Bechtold, E. B. Rudnyi, and J. G. Korvink. “Error indicators for fully automatic extraction of heat-transfer macromodels for MEMS”. In: *Journal of Micromechanics and Microengineering* 15.3 (2005), pp. 430–440. ISSN: 0960-1317. DOI: [10.1088/0960-1317/15/3/002](https://doi.org/10.1088/0960-1317/15/3/002).
- [41] R. S. Beddig, P. Benner, I. Dorschky, T. Reis, P. Schwerdtner, M. Voigt, and S. W. R. Werner. *Structure-preserving model reduction for dissipative mechanical systems*. 2020. URL: <http://arxiv.org/pdf/2010.06331v1>.
- [42] P. Benner and S. W. R. Werner. *SOMDDPA – Second-Order Modally-Damped Dominant Pole Algorithm (Version 2.0)*. Apr. 2021. DOI: [10.5281/zenodo.3997649](https://doi.org/10.5281/zenodo.3997649).
- [43] P. Benner and L. Feng. “A robust algorithm for parametric model order reduction based on implicit moment matching”. In: *Reduced Order Methods for Modeling and Computational Reduction*. Ed. by A. Quarteroni and G. Rozza. Modeling, Simulation and Applications. Cham: Springer, 2014, pp. 159–185. ISBN: 9783319020891. DOI: [10.1007/978-3-319-02090-7\\_6](https://doi.org/10.1007/978-3-319-02090-7_6).
- [44] P. Benner, P. Goyal, and I. P. Duff. *Identification of dominant subspaces for linear structured parametric systems and model reduction*. 2019. URL: <http://arxiv.org/pdf/1910.13945v1>.
- [45] P. Benner and S. Grundel. “Model order reduction for a family of linear systems with applications in parametric and uncertain systems”. In: *Applied Mathematics Letters* 39 (2015), pp. 1–6. ISSN: 08939659. DOI: [10.1016/j.aml.2014.08.002](https://doi.org/10.1016/j.aml.2014.08.002).
- [46] P. Benner, S. Grundel, and N. Hornung. “Parametric model order reduction with a small  $\mathcal{H}_2$ -error using radial basis functions”. In: *Advances in Computational Mathematics* 41.5 (2015), pp. 1231–1253. ISSN: 1019-7168. DOI: [10.1007/s10444-015-9410-7](https://doi.org/10.1007/s10444-015-9410-7).
- [47] P. Benner, S. Gugercin, and K. Willcox. “A survey of projection-based model reduction methods for parametric dynamical systems”. In: *SIAM Review* 57.4 (2015), pp. 483–531. ISSN: 0036-1445. DOI: [10.1137/130932715](https://doi.org/10.1137/130932715).
- [48] P. Benner, P. Kürschner, and J. Saak. “Frequency-limited balanced truncation with low-rank approximations”. In: *SIAM Journal on Scientific Computing* 38.1 (2016), A471–A499. ISSN: 1064-8275. DOI: [10.1137/15M1030911](https://doi.org/10.1137/15M1030911).

- [49] P. Benner, P. Kürschner, Z. Tomljanović, and N. Truhar. “Semi-active damping optimization of vibrational systems using the parametric dominant pole algorithm”. In: *ZAMM - Journal of Applied Mathematics and Mechanics / Zeitschrift für Angewandte Mathematik und Mechanik* 96.5 (2016), pp. 604–619. ISSN: 00442267. DOI: [10.1002/zamm.201400158](https://doi.org/10.1002/zamm.201400158).
- [50] P. Benner and S. W. R. Werner. “Frequency- and time-limited balanced truncation for large-scale second-order systems”. In: *Linear Algebra and its Applications* 623 (2021), pp. 68–103. ISSN: 00243795. DOI: [10.1016/j.laa.2020.06.024](https://doi.org/10.1016/j.laa.2020.06.024).
- [51] P. Benner and S. W. R. Werner. *SOLBT - Limited Balanced Truncation for Large-Scale Sparse Second-Order Systems*. Version 3.0. Apr. 2021. DOI: [10.5281/zenodo.4600763](https://doi.org/10.5281/zenodo.4600763). URL: <https://doi.org/10.5281/zenodo.4600763>.
- [52] J.-P. Berenger. “A perfectly matched layer for the absorption of electromagnetic waves”. In: *Journal of Computational Physics* 114.2 (1994), pp. 185–200. ISSN: 00219991. DOI: [10.1006/jcph.1994.1159](https://doi.org/10.1006/jcph.1994.1159).
- [53] H. Bériot and A. Modave. “An automatic perfectly matched layer for acoustic finite element simulations in convex domains of general shape”. In: *International Journal for Numerical Methods in Engineering* (2020). ISSN: 1097-0207. DOI: [10.1002/nme.6560](https://doi.org/10.1002/nme.6560).
- [54] H. Bériot, A. Prinn, and G. Gabard. “Efficient implementation of high-order finite elements for Helmholtz problems”. In: *International Journal for Numerical Methods in Engineering* 106.3 (2016), pp. 213–240. ISSN: 1097-0207. DOI: [10.1002/nme.5172](https://doi.org/10.1002/nme.5172).
- [55] H. Bériot and M. Tournour. “On the locally-conformal perfectly matched layer implementation for Helmholtz equation”. In: *Proceedings of NOVEM Noise and Vibration: Emerging Methods*. 2009, pp. 086-1–086-11.
- [56] A. Bermúdez, L. Hervella-Nieto, A. Prieto, and R. Rodríguez. “An optimal perfectly matched layer with unbounded absorbing function for time-harmonic acoustic scattering problems”. In: *Journal of Computational Physics* 223.2 (2007), pp. 469–488. ISSN: 00219991. DOI: [10.1016/j.jcp.2006.09.018](https://doi.org/10.1016/j.jcp.2006.09.018).
- [57] B. Besselink, U. Tabak, A. Lutowska, N. van de Wouw, H. Nijmeijer, D. J. Rixen, M. E. Hochstenbach, and W. Schilders. “A comparison of model reduction techniques from structural dynamics, numerical mathematics and systems and control”. In: *Journal of Sound and Vibration* 332.19 (2013), pp. 4403–4422. ISSN: 0022-460X. DOI: [10.1016/j.jsv.2013.03.025](https://doi.org/10.1016/j.jsv.2013.03.025).
- [58] M. A. Biot. “Theory of propagation of elastic waves in a fluid-saturated porous solid. I. Low-frequency range”. In: *The Journal of the Acoustical Society of America* 28.2 (1956), pp. 168–178. ISSN: 0001-4966. DOI: [10.1121/1.1908239](https://doi.org/10.1121/1.1908239).
- [59] M. A. Biot. “Theory of propagation of elastic waves in a fluid-saturated porous solid. II. Higher frequency range”. In: *The Journal of the Acoustical Society of America* 28.2 (1956), pp. 179–191. ISSN: 0001-4966. DOI: [10.1121/1.1908241](https://doi.org/10.1121/1.1908241).
- [60] M. A. Biot and D. G. Willis. “The elastic coefficients of the theory of consolidation”. In: *Journal of Applied Mechanics* 24 (1957), pp. 594–601.

- [61] P. E. Black. “Greedy algorithm”. In: *Dictionary of Algorithms and Data Structures*. Feb. 2, 2005. URL: <https://www.nist.gov/dads/HTML/greedyalgo.html> (visited on 09/21/2021).
- [62] R. D. Blevins. *Formulas for dynamics, acoustics and vibration*. Chichester West Sussex and Hoboken NY: John Wiley and Sons Inc, 2015. ISBN: 9781119038115.
- [63] A. Bodendiek and M. Bollhöfer. “Adaptive-order rational Arnoldi-type methods in computational electromagnetism”. In: *BIT Numerical Mathematics* 54.2 (2014), pp. 357–380. ISSN: 0006-3835. DOI: [10.1007/s10543-013-0458-9](https://doi.org/10.1007/s10543-013-0458-9).
- [64] T. Bonin, H. Faßbender, A. Soppa, and M. Zaeh. “A fully adaptive rational global Arnoldi method for the model-order reduction of second-order MIMO systems with proportional damping”. In: *Mathematics and Computers in Simulation* 122 (2016), pp. 1–19. ISSN: 03784754. DOI: [10.1016/j.matcom.2015.08.017](https://doi.org/10.1016/j.matcom.2015.08.017).
- [65] J. Borggaard, K. R. Pond, and L. Zietsman. “Parametric reduced order models using adaptive sampling and interpolation”. In: *IFAC Proceedings Volumes* 47.3 (2014), pp. 7773–7778. ISSN: 14746670. DOI: [10.3182/20140824-6-ZA-1003.02664](https://doi.org/10.3182/20140824-6-ZA-1003.02664).
- [66] C. A. Brebbia, ed. *Boundary element methods: Proceedings of the third international seminar, Irvine, California, July 1981 ; seminar sponsored by the International Society for Computational Methods in Engineering*. Vol. 3. CML publications. Berlin: Springer, 1981. ISBN: 3540108165.
- [67] H. F. Brinson and L. C. Brinson. *Polymer Engineering Science and Viscoelasticity*. Boston, MA: Springer US, 2008. ISBN: 978-0-387-73860-4. DOI: [10.1007/978-0-387-73861-1](https://doi.org/10.1007/978-0-387-73861-1).
- [68] S. L. Brunton and J. N. Kutz. *Data-Driven Science and Engineering*. Cambridge University Press, 2019. ISBN: 9781108380690. DOI: [10.1017/9781108380690](https://doi.org/10.1017/9781108380690).
- [69] S. L. Brunton, J. L. Proctor, and J. N. Kutz. “Discovering governing equations from data by sparse identification of nonlinear dynamical systems”. In: *Proceedings of the National Academy of Sciences of the United States of America* 113.15 (2016), pp. 3932–3937. DOI: [10.1073/pnas.1517384113](https://doi.org/10.1073/pnas.1517384113).
- [70] T. Bui-Thanh, K. Willcox, and O. Ghattas. “Model reduction for large-scale systems with high-dimensional parametric input space”. In: *SIAM Journal on Scientific Computing* 30.6 (2008), pp. 3270–3288. ISSN: 1064-8275. DOI: [10.1137/070694855](https://doi.org/10.1137/070694855).
- [71] A. Castagnotto and B. Lohmann. “A new framework for  $\mathcal{H}_2$ -optimal model reduction”. In: *Mathematical and Computer Modelling of Dynamical Systems* 24.3 (2018), pp. 236–257. ISSN: 1387-3954. DOI: [10.1080/13873954.2018.1464030](https://doi.org/10.1080/13873954.2018.1464030).
- [72] Y. de Castro, F. Gamboa, D. Henrion, R. Hess, and J.-B. Lasserre. “Approximate optimal designs for multivariate polynomial regression”. In: *The Annals of Statistics* 47.1 (2019). ISSN: 0090-5364. DOI: [10.1214/18-AOS1683](https://doi.org/10.1214/18-AOS1683).
- [73] T. K. Caughey. “Classical normal modes in damped linear dynamic systems”. In: *Journal of Applied Mechanics* 27.2 (1960), pp. 269–271. DOI: [10.1115/1.3643949](https://doi.org/10.1115/1.3643949).
- [74] Y. Chahlaoui, D. Lemonnier, A. Vandendorpe, and P. van Dooren. “Second-order balanced truncation”. In: *Linear Algebra and its Applications* 415.2-3 (2006), pp. 373–384. ISSN: 00243795. DOI: [10.1016/j.laa.2004.03.032](https://doi.org/10.1016/j.laa.2004.03.032).

- [75] S. Chaturantabut and D. C. Sorensen. “Nonlinear model reduction via discrete empirical interpolation”. In: *SIAM Journal on Scientific Computing* 32.5 (2010), pp. 2737–2764. ISSN: 1064-8275. DOI: [10.1137/090766498](https://doi.org/10.1137/090766498).
- [76] S. Chellappa, L. Feng, V. de La Rubia, and P. Benner. “Adaptive interpolatory MOR by learning the error estimator in the parameter domain”. In: *Model Reduction of Complex Dynamical Systems*. Ed. by P. Benner, T. Breiten, H. Faßbender, M. Hinze, T. Stykel, and R. Zimmermann. Cham: Springer International Publishing, 2021, pp. 97–117. ISBN: 978-3-030-72983-7. DOI: [10.1007/978-3-030-72983-7\\_5](https://doi.org/10.1007/978-3-030-72983-7_5).
- [77] C.-T. Chen. *Linear system theory and design*. 3. ed., 3. print. The Oxford series in electrical and computer engineering. New York: Oxford Univ. Press, 1999. ISBN: 0195117778.
- [78] F. Chinesta, A. Ammar, and E. Cueto. “Recent advances and new challenges in the use of the proper generalized decomposition for solving multidimensional models”. In: *Archives of Computational Methods in Engineering* 17.4 (2010), pp. 327–350. ISSN: 1134-3060. DOI: [10.1007/s11831-010-9049-y](https://doi.org/10.1007/s11831-010-9049-y).
- [79] F. Chinesta, P. Ladeveze, and E. Cueto. “A short review on model order reduction based on proper generalized decomposition”. In: *Archives of Computational Methods in Engineering* 18.4 (2011), pp. 395–404. ISSN: 1134-3060. DOI: [10.1007/s11831-011-9064-7](https://doi.org/10.1007/s11831-011-9064-7).
- [80] C.-C. Chu, M.-H. Lai, and W.-S. Feng. “Lyapunov-based error estimations of MIMO interconnect reductions by using the global Arnoldi algorithm”. In: *IEICE Transactions on Fundamentals of Electronics, Communications and Computer Sciences* E90-A.2 (2007), pp. 415–418. ISSN: 0916-8508. DOI: [10.1093/ietfec/e90-a.2.415](https://doi.org/10.1093/ietfec/e90-a.2.415).
- [81] C.-C. Chu, M.-H. Lai, and W.-S. Feng. “Model-order reductions for MIMO systems using global Krylov subspace methods”. In: *Mathematics and Computers in Simulation* 79.4 (2008), pp. 1153–1164. ISSN: 03784754. DOI: [10.1016/j.matcom.2007.09.007](https://doi.org/10.1016/j.matcom.2007.09.007).
- [82] C.-C. Chu, H.-C. Tsai, and M.-H. Lai. “Structure preserving model-order reductions of MIMO second-order systems using Arnoldi methods”. In: *Mathematical and Computer Modelling* 51.7-8 (2010), pp. 956–973. ISSN: 08957177. DOI: [10.1016/j.mcm.2009.08.028](https://doi.org/10.1016/j.mcm.2009.08.028).
- [83] A. Cicirello and R. S. Langley. “The vibro-acoustic analysis of built-up systems using a hybrid method with parametric and non-parametric uncertainties”. In: *Journal of Sound and Vibration* 332.9 (2013), pp. 2165–2178. ISSN: 0022-460X. DOI: [10.1016/j.jsv.2012.05.040](https://doi.org/10.1016/j.jsv.2012.05.040).
- [84] C. Claeys, E. Deckers, B. Pluymers, and W. Desmet. “A lightweight vibro-acoustic metamaterial demonstrator: Numerical and experimental investigation”. In: *Mechanical Systems and Signal Processing* 70-71 (2016), pp. 853–880. ISSN: 08883270. DOI: [10.1016/j.ymsp.2015.08.029](https://doi.org/10.1016/j.ymsp.2015.08.029).

- [85] C. Claeys, N. G. R. de Melo Filho, E. Deckers, B. Pluymers, and W. Desmet. “Experimental demonstrators of vibro-acoustic metamaterials for low frequent NVH insulation”. In: *Proceedings of the Inter-Noise 2016*. Ed. by W. Kropp. Berlin: Deutsche Gesellschaft für Akustik e.V, 2016. ISBN: 9783939296119.
- [86] S. C. Conlon, J. B. Fahnlne, and F. Semperlotti. “Numerical analysis of the vibroacoustic properties of plates with embedded grids of acoustic black holes”. In: *The Journal of the Acoustical Society of America* 137.1 (2015), pp. 447–457. ISSN: 0001-4966. DOI: [10.1121/1.4904501](https://doi.org/10.1121/1.4904501).
- [87] L. Cremer and M. Heckl. *Structure-Borne Sound: Structural Vibrations and Sound Radiation at Audio Frequencies*. Berlin and Heidelberg: Springer, 1973. ISBN: 978-3-662-10120-9. DOI: [10.1007/978-3-662-10118-6](https://doi.org/10.1007/978-3-662-10118-6). URL: <http://dx.doi.org/10.1007/978-3-662-10118-6>.
- [88] P. Dadvand, R. Rossi, and E. Oñate. “An object-oriented environment for developing finite element codes for multi-disciplinary applications”. In: *Archives of Computational Methods in Engineering* 17.3 (2010), pp. 253–297. ISSN: 1134-3060. DOI: [10.1007/s11831-010-9045-2](https://doi.org/10.1007/s11831-010-9045-2).
- [89] L. Daniel, O. C. Siong, L. S. Chay, K. H. Lee, and J. White. “A multiparameter moment-matching model-reduction approach for generating geometrically parameterized interconnect performance models”. In: *IEEE Transactions on Computer-Aided Design of Integrated Circuits and Systems* 23.5 (2004), pp. 678–693. ISSN: 0278-0070. DOI: [10.1109/tcad.2004.826583](https://doi.org/10.1109/tcad.2004.826583).
- [90] E. Davison. “A method for simplifying linear dynamic systems”. In: *IEEE Transactions on Automatic Control* 11.1 (1966), pp. 93–101. ISSN: 0018-9286. DOI: [10.1109/TAC.1966.1098264](https://doi.org/10.1109/TAC.1966.1098264).
- [91] P. Debergue, R. Panneton, and N. Atalla. “Boundary conditions for the weak formulation of the mixed  $(u,p)$  poroelasticity problem”. In: *The Journal of the Acoustical Society of America* 106.5 (1999), pp. 2383–2390. ISSN: 0001-4966. DOI: [10.1121/1.428075](https://doi.org/10.1121/1.428075).
- [92] E. Deckers, W. Desmet, K. Meerbergen, and F. Naets. “Case studies of model order reduction for acoustics and vibrations”. In: *Model order reduction*. Ed. by P. Benner, S. Grivet-Talocia, A. Quarteroni, G. Rozza, W. Schilders, and L. M. Silveira. De Gruyter, 2021, pp. 76–110. ISBN: 9783110499001. DOI: [10.1515/9783110499001-003](https://doi.org/10.1515/9783110499001-003).
- [93] J. Degroote, J. Vierendeels, and K. Willcox. “Interpolation among reduced-order matrices to obtain parameterized models for design, optimization and probabilistic analysis”. In: *International Journal for Numerical Methods in Fluids* (2009), pp. 207–230. ISSN: 02712091. DOI: [10.1002/flid.2089](https://doi.org/10.1002/flid.2089).
- [94] W. Desmet and D. Vandepitte. *Finite Element Modeling for Acoustics*. Ed. by International Seminar on Applied Acoustics. Leuven, 2005.
- [95] Z. Drmač and B. Peherstorfer. *Learning low-dimensional dynamical-system models from noisy frequency-response data with Loewner rational interpolation*. 2020. URL: <http://arxiv.org/pdf/1910.00110v2>.

- [96] S. J. Elliott, M. Ghandchi Tehrani, and R. S. Langley. “Nonlinear damping and quasi-linear modelling”. In: *Philosophical transactions. Series A, Mathematical, physical, and engineering sciences* 373.2051 (2015). DOI: [10.1098/rsta.2014.0402](https://doi.org/10.1098/rsta.2014.0402).
- [97] R. Everson and L. Sirovich. “Karhunen–Loève procedure for gappy data”. In: *Journal of the Optical Society of America A* 12.8 (1995), p. 1657. ISSN: 1084-7529. DOI: [10.1364/JOSAA.12.001657](https://doi.org/10.1364/JOSAA.12.001657).
- [98] F. J. Fahy. “Statistical energy analysis: a critical overview”. In: *Philosophical Transactions of the Royal Society of London. Series A: Physical and Engineering Sciences* 346.1681 (1994), pp. 431–447. ISSN: 0962-8428. DOI: [10.1098/rsta.1994.0027](https://doi.org/10.1098/rsta.1994.0027).
- [99] C. Farhat, M. Lesoinne, P. LeTallec, K. Pierson, and D. Rixen. “FETI-DP: a dual-primal unified FETI method – part I: A faster alternative to the two-level FETI method”. In: *International Journal for Numerical Methods in Engineering* 50.7 (2001), pp. 1523–1544. ISSN: 1097-0207. DOI: [10.1002/nme.76](https://doi.org/10.1002/nme.76).
- [100] H. Faßbender and J. Mayer. “A revised moment error expression for the AIRGA algorithm”. In: *Analele Universitatii "Ovidius" Constanta - Seria Matematica* 26.2 (2018), pp. 87–104. ISSN: 1844-0835. DOI: [10.2478/auom-2018-0020](https://doi.org/10.2478/auom-2018-0020).
- [101] J. Fehr, M. Fischer, B. Haasdonk, and P. Eberhard. “Greedy-based approximation of frequency-weighted Gramian matrices for model reduction in multibody dynamics”. In: *ZAMM - Journal of Applied Mathematics and Mechanics / Zeitschrift für Angewandte Mathematik und Mechanik* 93.8 (2013), pp. 501–519. ISSN: 00442267. DOI: [10.1002/zamm.201200014](https://doi.org/10.1002/zamm.201200014).
- [102] J. Fehr and P. Eberhard. “Error-controlled model reduction in flexible multibody dynamics”. In: *Journal of Computational and Nonlinear Dynamics* 5.3 (2010). ISSN: 15551423. DOI: [10.1115/1.4001372](https://doi.org/10.1115/1.4001372).
- [103] J. Fehr, J. Heiland, C. Himpe, and J. Saak. “Best practices for replicability, reproducibility and reusability of computer-based experiments exemplified by model reduction software”. In: *AIMS Mathematics* 1.3 (2016), pp. 261–281. ISSN: 2473-6988. DOI: [10.3934/Math.2016.3.261](https://doi.org/10.3934/Math.2016.3.261).
- [104] J. Fehr, P. Holzwarth, and P. Eberhard. “Interface and model reduction for efficient explicit simulations - a case study with nonlinear vehicle crash models”. In: *Mathematical and Computer Modelling of Dynamical Systems* 22.4 (2016), pp. 380–396. ISSN: 1387-3954. DOI: [10.1080/13873954.2016.1198385](https://doi.org/10.1080/13873954.2016.1198385).
- [105] J. Fehr, C. Tobias, and P. Eberhard. “Automated and error controlled model reduction for durability based structural optimization of mechanical systems”. In: *The Proceedings of the Asian Conference on Multibody Dynamics* 2010.5.0 (2010), pp. 57288-1–57288-10. DOI: [10.1299/jsmeacmd.2010.5.\\_57288-1\\_](https://doi.org/10.1299/jsmeacmd.2010.5._57288-1_).
- [106] L. Feng, A. C. Antoulas, and P. Benner. “Some a posteriori error bounds for reduced-order modelling of (non-)parametrized linear systems”. In: *ESAIM: Mathematical Modelling and Numerical Analysis* 51.6 (2017), pp. 2127–2158. DOI: [10.1051/m2an/2017014](https://doi.org/10.1051/m2an/2017014).

- [107] L. Feng and P. Benner. “A new error estimator for reduced-order modeling of linear parametric systems”. In: *IEEE Transactions on Microwave Theory and Techniques* 67.12 (2019), pp. 4848–4859. ISSN: 0018-9480. DOI: [10.1109/TMTT.2019.2948858](https://doi.org/10.1109/TMTT.2019.2948858).
- [108] L. Feng and P. Benner. *On Error Estimation for Reduced-order Modeling of Linear Non-parametric and Parametric Systems*. 2020. URL: <http://arxiv.org/pdf/2003.14319v2>.
- [109] L. Feng, J. G. Korvink, and P. Benner. “A fully adaptive scheme for model order reduction based on moment matching”. In: *IEEE Transactions on Components, Packaging and Manufacturing Technology* 5.12 (2015), pp. 1872–1884. ISSN: 2156-3950. DOI: [10.1109/TCPMT.2015.2491341](https://doi.org/10.1109/TCPMT.2015.2491341).
- [110] A. Franck. *Finite-Elemente-Methoden, Lösungsverfahren und Werkzeuge für die akustische Simulationstechnik: Zugl.: Aachen, Techn. Hochsch., Diss., 2008*. Vol. 9. Aachener Beiträge zur technischen Akustik. Berlin: Logos-Verl., 2009. ISBN: 978-3-8325-2313-8.
- [111] R. W. Freund. “Krylov-subspace methods for reduced-order modeling in circuit simulation”. In: *Journal of Computational and Applied Mathematics* 123.1-2 (2000), pp. 395–421. ISSN: 03770427. DOI: [10.1016/S0377-0427\(00\)00396-4](https://doi.org/10.1016/S0377-0427(00)00396-4).
- [112] M. I. Friswell, S. D. Garvey, and J. Penny. “Model reduction using dynamic and iterated IRS techniques”. In: *Journal of Sound and Vibration* 186.2 (1995), pp. 311–323. ISSN: 0022-460X. DOI: [10.1006/jsvi.1995.0451](https://doi.org/10.1006/jsvi.1995.0451).
- [113] K. Gallivan, A. Vandendorpe, and P. van Dooren. “Model reduction of MIMO systems via tangential interpolation”. In: *SIAM Journal on Matrix Analysis and Applications* 26.2 (2004), pp. 328–349. ISSN: 0895-4798. DOI: [10.1137/S0895479803423925](https://doi.org/10.1137/S0895479803423925).
- [114] L. Gaul, D. Brunner, and M. Junge. “Coupling a fast boundary element method with a finite element formulation for fluid–structure interaction”. In: *Computational Acoustics of Noise Propagation in Fluids - Finite and Boundary Element Methods*. Ed. by S. Marburg and B. Nolte. Berlin, Heidelberg: Springer Berlin Heidelberg, 2008, pp. 519–546. ISBN: 978-3-540-77447-1. DOI: [10.1007/978-3-540-77448-8\\_20](https://doi.org/10.1007/978-3-540-77448-8_20).
- [115] W. Gawronski and J.-N. Juang. “Model reduction in limited time and frequency intervals”. In: *International Journal of Systems Science* 21.2 (1990), pp. 349–376. ISSN: 0020-7721. DOI: [10.1080/00207729008910366](https://doi.org/10.1080/00207729008910366).
- [116] K. Gerdes. “A summary of infinite element formulations for exterior Helmholtz problems”. In: *Computer Methods in Applied Mechanics and Engineering* 164.1-2 (1998), pp. 95–105. ISSN: 00457825. DOI: [10.1016/S0045-7825\(98\)00048-6](https://doi.org/10.1016/S0045-7825(98)00048-6).
- [117] K. Gerdes. “A review of infinite element methods for exterior Helmholtz problems”. In: *Journal of Computational Acoustics* 08.01 (2000), pp. 43–62. ISSN: 0218-396X. DOI: [10.1142/S0218396X00000042](https://doi.org/10.1142/S0218396X00000042).

- [118] M. Geuss, D. Butnaru, B. Peherstorfer, H.-J. Bungartz, and B. Lohmann. “Parametric model order reduction by sparse-grid-based interpolation on matrix manifolds for multidimensional parameter spaces”. In: *2014 European Control Conference (ECC)*. IEEE, 2014, pp. 2727–2732. ISBN: 978-3-9524269-1-3. DOI: [10.1109/ECC.2014.6862414](https://doi.org/10.1109/ECC.2014.6862414).
- [119] D. Givoli. “Recent advances in the DtN FE Method”. In: *Archives of Computational Methods in Engineering* 6.2 (1999), pp. 71–116. ISSN: 1134-3060. DOI: [10.1007/BF02736182](https://doi.org/10.1007/BF02736182).
- [120] I. V. Gosea and A. C. Antoulas. *Approximation of a damped Euler-Bernoulli beam model in the Loewner framework*. 2017. URL: <http://arxiv.org/pdf/1712.06031v1>.
- [121] I. V. Gosea, D. S. Karachalios, and A. C. Antoulas. *Learning reduced-order models of quadratic control systems from input-output data*. 2020. URL: <http://arxiv.org/pdf/2012.02075v1>.
- [122] I. V. Gosea, Q. Zhang, and A. C. Antoulas. “Data-driven modeling from noisy measurements”. In: *PAMM* 20.S1 (2021). ISSN: 16177061. DOI: [10.1002/pamm.202000358](https://doi.org/10.1002/pamm.202000358).
- [123] C. Gräßle, M. Hinze, and S. Volkwein. “Model order reduction by proper orthogonal decomposition”. In: *Model Order Reduction*. Ed. by P. Benner, S. Grivet-Talocia, A. Quarteroni, G. Rozza, W. Schilders, and L. M. Silveira. De Gruyter, 2021, pp. 47–96. ISBN: 9783110671490. DOI: [10.1515/9783110671490-002](https://doi.org/10.1515/9783110671490-002).
- [124] E. J. Grimme. “Krylov projection methods for model reduction”. Dissertation. University of Illinois at Urbana-Champaign, 1997. URL: <http://hdl.handle.net/2142/81180> (visited on 01/15/2019).
- [125] M. J. Grote and C. Kirsch. “Dirichlet-to-Neumann boundary conditions for multiple scattering problems”. In: *Journal of Computational Physics* 201.2 (2004), pp. 630–650. ISSN: 00219991. DOI: [10.1016/j.jcp.2004.06.012](https://doi.org/10.1016/j.jcp.2004.06.012).
- [126] S. Gugercin, A. C. Antoulas, and C. Beattie. “ $\mathcal{H}_2$  model reduction for large-scale linear dynamical systems”. In: *SIAM Journal on Matrix Analysis and Applications* 30.2 (2008), pp. 609–638. ISSN: 0895-4798. DOI: [10.1137/060666123](https://doi.org/10.1137/060666123).
- [127] R. W. Guy. “The transmission of airborne sound through a finite panel, air gap, panel and cavity configuration—a steady state analysis”. In: *Acta Acustica united with Acustica* 49.4 (1981), pp. 323–333.
- [128] R. J. Guyan. “Reduction of stiffness and mass matrices”. In: *AIAA Journal* 3.2 (1965), p. 380. ISSN: 0001-1452. DOI: [10.2514/3.2874](https://doi.org/10.2514/3.2874).
- [129] S. Haider, A. Ghafoor, M. Imran, and F. M. Malik. “Frequency interval Gramians based structure preserving model order reduction for second order systems”. In: *Asian Journal of Control* 20.2 (2018), pp. 790–801. ISSN: 15618625. DOI: [10.1002/asjc.1598](https://doi.org/10.1002/asjc.1598).
- [130] S. Hain, M. Ohlberger, M. Radic, and K. Urban. “A hierarchical a posteriori error estimator for the reduced basis method”. In: *Advances in Computational Mathematics* 45.5-6 (2019), pp. 2191–2214. ISSN: 1019-7168. DOI: [10.1007/s10444-019-09675-z](https://doi.org/10.1007/s10444-019-09675-z).

- [131] I. Harari, M. Slavutin, and E. Turkel. “Analytical and numerical studies of a finite element PML for the Helmholtz equation”. In: *Journal of Computational Acoustics* 08.01 (2000), pp. 121–137. ISSN: 0218-396X. DOI: [10.1142/S0218396X0000008X](https://doi.org/10.1142/S0218396X0000008X).
- [132] D. Hartmann, M. Herz, M. Paffrath, J. Rommes, T. Tamarozzi, H. van der Auweraer, and U. Wever. “Model order reduction and digital twins”. In: *Model order reduction*. Ed. by P. Benner, S. Grivet-Talocia, A. Quarteroni, G. Rozza, W. Schilders, and L. M. Silveira. De Gruyter, 2021, pp. 379–430. ISBN: 9783110499001. DOI: [10.1515/9783110499001-012](https://doi.org/10.1515/9783110499001-012).
- [133] T. Hastie, R. Tibshirani, and J. Friedman. *The Elements of Statistical Learning*. New York, NY: Springer New York, 2009. ISBN: 978-0-387-84857-0. DOI: [10.1007/978-0-387-84858-7](https://doi.org/10.1007/978-0-387-84858-7).
- [134] U. Hetmaniuk, R. Tezaur, and C. Farhat. “Review and assessment of interpolatory model order reduction methods for frequency response structural dynamics and acoustics problems”. In: *International Journal for Numerical Methods in Engineering* 90.13 (2012), pp. 1636–1662. ISSN: 0029-5981. DOI: [10.1002/nme.4271](https://doi.org/10.1002/nme.4271).
- [135] U. Hetmaniuk, R. Tezaur, and C. Farhat. “An adaptive scheme for a class of interpolatory model reduction methods for frequency response problems”. In: *International Journal for Numerical Methods in Engineering* 93.10 (2013), pp. 1109–1124. ISSN: 0029-5981. DOI: [10.1002/nme.4436](https://doi.org/10.1002/nme.4436).
- [136] N. J. Higham, G. M. Negri Porzio, and F. Tisseur. *An Updated Set of Nonlinear Eigenvalue Problems*. 2019. URL: <http://eprints.maths.manchester.ac.uk/id/eprint/2699>.
- [137] C. Himpe. “Comparing (empirical-gramian-based) model order reduction algorithms”. In: *Model Reduction of Complex Dynamical Systems*. Ed. by P. Benner, T. Breiten, H. Faßbender, M. Hinze, T. Stykel, and R. Zimmermann. Cham: Springer International Publishing, 2021, pp. 141–164. ISBN: 978-3-030-72983-7. DOI: [10.1007/978-3-030-72983-7\\_7](https://doi.org/10.1007/978-3-030-72983-7_7).
- [138] M. Hornikx, M. Kaltenbacher, and S. Marburg. “A platform for benchmark cases in computational acoustics”. In: *Acta Acustica united with Acustica* 101.4 (2015), pp. 811–820. DOI: [10.3813/AAA.918875](https://doi.org/10.3813/AAA.918875).
- [139] T. J. Hughes. *The finite element method: Linear static and dynamic finite element analysis*. Repr. 1987, 1. publ. Mineola, NY: Dover Publ, 2000. ISBN: 9780486135021.
- [140] M. Hund, P. Mlinarić, and J. Saak. “An  $\mathcal{H}_2 \otimes \mathcal{L}_2$ -optimal model order reduction approach for parametric linear time-invariant systems”. In: *PAMM* 18.1 (2018). ISSN: 16177061. DOI: [10.1002/pamm.201800084](https://doi.org/10.1002/pamm.201800084).
- [141] R. Ibañez, E. Abisset-Chavanne, J. V. Aguado, D. Gonzalez, E. Cueto, and F. Chinesta. “A manifold learning approach to data-driven computational elasticity and inelasticity”. In: *Archives of Computational Methods in Engineering* 25.1 (2018), pp. 47–57. ISSN: 1134-3060. DOI: [10.1007/s11831-016-9197-9](https://doi.org/10.1007/s11831-016-9197-9).
- [142] F. Ihlenburg. *Finite Element Analysis of Acoustic Scattering*. Vol. 132. Applied Mathematical Sciences. New York, NY: Springer-Verlag New York Inc, 1998. ISBN: 9780387983196. DOI: [10.1007/b98828](https://doi.org/10.1007/b98828).

- [143] A. C. Ionita and A. C. Antoulas. “Data-driven parametrized model reduction in the Loewner framework”. In: *SIAM Journal on Scientific Computing* 36.3 (2014), A984–A1007. ISSN: 1064-8275. DOI: [10.1137/130914619](https://doi.org/10.1137/130914619).
- [144] D. J. Jagodzinski, M. Miksch, Q. Aumann, and G. Müller. “Modeling and optimizing an acoustic metamaterial to minimize low-frequency structure-borne sound”. In: *Mechanics Based Design of Structures and Machines* (2020), pp. 1–15. ISSN: 1539-7734. DOI: [10.1080/15397734.2020.1787842](https://doi.org/10.1080/15397734.2020.1787842).
- [145] L. Jaouen. *Acoustical porous material recipes*. 2021. URL: <http://apmr.matelys.com/> (visited on 05/17/2021).
- [146] L. Jaouen, E. Gourdon, and P. Glé. “Estimation of all six parameters of Johnson-Champoux-Allard-Lafarge model for acoustical porous materials from impedance tube measurements”. In: *The Journal of the Acoustical Society of America* 148.4 (2020), p. 1998. ISSN: 0001-4966. DOI: [10.1121/10.0002162](https://doi.org/10.1121/10.0002162).
- [147] F. B. Jensen, W. A. Kuperman, M. B. Porter, and H. Schmidt. *Computational Ocean Acoustics*. New York, NY: Springer New York, 2011. ISBN: 978-1-4419-8677-1. DOI: [10.1007/978-1-4419-8678-8](https://doi.org/10.1007/978-1-4419-8678-8).
- [148] S. G. Johnson. *Notes on Perfectly Matched Layers (PMLs)*. 2010. URL: <https://math.mit.edu/~stevenj/18.369/pml.pdf> (visited on 02/15/2021).
- [149] S. Jonckheere, E. Deckers, B. van Genechten, D. Vandepitte, and W. Desmet. “A direct hybrid Finite Element – Wave Based Method for the steady-state analysis of acoustic cavities with poro-elastic damping layers using the coupled Helmholtz–Biot equations”. In: *Computer Methods in Applied Mechanics and Engineering* 263 (2013), pp. 144–157. ISSN: 00457825. DOI: [10.1016/j.cma.2013.04.013](https://doi.org/10.1016/j.cma.2013.04.013).
- [150] E. Kausel. *Fundamental Solutions in Elastodynamics*. Cambridge: Cambridge University Press, 2006. ISBN: 9780511546112. DOI: [10.1017/CBO9780511546112](https://doi.org/10.1017/CBO9780511546112).
- [151] E. Kausel. *Advanced Structural Dynamics*. Cambridge University Press, 2017. ISBN: 9781316761403. DOI: [10.1017/9781316761403](https://doi.org/10.1017/9781316761403).
- [152] J. B. Keller and D. Givoli. “Exact non-reflecting boundary conditions”. In: *Journal of Computational Physics* 82.1 (1989), pp. 172–192. ISSN: 00219991. DOI: [10.1016/0021-9991\(89\)90041-7](https://doi.org/10.1016/0021-9991(89)90041-7).
- [153] S. M. Kim, J.-G. Kim, S.-W. Chae, and K. C. Park. “A strongly coupled model reduction of vibro-acoustic interaction”. In: *Computer Methods in Applied Mechanics and Engineering* 347 (2019), pp. 495–516. ISSN: 00457825. DOI: [10.1016/j.cma.2018.12.029](https://doi.org/10.1016/j.cma.2018.12.029).
- [154] D. D. Klerk, D. J. Rixen, and S. N. Voormeeren. “General framework for dynamic substructuring: history, review and classification of techniques”. In: *AIAA Journal* 46.5 (2008), pp. 1169–1181. ISSN: 0001-1452. DOI: [10.2514/1.33274](https://doi.org/10.2514/1.33274).
- [155] Y. Konkel, O. Farle, and R. Dyczij-Edlinger. “Ein Fehlerschätzer für die Krylov-Unterraum basierte Ordnungsreduktion zeitharmonischer Anregungsprobleme”. In: *Tagungsband GMA-Fachausschuss 1.30 "Modellbildung, Identifikation und Simulation in der Automatisierungstechnik"*. Ed. by B. Lohmann and A. Kugi. Vienna, 2008.

- [156] Y. Konkel, O. Farle, A. Sommer, S. Burgard, and R. Dyczij-Edlinger. “A posteriori error bounds for Krylov-based fast frequency sweeps of finite-element systems”. In: *IEEE Transactions on Magnetics* 50.2 (2014), pp. 441–444. ISSN: 0018-9464. DOI: [10.1109/TMAG.2013.2285442](https://doi.org/10.1109/TMAG.2013.2285442).
- [157] D. Krattiger and M. I. Hussein. “Bloch mode synthesis: ultrafast methodology for elastic band-structure calculations”. In: *Physical review. E, Statistical, nonlinear, and soft matter physics* 90.6 (2014), p. 063306. DOI: [10.1103/PhysRevE.90.063306](https://doi.org/10.1103/PhysRevE.90.063306).
- [158] D. Krattiger and M. I. Hussein. “Generalized Bloch mode synthesis for accelerated calculation of elastic band structures”. In: *Journal of Computational Physics* 357 (2018), pp. 183–205. ISSN: 00219991. DOI: [10.1016/j.jcp.2017.12.016](https://doi.org/10.1016/j.jcp.2017.12.016).
- [159] V. Krylov. “Acoustic black holes: Recent developments in the theory and applications”. In: *IEEE transactions on ultrasonics, ferroelectrics, and frequency control* 61.8 (2014), pp. 1296–1306. DOI: [10.1109/TUFFC.2014.3036](https://doi.org/10.1109/TUFFC.2014.3036).
- [160] D. Lafarge, P. Lemarinier, J. F. Allard, and V. Tarnow. “Dynamic compressibility of air in porous structures at audible frequencies”. In: *The Journal of the Acoustical Society of America* 102.4 (1997), pp. 1995–2006. ISSN: 0001-4966. DOI: [10.1121/1.419690](https://doi.org/10.1121/1.419690).
- [161] E. Lappano, M. Polanz, W. Desmet, and D. Mundo. “A parametric model order reduction technique for poroelastic finite element models”. In: *The Journal of the Acoustical Society of America* 142.4 (2017), p. 2376. ISSN: 0001-4966. DOI: [10.1121/1.5007845](https://doi.org/10.1121/1.5007845).
- [162] M. S. Lenzi, S. Lefteriu, H. Beriot, and W. Desmet. “A fast frequency sweep approach using Padé approximations for solving Helmholtz finite element models”. In: *Journal of Sound and Vibration* 332.8 (2013), pp. 1897–1917. ISSN: 0022-460X. DOI: [10.1016/j.jsv.2012.05.038](https://doi.org/10.1016/j.jsv.2012.05.038).
- [163] Y. C. Liang, H. P. Lee, S. P. Lim, W. Z. Lin, K. H. Lee, and C. G. Wu. “Proper orthogonal decomposition and its applications—Part I: Theory”. In: *Journal of Sound and Vibration* 252.3 (2002), pp. 527–544. ISSN: 0022-460X. DOI: [10.1006/jsvi.2001.4041](https://doi.org/10.1006/jsvi.2001.4041).
- [164] J. Lienemann, E. B. Rudnyi, and J. G. Korvink. “MST MEMS model order reduction: Requirements and benchmarks”. In: *Linear Algebra and its Applications* 415.2-3 (2006), pp. 469–498. ISSN: 00243795. DOI: [10.1016/j.laa.2005.04.002](https://doi.org/10.1016/j.laa.2005.04.002).
- [165] P. Lietaert and K. Meerbergen. “Comparing Loewner and Krylov based model order reduction for time delay systems”. In: *2018 European Control Conference (ECC)*. IEEE, 2018, pp. 545–550. ISBN: 978-3-9524-2698-2. DOI: [10.23919/ECC.2018.8550614](https://doi.org/10.23919/ECC.2018.8550614).
- [166] P. Lietaert, J. Pérez, B. Vandereycken, and K. Meerbergen. *Automatic rational approximation and linearization of nonlinear eigenvalue problems*. 2018. URL: <http://arxiv.org/pdf/1801.08622v2>.

- [167] T. Lieu, C. Farhat, and M. Lesoinne. “Reduced-order fluid/structure modeling of a complete aircraft configuration”. In: *Computer Methods in Applied Mechanics and Engineering* 195.41-43 (2006), pp. 5730–5742. ISSN: 00457825. DOI: [10.1016/j.cma.2005.08.026](https://doi.org/10.1016/j.cma.2005.08.026).
- [168] Y. Lin, L. Bao, and Y. Wei. “Model-order reduction of large-scale  $k$ th-order linear dynamical systems via a  $k$ th-order Arnoldi method”. In: *International Journal of Computer Mathematics* 87.2 (2010), pp. 435–453. ISSN: 0020-7160. DOI: [10.1080/00207160802130164](https://doi.org/10.1080/00207160802130164).
- [169] B. Lohmann, T. Bechtold, P. Eberhard, J. Fehr, D. J. Rixen, M. Cruz Varona, C. Lerch, C. D. Yuan, E. B. Rudnyi, B. Fröhlich, P. Holzwarth, D. Grunert, C. H. Meyer, and J. B. Rutzmoser. “Model order reduction in mechanical engineering”. In: *Model order reduction*. Ed. by P. Benner, S. Grivet-Talocia, A. Quarteroni, G. Rozza, W. Schilders, and L. M. Silveira. De Gruyter, 2021, pp. 33–73. ISBN: 9783110499001. DOI: [10.1515/9783110499001-002](https://doi.org/10.1515/9783110499001-002).
- [170] A. Low, R. M. Ridsdill Smith, M. Willford, P. Dallard, A. J. Fitzpatrick, A. Flint, and S. Le Bourva. “The London Millenium Footbridge”. In: *Structural Engineer* 79.22 (2001), pp. 17–21.
- [171] D. Lu, Y. Su, and Z. Bai. “Stability analysis of the two-level orthogonal Arnoldi procedure”. In: *SIAM Journal on Matrix Analysis and Applications* 37.1 (2016), pp. 195–214. ISSN: 0895-4798. DOI: [10.1137/151005142](https://doi.org/10.1137/151005142).
- [172] R. H. Lyon. *Theory and Application of Statistical Energy Analysis*. 2nd. Burlington: Elsevier Science, 2014. ISBN: 978-0750691116.
- [173] B. R. Mace and P. J. Shorter. “Energy flow models from finite element analysis”. In: *Journal of Sound and Vibration* 233.3 (2000), pp. 369–389. ISSN: 0022-460X. DOI: [10.1006/jsvi.1999.2812](https://doi.org/10.1006/jsvi.1999.2812).
- [174] B. Mace, W. Desmet, and B. Pluymers. “Mid-frequency methods in sound and vibration—Part A”. In: *Journal of Sound and Vibration* 332.8 (2013), pp. 1895–1896. ISSN: 0022-460X. DOI: [10.1016/j.jsv.2012.12.012](https://doi.org/10.1016/j.jsv.2012.12.012).
- [175] B. R. Mace and E. Manconi. “Modelling wave propagation in two-dimensional structures using finite element analysis”. In: *Journal of Sound and Vibration* 318.4-5 (2008), pp. 884–902. ISSN: 0022-460X. DOI: [10.1016/j.jsv.2008.04.039](https://doi.org/10.1016/j.jsv.2008.04.039).
- [176] S. Marburg. “Six boundary elements per wavelength: is that enough?” In: *Journal of Computational Acoustics* 10.01 (2002), pp. 25–51. ISSN: 0218-396X. DOI: [10.1142/S0218396X02001401](https://doi.org/10.1142/S0218396X02001401).
- [177] S. Marburg. “The Burton and Miller method: unlocking another mystery of its coupling parameter”. In: *Journal of Computational Acoustics* 24.01 (2016), p. 1550016. ISSN: 0218-396X. DOI: [10.1142/S0218396X15500162](https://doi.org/10.1142/S0218396X15500162).
- [178] S. Marburg and B. Nolte, eds. *Computational Acoustics of Noise Propagation in Fluids - Finite and Boundary Element Methods*. Berlin, Heidelberg: Springer Berlin Heidelberg, 2008. ISBN: 978-3-540-77447-1. DOI: [10.1007/978-3-540-77448-8](https://doi.org/10.1007/978-3-540-77448-8).

- [179] V. Mataix Ferrándiz, P. Bucher, R. Rossi, R. Zorrilla, J. Cotela, J. Maria, M. A. Celigueta, and G. Casas. *KratosMultiphysics/Kratos: KratosMultiphysics 8.1*. 2020. DOI: [10.5281/ZENODO.3234644](https://doi.org/10.5281/ZENODO.3234644).
- [180] A. J. Mayo and A. C. Antoulas. “A framework for the solution of the generalized realization problem”. In: *Linear Algebra and its Applications* 425.2-3 (2007), pp. 634–662. ISSN: 00243795. DOI: [10.1016/j.laa.2007.03.008](https://doi.org/10.1016/j.laa.2007.03.008).
- [181] N. G. R. de Melo Filho, A. Angeli, S. van Ophem, B. Pluymers, C. C. Claeys, E. Deckers, and W. Desmet. “Design space exploration for resonant metamaterials using physics guided neural networks”. In: *Proceedings of ISMA 2020*. KU Leuven - Department of Mechanical Engineering, 2020, pp. 2503–2512.
- [182] N. G. R. de Melo Filho, C. Claeys, E. Deckers, and W. Desmet. “Metamaterial foam core sandwich panel designed to attenuate the mass-spring-mass resonance sound transmission loss dip”. In: *Mechanical Systems and Signal Processing* 139 (2020), p. 106624. ISSN: 08883270. DOI: [10.1016/j.ymsp.2020.106624](https://doi.org/10.1016/j.ymsp.2020.106624).
- [183] D. G. Meyer and S. Srinivasan. “Balancing and model reduction for second-order form linear systems”. In: *IEEE Transactions on Automatic Control* 41.11 (1996), pp. 1632–1644. ISSN: 0018-9286. DOI: [10.1109/9.544000](https://doi.org/10.1109/9.544000).
- [184] M. Miksch, J. D. Perez Ramirez, and G. Müller. “Numerical computation of the spatial decaying wave characteristics for the design of locally resonant acoustic metamaterials”. In: *Journal of Physics: Conference Series* 1264 (2019), p. 012015. ISSN: 1742-6588. DOI: [10.1088/1742-6596/1264/1/012015](https://doi.org/10.1088/1742-6596/1264/1/012015).
- [185] M. Miksch. “Modeling and designing lightweight acoustic metamaterials with tailored vibroacoustic properties”. Dissertation. Munich: Technical University of Munich, 2021.
- [186] M. Miksch, Q. Aumann, and G. Müller. “Reducing structure-borne noise in thin-walled structures by local thickness variations”. In: *PAMM* 18.1 (2018), e201800177. ISSN: 16177061. DOI: [10.1002/pamm.201800177](https://doi.org/10.1002/pamm.201800177).
- [187] M. A. Mironov. “Propagation of a flexural wave in a plate whose thickness decreases smoothly to zero in a finite interval”. In: *Soviet Physics - Acoustics* 34.3 (1988), pp. 318–319.
- [188] F. Mittermeier, J. Schauer, M. Miksch, and G. Müller. “Numerical investigation of the potential of tailored inclusions as noise reduction measures”. In: *Journal of Physics: Conference Series* 1264 (2019), p. 012013. ISSN: 1742-6588. DOI: [10.1088/1742-6596/1264/1/012013](https://doi.org/10.1088/1742-6596/1264/1/012013).
- [189] G. Müller and M. Möser, eds. *Handbook of Engineering Acoustics*. Berlin and Heidelberg: Springer, 2013. ISBN: 9783540240525. DOI: [10.1007/978-3-540-69460-1](https://doi.org/10.1007/978-3-540-69460-1).
- [190] Y. Nakatsukasa, O. Sète, and L. N. Trefethen. “The AAA algorithm for rational approximation”. In: *SIAM Journal on Scientific Computing* 40.3 (2018), A1494–A1522. ISSN: 1064-8275. DOI: [10.1137/16M1106122](https://doi.org/10.1137/16M1106122).
- [191] L. Nannen and M. Wess. “Computing scattering resonances using perfectly matched layers with frequency dependent scaling functions”. In: *BIT Numerical Mathematics* 58.2 (2018), pp. 373–395. ISSN: 0006-3835. DOI: [10.1007/s10543-018-0694-0](https://doi.org/10.1007/s10543-018-0694-0).

- [192] *Night noise guidelines for Europe*. Copenhagen: World Health Organization Regional Office for Europe, 2009. ISBN: 978 92 890 4173 7.
- [193] X. Olny and R. Panneton. “Acoustical determination of the parameters governing thermal dissipation in porous media”. In: *The Journal of the Acoustical Society of America* 123.2 (2008), pp. 814–824. ISSN: 0001-4966. DOI: [10.1121/1.2828066](https://doi.org/10.1121/1.2828066).
- [194] K. C. Opiela, T. G. Zieliński, T. Dvorák, and S. Kúdela Jr. “Perforated closed-cell aluminium foam for acoustic absorption”. In: *Applied Acoustics* 174 (2021), p. 107706. DOI: [10.1016/j.apacoust.2020.107706](https://doi.org/10.1016/j.apacoust.2020.107706).
- [195] O. Ozgun and M. Kuzuoglu. “Multicenter perfectly matched layer implementation for finite element mesh truncation”. In: *Microwave and Optical Technology Letters* 49.4 (2007), pp. 827–832. ISSN: 08952477. DOI: [10.1002/mop.22258](https://doi.org/10.1002/mop.22258).
- [196] O. Ozgun and M. Kuzuoglu. “Near-field performance analysis of locally-conformal perfectly matched absorbers via Monte Carlo simulations”. In: *Journal of Computational Physics* 227.2 (2007), pp. 1225–1245. ISSN: 00219991. DOI: [10.1016/j.jcp.2007.08.025](https://doi.org/10.1016/j.jcp.2007.08.025).
- [197] D. Panagiotopoulos, W. Desmet, and E. Deckers. “An automatic Krylov subspaces recycling technique for the construction of a global solution basis of non-affine parametric linear systems”. In: *Computer Methods in Applied Mechanics and Engineering* 373 (2021), p. 113510. ISSN: 00457825. DOI: [10.1016/j.cma.2020.113510](https://doi.org/10.1016/j.cma.2020.113510).
- [198] R. Panneton and X. Olny. “Acoustical determination of the parameters governing viscous dissipation in porous media”. In: *The Journal of the Acoustical Society of America* 119.4 (2006), pp. 2027–2040. ISSN: 0001-4966. DOI: [10.1121/1.2169923](https://doi.org/10.1121/1.2169923).
- [199] H. K. F. Panzer. *Model order reduction by Krylov subspace methods with global error bounds and automatic choice of parameters: Zugl.: München, Techn. Univ., Diss., 2014*. Ingenieurwissenschaften. München: Dr. Hut, 2014. ISBN: 978-3-8439-1852-7.
- [200] H. K. F. Panzer, J. Hubele, R. Eid, and B. Lohmann. “Generating a parametric finite element model of a 3d cantilever timoshenko beam using matlab”. In: *Tech. reports on aut. control, Inst. Aut. Control, TU München* (2009). URL: <https://mediatum.ub.tum.de/1072355> (visited on 10/14/2021).
- [201] H. K. F. Panzer, J. Mohring, R. Eid, and B. Lohmann. “Parametric model order reduction by matrix interpolation”. In: *at - Automatisierungstechnik* 58.8 (2010), p. 958. ISSN: 0178-2312. DOI: [10.1524/auto.2010.0863](https://doi.org/10.1524/auto.2010.0863).
- [202] H. K. F. Panzer, T. Wolf, and B. Lohmann. “ $\mathcal{H}_2$  and  $\mathcal{H}_\infty$  error bounds for model order reduction of second order systems by Krylov subspace methods”. In: *2013 European Control Conference (ECC)*. IEEE, 2013, pp. 4484–4489. ISBN: 978-3-033-03962-9. DOI: [10.23919/ECC.2013.6669657](https://doi.org/10.23919/ECC.2013.6669657).
- [203] M. Papadopoulos, R. van Beeumen, S. François, G. Degrande, and G. Lombaert. “Modal characteristics of structures considering dynamic soil-structure interaction effects”. In: *Soil Dynamics and Earthquake Engineering* 105 (2018), pp. 114–118. ISSN: 0267-7261. DOI: [10.1016/j.soildyn.2017.11.012](https://doi.org/10.1016/j.soildyn.2017.11.012).

- [204] A. Parrott and L. Warshaw. *Industry 4.0 and the digital twin*. 2017. URL: <https://www2.deloitte.com/us/en/insights/focus/industry-4-0/digital-twin-technology-smart-factory.html> (visited on 07/19/2021).
- [205] B. Peherstorfer and K. Willcox. “Dynamic data-driven reduced-order models”. In: *Computer Methods in Applied Mechanics and Engineering* 291 (2015), pp. 21–41. ISSN: 00457825. DOI: [10.1016/j.cma.2015.03.018](https://doi.org/10.1016/j.cma.2015.03.018).
- [206] B. Peherstorfer, K. Willcox, and M. Gunzburger. “Survey of multifidelity methods in uncertainty propagation, inference, and optimization”. In: *SIAM Review* 60.3 (2018), pp. 550–591. ISSN: 0036-1445. DOI: [10.1137/16M1082469](https://doi.org/10.1137/16M1082469).
- [207] A. Pelat, F. Gautier, S. C. Conlon, and F. Semperlotti. “The acoustic black hole: A review of theory and applications”. In: *Journal of Sound and Vibration* 476 (2020), p. 115316. ISSN: 0022-460X. DOI: [10.1016/j.jsv.2020.115316](https://doi.org/10.1016/j.jsv.2020.115316).
- [208] A. A. Phoenix and P. A. Tarazaga. “Dynamic model reduction using data-driven Loewner-framework applied to thermally morphing structures”. In: *Journal of Sound and Vibration* 396 (2017), pp. 274–288. ISSN: 0022-460X. DOI: [10.1016/j.jsv.2017.01.039](https://doi.org/10.1016/j.jsv.2017.01.039).
- [209] F. Pled and C. Desceliers. “Review and recent developments on the perfectly matched layer (PML) method for the numerical modeling and simulation of elastic wave propagation in unbounded domains”. In: *Archives of Computational Methods in Engineering* (2021). ISSN: 1134-3060. DOI: [10.1007/s11831-021-09581-y](https://doi.org/10.1007/s11831-021-09581-y).
- [210] C. Poussot-Vassal. “Large-scale dynamical model approximation and its applications”. Habilitation à diriger des recherches. INP DE TOULOUSE, 2019. URL: <https://tel.archives-ouvertes.fr/tel-02188802>.
- [211] C. Poussot-Vassal. “An iterative SVD-tangential interpolation method for medium-scale MIMO systems approximation with application on flexible aircraft”. In: *IEEE Conference on Decision and Control and European Control Conference*. IEEE, 122011, pp. 7117–7122. ISBN: 978-1-61284-801-3. DOI: [10.1109/CDC.2011.6160331](https://doi.org/10.1109/CDC.2011.6160331).
- [212] Pride, Morgan, and Gangi. “Drag forces of porous-medium acoustics”. In: *Physical review. B, Condensed matter* 47.9 (1993), pp. 4964–4978. ISSN: 0163-1829. DOI: [10.1103/PhysRevB.47.4964](https://doi.org/10.1103/PhysRevB.47.4964).
- [213] J. L. Proctor, S. L. Brunton, and J. N. Kutz. “Dynamic mode decomposition with control”. In: *SIAM Journal on Applied Dynamical Systems* 15.1 (2016), pp. 142–161. DOI: [10.1137/15M1013857](https://doi.org/10.1137/15M1013857).
- [214] E. Y. Qian, B. Kramer, B. Peherstorfer, and K. Willcox. “Lift & Learn: Physics-informed machine learning for large-scale nonlinear dynamical systems”. In: *Physica D: Nonlinear Phenomena* 406 (2020), p. 132401. ISSN: 01672789. DOI: [10.1016/j.physd.2020.132401](https://doi.org/10.1016/j.physd.2020.132401).
- [215] Z.-Q. Qu. *Model Order Reduction Techniques: With Applications in Finite Element Analysis*. London and s.l.: Springer London, 2004. ISBN: 978-1-84996-924-6. DOI: [10.1007/978-1-4471-3827-3](https://doi.org/10.1007/978-1-4471-3827-3).

- [216] A. Rasheed, O. San, and T. Kvamsdal. “Digital twin: values, challenges and enablers from a modeling perspective”. In: *IEEE Access* 8 (2020), pp. 21980–22012. DOI: [10.1109/ACCESS.2020.2970143](https://doi.org/10.1109/ACCESS.2020.2970143).
- [217] T. Reis and T. Stykel. “Balanced truncation model reduction of second-order systems”. In: *Mathematical and Computer Modelling of Dynamical Systems* 14.5 (2008), pp. 391–406. ISSN: 1387-3954. DOI: [10.1080/13873950701844170](https://doi.org/10.1080/13873950701844170).
- [218] A. C. Rodriguez and S. Gugercin. *The p-AAA algorithm for data driven modeling of parametric dynamical systems*. 2020. URL: <http://arxiv.org/pdf/2003.06536v2>.
- [219] J. Rommes and N. Martins. “Computing transfer function dominant poles of large-scale second-order dynamical systems”. In: *SIAM Journal on Scientific Computing* 30.4 (2008), pp. 2137–2157. ISSN: 1064-8275. DOI: [10.1137/070684562](https://doi.org/10.1137/070684562).
- [220] L. Rouleau, J.-F. Deü, and A. Legay. “A comparison of model reduction techniques based on modal projection for structures with frequency-dependent damping”. In: *Mechanical Systems and Signal Processing* 90 (2017), pp. 110–125. ISSN: 08883270. DOI: [10.1016/j.ymssp.2016.12.013](https://doi.org/10.1016/j.ymssp.2016.12.013).
- [221] R. Rumpler, P. Göransson, and J.-F. Deü. “A finite element approach combining a reduced-order system, Padé approximants, and an adaptive frequency windowing for fast multi-frequency solution of poro-acoustic problems”. In: *International Journal for Numerical Methods in Engineering* 97.10 (2014), pp. 759–784. ISSN: 0029-5981. DOI: [10.1002/nme.4609](https://doi.org/10.1002/nme.4609).
- [222] R. Rumpler. *Efficient finite element approach for structural-acoustic applications including 3D modelling of sound absorbing porous materials*. Vol. 2012:10. TRITA-AVE. Stockholm: Engineering Sciences, Royal Institute of Technology, 2012. ISBN: 978-91-7501-279-7.
- [223] R. Rumpler. “Padé approximants and the modal connection: Towards increased robustness for fast parametric sweeps”. In: *International Journal for Numerical Methods in Engineering* 113.1 (2018), pp. 65–81. ISSN: 0029-5981. DOI: [10.1002/nme.5603](https://doi.org/10.1002/nme.5603).
- [224] Y. Saad. *Iterative methods for sparse linear systems*. 2nd ed. Philadelphia, Pa.: Society for Industrial and Applied Mathematics (SIAM 3600 Market Street Floor 6 Philadelphia PA 19104), 2003. ISBN: 9780898718003. URL: [http://epubs.siam.org/ebooks/siam/other\\_titles\\_in\\_applied\\_mathematics/ot82](http://epubs.siam.org/ebooks/siam/other_titles_in_applied_mathematics/ot82).
- [225] M. Saadvandi, K. Meerbergen, and E. Jarlebring. “On dominant poles and model reduction of second order time-delay systems”. In: *Applied Numerical Mathematics* 62.1 (2012), pp. 21–34. ISSN: 01689274. DOI: [10.1016/j.apnum.2011.09.005](https://doi.org/10.1016/j.apnum.2011.09.005).
- [226] J. Saak, D. Siebelts, and S. W. R. Werner. “A comparison of second-order model order reduction methods for an artificial fishtail”. In: *at - Automatisierungstechnik* 67.8 (2019), pp. 648–667. ISSN: 0178-2312. DOI: [10.1515/auto-2019-0027](https://doi.org/10.1515/auto-2019-0027).
- [227] T. Sakuma, S. Schneider, and Y. Yasuda. “Fast Solution Methods”. In: *Computational Acoustics of Noise Propagation in Fluids - Finite and Boundary Element Methods*. Ed. by S. Marburg and B. Nolte. Berlin, Heidelberg: Springer Berlin Heidelberg, 2008, pp. 333–366. ISBN: 978-3-540-77447-1. DOI: [10.1007/978-3-540-77448-8\\_13](https://doi.org/10.1007/978-3-540-77448-8_13).

- [228] S. B. Salimbahrami. “Structure preserving order reduction of large scale second order models”. Dissertation. München: Technische Universität München, 2005.
- [229] M. Sasso, G. Palmieri, and D. Amodio. “Application of fractional derivative models in linear viscoelastic problems”. In: *Mechanics of Time-Dependent Materials* 15.4 (2011), pp. 367–387. ISSN: 1385-2000. DOI: [10.1007/s11043-011-9153-x](https://doi.org/10.1007/s11043-011-9153-x).
- [230] P. J. Schmid. “Dynamic mode decomposition of numerical and experimental data”. In: *Journal of Fluid Mechanics* 656 (2010), pp. 5–28. ISSN: 0022-1120. DOI: [10.1017/S0022112010001217](https://doi.org/10.1017/S0022112010001217).
- [231] F. Schneider, I. Papaioannou, M. Ehre, and D. Straub. “Polynomial chaos based rational approximation in linear structural dynamics with parameter uncertainties”. In: *Computers & Structures* 233 (2020), p. 106223. ISSN: 00457949. DOI: [10.1016/j.compstruc.2020.106223](https://doi.org/10.1016/j.compstruc.2020.106223).
- [232] G. Schrag, L. Feng, and T. Bechtold, eds. *System-Level Modeling of MEMS*. Vol. 10. Advanced micro et nanosystems. Weinheim: Wiley-VCH Verlag GmbH & Co. KGaA, 2013. ISBN: 9783527647132. DOI: [10.1002/9783527647132](https://doi.org/10.1002/9783527647132).
- [233] P. Schulze and B. Unger. “Data-driven interpolation of dynamical systems with delay”. In: *Systems & Control Letters* 97 (2016), pp. 125–131. ISSN: 01676911. DOI: [10.1016/j.sysconle.2016.09.007](https://doi.org/10.1016/j.sysconle.2016.09.007).
- [234] P. Schulze, B. Unger, C. Beattie, and S. Gugercin. “Data-driven structured realization”. In: *Linear Algebra and its Applications* 537 (2018), pp. 250–286. ISSN: 00243795. DOI: [10.1016/j.laa.2017.09.030](https://doi.org/10.1016/j.laa.2017.09.030).
- [235] F. Semperlotti and H. Zhu. “Acoustic meta-structures based on periodic acoustic black holes”. In: *The Journal of the Acoustical Society of America* 137.4 (2015), p. 2265. ISSN: 0001-4966. DOI: [10.1121/1.4920263](https://doi.org/10.1121/1.4920263).
- [236] P. J. Shorter and R. S. Langley. “Vibro-acoustic analysis of complex systems”. In: *Journal of Sound and Vibration* 288.3 (2005), pp. 669–699. ISSN: 0022-460X. DOI: [10.1016/j.jsv.2005.07.010](https://doi.org/10.1016/j.jsv.2005.07.010).
- [237] V. Simoncini and F. Perotti. “On the numerical solution of  $(\lambda^2 a + \lambda b + c)x = b$  and application to structural dynamics”. In: *SIAM Journal on Scientific Computing* 23.6 (2002), pp. 1875–1897. ISSN: 1064-8275. DOI: [10.1137/S1064827501383373](https://doi.org/10.1137/S1064827501383373).
- [238] K. Sinani, S. Gugercin, and C. Beattie. “A structure-preserving model reduction algorithm for dynamical systems with nonlinear frequency dependence”. In: *IFAC-PapersOnLine* 49.9 (2016), pp. 56–61. ISSN: 24058963. DOI: [10.1016/j.ifacol.2016.07.492](https://doi.org/10.1016/j.ifacol.2016.07.492).
- [239] R. D. Slone, R. Lee, and J.-F. Lee. “Well-conditioned asymptotic waveform evaluation for finite elements”. In: *IEEE Transactions on Antennas and Propagation* 51.9 (2003), pp. 2442–2447. ISSN: 0018-926X. DOI: [10.1109/TAP.2003.816321](https://doi.org/10.1109/TAP.2003.816321).
- [240] A. Sommerfeld. *Partial differential equations in physics*. 1st ed. Vol. 1. Pure and applied mathematics (Academic Press). New York, N.Y.: Elsevier textbooks, 1949. ISBN: 978-0-12-654656-9. URL: <http://site.ebrary.com/lib/alltitles/docDetail.action?docID=10259308>.

- [241] T.-J. Su and R. R. Craig. “Model reduction and control of flexible structures using Krylov vectors”. In: *Journal of Guidance, Control, and Dynamics* 14.2 (1991), pp. 260–267. ISSN: 0731-5090. DOI: [10.2514/3.20636](https://doi.org/10.2514/3.20636).
- [242] J. Q. Sun, M. R. Jolly, and M. A. Norris. “Passive, adaptive and active tuned vibration absorbers—A survey”. In: *Journal of Mechanical Design* 117.B (1995), pp. 234–242. ISSN: 1050-0472. DOI: [10.1115/1.2836462](https://doi.org/10.1115/1.2836462).
- [243] R. Swischuk, L. Mainini, B. Peherstorfer, and K. Willcox. “Projection-based model reduction: Formulations for physics-based machine learning”. In: *Computers & Fluids* 179 (2019), pp. 704–717. ISSN: 00457930. DOI: [10.1016/j.compfluid.2018.07.021](https://doi.org/10.1016/j.compfluid.2018.07.021).
- [244] F. Theakston, ed. *Burden of disease from environmental noise: Quantification of healthy life years lost in Europe*. Copenhagen: World Health Organization Regional Office for Europe, 2011. ISBN: 978 92 890 0229 5.
- [245] F. Tisseur and K. Meerbergen. “The quadratic eigenvalue problem”. In: *SIAM Review* 43.2 (2001), pp. 235–286. ISSN: 0036-1445. DOI: [10.1137/S0036144500381988](https://doi.org/10.1137/S0036144500381988).
- [246] Z. Tomljanović, C. Beattie, and S. Gugercin. “Damping optimization of parameter dependent mechanical systems by rational interpolation”. In: *Advances in Computational Mathematics* 216.1 (2018), p. 317. ISSN: 1019-7168. DOI: [10.1007/s10444-018-9605-9](https://doi.org/10.1007/s10444-018-9605-9).
- [247] J. H. Tu, C. W. Rowley, D. M. Luchtenburg, S. L. Brunton, and N. J. Kutz. “On dynamic mode decomposition: Theory and applications”. In: *Journal of Computational Dynamics* 1.2 (2014), pp. 391–421. ISSN: 2158-2505. DOI: [10.3934/jcd.2014.1.391](https://doi.org/10.3934/jcd.2014.1.391).
- [248] R. Ullmann, S. Sicklinger, and G. Müller. “Optimization-Based Parametric Model Order Reduction for the Application to the Frequency-Domain Analysis of Complex Systems”. In: *Model Reduction of Complex Dynamical Systems*. Ed. by P. Benner, T. Breiten, H. Faßbender, M. Hinze, T. Stykel, and R. Zimmermann. Vol. 171. International Series of Numerical Mathematics. Cham: Springer International Publishing, 2021, pp. 165–189. ISBN: 978-3-030-72982-0. DOI: [10.1007/978-3-030-72983-7\\_8](https://doi.org/10.1007/978-3-030-72983-7_8).
- [249] D. A. Vaccari and H.-K. Wang. “Multivariate polynomial regression for identification of chaotic time series”. In: *Mathematical and Computer Modelling of Dynamical Systems* 13.4 (2007), pp. 395–412. ISSN: 1387-3954. DOI: [10.1080/13873950600883691](https://doi.org/10.1080/13873950600883691).
- [250] R. van Beeumen, K. Meerbergen, and W. Michiels. “A rational Krylov method based on Hermite interpolation for nonlinear eigenvalue problems”. In: *SIAM Journal on Scientific Computing* 35.1 (2013), A327–A350. ISSN: 1064-8275. DOI: [10.1137/120877556](https://doi.org/10.1137/120877556).
- [251] L. van Belle, N. G. R. de Melo Filho, M. Clasing Villanueva, C. C. Claeys, E. Deckers, F. Naets, and W. Desmet. “Fast metamaterial design optimization using reduced order unit cell modeling”. In: *Proceedings of ISMA 2020*. KU Leuven - Department of Mechanical Engineering, 2020, pp. 2487–2501.

- [252] A. van de Walle. “The power of model order reduction in vibroacoustics and its applications in model-based sensing”. PhD Thesis. Leuven, 2018. URL: <https://lirias.kuleuven.be/retrieve/481989>.
- [253] S. van Ophem. “Novel Reduction Techniques for Exterior Vibro-acoustic Models and their use in Model-based Sensing and Identification”. PhD thesis. 2019. URL: <https://lirias.kuleuven.be/retrieve/538082>.
- [254] S. van Ophem, O. Atak, E. Deckers, and W. Desmet. “Stable model order reduction for time-domain exterior vibro-acoustic finite element simulations”. In: *Computer Methods in Applied Mechanics and Engineering* 325 (2017), pp. 240–264. ISSN: 00457825. DOI: [10.1016/j.cma.2017.06.022](https://doi.org/10.1016/j.cma.2017.06.022).
- [255] S. van Ophem, E. Deckers, and W. Desmet. “Parametric model order reduction without a priori sampling for low rank changes in vibro-acoustic systems”. In: *Mechanical Systems and Signal Processing* 130 (2019), pp. 597–609. ISSN: 08883270. DOI: [10.1016/j.ymsp.2019.05.035](https://doi.org/10.1016/j.ymsp.2019.05.035).
- [256] S. van Ophem, A. van de Walle, E. Deckers, and W. Desmet. *Efficient MIMO Krylov subspace model order reduction for vibro-acoustic systems*. ANTARES - Advanced Training and Research in Energy. KU Leuven - Faculty of Engineering, 2018. ISBN: 9789082893106. URL: <https://lirias.kuleuven.be/2238457>.
- [257] V. N. Vapnik. *The Nature of Statistical Learning Theory*. New York, NY: Springer New York, 1995. ISBN: 978-1-4757-2442-4. DOI: [10.1007/978-1-4757-2440-0](https://doi.org/10.1007/978-1-4757-2440-0).
- [258] K. Vergote, C. Vanmaele, D. Vandepitte, and W. Desmet. “An efficient wave based approach for the time-harmonic vibration analysis of 3D plate assemblies”. In: *Journal of Sound and Vibration* 332.8 (2013), pp. 1930–1946. ISSN: 0022-460X. DOI: [10.1016/j.jsv.2012.11.018](https://doi.org/10.1016/j.jsv.2012.11.018).
- [259] A. Vermeil de Conchard, H. Mao, and R. Rumpfer. “A perfectly matched layer formulation adapted for fast frequency sweeps of exterior acoustics finite element models”. In: *Journal of Computational Physics* 398 (2019), p. 108878. ISSN: 00219991. DOI: [10.1016/j.jcp.2019.108878](https://doi.org/10.1016/j.jcp.2019.108878).
- [260] Vigran, T. E., Kelders, L., Lauriks, W., Leclaire, P., Johansen, T. F. “Prediction and measurements of the influence of boundary conditions in a standing wave tube”. In: *Acta Acustica united with Acustica* 83.3 (1997), pp. 419–423.
- [261] P. Vuillemin. “Frequency-limited approximation of large-scale LTI dynamical models”. PhD Thesis. University of Toulouse, 2014. URL: <https://hal.archives-ouvertes.fr/tel-01092051> (visited on 07/14/2021).
- [262] X. Wang, Y. Jiang, and X. Kong. “Laguerre functions approximation for model reduction of second order time-delay systems”. In: *Journal of the Franklin Institute* 353.14 (2016), pp. 3560–3577. ISSN: 00160032. DOI: [10.1016/j.jfranklin.2016.06.024](https://doi.org/10.1016/j.jfranklin.2016.06.024).
- [263] K. Willcox. “Unsteady flow sensing and estimation via the gappy proper orthogonal decomposition”. In: *Computers & Fluids* 35.2 (2006), pp. 208–226. ISSN: 00457930. DOI: [10.1016/j.compfluid.2004.11.006](https://doi.org/10.1016/j.compfluid.2004.11.006).

- [264] K. Willcox and J. Peraire. “Balanced model reduction via the proper orthogonal decomposition”. In: *AIAA Journal* 40.11 (2002), pp. 2323–2330. ISSN: 0001-1452. DOI: [10.2514/2.1570](https://doi.org/10.2514/2.1570).
- [265] C. Winter, M. Buchschmid, and G. Müller. “Robust estimation of the energy flow in timber structures”. In: *Proceedings of the 24th International Congress on Sound and Vibration*. London, 2017.
- [266] C. Winter. “Frequency dependent modeling for the prediction of the sound transmission in timber constructions”. Dissertation. München: Technische Universität München, 2018. URL: <http://mediatum.ub.tum.de/?id=1436735> (visited on 09/24/2021).
- [267] J. P. Wolf and C. Song. *Finite-element modelling of unbounded media*. Reprinted. Chichester: Wiley, 1997. ISBN: 0471961345.
- [268] S. A. Wyatt. “Issues in interpolatory model reduction: Inexact solves, second-order systems and DAEs”. Dissertation. Virginia Polytechnic Institute and State University, 2012.
- [269] X. Xie, H. Zheng, S. Jonckheere, and W. Desmet. “Explicit and efficient topology optimization of frequency-dependent damping patches using moving morphable components and reduced-order models”. In: *Computer Methods in Applied Mechanics and Engineering* 355 (2019), pp. 591–613. ISSN: 00457825. DOI: [10.1016/j.cma.2019.06.039](https://doi.org/10.1016/j.cma.2019.06.039).
- [270] X. Xie, H. Zheng, S. Jonckheere, and W. Desmet. “Acoustic simulation of cavities with porous materials using an adaptive model order reduction technique”. In: *Journal of Sound and Vibration* 485 (2020), p. 115570. ISSN: 0022-460X. DOI: [10.1016/j.jsv.2020.115570](https://doi.org/10.1016/j.jsv.2020.115570).
- [271] X. Xie, H. Zheng, S. Jonckheere, B. Pluymers, and W. Desmet. “A parametric model order reduction technique for inverse viscoelastic material identification”. In: *Computers & Structures* 212 (2019), pp. 188–198. ISSN: 00457949. DOI: [10.1016/j.compstruc.2018.10.013](https://doi.org/10.1016/j.compstruc.2018.10.013).
- [272] X. Xie, H. Zheng, S. Jonckheere, A. van de Walle, B. Pluymers, and W. Desmet. “Adaptive model reduction technique for large-scale dynamical systems with frequency-dependent damping”. In: *Computer Methods in Applied Mechanics and Engineering* 332 (2018), pp. 363–381. ISSN: 00457825. DOI: [10.1016/j.cma.2017.12.023](https://doi.org/10.1016/j.cma.2017.12.023).
- [273] Y. Yue, L. Feng, and P. Benner. *An Adaptive Pole-Matching Method for Interpolating Reduced-Order Models*. 2019. URL: <http://arxiv.org/pdf/1908.00820v1>.
- [274] A. Zangeneh, S. François, G. Lombaert, and C. Pacoste. “Modal analysis of coupled soil-structure systems”. In: *Soil Dynamics and Earthquake Engineering* 144 (2021), p. 106645. ISSN: 0267-7261. DOI: [10.1016/j.soildyn.2021.106645](https://doi.org/10.1016/j.soildyn.2021.106645).
- [275] Q. Zhou and P. F. Joseph. “A numerical method for the calculation of dynamic response and acoustic radiation from an underwater structure”. In: *Journal of Sound and Vibration* 283.3-5 (2005), pp. 853–873. ISSN: 0022-460X. DOI: [10.1016/j.jsv.2004.05.028](https://doi.org/10.1016/j.jsv.2004.05.028).

- 
- [276] O. C. Zienkiewicz, R. L. Taylor, and D. Fox. *The Finite Element Method for Solid and Structural Mechanics*. 7th ed. Elsevier, 2014. ISBN: 9781856176347. DOI: [10.1016/C2009-0-26332-X](https://doi.org/10.1016/C2009-0-26332-X).
- [277] O. C. Zienkiewicz, R. L. Taylor, and J. Z. Zhu. *The Finite Element Method: Its Basis and Fundamentals*. 7th ed. Elsevier, 2013. ISBN: 9781856176330. DOI: [10.1016/C2009-0-24909-9](https://doi.org/10.1016/C2009-0-24909-9).
- [278] M. Zinner and F. Duddeck. “Efficient simulation of acoustic measures using Krylov subspaces and system simulation”. In: *Tagungsband - DAGA 2018*. Berlin: Deutsche Gesellschaft für Akustik e.V. (DEGA), 2018, pp. 1007–1010. ISBN: 978-3-939296-13-3. URL: [https://pub.dega-akustik.de/DAGA\\_2018/data/articles/000261.pdf](https://pub.dega-akustik.de/DAGA_2018/data/articles/000261.pdf) (visited on 07/15/2021).